



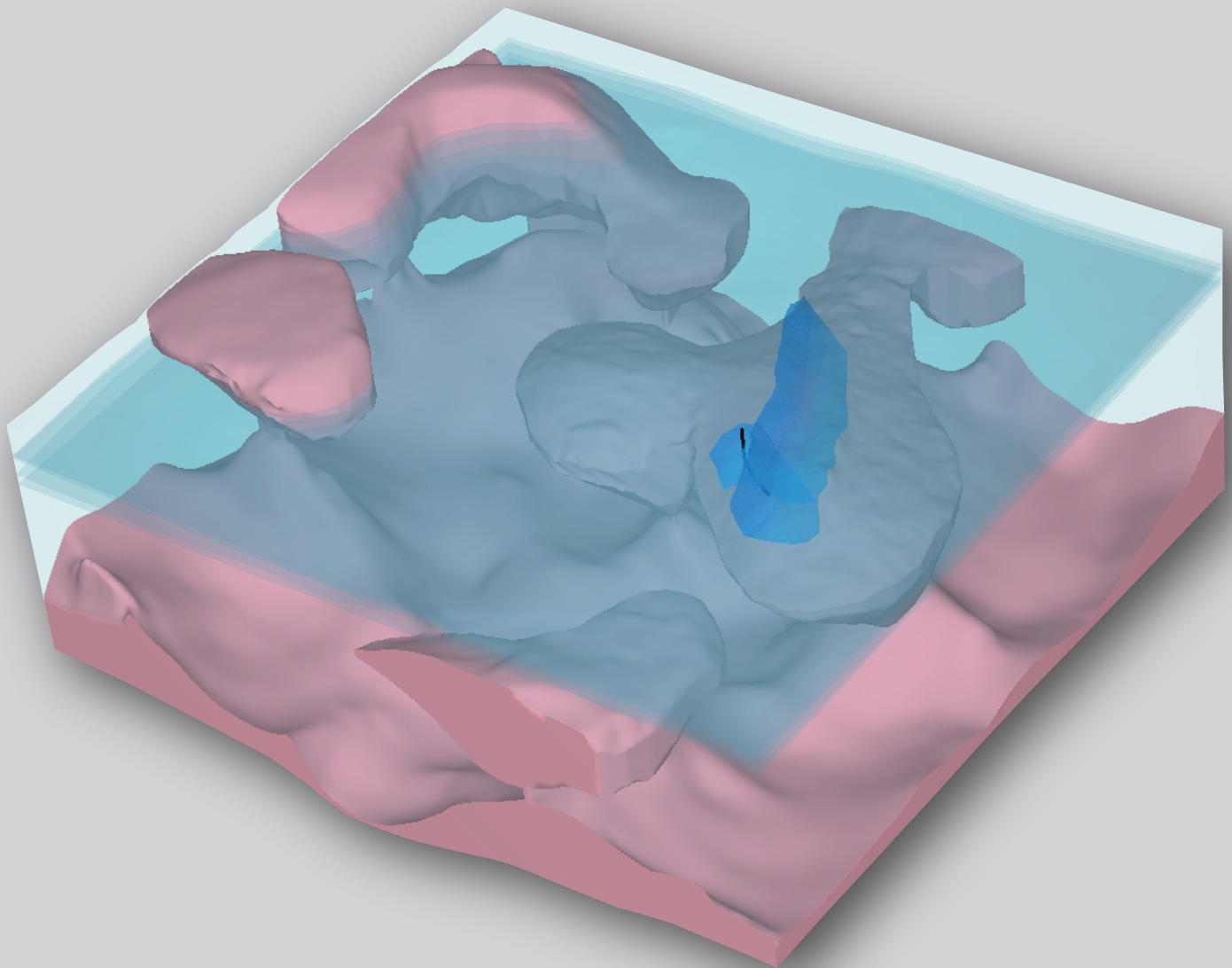
UNIVERSITAT DE
BARCELONA



TEXAS Geosciences

The University of Texas at Austin
Jackson School of Geosciences

GEOMECHANICAL STUDY OF THE TARFAYA BASIN WEST AFRICAN COAST USING 3D/2D STATIC MODELS AND 2D EVOLUTIONARY MODELS



Directors de tesi:
Toby W. D. Harrold
Maria A. Nikolinakou

Jean Joseph van der Linden
d'Hooghvorst Roríguez

Abril 2021

Tutor de tesi:
Alejandro Marcuello Pascual

Departament de Dinàmica de la Terra i de l'Oceà
Facultat Ciències de la Terra, Universitat de Barcelona



UNIVERSITAT DE
BARCELONA



TEXAS Geosciences
The University of Texas at Austin
Jackson School of Geosciences

Departament de Dinàmica de la Terra i de l'Oceà

Facultat de Ciències de la Terra

UNIVERSITAT DE BARCELONA

**GEOMECHANICAL STUDY OF THE TARFAYA BASIN
WEST AFRICAN COAST
USING 3D/2D STATIC MODELS AND 2D
EVOLUTIONARY MODELS**

Memòria de Tesi Doctoral -com a compendi d'articles- presentada per **Jean Joseph van der Linden d'Hooghvorst Rodríguez** per optar al grau de Doctor en Ciències Geològiques per la Universitat de Barcelona. Aquesta tesi ha estat realitzada dintre del Programa de Doctorat de Ciències de la Terra (HDK09) sota la direcció dels **Dr Maria A. Nikolinakou, Dr. Toby W. D. Harrold** i tutelada per **Dr. Alejandro Marcuello Pascual**.

Jean Joseph van der Linden d'Hooghvorst Rodríguez

Barcelona, abril 2021

Dr. Maria A. Nikolinakou

Dr. Toby D. W. Harrold

Dr. Alejandro Marcuello Pascual

The cover photo shows the representation of the salt geometry (in pink) from the study location in the Tarfaya basin using Elfen software. The suprasalt sediments and the faults located above the salt structures are shown with different levels of transparency and in blue colours. The Sandia-1 exploratory well is shown as a black trajectory crossing the faults and targeting the Sandia salt diapir.

This work has been carried out in the Departament de Dinàmica de la Terra i de l'Oceà, within the Facultat de Ciències de la Terra from the Universitat de Barcelona. This thesis has been funded by Repsol Exploración S.A. We wish to thank UT Geofluids consortium, funded by Shell, Hess, ConocoPhillips, BP, Oxy, BHP, ExxonMobil, Chevron and Petrobras. This research project has used academic software licenses of Elfen and Elfen Horizon provided by Rockfield Software Ltd. We also wish to thank Repsol Exploración S.A. for providing and allowing publication of the data used in this research.

*To my father and mother,
And to my brothers.*

To Marisol, I love you.

La nature enseigne celui qui la regarde en face
et qui l'explore jusqu'au fondement secret.

Louis Cattiaux
I, 62', Le Message Retrouvé

Acknowledgements

There is an author of this thesis, together with two thesis directors and one thesis tutor, all of them with their name at the front of this collection of pages. However, I have learned that a PhD is not only a thesis and scientific contributions. The greatest part of a PhD is composed by experiences, interactions with other researchers, travels, excitements and disappointments, happiness and a good deal of suffering! In my case, all this collection of experiences has been shared with other people that have added value and weight to this final product, my research. Without them, the process would have been much more dull and, I have no doubt, impossible to accomplish. For that, I want to dedicate these lines to all of them, because they are the cause for the evolution that now I see in myself, not only as a researcher, but also as a person. Thanks to all of you!

First of all, thanks to my thesis director Maria Nikolinakou, thanks for your tireless help all the way up to the end. I still remember the first time I met you in an evening during the Geofluids poster session in Austin, 2016. That was my first real contact with my PhD, without even being officially engaged in it! Since then, your support and guidance have been invaluable to continue this adventure. The endless revisions of papers and presentations, the suffering with our models, the discussions about geomechanics, the stressful Geofluids preparations, etc. I have learned so much from all of that and I am very grateful that the quality of your research and work has been added to my thesis. I feel really lucky to have been able to work with you all these years. For all that and for a lot more, thanks a lot Maria!

And thanks to my other thesis director Toby Harrold, thanks for engaging me into the complex beginning of this PhD. Thanks for the faith you put in me during the first days, when we barely knew each other and we had a totally new path ahead of us. It was you that introduced me to Geofluids and, thanks to that, I became part of this awesome consortium. You are the person who forced me to move, to try harder, to go forwards even if it is scary out there! Your positive thinking, good mood and your “enjoy the good things” has allowed me to remain sane and avoid being swallowed by the research. Our nights enjoying Austin and our micheladas for “a successful presentation” will now be part of my most cherished memories of the past four years. Thanks Toby!

Moltes gràcies també al meu tutor de tesis, Alejandro Marcuello. La teva predisposició a ajudar i a discutir de qualsevol cosa ha facilitat en gran mesura l'èxit d'aquesta aventura que ha estat el doctorat. Gràcies per haver-me ajudat en tots els processos burocràtics de la universitat, cosa que no t'estaré mai prou agraït. Sempre has estat disposat a parlar de tot, a ajudar en el que fos i a fer l'esforç d'entendre i de llegir un tipus de recerca fora de la teva zona d'actuació, aportant nous punts de vista i ajudant a clarificar el missatge. Per tot això, gràcies!

Huge thanks also to the individuals that may be considered my “unofficial thesis directors”. The first of them is Peter Flemings. I am more than grateful to you for making me part of the Geofluids consortium. You taught me to move outside my comfort zone. The opportunities you brought me during these years have contributed to this thesis success, such as the retreats to Marble Falls, the stays in Austin, the opportunity to be part of the University of Texas at Austin community, etc. I also thank you for your invaluable contribution to the papers we published during this years. Your high level of rigorousness have given a quality to my research that would have been impossible to achieve otherwise. You have created a school of thought and I am honoured to have been part of it during my PhD.

L'altre “director a l'ombra” és l'Oscar Fernández, però tu ets el primer responsable que aquest doctorat vegi la llum. Has estat la persona que va dissenyar en un inici la idea d'aquesta recerca, més de 5 anys enrere. Recordo la teva proposta com si fos ahir: “i si tens ganes de tirar-te a la part fonda de la piscina, hi ha aquesta proposta de doctorat que et pot interessar”. Doncs si, al final la piscina era més fonda del que jo creia, però ha valgut la pena. La teva visió ha donat una dimensió extra a la tesi, en especial la part de modelat evolucionari. Gràcies per la confiança i per tota l'ajuda que m'has donat!

Thanks also to John “Jack” Germaine and to Michael Hudec. Their help in the geomechanics and salt tectonics side, respectively, has helped me to understand the area of study I have been exploring the last years and to learn from the best professionals in their fields. I consider it an honour to have been under your teachings.

I would like to thank Repsol for the opportunity they gave me in using all the data and resources to complete this research. Thanks also for allowing me to share in countless conferences and events the knowledge and results we have been generating during these years.

To all the good friends that I have acquired during the time spent in Austin, big thanks! Thanks to Baiyuan, who had the infinite patience to teach me Elfen for the first time. Your research and your achievements have been an example for me to continue and finish this thesis. Thanks to Mahdi, for your help, teachings and advice on all the aspects concerning modelling, Elfen and geomechanics. Thanks to Stephanie, who began as a AirBnB host during my Austin visits but after all these years I consider you one of the best friends I made there. I will miss our interesting “philosophic” discussions and our “horror movie” nights. I hope you the best on your PhD and on your life! And thanks also to Vinyet, Naiara, Ibai and Sebastian, thanks for the laughs, the time spent enjoying life, the beers, etc. Thanks for all!

And thanks also to all the people I met in Repsol during these years, my Repsol friends! Thanks to all the Geohazards team, to Toby, Pascal, Sara, Juanma, German and Marius. Thanks for adopting me as one of you, despite not being part of the company by itself. Thanks also to the “tupper club”, Oscar, Pablo, Álvaro and Nino. Thanks to Pablo especially,

because he helped me with the kinematic models and all things concerning Move and structural geology. Thanks to all of you!

I also want to extend my gratitude to Rockfield and the great people I met there. Thanks to Adam Bere and John Cain for their engagement in providing Elfen licences to use during this research. I am grateful to you for letting me spend some time in your offices and learn in two weeks as much as five months dealing with Elfen on my own! Thanks also to Melanie and Fen for their tireless help dealing with bugs, software errors, model crashes and numerical desperation. My final models are a product of your guidance and advice. And thanks to Dan and Glyn, for their contributions in this research by discussing results, suggesting changes and helping with the evolutionary models. Thanks to all of you!

Gracias eternas a mi familia. A mi padre y a mi madre, a mis hermanos Louis e Isidro. El soporte y el interés que me habéis otorgado han hecho posible que acabe esta nueva etapa de mi vida. A pesar de la distancia, el calor de la familia ha sido el motor que me ha ayudado a superar los malos momentos, pero también a darme cuenta de todo lo que os debo y de lo fuerte que me siento sabiendo que estaréis a mi lado toda mi vida. Todo paso que dé en este camino será apoyado en vosotros, así que gracias por todo. Y gracias también por todo ello a mi familia Alicantina: a Marisol, a Paco y a Marta. Gracias por haberme adoptado como “el catalán” de la familia.

Finalmente, pero no por ello menos importante, Marisol. Gracias. Gracias infinitas por estar a mi lado estos últimos siete años. Espero que sean unas cuantas eternidades más, porque contigo las cosas se ven nítidas, los objetivos claros. Tu cariño es mi motivación, tus ganas de vivir son mi estímulo, tu alegría es mi filosofía. Gracias por animarme en los momentos más oscuros, aunque en esos momentos ambos sufrimos. La paciencia que has tenido durante estos duros años de doctorado no te los voy a poder agradecer lo suficiente. Pero lo intentaré, prometido.

25th March 2021

Table of Contents

ABSTRACT	1
PREFACE	7
Motivation and objectives	9
Thesis structure.....	11
CHAPTER 1. INTRODUCTION	15
1.1 Modelling of salt systems	17
1.1.1 Kinematic restoration.....	17
1.1.2 Physical modelling	18
1.1.3 Basin modelling.....	18
1.1.4 Geomechanical modelling	19
1.1.4.1 Static geomechanical models.....	19
1.1.4.2 Evolutionary (forward) geomechanical models	20
1.2 Geologic environment.....	21
1.2.1 Geological history	22
1.2.2 Seismic data and interpretation.....	23
1.2.3 Kinematic restoration.....	24
1.2.4 Well data.....	27
CHAPTER 2. SUMMARY OF RESULTS.....	31
2.1 Introduction	33
2.2 3D static geomechanical model.....	34
2.2.1 Model setup	34
2.2.2 Model results.....	38
2.2.3 Sensitivity analysis results.....	44
2.3 2D static geomechanical model.....	47
2.3.1 Model setup	47
2.3.2 Model results.....	48
2.3.3 Sensitivity analysis results.....	51

2.4	2D evolutionary geomechanical model.....	56
2.4.1	Model setup	56
2.4.2	Model results.....	60
2.4.3	Sensitivity analysis results.....	63
2.4.3.1	MV1 results (variation of shortening rates)	64
2.4.3.2	MV2 results (basal triangular feature).....	66
2.4.3.3	MV3 results (variation of temperature gradient).....	67
2.4.3.4	MV4 results (variation of burial history)	68
2.4.3.5	MV5 results (variation Plio-Quaternary sedimentation rates).....	69
CHAPTER 3. SUMMARY OF DISCUSSIONS		73
3.1	Introduction	75
3.2	Static modelling	76
3.2.1	Stress reduction mechanism	76
3.2.2	Static model comparison.....	77
3.2.3	Input uncertainty.....	80
3.2.4	Limitations and future lines.....	80
3.3	Evolutionary modelling.....	83
3.3.1	Influence of sedimentation rates on diapir evolution.....	83
3.3.2	Influence of shortening rates on stress distribution	84
3.3.3	Layer thicknesses comparison between kinematic restoration and evolutionary geomechanical models	85
3.3.4	Parameters with minor influence on the Tarfaya basin evolution.....	87
3.3.5	Limitations and future lines.....	88
CHAPTER 4. CONCLUSIONS		91
4.1	Introduction	93
4.2	Static geomechanical modelling conclusions.....	93
4.3	Evolutionary geomechanical modelling conclusions	95

REFERENCES 99

ANNEXES 113

Annex 1: Comparison of stresses in 3D vs. 2D geomechanical modelling of salt structures in the Tarfaya Basin, West African coast..... 114

Annex 2: Insights from sensitivity analysis of geomechanical modelling of a salt structure offshore west Africa 130

Annex 3: Geologically constrained evolutionary geomechanical modelling of diapir and basin evolution: A case study from the Tarfaya basin, West African coast 140

Annex 4: Sandia-1 well log data and CBIL data..... 162

List of Figures

CHAPTER 1

Figure 1.1: Location map for the Tarfaya basin and geological features. Seismic section (Figure 1.2) is indicated by the red line PP'. Restored section (Figure 1.3) is indicated by the green line QQ'. Sandia-1 (black circle) and Cap Juby-1 (black triangle) well-head locations are also shown. The offset wells (black squares) used for the pre-drill pore pressure and stress predictions are also shown. The Geographic Coordinate System used is ETRS 1989.21

Figure 1.2: Seismic interpretation across a transect in the deep part of Tarfaya basin (red line PP', Figure 1.1). This section combines 3D seismic (NW side) with vintage 2D reflection multi-channel (SE side). Location of the seismic line is also highlighted with the red rectangle on the present-day section in the sequential kinematic restoration model (Figure 1.3).....23

Figure 1.3: Sequential kinematic restoration of a regional section across the Tarfaya basin (green line QQ', Figure 1.1), whose present-day geometry is based on 2D and 3D seismic interpretation, from Triassic to present day. Locations Y and Z in red are used for thickness extraction and burial history reconstruction (Figure 2.16). Location of Sandia-1 exploratory well and projection of Cap Juby-1 well are shown on the present-day panel. Dashed red box indicates location of seismic section in Figure 1.2. WD: Western diapir; SD: Sandia diapir.26

Figure 1.4: (a) section showing Tertiary sediments above the Sandia diapir (in pink). The four sand reservoirs (yellow layers) targeted by the Sandia-1 well (dashed red line) are affected by an array of faults (black lines). (b) Structural map of the top of reservoir R1 and the faults affecting it. Position of Sandia-1 well-head and its trajectory are shown by red dot and red line, respectively.....27

Figure 1.5: Profile along Sandia-1 well showing overburden stress (solid brown line) and minimum horizontal stress, σ_h (solid black line) from the predrill study. The σ_h prediction from 3D static model (dashed black line; see Figure 2.2b) is included for comparison. The data points from the well drilling are represented by leak-off tests (LOT) measurements, formation integrity tests (FIT) measurements and drilling induce tensile fractures (DITF) observed (yellow, red and green dots, respectively). The decrease of σ_h near the salt interface (at 3,000 m) predicted by the 3D model is consistent with data obtained during the drilling operations.28

Figure 1.6: Stratigraphic log showing the lithologies prognosed before and after the drilling of the Sandia-1 exploratory well, both in measured depth (MD) and true vertical depth (TVD). R1, R2, R3 and R4 correspond to the targeted reservoirs by the Sandia-1 well (Table 1.1).29

CHAPTER 2

- Figure 2.1:** Static 3D geomechanical model. (a) Model geometry representing the stratigraphic distribution of sand, shale and salt horizons. The green dot represents the position of the Sandia 1 well head. (b) 3D salt structure, major faults and the Sandia well trajectory (green line).35
- Figure 2.2:** (a) Minimum stress ratio results (K) for different vertical sections across the model. The stress ratio is higher than its corresponding initial value for sediments below salt or near deeper salt structures. In contrast, the stress ratio is lower than its initial value at shallow depths above salt, around the faults and near the crest of the Sandia diapir. (b) Minimum stress ratio (K) for section A-A' near the well location. The stress ratio is notably reduced at the bottom part of the well above salt. Initial minimum stress ratio is 0.8 (light green contour colour) for intermediate and deepest shales, and 0.75 (dark green contour colours) for the shallowest shales and two reservoirs.40
- Figure 2.3:** Minimum principal stress plunge results for different vertical sections across the model. The minimum principal stress remains horizontal in most part of the model, except in few localized areas near salt, where the orientation varies less than 20° from the horizontal plane.....41
- Figure 2.4:** Orientation of maximum and minimum horizontal stresses, σ_H and σ_h , for two horizontal sections of the 3D model. Contours represent the azimuth of σ_H . The blue and red arrows illustrate the directions of σ_H and σ_h , respectively. The original east-west direction of σ_H changes in locations near the salt structures and around the major fault.41
- Figure 2.5:** (a) Horizontal east-west displacements across the model, showing mostly westward displacements (blue contours) concentrated above the eastern diapir and around the major fault. Near the well location (section A-A'), the results display greater westward displacements for the sediments in the footwall compared to the hanging wall. (b) Horizontal north-south displacements across the model, showing mostly northward displacements (orange contours) located on the north end of the Sandia diapir. Near the well location (section A-A'), the results show no significant north south displacements. (c) Vertical displacements across the model, showing downward movement (blue contours) around the hanging wall of the major fault. Near the well location (section A-A'), the vertical displacements are concentrated on the hanging-wall side of the fault.43
- Figure 2.6:** Difference in prediction of horizontal stress σ_h between sensitivity analysis and base-case models along the Sandia-1 exploration well. The major difference is obtained when varying the Elastic Modulus, but it does not exceed 0.15 ppg. This indicates little effect of the elastic parameter variation on horizontal stress. Sea surface located at upper part of the plot and salt diapir located at bottom.45

Figure 2.7: (a) 3D model showing the geometry of the salt and faults, together with the cross section (in red) used for the 2D model geometry. (b) Geometry of the 2D model.....	47
Figure 2.8: (a) Horizontal to vertical stress ratio predicted by the 2D model. The ratio changes near the salt structures, compared to its initial value of 0.8 (green contours). Specifically, it decreases above the Sandia diapir, reaching values around 0.6. (b) Geomechanical prediction (solid lines) for horizontal (green) and vertical (blue) stress along a vertical profile W (in a) compared with uniaxial stresses (dashed lines). Geomechanical horizontal stress is lower than uniaxial, reaching a maximum difference of 4.5 MPa at the salt-sediment interface.	49
Figure 2.9: Sediment-displacement magnitude (colour contours) and displacement direction (arrows). Displacements have an overall westwards trend across the model and are largest on the footwall side of the fault located above the Sandia diapir (red contours). The detailed section around the Sandia diapir shows the relation between the salt flux and the displacement of the sediments located above.	50
Figure 2.10: Horizontal strain across the 2D model. Red contours represent extensional strains and blue contours represent shortening strains. A region of extensional horizontal strain develops at the crest of the Sandia diapir, between the two faults. Shortening horizontal strains develop at both sides of the Western diapir.	51
Figure 2.11: Stress profiles along vertical section located at the crest of the Sandia diapir for the base-case model (solid lines) and the model where the salt lithology is changed by shale (dashed lines). The horizontal stress reduction near the salt structure is not present when the diapirs are substituted by shale lithology. Vertical stress is similar in both cases (blue lines).....	52
Figure 2.12: Results of stress ratio (contours) and sediment displacements (arrows) for (a) 2D basecase model and (b) 2D model with flat sea floor. The leftwards displacement trend in (a) disappears when the sea floor is flat. The stress ratio reduction above the Sandia diapir in the basecase model is slightly reduced when the sea floor is flattened.	53
Figure 2.13: Stress ratio results above the Sandia diapir predicted by (a) the base-case model; (b) the model without the western diapirs; (c) the model with thicker salt columns.....	54
Figure 2.14: Change in principal stress values between 2D sensitivity analyses and base-case model results. Salt rheology and additional salt diapirs yield the greatest stress changes. Variation of elastic parameters does not noticeably affect the stress results.....	55
Figure 2.15: (a) Initial geometry for the salt (pink) and shale (gray) layers in the geomechanical evolutionary Elfen model (BC model), along with basic model dimensions and boundary conditions. (b) Definition of deposition horizons: at	

the beginning of each stage, the upcoming layer thickness is obtained from burial history curve (Figure 2.16a) and applied at the right side of the model (location A), starting at the current top surface. For example, for the Jurassic modelling stage, the deposited-layer thickness is 4500 m (blue line, Figure 2.16a) defines the elevation of the Jurassic deposition horizon at the right end of the evolutionary model (A). The Jurassic bathymetric slope obtained from the kinematic restoration (Figure 1.3; Table 2.7) is then used to define the Jurassic horizon across the model. Sediment compaction and salt mobilization modify the geometry of the sea floor, which becomes the baseline for the next deposition stage (b2) (c) Shortening application curves for the base-case model (solid line) and a variant model (sigmoid dashed line).57

Figure 2.16: Burial history curves resulting from thickness extractions in the sequential kinematic restoration model of the Tarfaya basin section (Figure 1.3). (a) Burial history curve at location Y (SE of Sandia diapir, Figure 1.3). (b) Burial history curve at location Z (NW of Western diapir, Figure 1.3).....57

Figure 2.17: Hardening parameters for SR3 material model used for the sediments (Rockfield 2017).....60

Figure 2.18: Evolution of the Sandia diapir predicted by the base-case geomechanical model. Profile A (vertical black line) indicates the location where the layer thicknesses from burial history diagram (Figure 2.16a) are applied. (a) Initial geometry representing the top Triassic evaporites (pink) and an initial thin layer of Jurassic sediments (blue); (b) End of Jurassic deposition (blue). The salt diapir reaches the sea floor; (c) Mid-stage of Lower Cretaceous sediment deposition (dark green). Salt is about to break out into a salt sheet and source layer has thinned; (d) End of Lower Cretaceous deposition (dark green) with salt sheet formed downslope and salt overhang upslope. The source layer is welded on both sides of diapir and connected to the upper part by a salt stem; (e) End of Upper Cretaceous deposition (light green). Diapir is buried. Regional shortening is activated during this stage; (f) Paleocene to Miocene deposition. Shortening continues. Salt volume in pedestal decreases and diapir stem thins, while the diapir bulges upwards, arching its roof sediments; (g) Present-day, following Pliocene and Quaternary deposition. Shortening continues. Salt volume in pedestal and in stem further decreases, as does the extent of the salt sheets. The diapir bulges upwards arching its roof sediments.62

Figure 2.19: (a) Final geometry of the Sandia diapir as predicted by the BC model; (b) final geometry of the Sandia diapir as predicted by the MV1 model, using the sigmoidal shortening rates (dashed line Figure 2.15c); (c) present-day geometry and contours of the horizontal-to-vertical effective stress ratio K for BC model; (d) present-day geometry and contours of the horizontal-to-vertical effective stress ratio K for MV1 model. The uniaxial K_0 value is 0.8 (light blue contour colours). K higher than 1 (warm contour colours) represent σ'_h higher than σ'_v .

K below 0.8 (darker blue contour colours) represent decreased σ'_h and lateral extension.	65
Figure 2.20: Stress profiles at vertical section along the sedimentary roof at present-day (inset) for (a) BC model and (b) model MV1. Depth zero indicates sea floor.	65
Figure 2.21: Final geometry of the Sandia diapir as predicted by (a) the BC model and (b) the MV2 model, with a flat salt base. The lack of the basal triangular feature below the diapir generates a shorter and thicker final salt geometry.	66
Figure 2.22: Final geometry of the Sandia diapir as predicted by (a) the BC model, using a temperature gradient of 31°C/km and (b) the MV3 model, using a temperature gradient of 36 °C/km. The higher temperature gradient used in MV4 generates a final diapir geometry that is shorter and thicker compared to the BC geometry.	67
Figure 2.23: Stages of evolutionary model using the burial history curve from the NW end of the basin (Figure 2.16b) and applied at location B, together with a thicker initial salt source layer compared to the BC model. (a) Initial geometry representing the top Triassic, with salt layer (pink) and initial thin layer of Jurassic sediments (blue); (b) Salt diapir reaches the sea floor at the end of Jurassic; (c) Salt forms overhangs at both sides, buried by Early-Cretaceous sediments (dark green). Source layer welds. (d) Further Early-Cretaceous sedimentation buries the diapir. Salt from pedestals increases overhang thickness; (e) Late-Cretaceous sedimentation (light green) drive bulging of diapir crest. Shortening begins; (f) Shortening narrows the diapir stem and drives salt from overhangs toward the diapir centre. Salt bulges upward; (g) Salt pierces the roof and upbuilds to the surface at present day.	69
Figure 2.24: Rate of deposition for different geologic intervals from Jurassic until present day. Each interval is represented by a coloured block, the width of which is proportional to the duration of the geologic interval. The application of the tectonic shortening in the model is represented by the grey horizontal bar. The different diapir evolution phases are shown by the blue horizontal bars.	70

CHAPTER 3

Figure 3.1: Horizontal to vertical effective stress ratio predicted for sediments above the Sandia diapir for (a) the 3D static model and (b) the 2D static model. Both models present a reduction of stress ratio of about 0.6 at the crest of the structure, compared with the initial 0.8. However, the reduction in the 2D model affects a broader area above the diapir. Vertical profiles W and W' are used to quantitatively compare the stress change between the 3D and 2D model (Figure 3.2).	77
Figure 3.2: Horizontal stress change with depth normalized by salt depth for 3D static (red line) and 2D static (green line) models along vertical locations W and W'	

(Figure 3.1) above the salt body, respectively. The stress perturbation due to salt attenuates faster with distance from the salt body in the 3D model compared to the 2D case. Normalized depth of zero represents the sea floor and 1 represents the diapir crest.78

Figure 3.3: Illustration of the solution for the vertical stress distribution in an elastic, semi-infinite medium caused by the application of a 2D load (represented as a strip load) and a 3D load (represented as a circular load) using the solution from Boussinesq (1885). There is no gravity load. Blue and red dots correspond to the values of vertical stress at 6 m from the load for the 3D and 2D case, respectively, where $B = 1$ m and $q = 1$ MPa/m. The load in this figure is applied from below to represent the influence of the salt diapir on its sedimentary roof. Modified from US Army Corps of Engineers (1990).....79

Figure 3.4: Comparison of horizontal salt pressure gradient between BC model (blue line) and MV4 model (green line). We define horizontal salt pressure gradient as the difference between the sediment overburden load on salt away from the diapir and the salt pressure inside the diapir at the same depth (inset). The higher sedimentation rates in model MV4 generate a consistently higher horizontal salt pressure gradient with time. The point in each line represents the time when the source layer welds.....84

Figure 3.5: Comparison of layer thickness predicted by the kinematic restoration model (Figure 1.3) and the BC evolutionary geomechanical model (Figure 2.18) at 2 locations: (a) far from the diapir above a salt high (Y vs. A in Figure 1.3 & Figure 2.18; solid shapes); and (b) near the diapir, above a salt weld (X vs. C in Figure 1.3 & Figure 2.18; empty shapes). Layers considered: Jurassic, Upper Cretaceous and Oligocene units (blue, green and orange colours, respectively). Comparison times: Late Cretaceous, Oligocene and present day (triangular, circle and square shapes, respectively). Points on the 1:1 dashed line indicate agreement between the two models. Points closer to the 1:1.2 dashed line indicate that the evolutionary geomechanical model predicts more compaction.86

List of Tables

CHAPTER 1

Table 1.1: Tertiary sand reservoirs targeted by the Sandia-1 well (black circle, Figure 1.1).	27
--	----

CHAPTER 2

Table 2.1: Summary of input properties for the different horizon layers defined in the 3D static model.....	36
Table 2.2: Input material parameter values for poroelastic sand and shale sediments.	38
Table 2.3: Input material parameter values for viscoplastic Munson-Dawson model (Munson 1997; Fredrich et al. 2007b).....	38
Table 2.4: Summary of sensitivity analysis for the 3D static model	44
Table 2.5: Statistical summary of sensitivity analyses results, reporting comparison ratio S (eq. 7).....	46
Table 2.6: Summary of the sensitivity analysis run for the 2D static model.....	51
Table 2.7: Thickness and sea floor angles from sequential kinematic restoration model at the end of each geologic time interval.	58
Table 2.8: Material properties for salt (Munson 1997; Fredrich et al. 2007a)	59
Table 2.9: Material properties for sediments (Nygard et al. 2006; Rockfield 2017)	60
Table 2.10: Summary of the sensitivity analysis run for the 2D evolutionary model.....	63

ABSTRACT

This thesis uses different variants of geomechanical modelling approaches to investigate stress, strain and geometry distribution and evolution through time of the Tarfaya salt basin, located on the West African coast. This work has been conducted by geomechanically simulating a sector of the Tarfaya basin containing key features such as diapirs, faults and encasing sediments using 3D and 2D static models and 2D evolutionary models. The study will allow to conclude whether it is possible to adopt 2D models as a good approximation of the more complex 3D models. In addition, this research will test the viability of applying evolutionary geomechanical modelling to a real basin to obtain insights of the basin formation and evolution through time.

The 3D and 2D static geomechanical models of the Tarfaya basin system allowed to predict the stresses and strains in the basin at present day and compare the results between both approaches and with wellbore data. Both models are based on present-day basin geometries extracted from seismic data and use a poro-elastic description for the sediments based on calibrated log data and a visco-plastic description for the salt based on values from Avery Island. The models predict a significant horizontal stress reduction in the sediments located at the top of the principal salt structure that was modelled, named the Sandia diapir. This stress reduction is consistent with the measured data coming from an exploratory well drilled above Sandia. However, the 2D static geomechanical model shows broader areas affected by the stress reduction compared to the 3D model and overestimates its magnitude by less than 1.5 MPa. The pattern of differential displacements seen in both 3D and 2D models for the sediments on top of the Sandia diapir is similar. These results highlight the possibility of using 2D static modelling as a valid approximation to the more complex and time consuming 3D static models.

A more in-depth study of the 2D static model using sensitivity analysis yielded a series of interesting observations: (1) the salt bodies and their geometry have the strongest impact on the final model results, controlling the stress distribution for the sediments on top of the diapir; (2) the elastic properties of the sediments do not impact the model results neither in the 3D approach nor in the 2D. What seems to affect most the model results are the material contrasts defined in the model; (3) the sea floor geometry (as tested in 2D) also seems to contribute to changes in the stress distribution of the sediments, although to a lesser extent than the effect of the salt bodies. In other words, the correct definition of the sediments with the highest material contrasts such as salt should be a priority when building static models. Such definition should be ranked ahead of the precise determination of the rheologic parameters for the sediments present in the basin.

In this thesis, we also present the results of introducing an evolutionary geomechanical modelling approach to the Tarfaya basin. This study incorporates information of burial history, sea floor geometry and tectonic loads from a sequential kinematic restoration model to geologically constrain the 2D evolutionary geomechanical model. The sediments in the

model follow a poro-elastoplastic description and the salt follows a visco-plastic description. The 2D evolutionary model predicts a similar Sandia diapir evolution when compared to the kinematic restoration model and the present-day seismic information. This proves that 2D evolutionary geomechanical modelling can offer a significant advance in the study of the basin, by not only providing the stress and strain distribution and salt geometry at present day, but also reproducing their evolution during the Tarfaya basin history.

Sensitivity analysis on the evolutionary model indicates that temporal and spatial variation in sedimentation rate is a key control on the kinematic structural evolution of the salt system. The variation of sedimentation rates in the model controls whether the modelled salt body gets buried by Tertiary sediments (after a continuous growth during the Jurassic and Cretaceous periods) or is able to remain active until the present day. Also, the study location is affected by the Atlas orogenic inversion during the Cenozoic. The imposed shortening affects the final stress distribution of the sediments at the present day. We found that a rate of shortening that increases progressively, peaks and decreases progressively leads to a reduction of stresses in the sediments located above the salt structure, in line with the results obtained by the static modelling approach.

To conclude, the results obtained during this study allowed us to understand the formation and evolution of the diapirs in the Tarfaya basin using carefully built geomechanical models. In particular, the 3D and 2D static models have provided useful insights in the mechanics of the present-day distribution of stresses above the salt. Although the 3D static models are a more complete description of the problem, the study demonstrates that carefully built 2D static models can provide information comparable to the 3D models, but without the time and computational power requirements of the 3D models. That makes the 2D approach very appropriate for the exploration stages of a particular prospect. If carefully built, such 2D models can approximate and yield useful information, even from complex 3D structures such as the Tarfaya basin salt structures. This thesis also concludes that incorporating kinematic restoration data into 2D evolutionary models provides insights into the key parameters controlling the evolution of the studied system. Furthermore, it enables more realistic geomechanical models, which, in turn, provide more insights into sediment stress and porosity.

PREFACE

Motivation and objectives

Geomechanical modelling techniques are becoming an increasingly popular approach to obtain stress and strain information from potential hydrocarbon targets for oil and gas exploitation (e.g., Fredrich *et al.* 2007b; Fernandez *et al.* 2015; Segura *et al.* 2016; Heidari *et al.* 2018). This approach offers a complement to the pore pressure and fracture gradient studies traditionally performed in these settings, such as offset well, basin modelling and seismic velocity analysis. Geomechanical models can also be built using the inputs of these traditional studies to improve or increase confidence in the pore pressure and stress predictions.

A geomechanical model can represent 3D or 2D geometries, and can be a static or evolutionary (or forward) model. The selection between these different approaches becomes important during hydrocarbon exploration and can be affected by time and budget constraints or required accuracy of the results. For example, 3D static models can provide the user with a full stress, strain and pressure description of the studied basin. These models, however, have the limitation of being time-consuming to build and are computationally more expensive to run. The 2D static geomechanical modelling may be a good alternative to the 3D but requires additional geometric simplifications and assumptions. In some cases, these simplifications may lead to inaccurate results or final geometries that do not capture the full complexity of the modelled basin. Even in understood cases, both approaches may need parameters that are uncertain for the user, requiring sensitivity analysis to understand their influence and calibrate them.

On the other hand, both 3D and 2D geomechanical static models do not account for the processes taking place during the basin formation and evolution. While static models can conveniently represent the present basin geometries, they fail to reproduce their evolution in time. Here is where the geomechanical evolutionary models can provide greater insights. Nevertheless, the final geometries produced by an evolutionary approach may not necessarily match the ones present in the studied basin. This fact requires the user to use various geological constraints and a painstaking iterative process to achieve the desired final geometric results.

Previous studies have successfully used static geomechanical models to investigate the present geologic processes in salt basins, either using idealized salt geometries (e.g., Fredrich *et al.* 2003; Mackay *et al.* 2008; Luo *et al.* 2012; Nikolinakou *et al.* 2012) or actual salt geometries derived from seismic surveys (e.g. Fredrich *et al.* 2007b; van der Zee *et al.* 2011; Segura *et al.* 2016; Heidari *et al.* 2018). Other authors have studied the evolution of salt basins using evolutionary geomechanical models (e.g., Ismail-Zadeh *et al.* 2004; Goteti *et al.* 2012; Gradmann *et al.* 2012; Crook *et al.* 2018; Hamilton-Wright *et al.* 2018; Nikolinakou *et al.* 2018a; Thigpen *et al.* 2019). In those cases, the authors have used kinematic restoration models as geologic constrains to drive their models to the desired final basin geometries. While all these studies highlight the value of using geomechanical modelling to understand salt tectonics,

rarely has the same salt basin been studied using all the modelling approaches available. This would provide a global view of both the evolution and the present state of stress and strain of the studied salt basin.

To this end, this thesis aims to apply a full static and evolutionary geomechanical modelling study (both using 3D and 2D) in the same area, the Tarfaya basin. This approach allows investigation of a series of points that make up the objectives of this thesis:

- To investigate the 3D static geomechanical modelling built by the oil company Repsol Exploración S.A. together with Rockfield Software Ltd for the Tarfaya basin. This particular model successfully predicted the stress distribution above the targeted diapir for the planning and drilling of an exploratory well. We aim to answer whether the accurate selection of input parameters was the cause of this success or, on the other hand, the robustness of the model would provide the same answer if another set of parameters for the sediments and salt are introduced.
- To provide insights on the use of more simplified 2D static geomechanical models as a valid approximation to more complicated 3D static models. If those 2D models would provide similar results compared to the 3D model, that means the 2D static approximation is valid and would save time and money for future modelling in other basins.
- To investigate 2D static models and establish which input parameters are critical for the correct definition of these models. In addition, that will provide a way to understand the mechanisms that cause the stress and strain distribution of this particular basin at present day.
- Finally, to test if 2D evolutionary models can be used in a simple way to represent the history of the studied basin. In addition, and similarly to the static approach, to study the influence of input parameters to allow establishment of which ones are critical for the correct definition of these models.

Consequently, we list below the list of tasks that the present thesis will need to address in order to answer all the objectives exposed previously:

- Interpret the results and stress and strain generation mechanisms from the full 3D static geomechanical model of the Sandia salt structure in the Tarfaya basin.
- Build a representative 2D static geomechanical model able to capture the key findings of the 3D model version, allowing a faster and simpler model definition and facilitating (or helping) the interpretation of the model results.
- To build a 2D evolutionary geomechanical model of the Tarfaya salt basin to investigate the geological processes that took place during its formation and lead to the present geometries and state of stress and strain.
- To perform a sensitivity analysis study of the principal model inputs for the three model approaches (3D static, 2D static and 2D evolutionary) and assess their impact

on the overall modelling results. This will allow a more complete understanding of which model inputs need to be accurately constrained for a successful representation of a salt basin.

Thesis structure

The present thesis has been written as a compilation of scientific articles published in journals indexed by the Journal of Citation Reports (JCR) or by Scopus. The memoir has been organised in four chapters:

- CHAPTER 1 is an introductory section that aims to provide the reader with some contextual information to fully understand the results and discussions tackled in the subsequent chapters. On this basis, the chapter has been organised in two differentiated parts. Section 1.1 presents and briefly describes the principal modelling approaches used for the understanding of salt basins. The geomechanical modelling approach (both static and evolutionary) is introduced here. Section 1.2 presents the study area in which the thesis focuses on (the Tarfaya basin). This subsection explains the geological history of the basin, the seismic data and kinematic restoration models available for this study and the well data from an exploratory well drilled in the area.
- CHAPTER 2 presents the compilation of the main results of the PhD thesis, which are published in the three articles annexed at the end of this memoir (see annexes 1, 2 and 3). After a brief introduction, this chapter is divided into three sections, one for each geomechanical modelling technique used to model the Tarfaya basin. For each section, we explain the process followed to set up the model, we list the key model results for a reference model (called the base-case model) and we show the results for the different model variants used for the sensitivity analysis. Sections 2.2 and 2.3 are devoted to the 3D static and 2D static geomechanical modelling, respectively. The results of both approaches are published in the first two papers:
 - Hooghvorst, J.J., Harrold, T.W.D., Nikolinakou, M.A., Fernandez, O. & Marcuello, A. 2020. Comparison of stresses in 3D v. 2D geomechanical modelling of salt structures in the Tarfaya Basin, West African coast. *Petroleum Geoscience*, 26, 36–49 (Annex 1).
 - Hooghvorst, J. J., Harrold, T. W. D., Nikolinakou, M. A., Fernández, O., & Marcuello, A. (2019). Insights from Sensitivity Analysis of Geomechanical Modelling of a Salt Structure Offshore West Africa. *American Rock Mechanics Association*. (Annex 2).

The second paper mentioned represents an extension of the sensitivity analysis results for the 2D static approach, introduced in the first paper. Chapter 2.4 addresses the results of the 2D evolutionary geomechanical modelling, published in the third paper:

- Hooghvorst, J.J., Nikolinakou, M.A., Harrold, T.W.D., Fernandez, O., Flemings, P.B., Marcuello, A., 2021. Geologically constrained evolutionary geomechanical modelling of diapir and basin evolution: A case study from the Tarfaya basin, West African Coast. *Basin Research*, 00, 1-20 (Annex 3).

- CHAPTER 3 presents a discussion of the principal modelling drivers for both the studied static and evolutionary models, as well as a comparison between the different models. This chapter is divided into two sections, each of which addresses a different modelling approach (either static or evolutionary). Chapter 3.2 discusses the mechanisms for the stress reduction observed in both the 3D and the 2D static models, compares both approaches and ends by listing the principal modelling inputs that most influence the results, identified by the sensitivity analyses. Chapter 3.3 discusses the contributors for the evolution of the studied diapir, compares the modelled diapir structure with the seismic sections available from the basin and finishes by comparing different diapir evolution scenarios depending on their different geologic constraints applied.

- CHAPTER 4 lists the general conclusions of the present thesis, addressing the initial objectives proposed at the start of this research project (see Motivation and objectives).

CHAPTER 1. INTRODUCTION

1.1 Modelling of salt systems

A great number of hydrocarbon reservoirs in sedimentary basins around the world are located in the vicinity of salt structures (Meyer *et al.* 2005; Warren 2006; Beltrao *et al.* 2009; Yu *et al.* 2014). In salt tectonics, the term “salt” refers to a type of rock that is composed mainly by the mineral halite, although other minerals can also be present in its composition, such as anhydrite, gypsum, sylvite, etc (Jackson & Hudec 2017). Salt rocks are well known in geology for having a viscous rheology that causes them to flow under deviatoric stresses over geologic timescales. As a result, the presence of salt rocks can perturb the stress, strain and pore pressure distribution of the surrounding sediments (Dusseault *et al.* 2004; Orlic & Wassing 2013; Luo *et al.* 2017; Nikolinakou *et al.* 2018a). Traditional methods to predict stresses and pore pressures (Althaus 1977; Zoback 2007) may not be valid, therefore, in such areas and can lead to drilling difficulties, time-consuming operations, wellbore stability problems and, potentially, to endangerment of human life and the environment (Bradley 1978; Seymour *et al.* 1993; Sweatman *et al.* 1999; Dusseault *et al.* 2004).

The understanding of salt basins and their formation and evolution can provide valuable information to minimize the risks associated to drilling in such areas. This understanding is vital, not only in the oil and gas industry, but also for sectors such as the underground storage of H₂ or CO₂. To address this need, a series of modelling approaches have been developed and extensively used in recent years, some of which are briefly introduced below.

1.1.1 Kinematic restoration

Kinematic restoration (McGuinness & Hossack 1993; Rowan 1993; Hudec & Jackson 2004; Trudgill & Rowan 2004; Rowan *et al.* 2016) is an inverse approach that starts with the present-day geometry of a particular basin and aims to reconstruct its past states of deformation. This method uses the structural interpretation of a basin at present-day as a starting point for the restoration process. The subsequent reconstruction of the past basin geometries takes into account processes such as the sedimentation and compaction of material, eustasy, fault-related deformation, salt movement, isostasy and thermal subsidence (Rowan 1993; Rowan & Ratliff 2012). The kinematic restoration methodology reverses these processes and removes their effects on the studied basin. This approach assumes a variety of geometrical models to represent different types of deformation mechanisms, such as bed-length balance (flexural slip), vertical simple shear, inclined simple shear, fault-parallel slip, rigid-body rotation or area preservation (Rowan & Kligfield 1989; Schultz-Ela 1992). It also models processes such as isostasy, thermal subsidence or material compaction analytically, as time – and/or space – dependent functions.

In recent times, some authors have presented restoration approaches using finite element methods to incorporate mechanical material behaviours (usually elastic laws) to aid the approximation of past deformations (Maerten & Maerten 2006; Moretti & Guiton 2006; Durand-Riard *et al.* 2013; Crook *et al.* 2018). Despite the additional constraint, kinematic

restoration approach has the limitation of lacking any prediction of the stress and pore pressure evolution during the basin restoration. In addition, it does not include any mathematical algorithms to constrain flow of viscous materials such as salt (Ismail-Zadeh *et al.* 2001).

1.1.2 Physical modelling

Physical (analogue) modelling is a forward approach that reproduces the evolution of geologic systems at laboratory scale. They use rock analogues with known rheologies such as sand, glass microbeads, silicon, etc. and predefined boundary conditions within a controlled laboratory setup that deforms at smaller spatial and temporal scales (Schellart & Strak 2016; Reber *et al.* 2020). King Hubbert (Hubbert 1937) established three rules for the scaling of physical models based on aspects of similarity: geometric similarity (model lengths must be proportional to natural system and angles must be equal), kinematic similarity (the process timing must be proportional) and dynamic similarity (the acting forces must be proportional). Physical models have been used to represent a wide variety of processes including faulting (Hubbert 1951; Dooley & Schreurs 2012; Corti & Dooley 2015), fold and thrust belts (Ramberg 1981; Massoli *et al.* 2006; Nilforoushan & Koyi 2007; Farzipour-Saein & Koyi 2014), plutonism (Dietl & Koyi 2011) or halokinesis (Koyi 1998; Dooley *et al.* 2015, 2017; Dooley & Hudec 2017). The vertical and horizontal slicing of the resulting analog system can be combined with photography and with topography scanning to provide insights in the evolution and formation of structures observed in geology at present time.

The principal limitations of these models are associated with material and topography scaling, leading to uncertainty on the timing and duration of the geological processes and exaggerated topographies (Schellart & Strak 2016). In addition, this approach does not provide information on the state of stress and pore pressures of the modelled systems. Furthermore, model reproducibility is highly related to human factors affecting model set-up (Schreurs *et al.* 2016).

1.1.3 Basin modelling

Basin modelling is a forward method that studies geological processes in sedimentary basins using geological, petrophysical, geophysical and geochemical data (Hantschel & Kauerauf 2009). Basin modelling has been extensively used by the oil and gas industry to model petroleum systems. Some of the processes simulated by basin models range from deposition and compaction, erosion, heat flow, phase dissolution, to hydrocarbon generation and its accumulation and migration (Ben-Awuah *et al.* 2013). This approach is often used for evaluation of hydrocarbon potential in prospected areas.

In contrast to physical modelling and kinematic restoration, basin modelling incorporates stress and pressure calculations. However, the method commonly assumes that the sediments deform uniaxially (e.g., Bolas *et al.* 2004; Gutierrez & Wangen 2005). This makes

it unable to capture the stress, strain and pore pressure perturbations caused by complex deformation processes such as faulting or halokinesis (e.g., Stigall & Dugan 2010; Thibaut *et al.* 2014).

1.1.4 Geomechanical modelling

Recently, numerical modelling has become a successful option to reproduce the evolution of geologic systems (e.g., Beaumont *et al.* 2000; Kaus *et al.* 2008; Fernandez & Kaus 2014; Duffy *et al.* 2019). In particular, they can be applied in salt tectonics to integrate the basin sedimentation, the salt flow and other processes interacting with them (e.g., Albertz & Beaumont 2010; Allen & Beaumont 2012; Fernandez & Kaus 2015; Baumann *et al.* 2017; Pichel *et al.* 2017).

The geomechanical modelling technique is a numerical approach that allows the incorporation of the poromechanical behavior of the simulated sediments, including non-uniaxial loading and porous fluid flow. It mostly uses finite element techniques to discretize the studied space and solve the governing equations for sediment and fluid flow behavior. Geomechanical modelling is now commonly used for the study of hydrocarbon prospects, especially in non-uniaxial frontier settings such as salt systems or compressional systems (e.g., Willson *et al.* 2002; Dusseault *et al.* 2004). This approach has the advantage of providing valuable insights on the geologic processes affecting the Earth (Nikolinakou *et al.* 2018b).

Geomechanical models can be separated into two categories: static models and evolutionary (or forward) models. The present thesis will use both approaches to study the same salt basin, allowing us to acquire a more complete understanding of the processes affecting the area.

1.1.4.1 Static geomechanical models

Static geomechanical models are based on the present-day geological geometries, making them a convenient technique for the study of hydrocarbon prospects. They simulate the present-day state of stress and pore pressure, not accounting for the processes that took place during the evolution of the basin. Static geomechanical models can be built using the basin geometry at present day acquired from seismic data (e.g., Fredrich *et al.* 2007b; Segura *et al.* 2016; Heidari *et al.* 2018).

These models usually include an initialization step in which the user introduces the gravitational force and the model calculates the initial stresses in the modeled field. A calculation step can then simulate geologic loadings such as salt relaxation, tectonic extension or shortening, or reservoir depletion, that cause stress changes and deformation. At the end of the calculation stage, the model reaches a quasi-static equilibrium, and it is considered to represent the current day conditions of stress and pore pressure for the studied area.

The principal limitation of the static models is their inability to capture geological processes that develop as a result of basin evolution (Nikolinakou *et al.* 2014). Similarly, they do not

show the evolution of basin geometries during geologic time spans. This limitation can be overcome using the evolutionary model approach.

1.1.4.2 Evolutionary (forward) geomechanical models

In contrast to static models, evolutionary geomechanical models can simulate time-dependent processes such as deposition, tectonic loading, salt flow, and porous fluid flow. These models combine the development of the geologic systems with the deformation and the strength of the modelled sediments (e.g., Goteti *et al.* 2012; Gradmann & Beaumont 2012; Hamilton-Wright *et al.* 2018; Nikolinakou *et al.* 2018a; Thigpen *et al.* 2019). The model results can provide information on the evolution of the studied basin with time; stress-strain calculations are not limited to the present-day geometry configuration. Thus, evolutionary geomechanical models are a useful tool to simulate time-dependent processes, such as deposition and compaction, tectonic loading, salt flow, porous fluid flow, fault development, etc.

However, the evolutionary models do not ensure that the final basin geometries will match the present-day basin geometries. In some cases, the evolution of these models can lead to totally different basin configurations, especially when large deformation processes are involved, such as in salt tectonics or faulting. To reproduce the present-day geometries, evolutionary models require of an iterative and painstaking process that increases disproportionately the time and effort spent building them. To overcome this limitation, some authors have combined the evolutionary approach with kinematic restoration to inform their evolutionary models and achieve final geometries more in line with the observed present-day basin geometries (Crook *et al.* 2018; Thigpen *et al.* 2019). The present thesis focuses part of the effort on using results from a kinematic restoration to constrain an evolutionary geomechanical model.

1.2 Geologic environment

The area of interest of the present thesis is located in the distal part of the Tarfaya basin (red polygon, Figure 1.1) and centres around two salt structures, the Sandia diapir and the Western diapir (Figure 1.2). The Sandia diapir was the target for the drilling of an exploratory well (Sandia-1, black circle, Figure 1.1) by the oil-company Repsol Exploración S.A. in 2015.

The Tarfaya basin sits on the north-western African passive continental margin. The basin is bounded by the Agadir and Essaouira basins to the north and by the Aaiun basin to the south. To the west, the basin terminates against the eastern Canary Islands (Lanzarote and Fuerteventura Islands) and the submarine Conception Bank. These two geographic features separate the Tarfaya basin from the deep Atlantic abyssal plain (Gouiza 2011). The bathymetrically deepest part of the basin forms a SW-NE trending bathymetric trough with roughly 2000 m water depth located beyond the edge of the continental shelf.

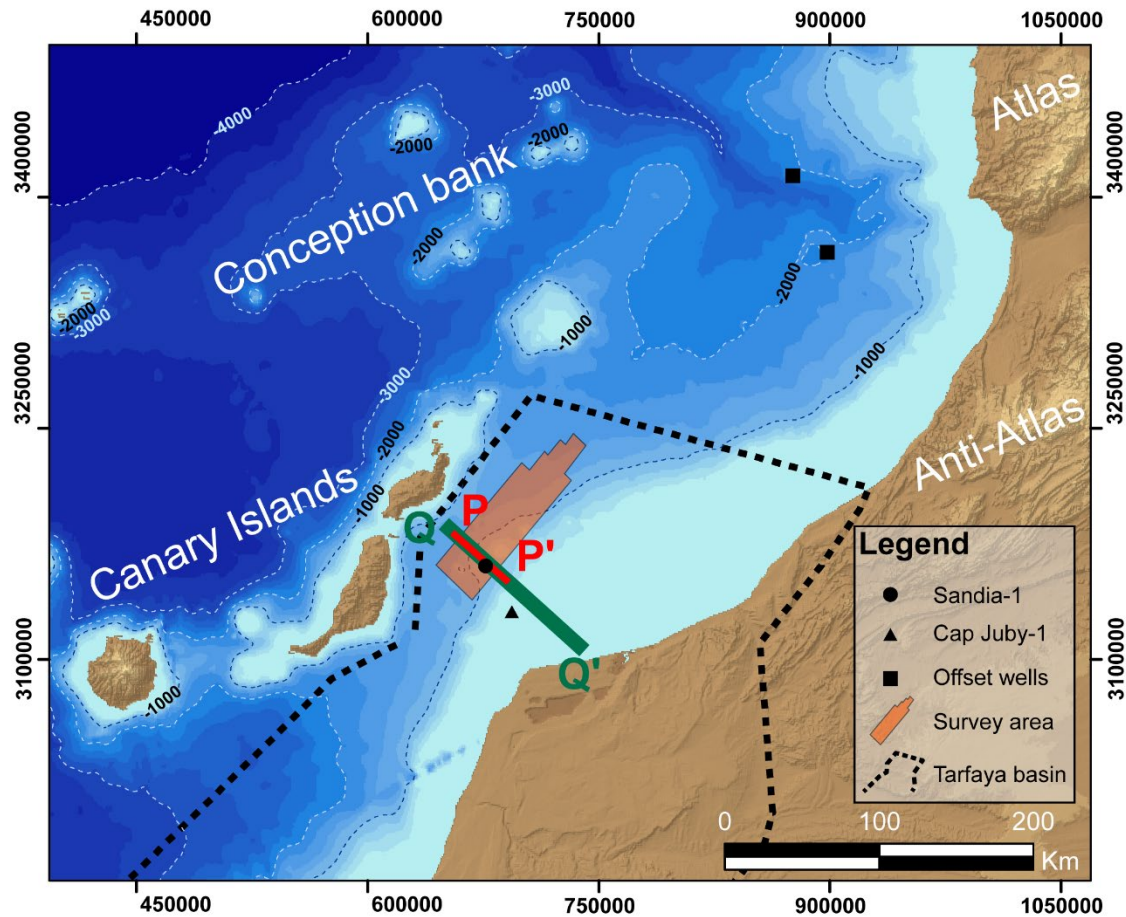


Figure 1.1: Location map for the Tarfaya basin and geological features. Seismic section (Figure 1.2) is indicated by the red line PP'. Restored section (Figure 1.3) is indicated by the green line QQ'. Sandia-1 (black circle) and Cap Juby-1 (black triangle) well-head locations are also shown. The offset wells (black squares) used for the pre-drill pore pressure and stress predictions are also shown. The Geographic Coordinate System used is ETRS 1989.

1.2.1 **Geological history**

The Tarfaya basin developed initially from the Late Triassic to Early Jurassic, during the rifting and opening of the Central Atlantic Ocean and the separation of the NW African margin from the North American margin. The rifting processes caused basement extension, forming fault controlled half-grabens trending NNE-SSW to NE-SW, with large tilted blocks being on average 20 to 30 km wide and 50 to 100 km long (Piqué *et al.* 1998; Le Roy & Piqué 2001). These half-grabens were infilled by thick syn-rift sequences of continental siliciclastic red beds and evaporites of Triassic age. The Triassic evaporites were the source layer for the present-day salt structures that populate this area (Tari & Jabour 2013). Rifting culminated with break-up and oceanization in the Early to Middle Jurassic (Tari & Jabour 2013).

The initial development of salt structures began during the Jurassic and continued during Early Cretaceous, affecting the sea floor at these times (Michard *et al.* 2008). The location of the different salt structures was strongly controlled by the uneven distribution of Triassic salt thickness within the half-graben system (Tari & Jabour 2013). In other words, locations with thicker initial salt source layers were able to generate larger and more developed salt structures.

During the Jurassic period, post-breakup thermal subsidence of the margin caused the western end of the Tarfaya basin to deepen, while a carbonate platform formed along its eastern, shallower continental margin. A relative sea-level fall during the Late Jurassic-Early Cretaceous (Berriasian to Valanginian) caused subaerial exposure and karstification of the Jurassic carbonate platform. This event was followed by sedimentation of alluvial siliciclastic materials forming the Tan Tan Delta complex (Michard *et al.* 2008; Wenke *et al.* 2011).

The Tarfaya basin was then compressed by inversion of the Atlas and Anti-Atlas and uplift of northwestern Africa. This started during the Late Cretaceous (Coniacian) and lasted until the Quaternary with episodes of activity followed by quiescence (Frizon de Lamotte *et al.* 2008). Atlasic uplift increased the sediment input (Wenke *et al.* 2011) and the compression reactivated the pre-existing salt structures formed during the Jurassic and Early Cretaceous (Tari & Jabour 2013). In addition, volcanic emplacement of the Canary Islands archipelago occurred during the Cenozoic (Carracedo & Perez-Torrado 2013).

The present-day salt structures of the area are mainly composed by an autochthonous continuous salt source layer located approximately 9 km below sea level and by allochthonous salt bodies embedded within the Mesozoic and Tertiary sediments. Some of these salt structures are still active at the present day, affecting the sea-floor bathymetry. Other salt diapirs do not reach the sea floor.

1.2.2 Seismic data and interpretation

The structure of the study area has been characterized using 3D seismic data acquired by Repsol in 2003 (red polygon, Figure 1.1) covering a surface of approximately 3250 km². This data was migrated in time and depth and was complemented with vintage 2D reflection multi-channel seismic profiles (acquired in 1983) migrated in time. The seismic interpretation was constrained using data from the Cap Juby-1 well (black triangle, Figure 1.1), drilled by Mobil in 1983, reaching diapirized Triassic evaporites located below Upper Jurassic carbonates. The interpretation of the deeper units in the area is rather ambiguous because of the different geologic history of the deeper water basin (in the NW) compared to the shallower platform area (in the SE), where the Cap Juby-1 control well is located. In the platform area, the Jurassic and Triassic units are found at shallower depths as a result of the initial passive margin configuration and the overprint of Atlasic inversion, that uplifted the more proximal part of the passive margin starting in the Late Cretaceous. Seismic reflection data suggests that this inversion resulted in significant erosional truncation of units and accounted for 500-1000 m of uplift of the shelf area. Because thicknesses of pre-inversion (Mesozoic) units in the platform area were used as guides for their interpretation in the deep-water, distal sector (Figure 1.2) there is more uncertainty in the interpretation of this distal domain.

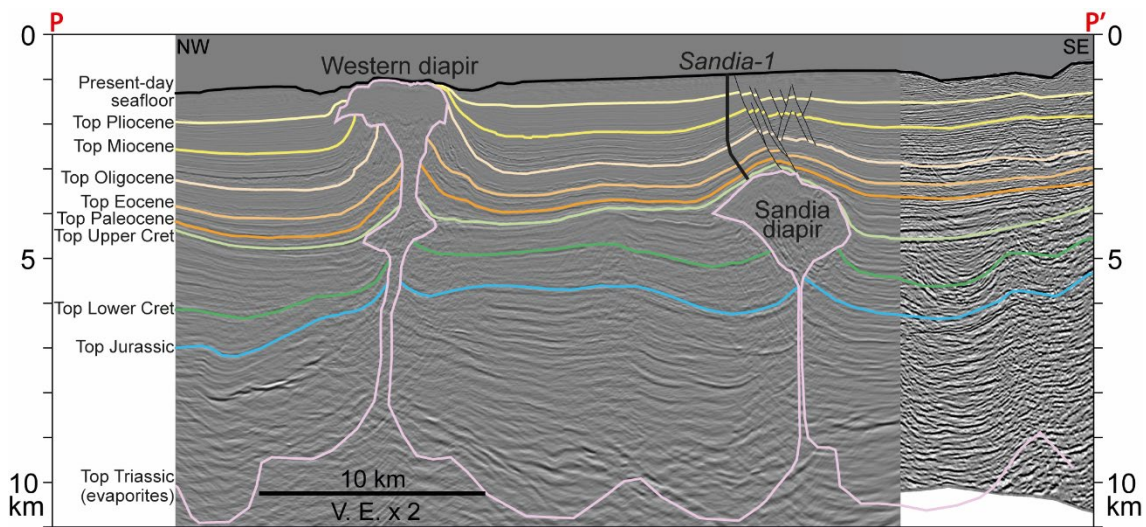


Figure 1.2: Seismic interpretation across a transect in the deep part of Tarfaya basin (red line PP', Figure 1.1). This section combines 3D seismic (NW side) with vintage 2D reflection multi-channel (SE side). Location of the seismic line is also highlighted with the red rectangle on the present-day section in the sequential kinematic restoration model (Figure 1.3)

The thick Tertiary basin (up to 4 km thick) located in the deep-water domain (Figure 1.2) wedges towards the SE onto the continental shelf area and overlies a regional-scale erosional unconformity in the continental shelf and across the shelf break. Basinward, and barring areas deformed by diapirism, Tertiary units lie conformably over Cretaceous sediments. Both Tertiary and Mesozoic (Jurassic and Cretaceous) sediments display thickness changes and

deformation related to diapirism of the underlying Triassic evaporites. These evaporites cut through the overlying units in the form of the Western diapir (NW side, Figure 1.2) and the Sandia diapir (SE side, Figure 1.2). Published observations of half-graben geometries suggest that these salt diapirs may have nucleated above rotated basement fault-blocks along the Moroccan Atlantic margin (Le Roy & Piqué 2001; Tari & Jabour 2013). The Western diapir is active at present-day and deforms the sea floor. The Sandia diapir, which was the target of the Sandia-1 exploratory well (black circle, Figure 1.1), ceased its growth during the Tertiary. Both diapirs display geometries that are consistent with passive down-building development during the Mesozoic, and a phase of flaring (lateral expansion) during the Cretaceous. Folding of Paleogene strata above the diapirs indicates that they were reactivated by shortening during the Tertiary, causing further growth of the Western diapir and extrusion onto the sea floor. However, in the case of the Sandia diapir, shortening only caused folding of the overburden and lateral flow of salt toward the centre of the salt structure.

1.2.3 Kinematic restoration

The interpretation of the acquired seismic data allowed the construction of a regional-scale cross-section (section QQ', Figure 1.1) that was the basis for a sequential kinematic restoration back to Triassic times, the time of deposition of the evaporites (Figure 1.3). This restoration accounted for compaction of sediments by assuming average shale or sandy shale lithology (as proven by the Sandia-1 well) and using the compaction curves of Sclater & Christie (1980). It also considered local isostasy and corrected for the effect of thermal subsidence by applying the curves of McKenzie (1978) (the beta factor was estimated from the expected crustal thickness based on the interpreted top of the basement and assuming an isostatically equilibrated crust). The effects of salt diapirism were accounted in the model following the approach of Rowan & Ratliff (2012). Finally, the sequential restoration accounted for Atlasic shortening and uplift. Horizontal shortening of 5 km was added to represent the 500-1000 m of uplift and the shelf segment was lowered progressively back to Cretaceous times to account for this uplift. Maintaining the section below sea level honours evidence of a shallow marine setting (less than 50 m water depth) present at that location from present-day back to Cretaceous times.

The kinematic restoration model begins at the end of Triassic with a flat salt layer (pink unit, Figure 1.3). The salt is located on top of Triassic syn-rift siliciclastic red beds (purple unit, Figure 1.3). The evaporites are filling the half-grabens formed by the faulted basement (brown units, Figure 1.3).

The deposition of the Jurassic (blue units, Figure 1.3) and Cretaceous sediments (dark green and light green units, Figure 1.3) triggers salt diapirism and forms the two major structures studied in this thesis: the Sandia diapir at the SE and the Western diapir at the NW (Figure 1.3). During the Cretaceous interval, both diapirs flare: the Western diapir forms overhangs (enlarged periphery of the diapir crest; Jackson & Hudec, 2017) at both sides and the Sandia

diapir forms an overhang at its SE side and a salt sheet (salt breadth several times greater than its thickness; Jackson & Hudec, 2017) at its NW side. At the end of Cretaceous, the Western diapir is emergent at the sea floor, contrary to the Sandia diapir that was buried.

From Paleocene until present day, the Western diapir grows by downbuilding and remains at sea floor. On the other hand, the Sandia diapir remains buried, with a welded salt stem (slender part of the salt diapir connecting its upper part with the pedestal; Jackson & Hudec, 2017). The ongoing sedimentation combined with the tectonic shortening applied from Paleocene until present-day times causes the diapir crest to inflate, arching the Tertiary sediments deposited above (orange to gray materials, Figure 1.3).

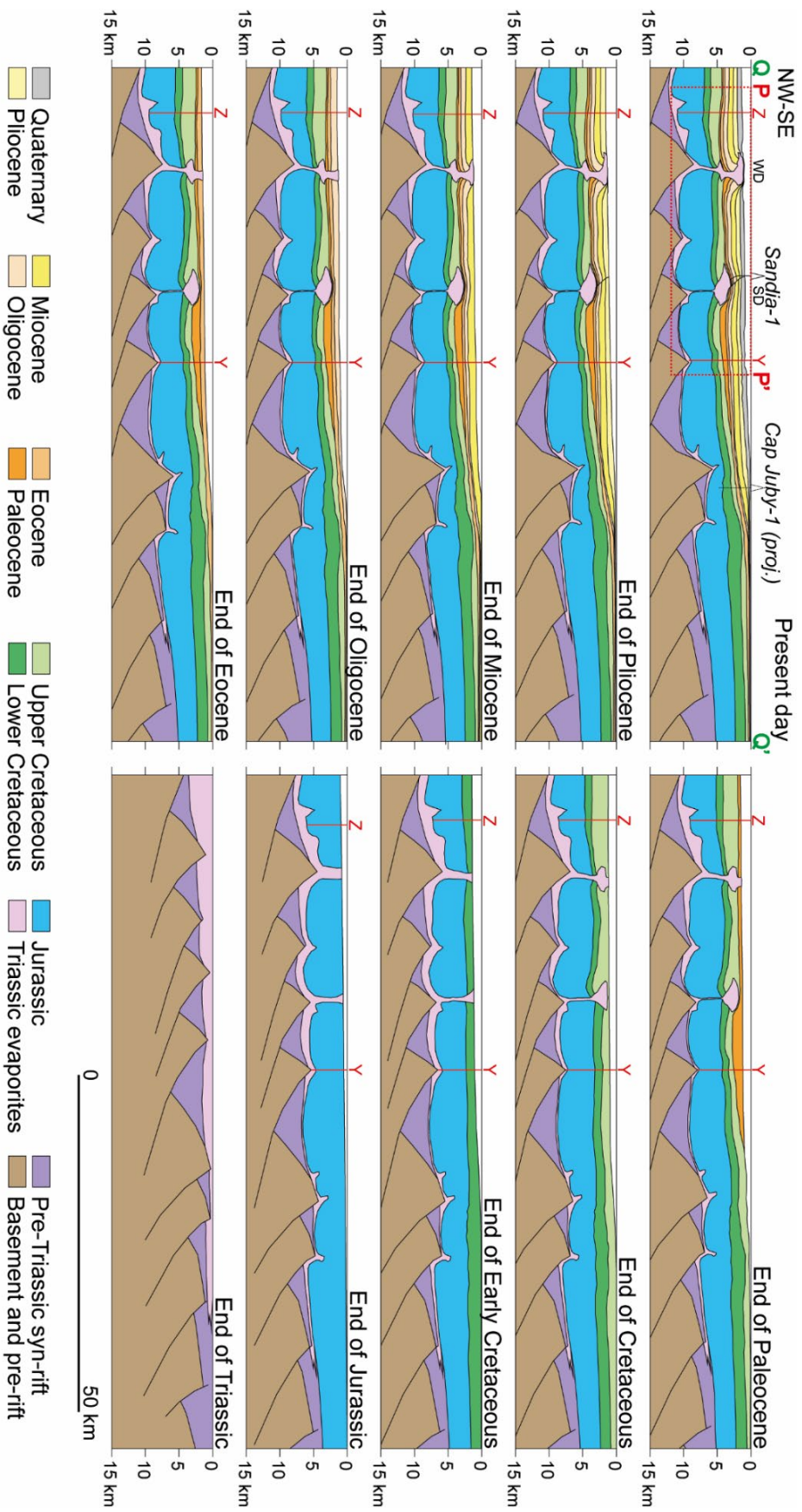


Figure 1.3: Sequential kinematic restoration of a regional section across the Tarfaya basin (green line QQ, Figure 1.1), whose present-day geometry is based on 2D and 3D seismic interpretation, from Triassic to present day. Locations Y and Z in red are used for thickness extraction and burial history reconstruction (Figure 2.16). Location of Sandia-1 exploratory well and projection of Cap Juby-1 well are shown on the present-day panel. Dashed red box indicates location of seismic section in Figure 1.2. WD: Western diapir; SD: Sandia diapir.

1.2.4 Well data

The Sandia-1 frontier exploratory well (black circle, Figure 1.1) was planned to drill close to the crest of the Sandia diapir. Its location was hundreds of kilometres away from the nearest comparable well, being the stratigraphy of the subsurface highly uncertain. The targets of the well were four different sand-rich turbiditic deposits in the supra-salt Tertiary sediment package (Table 1.1). The Miocene to Quaternary shales are the seal for these reservoirs. The Tertiary sediments on top of the diapir are affected by an array of faults that result in complex trap geometries for hydrocarbons (Figure 1.4). The well trajectory crosses one of these major faults at a depth of approximately 1500 m below sea level (Figure 1.4a).

Table 1.1: Tertiary sand reservoirs targeted by the Sandia-1 well (black circle, Figure 1.1).

Reservoir name	Depth below sea level (TVD, m)	Age	Geology	Target
R1	1600	Miocene	Turbiditic sands	
R2	1956	Miocene	Turbiditic sands	Main
R3	2370	Oligocene	Turbiditic sands	
R4	2787	Paleocene	Turbiditic sands	Secondary

Repsol performed a predrill prediction using offset wells and seismic velocity data to estimate the pore pressures and stresses near the drilling location (solid lines, Figure 1.5). This prediction used data from two offset wells (black squares, Figure 1.1) located 300 km from the study area, which were considered the closest deep-water analogues for the Sandia-1 well location. Closer wells like Cap Juby (black triangle, Figure 1.1), were not used as they were located on the continental shelf, a too dissimilar environment when compared with the studied area.

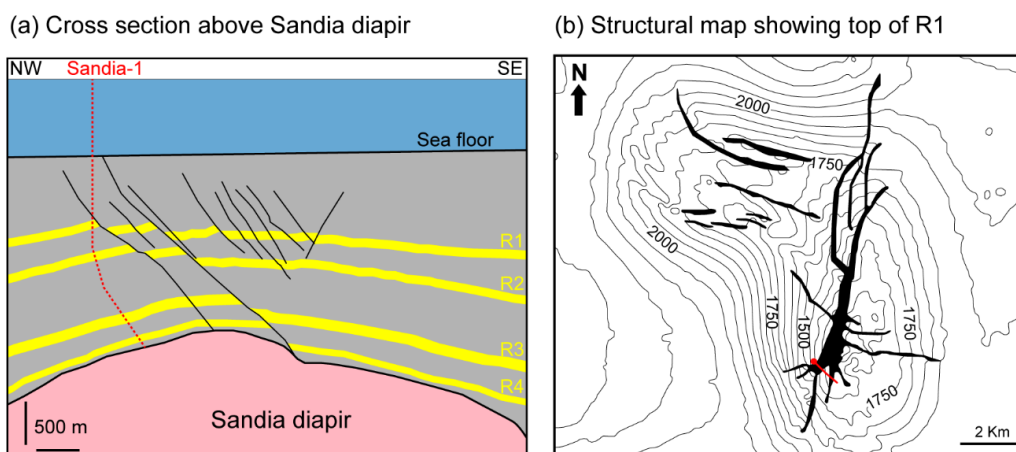


Figure 1.4: (a) section showing Tertiary sediments above the Sandia diapir (in pink). The four sand reservoirs (yellow layers) targeted by the Sandia-1 well (dashed red line) are affected by an array of faults (black lines). (b) Structural map of the top of reservoir R1 and the faults affecting it. Position of Sandia-1 well-head and its trajectory are shown by red dot and red line, respectively.

The drilling of the Sandia-1 well was completed on the 28th January 2015 and took a total of 74 days, six of which were non-productive because of losses near the bottom part of the section. Posterior CBIL image logs from this problematic section (see Annex 4: Sandia-1 well log data and CBIL data) revealed a series of drilling induced tensile fractures (DITF) that indicated a lower minimum horizontal stress (green dots, Figure 1.5) compared to the values expected by the predrill prediction (solid black line, Figure 1.5). This stress reduction is consistent with the Leak-off tests performed near the problematic section (yellow dots, Figure 1.5).

The different stratigraphic units drilled by the well are shown in Figure 1.6. The well reached a total depth (TD) of 2946 m below sea level (equivalent to 3093 m in measured depth, MD).

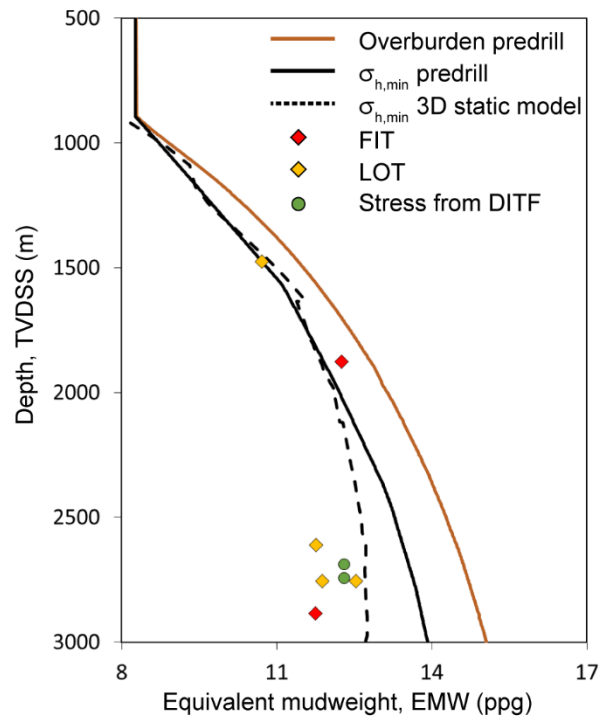


Figure 1.5: Profile along Sandia-1 well showing overburden stress (solid brown line) and minimum horizontal stress, σ_h (solid black line) from the predrill study. The σ_h prediction from 3D static model (dashed black line; see Figure 2.2b) is included for comparison. The data points from the well drilling are represented by leak-off tests (LOT) measurements, formation integrity tests (FIT) measurements and drilling induce tensile fractures (DITF) observed (yellow, red and green dots, respectively). The decrease of σ_h near the salt interface (at 3,000 m) predicted by the 3D model is consistent with data obtained during the drilling operations.

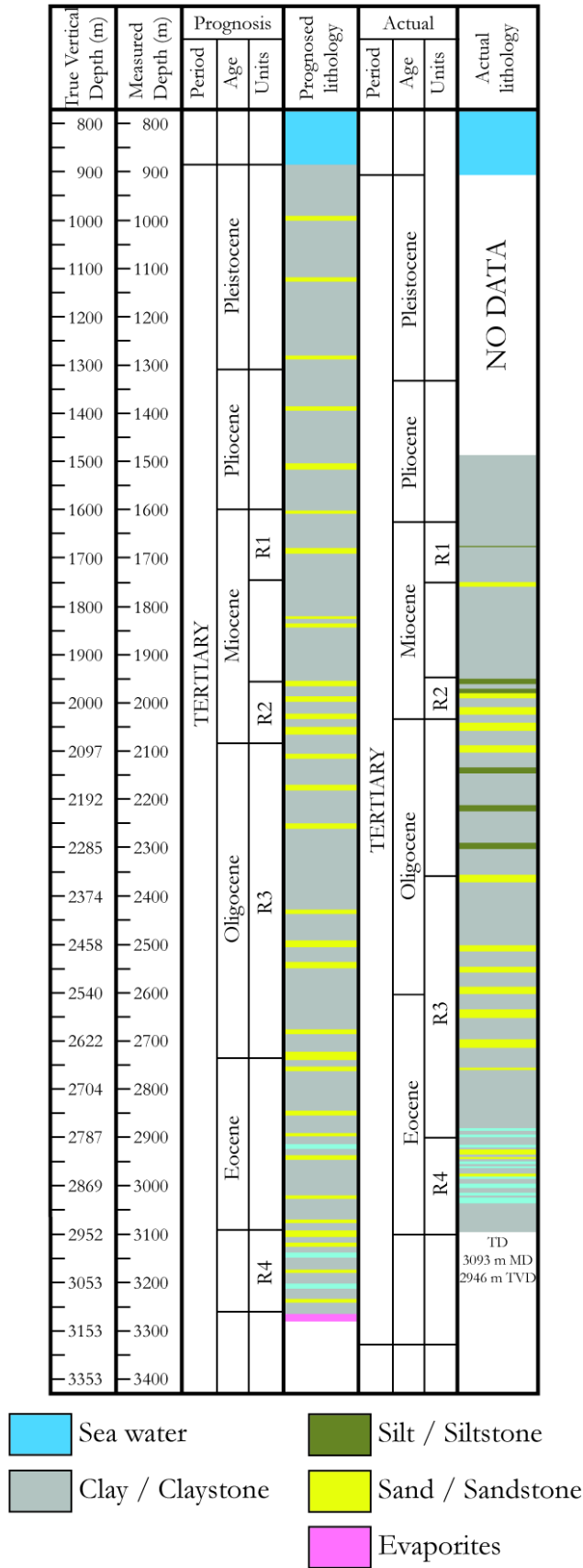


Figure 1.6: Stratigraphic log showing the lithologies prognosed before and after the drilling of the Sandia-1 exploratory well, both in measured depth (MD) and true vertical depth (TVD). R1, R2, R3 and R4 correspond to the targeted reservoirs by the Sandia-1 well (Table 1.1).

CHAPTER 2. SUMMARY OF RESULTS

2.1 Introduction

In this chapter, we present a summary of the results obtained to fulfil the objectives outlined in the Preface of this thesis. We structure this section in three separate subchapters that focus on the results of: the 3D static modelling, the 2D static modelling and the 2D evolutionary modelling. The two first subchapters summarize the static results that appear in the publications:

- Hooghvorst et al, 2019: Insights from sensitivity analysis of geomechanical modelling of a salt structure offshore west Africa (Annex 2).
- Hooghvorst et al, 2020: Comparison of stresses in 3D v. 2D geomechanical modelling of salt structures in the Tarfaya Basin, West African coast (Annex 1).

These static models aim to represent the stresses and strains of the modelled location at the present day. In other words, they provide the present-day geomechanical conditions of the studied area before any drilling activity or hydrocarbon extraction.

The third subchapter summarizes the evolutionary results that appear in the publication:

- Hooghvorst et al, 2021: Geologically constrained evolutionary geomechanical modelling of diapir and basin evolution: A case study from the Tarfaya basin, West African coast (Annex 3).

The evolutionary model aims to simulate the evolution of the Sandia diapir over time. This technique allows the modelling of the geologic processes taking place during the diapir evolution, such as deposition, tectonic loading, salt flow, etc.

We begin each of the subchapters by giving a general overview of the corresponding model setup and initial parameters and conditions. We follow by exploring results obtained from the model. These results are considered the base-case reference for subsequent comparisons. Finally, we present the sensitivity analysis results performed for each of the models. The modelling results and their sensitivity analyses create the base for the modelling discussion presented in the following CHAPTER 3.

2.2 3D static geomechanical model

2.2.1 Model setup

The 3D geomechanical static model presented here has been built using the software Elfen (Rockfield 2017) and using a quasistatic, drained, finite-element formulation. The model is based on the pre-drill stratigraphy obtained by Repsol but simplifying the sand formations representing the reservoirs from 4 to two layers. In this study, we are not updating the stratigraphy to the actual depths known after drilling for various reasons:

- The pre-drill and post-drill stratigraphy are not very different. It was considered the changes in the model results produced by updating the stratigraphy would not introduce important differences.
- The present study is based on building on the work conducted initially by Repsol. The 3D geomechanical modelling was the first step to understand the prospect and this study uses it to derive further approaches to improve the knowledge we can obtain in the exploratory stage, where data is not always available and uncertainties are high.

The 3D model domain is discretised by an unstructured finite-element mesh formed by linear tetrahedral elements of 400 m in size. This model also incorporates a region of 4 km² centred around the well location and composed by a finer mesh of 50 m. As a result, the model contains a total of 3.97 million elements.

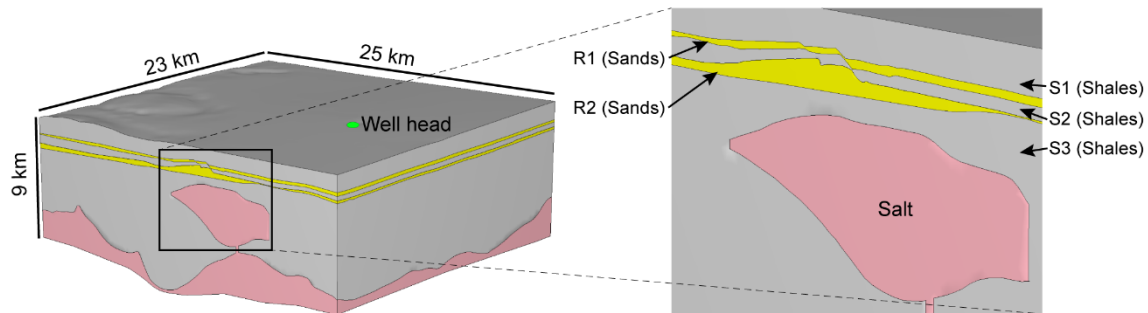
The domain modelled covers an extension of 23 km by 25 km and a depth of 9 km (Figure 2.1a). It comprises the location of the Sandia-1 exploratory well, in addition to the different horizons, faults and salt structures extracted from the seismic survey. Two sand layers and three, thicker shale layers compose the sedimentary materials (Figure 2.1a). The sand represents the system of reservoirs present in that area. The model also includes an autochthonous and continuous salt layer at the bottom and a series of allochthonous salt structures embedded within the sedimentary materials (Figure 2.1b). Both the autochthonous and allochthonous salt structures are connected by 200m-wide salt columns. These features are not seen in seismic, which shows independent salt bodies, but are necessary for the software's initialization procedures. Finally, the model includes a simplified fault network located on top of one of the main allochthonous salt structures (the Sandia diapir, Figure 2.1b), composed by two faults: a north-south trending fault with a maximum throw of 400 m; and a secondary fault that intersects the trajectory of the exploratory well. These faults use a Coulomb friction law with no cohesion and a friction coefficient of 0.3.

We apply the boundary conditions at the four lateral sides of the model domain in the form of horizontal displacement restriction. The base of the model also includes a restriction for the vertical displacements. The upper part of the model, representing the present-day sea floor, has no restriction of displacements in any direction.

The input parameters of the model that are discussed below include the initial pore-pressure profile, the initial stress ratios (the ratio between the vertical and horizontal effective stresses under uniaxial conditions), the material properties and the temperature gradient used. These inputs were calibrated using information coming from offset wells (black squares; Figure 1.1) and from velocity analysis. For the case of the offset wells, we used the closest deep-water analogues to the studied location (black squares, Figure 1.1). We discarded the wells closer to the Sandia-1 well (Cap Juby well, black triangle, Figure 1.1) for being located on the continental shelf, in an environment considered too dissimilar compared with the prospected area.

We used a drained analysis to run the geomechanical model for this study. That means the stress calculations for the modelled sediments are uncoupled from the porous fluid flow. The initial pore pressure profile for each horizon is obtained from a pre-drill offset well analysis, using the offset wells in equivalent depths from the sea surface (black squares; Figure 1.1). The pore pressure profile for shallowest and intermediate shale layers (S1 and S2, Table 2.1) is hydrostatic, whereas a constant overpressure is present in sand layers and the deepest shale layer (R1, R2 and S3 layers, Table 2.1). There is zero pore pressure in salt.

(a) Full 3D static model geometry, well-head location and zoomed section showing model stratigraphy



(b) 3D static model showing salt and fault geometry, well trajectory and zoomed section near well

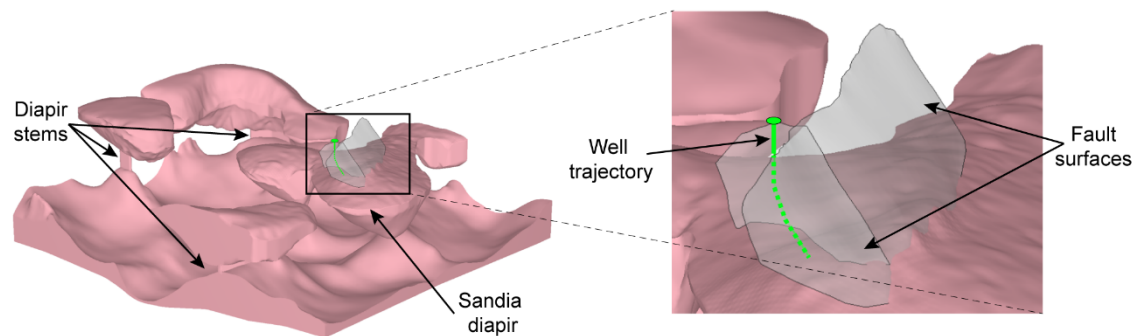


Figure 2.1: Static 3D geomechanical model. (a) Model geometry representing the stratigraphic distribution of sand, shale and salt horizons. The green dot represents the position of the Sandia 1 well head. (b) 3D salt structure, major faults and the Sandia well trajectory (green line).

Table 2.1: Summary of input properties for the different horizon layers defined in the 3D static model.

Stratigraphy	Description	Depth at well location (m)	ρ_s (Kg/m ³)	ρ_f (Kg/m ³)	Overpressure (Mpa)	ν	Range of E (Mpa)	K_H	K_h
S1	Shales & siltstones	885 - 1600	2650	1025	-	0.3	290 - 2250	0.87	0.73
R1	Sand	1600 - 1746	2650	1025	0.9	0.3	2500	0.89	0.77
S2	Shales & silt	1746 - 1950	2650	1025	-	0.3	2800	0.90	0.80
R2	Sand	1950 - 2075	2650	1025	2.7	0.3	3100	0.88	0.75
S3	Shales & siltstones	2075 - 3100	2600	1300	1.3	0.3	3650 - 50000	0.90	0.80

The initialization of the geomechanical model requires the input values for the stress ratios (K_H and K_h) to obtain the initial horizontal effective stresses (σ'_H , σ'_h) as a fraction of the initial vertical effective stress, σ'_v :

$$\sigma'_v = \sigma_v - u \quad (1)$$

$$K_H = \frac{1}{2}(1 + K_h) \quad (2)$$

$$K_h = \frac{\sigma'_h}{\sigma'_v}, K_H = \frac{\sigma'_H}{\sigma'_v} \quad (3)$$

where σ_v is the overburden, u the pore pressure, σ_H the maximum horizontal stress and σ_h the minimum horizontal stress.

It is assumed that the maximum horizontal stress, σ_H in the studied area acts in the east-west direction due to basinward gliding of sediments on the basal salt layer. Consequently, the minimum horizontal stress, σ_h , is oriented in north-south direction. K_h and K_H (eq. 2) are used to obtain the initial σ'_h and σ'_H respectively (eq. 3). The initial stress ratio values for each layer can be found in Table 2.1 and have been obtained using the offset well data from the well analogues (black squares; Figure 1.1). As for the salt, its viscous rheology makes it unable to sustain deviatoric stresses, generating a uniform stress state and having an initial stress ratio of one.

The sediment materials in this model have a porosity-depth profile for each horizon that was calibrated at the well location based on log data. The measured interval velocity at the well location gives us an estimate for the bulk density, ρ_b , of the sediments. The porosity is then calculated assuming values of grain and fluid densities (Table 2.1):

$$n = \frac{\rho_b - \rho_s}{\rho_w - \rho_s} \quad (4)$$

where ρ_w and ρ_s are the water and grain densities, respectively. Because horizons have different thicknesses across the field than at the well location, porosity-depth profiles for each horizon are extrapolated for the maximum depth of the given horizon.

The model uses a poroelastic material model to represent the rheology of the shale and sand sediments. Because of very limited experimental or field data, the input elastic parameters are calibrated based on observations from regional wells (Table 2.1). The poroelastic behaviour is defined using an empirical expression to incorporate porosity changes (Rockfield 2017):

$$E = E_{ref} \left[\frac{\sigma' + A}{B} \right]^r n^c \quad (5)$$

where E is the elastic modulus, E_{ref} a reference elastic modulus, n the porosity and A , B , r and c are material constants used to define the shape of the elastic modulus profile (Table 2.2). The shallowest and deepest shale horizons have an elastic modulus that varies with depth. This allows us to account for depth variations of material properties within these thicker horizons. The range of values of the elastic modulus, E , for each horizon is shown in Table 2.1.

The salt bodies are modelled using a steady state creep model. This is a reduced form of the Munson-Dawson formulation (the two steady-state terms are included and the transient term is omitted, considered negligible over geological time scales) (Munson & Dawson 1979). This constitutive model considers the salt viscosity as a function of both stress and temperature. The Munson-Dawson model has been extensively used to simulate the viscous flow of salt in deep-water basins such as the Gulf of Mexico or the offshore of Brazil (Fredrich *et al.* 2003; Marketos *et al.* 2016; Segura *et al.* 2016; Thigpen *et al.* 2019). The viscosity of the salt depends on both the differential stress and the temperature. The input parameters for the salt model are based on Avery Island salt (Munson 1997; Fredrich *et al.* 2007a) because of the lack of field data for this specific area (Table 2.3). The Avery Island salt is considered to represent average salt behaviour.

Finally, we introduce in our model a constant temperature gradient of 3.61 °C per 100 m, based on an integrated 2D and 3D petroleum system model for thermal maturity evaluation. The model was calibrated using the offset wells, taking into consideration the variation in sedimentation, salt presence and crustal structure. The gradient value used is in line with published results from the area (Rimi 2001; Zarhloule *et al.* 2010).

Table 2.2: Input material parameter values for poroelastic sand and shale sediments.

	E_{ref} (MPa)	A (MPa)	B (MPa)	r	c
Shallow shales (S1)	100	-1	-1	0.4	-2.1
Sands (R1)	2500	-1	-1	0	0
Intermediate shales (S2)	2800	-1	-1	0	0
Sands (R2)	3100	-1	-1	0	0
Deep shales (S3)	150	-1	-1	0.55	-1.4

Table 2.3: Input material parameter values for viscolpastic Munson-Dawson model (Munson 1997; Fredrich *et al.* 2007b).

Parameter	Units	Value	Parameter	Units	Value
E	MPa	31000	N_2		5
ν		0.25	Q_2	cal/mol	10000
ρ	Kg/m ³	2100	R	cal/°K/mol	1.987
A_1	1/s	5.95E+22	T_0	°K	0
N_1		5.5	T_{const}	°K	273
Q_1	cal/mol	25000	G_0	MPa	12400
A_2	1/s	6.87E+12	dG/dT	MPa/°K	10

2.2.2 Model results

We explore the results of the 3D static model using the minimum horizontal-to-vertical effective stress ratio (K , eq. 6).

$$K = \frac{\sigma'_h}{\sigma'_v} \quad (6)$$

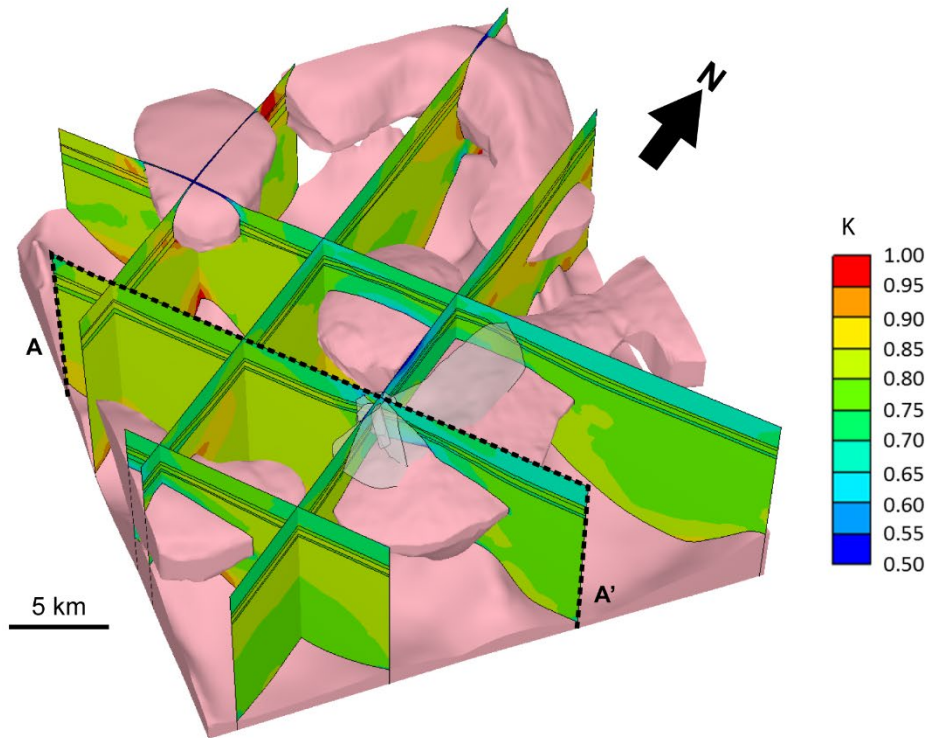
This ratio shows the locations where the stress state has been changed compared to the initial conditions. Because the analysis is static (no deposition) and drained, the overburden profile and the pore pressure do not change during the simulation. As a result, the vertical effective stress (σ'_v) does not change either. Hence, an increase in the value of K compared to the uniaxial conditions (Table 2.1) is translated to an increase of the horizontal effective stress (σ'_h). Contrarily, a decrease in K relative to the uniaxial values means a reduction of σ'_h .

In the 3D static model, K remains higher than the uniaxial conditions (green contours, Figure 2.2a) in locations near the salt source layer, adopting values higher than 0.9 in some locations (orange and red contours, Figure 2.2a). K also increases in regions adjacent to the allochthonous salt structures. In contrast, K decreases to values below 0.7 (light blue contours, Figure 2.2a) above the allochthonous structures. Values of K fall below 0.55 (dark blue contours, Figure 2.2b) in places around the fault located above the Sandia diapir, both at sea floor (around the shallowest part of the fault) and near the crest of the salt body.

The stress results of the 3D static model also include the orientation of the principal stresses. In particular, the maximum principal stress (σ_1) remains vertical across the model, except in some localized areas near salt structures. At these places, the maximum σ_1 rotation on a vertical plain does not exceed 10° . Consequently, both the intermediate and the minimum principal stresses (σ_2 and σ_3 , respectively) are mainly located in a horizontal plain (Figure 2.3). This implies that σ_2 can be approximated by the maximum horizontal stress σ_H and that σ_3 can be approximated to the minimum horizontal stress (σ_h). The orientations of σ_H and σ_h show notable changes across the model (Figure 2.4). Areas not affected by salt or faults remain with azimuth values for σ_H of 90° (dark green contours, Figure 2.4), corresponding to an east-west direction. This orientation changes for the sediments near the faults and the salt diapirs. At these locations, the azimuth angle for σ_H can vary $\pm 30^\circ$.

In this model, when looking at the displacement results, we focus on the direction of displacements rather than their predicted magnitudes. This is because the model underestimates the displacement magnitudes due to the assumption of an elastic behaviour for the sediment materials. On the other hand, the displacement direction provides insights on possible patterns of salt relaxation and the interaction between diapirs and their neighbouring sediments.

(a) K results across the 3D model



(b) K results at section A-A

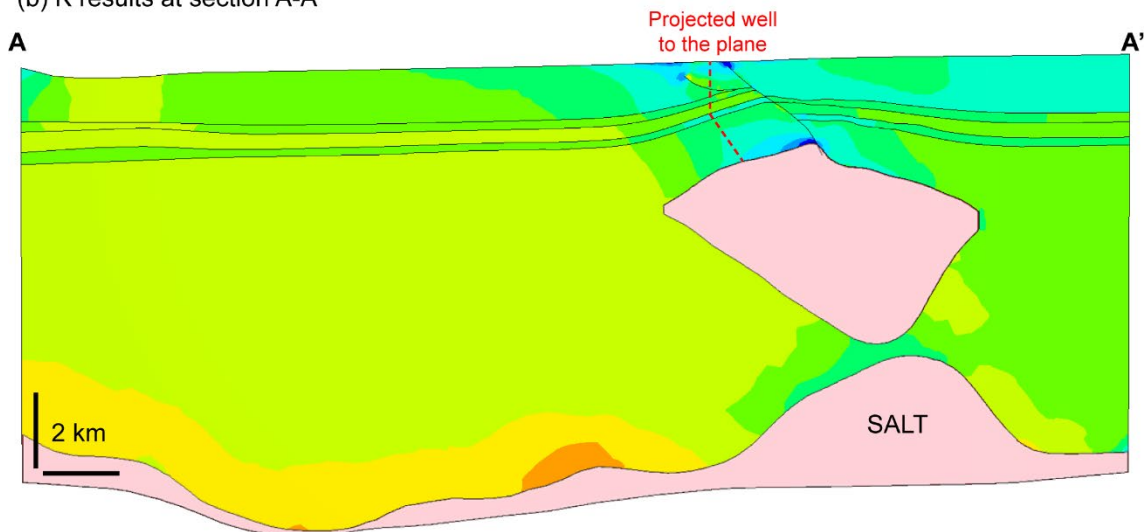


Figure 2.2: (a) Minimum stress ratio results (K) for different vertical sections across the model. The stress ratio is higher than its corresponding initial value for sediments below salt or near deeper salt structures. In contrast, the stress ratio is lower than its initial value at shallow depths above salt, around the faults and near the crest of the Sandia diapir. (b) Minimum stress ratio (K) for section A-A' near the well location. The stress ratio is notably reduced at the bottom part of the well above salt. Initial minimum stress ratio is 0.8 (light green contour colour) for intermediate and deepest shales, and 0.75 (dark green contour colours) for the shallowest shales and two reservoirs.

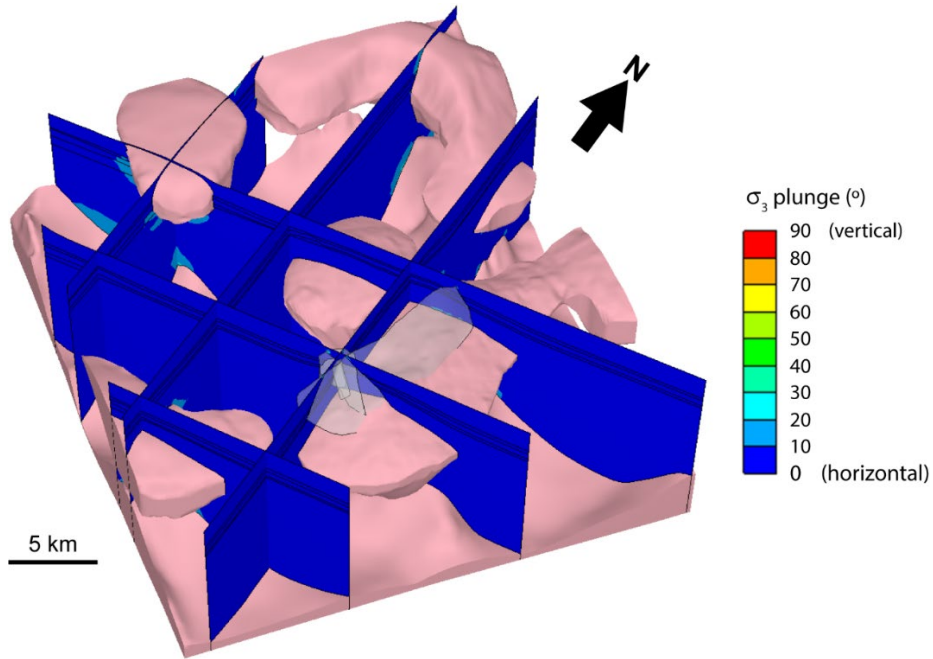


Figure 2.3: Minimum principal stress plunge results for different vertical sections across the model. The minimum principal stress remains horizontal in most part of the model, except in few localized areas near salt, where the orientation varies less than 20° from the horizontal plane.

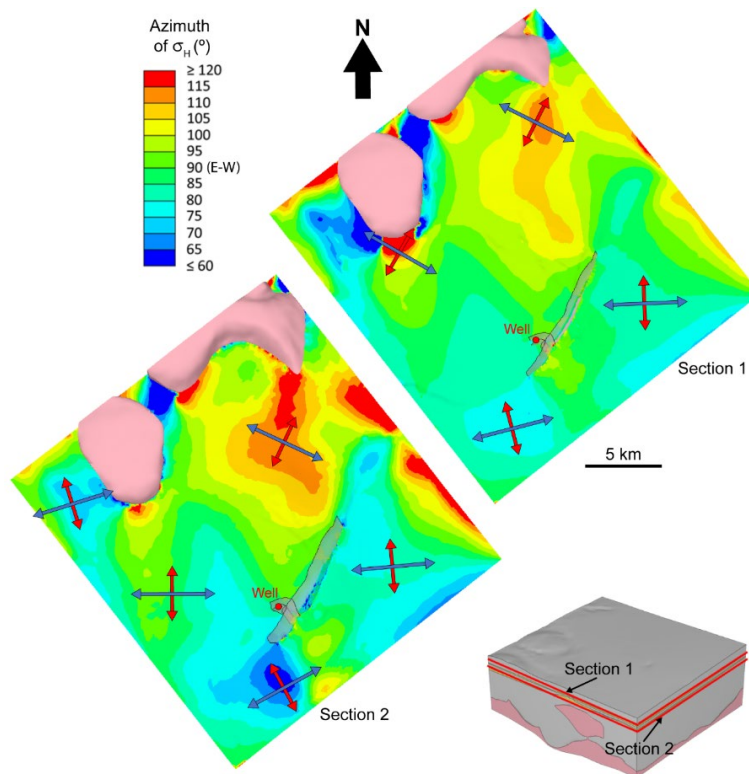
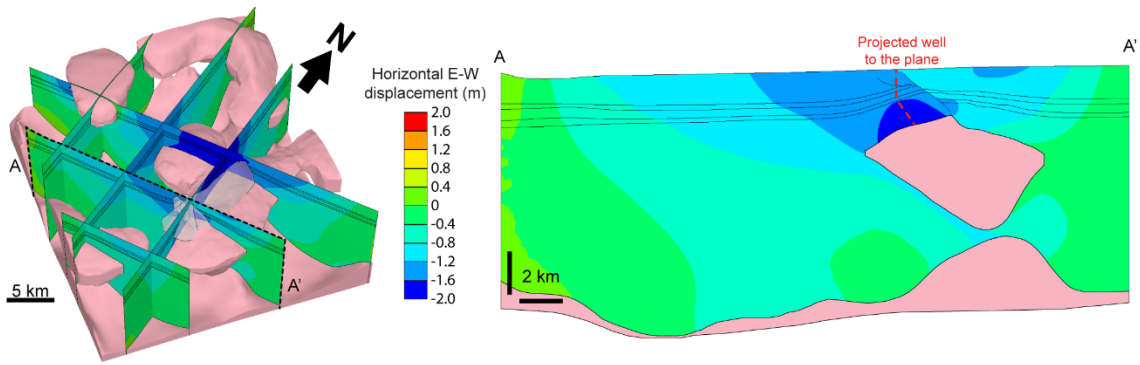


Figure 2.4: Orientation of maximum and minimum horizontal stresses, σ_H and σ_h , for two horizontal sections of the 3D model. Contours represent the azimuth of σ_H . The blue and red arrows illustrate the directions of σ_H and σ_h , respectively. The original east-west direction of σ_H changes in locations near the salt structures and around the major fault.

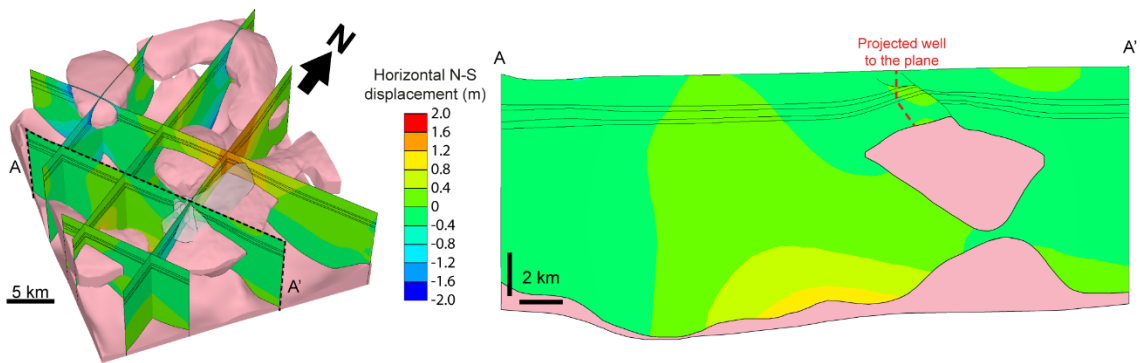
The horizontal displacements are mainly oriented east-west, with a westward direction trend (green to dark blue contours, Figure 2.5a). They are maximum around the fault and on the sediments located on top of the Sandia diapir. The footwall side of the fault shows greater displacements compared to the hanging wall (darker blue contours, Figure 2.5a). This difference in displacements between both sides of the fault is in agreement with the reduction in stresses (K reduction) present around the crest of the salt diapir (Figure 2.2b). The horizontal north-south displacements indicate a relatively small area near the north end of the major fault where the sediments undergo a northward displacement (Figure 2.5b). North-south displacements are negligible in the rest of the model.

Finally, the vertical displacements are strongly localized around the major fault above the Sandia diapir (Figure 2.5c). These displacements show a downward movement of the hanging wall (dark blue contours, Figure 2.5c). The footwall of the fault does not show appreciable vertical displacements.

(a) Horizontal E-W displacement results across 3D model and at A-A' section near well location



(b) Horizontal N-S displacement results across 3D model and at A-A' section near well location



(c) Vertical displacement results across 3D model and at A-A' section near well location

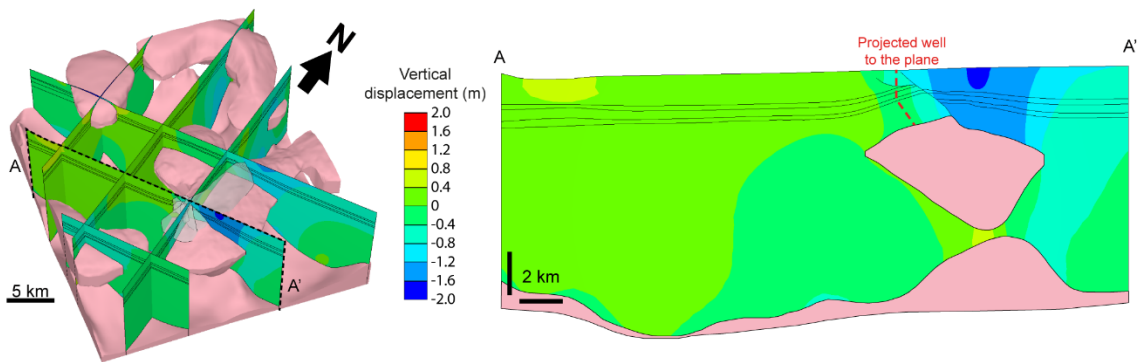


Figure 2.5: (a) Horizontal east-west displacements across the model, showing mostly westward displacements (blue contours) concentrated above the eastern diapir and around the major fault. Near the well location (section A-A'), the results display greater westward displacements for the sediments in the footwall compared to the hanging wall. (b) Horizontal north-south displacements across the model, showing mostly northward displacements (orange contours) located on the north end of the Sandia diapir. Near the well location (section A-A'), the results show no significant north south displacements. (c) Vertical displacements across the model, showing downward movement (blue contours) around the hanging wall of the major fault. Near the well location (section A-A'), the vertical displacements are concentrated on the hanging-wall side of the fault.

2.2.3 Sensitivity analysis results

Some of the input parameters used in the 3D base-case model have a high uncertainty caused by the lack of field data. We perform a sensitivity analysis study to assess their influence on the final geomechanical results. A list of the tested parameters is provided in Table 2.4.

Table 2.4: Summary of sensitivity analysis for the 3D static model

Variable changed	Original value	Modified value
Poisson's Ratio	0.3	0.25
		0.4
Elastic Modulus	Horizon and depth dependent (Table 2.1)	increased 20%
		decreased 20%

The elastic parameters used for the modelled materials are one of the main sources of uncertainty. In particular, the sensitivity analyses we perform focus on the elastic modulus and the Poisson's Ratio of the shale layers, representing the predominant fraction of the sediment material. For each parameter changed, we compare the resulting model with the base-case model, obtaining the comparison ratio S :

$$\text{Comparison ratio } (S) = \frac{\text{Basecase model} - \text{Sensitivity model}}{\text{Basecase model}} \quad (7)$$

This direct subtraction between models is possible because all models have the same numerical mesh, allowing a node-by-node comparison. According to eq. 7, values of S close to zero represent small variations between the base-case and the changed models when the studied parameter is changed, meaning that this parameter has a low influence on the model results. On the other hand, larger values of S represent larger variations between the base-case and the changed model, meaning the parameter that has been varied has a higher influence on the model results.

The statistical results for the sensitivity analysis using the comparison ratio S are shown in Table 2.5. This table lists the average, the median and the standard deviation results of S for each of the varied models (by rows) and comparing different model results (by columns). In addition, we add the number of points omitted for each comparison, that represent points with unrealistic values that would skew the comparison. This number is usually low for all the comparisons performed, varying between 0 and 2%. The median values in Table 2.5 for the principal stresses results show a very small S for all the changes considered, with small standard deviations. These results mean that the imposed changes in the elastic parameters have a very low influence on the principal stress results. The median and standard deviation values in Table 2.5 for the displacement results have S values higher than the ones for the stress results, especially when the input elastic modulus is varied. This is explained by the small overall magnitude of the displacements in these models, a consequence of the elastic

assumption for sediment behaviour. Slight changes in the already small base-case displacement results produce values of S that are far higher when compared to the S values for the stress results. Despite that, the median values of S for the displacements are still small, not exceeding 0.21.

Another way to compare results between the base-case model and the sensitivity analyses is to directly subtract stress results along the exploratory well trajectory (Figure 2.6). This figure shows that the change in elastic parameters has a minor effect on the predicted horizontal stress, σ_h along the exploratory well, with the greatest difference being less than 0.15 ppg. Specifically, the elastic modulus has a greater influence on the stress results when compared to the Poisson's Ratio, that has a negligible effect along all the well trajectory.

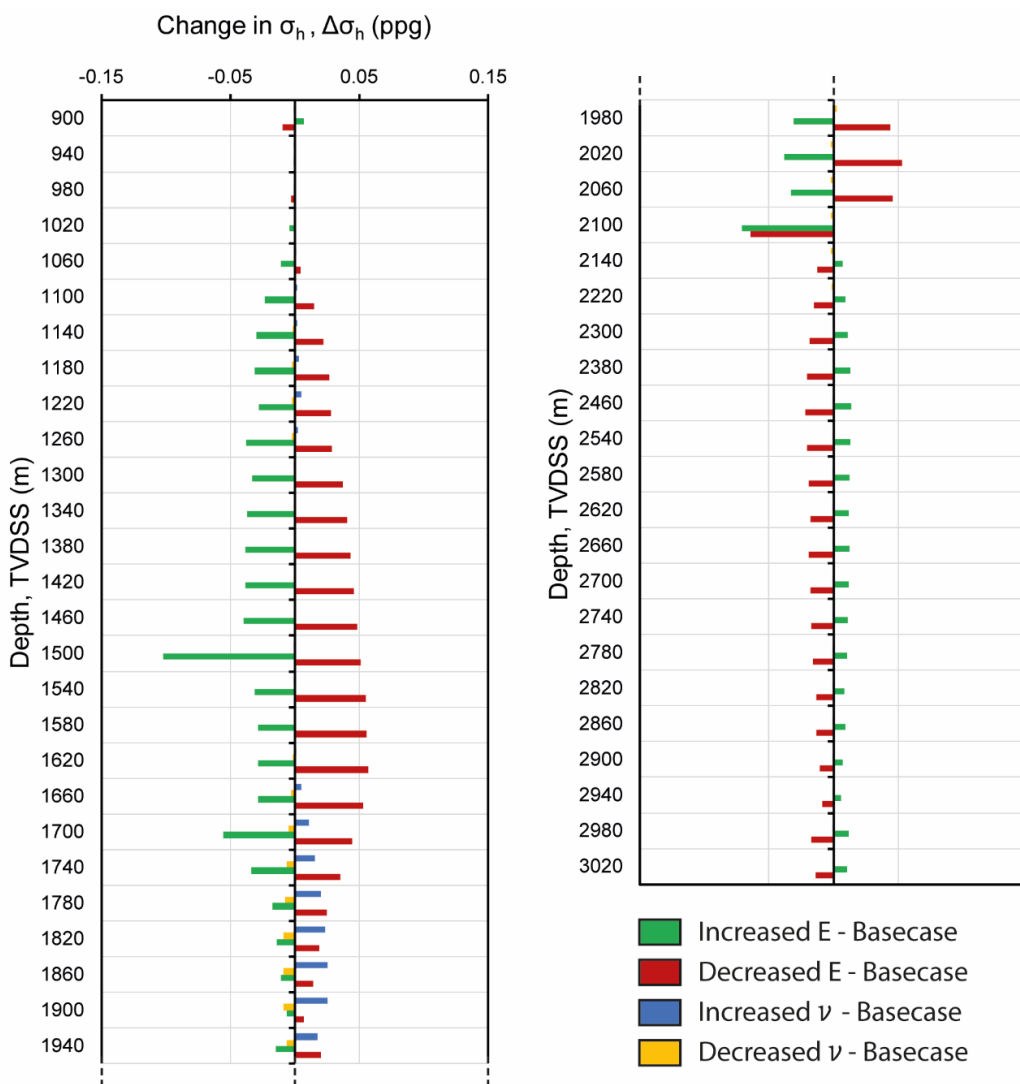


Figure 2.6: Difference in prediction of horizontal stress σ_h between sensitivity analysis and base-case models along the Sandia-1 exploration well. The major difference is obtained when varying the Elastic Modulus, but it does not exceed 0.15 ppg. This indicates little effect of the elastic parameter variation on horizontal stress. Sea surface located at upper part of the plot and salt diapir located at bottom.

Table 2.5: Statistical summary of sensitivity analyses results, reporting comparison ratio S (eq. 7).

	σ_1	σ_2	σ_3	E-W displacement	N-S displacement	Vertical displacement	
Increase ν	Average	-4.45E-05	7.34E-05	-1.70E-05	1.02E-03	7.06E-04	-3.87E-03
	Median	-2.40E-05	-2.70E-05	-2.00E-06	2.08E-03	4.18E-04	8.60E-05
	Stand. Dev	5.07E-03	3.02E-03	1.86E-03	0.02	0.04	0.06
	Points omitted (%)	1.80E-03	2.28E-04	0	0.04	0.13	0.47
Decrease ν	Average	3.02E-05	-5.09E-05	-9.71E-07	-2.75E-04	-1.97E-03	3.42E-03
	Median	6.00E-06	4.00E-06	-1.00E-06	-9.10E-04	-1.10E-05	-1.07E-04
	Stand. Dev	2.43E-03	1.26E-03	6.44E-04	0.01	0.03	0.04
	Points omitted (%)	4.06E-04	5.07E-05	0	0.02	0.08	0.20
Increase E	Average	-3.62E-05	-3.34E-04	-7.21E-05	0.15	0.12	0.18
	Median	9.10E-05	-3.71E-04	3.90E-05	0.16	0.16	0.15
	Stand. Dev	0.02	6.84E-03	3.14E-03	0.04	0.09	0.11
	Points omitted (%)	0.02	2.46E-03	0	0.15	0.83	1.31
Decrease E	Average	-4.19E-05	4.02E-04	6.03E-05	-0.21	-0.15	-0.30
	Median	-2.24E-04	5.37E-04	-4.70E-05	-0.22	-0.22	-0.21
	Stand. Dev	0.02	7.90E-03	3.87E-03	0.06	0.12	0.14
	Points omitted (%)	0.03	3.35E-03	0	0.25	1.43	2.42

2.3 2D static geomechanical model

The 3D modelling approach is the best approximation to the actual basin geometries obtained from the seismic survey. Despite that, the 3D model has the important limitation of being time-consuming to design and computationally more expensive to run. This fact has limited our ability to further test and reproduce different versions of the 3D geomechanical model and has motivated the use of a plane-strain 2D version. Part of the objectives of the present thesis is to investigate whether the 2D approach, while simplified, can be adopted as a convenient tool to approximate the stress and strain prediction from the 3D model. In addition, the 2D model approach will allow us to better explore the contribution of the various input assumptions.

2.3.1 Model setup

Similarly to the 3D model, we build the 2D geomechanical static model using the software Elfen (Rockfield 2017). The 2D model is a plane-strain, quasistatic, drained, finite-element model. We define the model geometry by extracting a cross-section of the 3D model (Figure 2.7) oriented SE-NW on a plane that contains the exploratory well. We chose the orientation of this section to capture the key elements of the 3D model, such as the faults crossing the well trajectory, the salt structure located below the well and the anticline formed by the salt-roof sediments. This section also captures part of a salt structure located at the NW of the study area (the Western diapir) as well as a small portion of a third salt structure in between. It should be noted that the orientation of the 2D model does not exactly correspond to the east-west orientation of the maximum principal stress. However, the difference between the initial stress ratios K_H and K_h is small, averaging 0.11. Hence, the orientation chosen should have a low impact on the final stress results.

The 2D model domain is discretised by an unstructured finite-element mesh formed by linear rectangular elements of 200 m in size, with a finer mesh region with elements 50 m in size and located on top of the Sandia diapir structure.

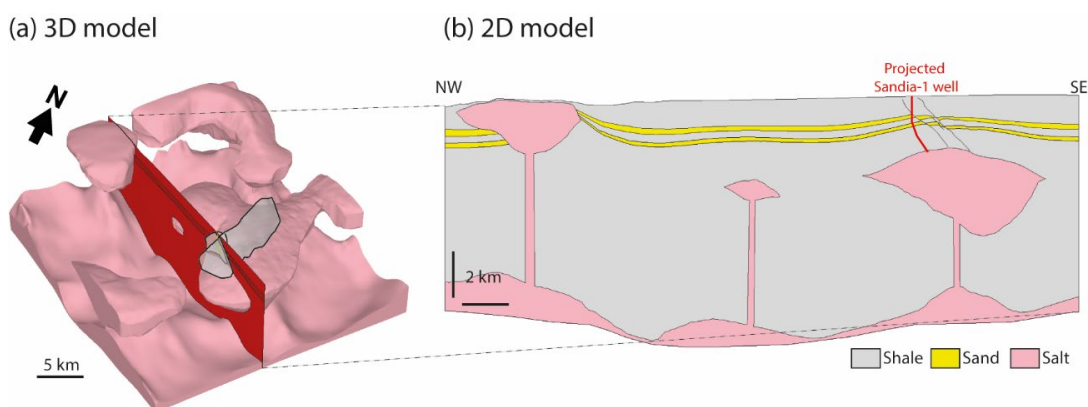


Figure 2.7: (a) 3D model showing the geometry of the salt and faults, together with the cross section (in red) used for the 2D model geometry. (b) Geometry of the 2D model.

The boundary conditions applied in this model restrict horizontal displacements at the vertical sides of the model domain and both horizontal and vertical displacements at the base of the model. The upper part of the model is a free surface representing the present-day sea floor.

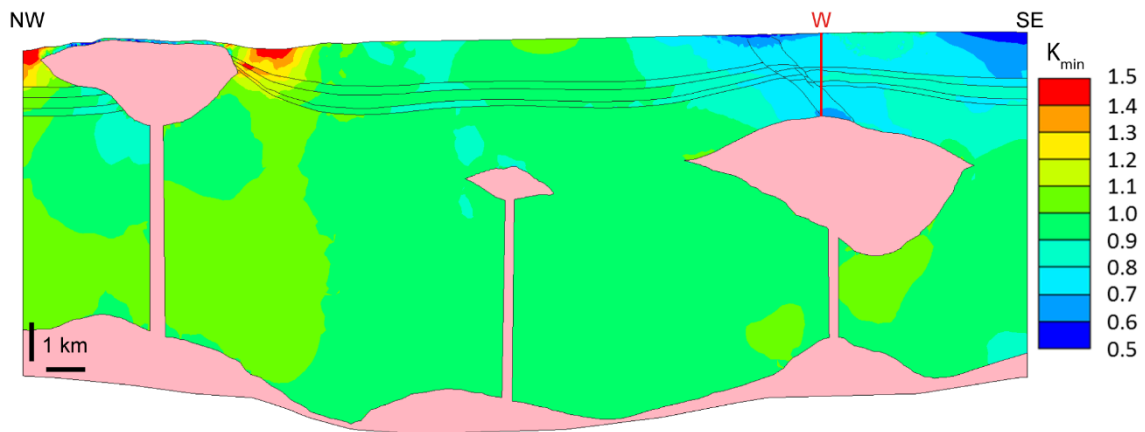
Finally, we use the same input values as in the 3D static model (see section 2.2.1) for the fault properties, the initial pore pressure and initial stress ratios (Table 2.1), the material properties (Table 2.2 and Table 2.3), and the temperature gradients. This allows a more consistent comparison between the 3D and the 2D model results, which is part of the scope of this study.

2.3.2 Model results

As for the 3D static model prediction, we use the minimum horizontal-to-vertical effective stress ratio (K , eq. 6) to explore the stress prediction of the 2D static model. We can compare the final stress state of the sediments to their initial K_0 value of 0.8 (light blue contours, Figure 2.8a). These contours show a region around the Western diapir where K has increased to values near 1.5 (red contours, Figure 2.8a). More importantly, there is a reduction of K for the sediments located above the Sandia diapir. In particular, the stress ratio remains below 0.8 around the faults and reaches its minimum value both near the sea floor surface and on the sediments located immediately on top of the salt crest. It should be noted that the stress reduction located at the upper SE corner of the model is probably related to boundary effects and it is not discussed further.

We extract the stress values along a vertical profile W located on top of the Sandia diapir to further investigate the stress state of the sediments at that location (solid lines, Figure 2.8b). We compare with the stress profiles for the same sediment material loaded under uniaxial conditions or, in other words, without any perturbations caused by salt, faults, etc (dashed lines, Figure 2.8b). Comparison between the uniaxial stresses and the stresses resulting from the model illustrates the effect of the fault and the salt body on the overall stress state of the sediments. The model vertical stress (solid blue line, Figure 2.8b) shows a very similar trend when compared to the uniaxial vertical stress (dashed blue line, Figure 2.8b), with a slight increase just above the salt. In contrast, the model horizontal stress (solid green line, Figure 2.8b) shows a consistently lower trend compared to the uniaxial horizontal stresses (dashed blue line, Figure 2.8b). The difference between the model prediction and the uniaxial profile increases with depth and reaches its maximum value of 4.5 MPa at the salt-sediment interface located at 3 km below sea level. This reduction is the cause of the stress ratio drop around the salt crest seen in Figure 2.8a.

(a) 2D model prediction for K



(b) Stress profile along well W

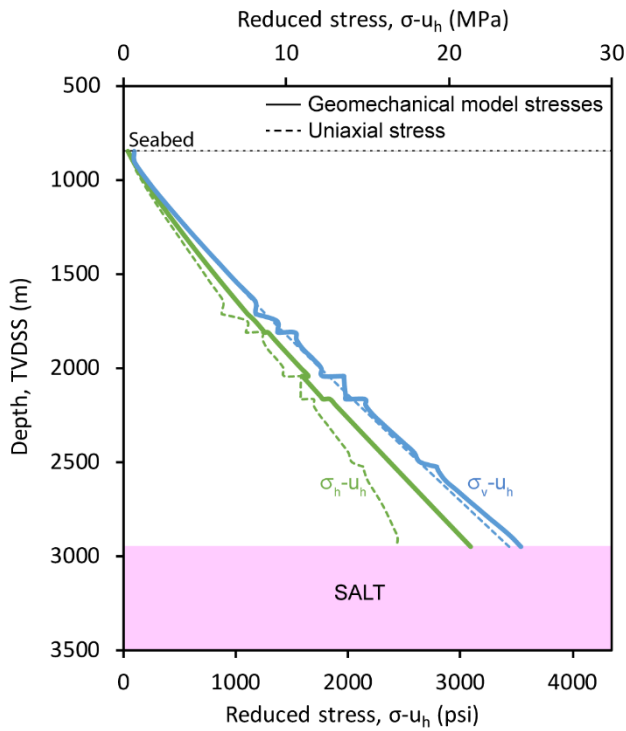


Figure 2.8: (a) Horizontal to vertical stress ratio predicted by the 2D model. The ratio changes near the salt structures, compared to its initial value of 0.8 (green contours). Specifically, it decreases above the Sandia diapir, reaching values around 0.6. (b) Geomechanical prediction (solid lines) for horizontal (green) and vertical (blue) stress along a vertical profile W (in a) compared with uniaxial stresses (dashed lines). Geomechanical horizontal stress is lower than uniaxial, reaching a maximum difference of 4.5 MPa at the salt-sediment interface.

As for the discussion of the 3D model displacement results, here we focus on direction of sediment and salt displacements rather than their absolute magnitude. We find that sediments move towards the NW across nearly all of the model. This NW displacement is maximum on the footwall side of the fault and responds to the overall NW slope of the sea floor. Sediment vertical displacements show a general downwards movement that is maximum both at the hanging wall side of the SE fault above Sandia and at the central part of the model. A combination of both displacement magnitudes and their direction is shown in Figure 2.9. A detailed section at the Sandia diapir (Figure 2.9) illustrates how the displacements of the sediments above the diapir are linked to the salt flow below. The SE side of the Sandia diapir experiences a downwards salt flux, while the NW side of the Sandia diapir moves towards the west. This differential movement of salt causes the diapir to collapse on its SE side and to spread laterally on its NW side. The sediments located on top of the diapir respond to that salt flux in a similar fashion: the hanging wall side moves downwards whereas the footwall side moves towards the west. These two movements generate a region of horizontal extension focussed on the crest of the salt structure.

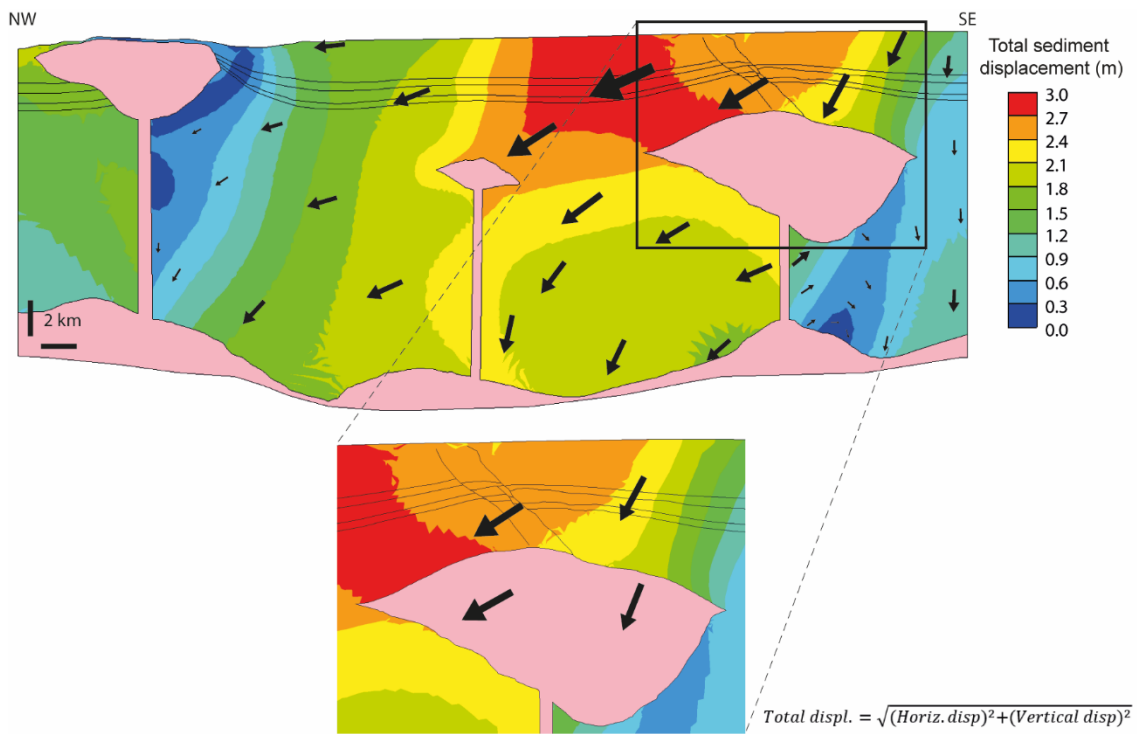


Figure 2.9: Sediment-displacement magnitude (colour contours) and displacement direction (arrows). Displacements have an overall westwards trend across the model and are largest on the footwall side of the fault located above the Sandia diapir (red contours). The detailed section around the Sandia diapir shows the relation between the salt flux and the displacement of the sediments located above.

The horizontal strain prediction (Figure 2.10) further illustrate this horizontal extension at the crest of the diapir caused by the differential sediment displacement. Extension is largest above the Sandia diapir (warm contours, Figure 2.10). Near the flanks of the Western diapir, a localized zone of shortening strain develops (blue contours, Figure 2.10), resulting from the lateral expansion of the salt diapir in the shallow section.

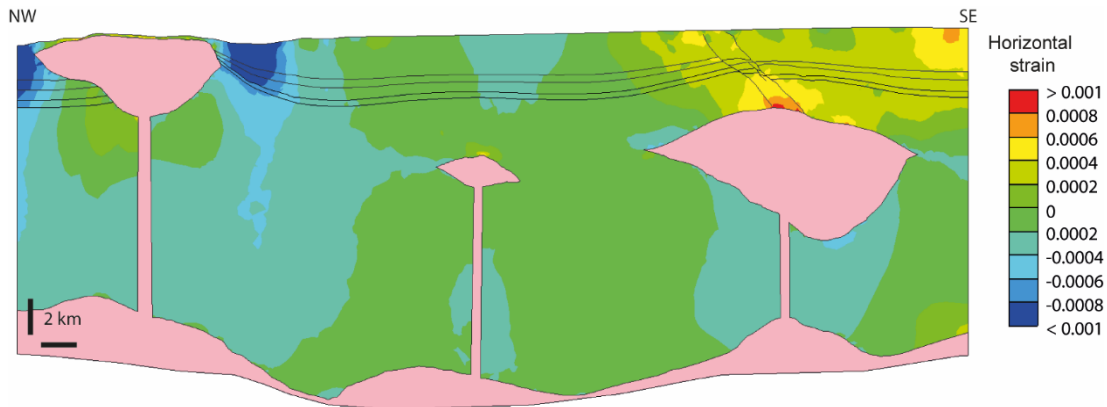


Figure 2.10: Horizontal strain across the 2D model. Red contours represent extensional strains and blue contours represent shortening strains. A region of extensional horizontal strain develops at the crest of the Sandia diapir, between the two faults. Shortening horizontal strains develop at both sides of the Western diapir.

2.3.3 Sensitivity analysis results

We use sensitivity analysis in the 2D model to provide insights on the influence of the different model assumptions on the final results. In addition to changes in elastic parameters examined in the 3D sensitivity study, other structural framework changes have been tested using 2D models (Table 2.6). These additional changes were too complex to test in 3D due to limitations of computational power and time availability. Their study in 2D models allows a more complete assessment of the mechanisms that change the stress and strain state in this particular salt system.

Table 2.6: Summary of the sensitivity analysis run for the 2D static model.

Variable changed	Original value	Changed value
Poisson's Ratio	0.3	0.25 0.4
Young Modulus	Horizon and depth dependent (Table 2.1)	increased 20% decreased 20%
Salt replaced by shale	Salt	Shale
Sea floor geometry	1° sea floor slope	Horizontal sea floor
Number of diapirs	3 diapirs	1 diapir (eastern diapir)
Width of salt columns	200 m	400 m

The change in the elastic shale parameters in the 2D model resulted in a very small variation in the magnitude of stress relative to the base-case model. Even though the magnitude of this change is ten times greater than in 3D, the overall influence is insignificant. Consequently, the 3D conclusion is still valid in the 2D study: changing the elastic parameters within reasonable values does not affect the overall results.

The replacement of the salt lithology in the modelled diapirs by shale lithology helps to illustrate the contribution of the salt viscous behaviour over the stress changes across the model. We compare the results of vertical and horizontal stress along a vertical location above the Sandia salt structure (Figure 2.11, inset). The vertical stress (blue lines, Figure 2.11) does not greatly vary between the base-case model and the model with shale lithology in the diapirs. On the other hand, the decrease in horizontal stress (green lines Figure 2.11) only occurs above a diapir composed by salt. This decrease is not present when shale lithology forms the diapir structure. This result highlights that the stress changes near the crest of the base-case salt diapir are mainly caused by the viscous salt deformation.

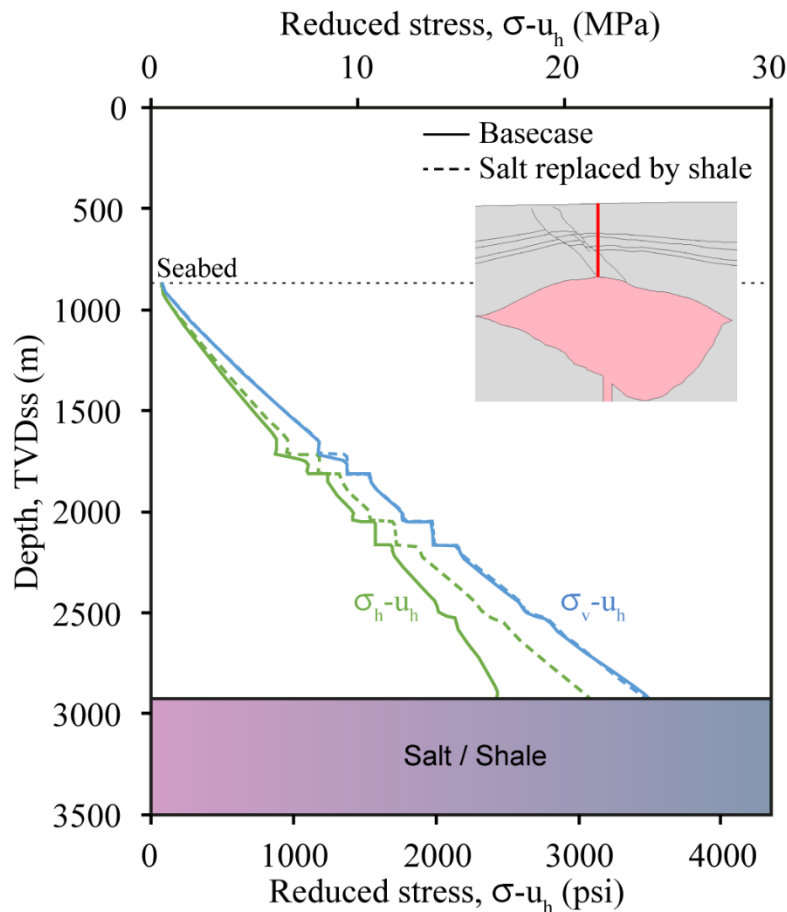


Figure 2.11: Stress profiles along vertical section located at the crest of the Sandia diapir for the base-case model (solid lines) and the model where the salt lithology is changed by shale (dashed lines). The horizontal stress reduction near the salt structure is not present when the diapirs are substituted by shale lithology. Vertical stress is similar in both cases (blue lines).

The 2D base-case model has a sea floor geometry with a 1° slope towards the NW that causes a general NW displacement of the sediments (Figure 2.12a). We define a new model where the sea floor is horizontal (Figure 2.12b). This change causes the sediment displacements to become mainly vertical across the modelled section. The contours of stress ratio above the Sandia diapir indicates a less pronounced stress reduction when compared to the base-case model. Thus, the displacements caused by the sea floor slope also contribute to the stress reduction above the Sandia diapir.

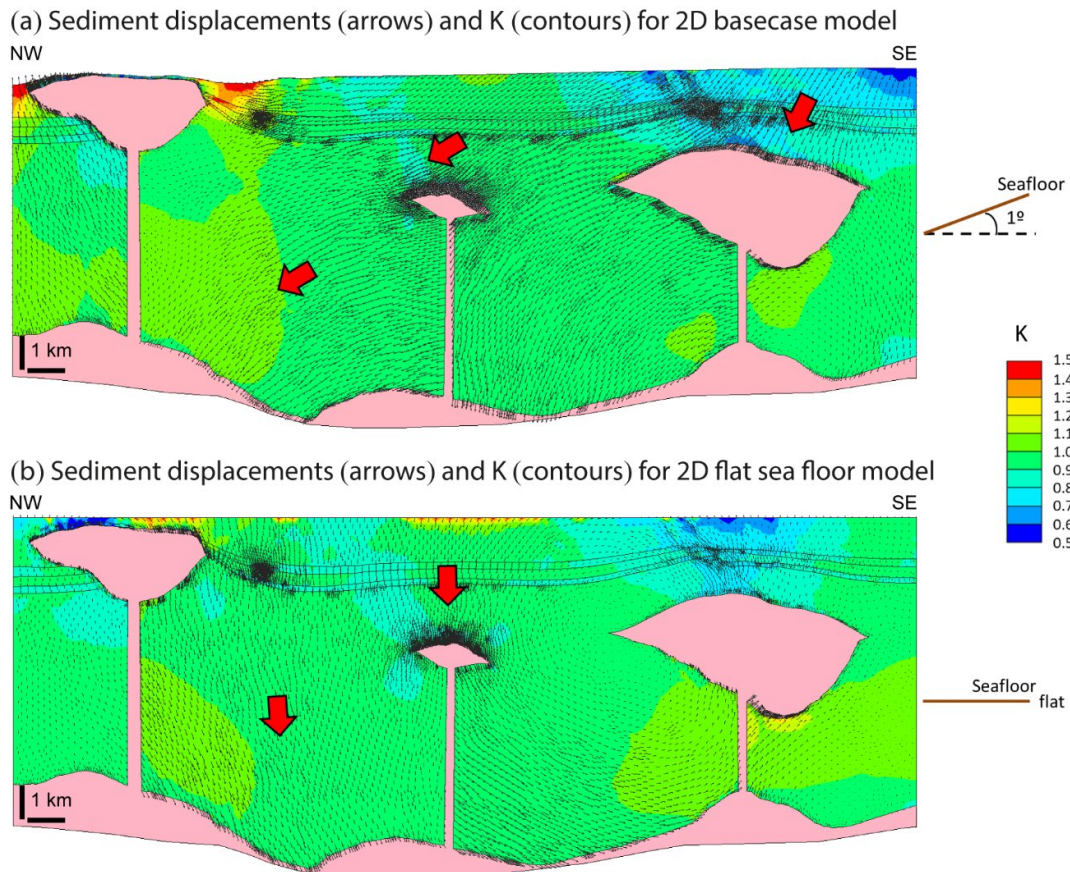


Figure 2.12: Results of stress ratio (contours) and sediment displacements (arrows) for (a) 2D basecase model and (b) 2D model with flat sea floor. The leftwards displacement trend in (a) disappears when the sea floor is flat. The stress ratio reduction above the Sandia diapir in the basecase model is slightly reduced when the sea floor is flattened.

We continue the sensitivity analysis by running a 2D model version of the base-case model where the two western salt diapirs have been removed and only the Sandia salt diapir is present. This change allows to identify the interaction between the modelled diapirs and the stress reduction detected above Sandia on the base-case model. The results show that the stress changes are less pronounced in the changed model (Figure 2.13b) compared to the base-case model (Figure 2.13a), indicating that the presence of deformable salt west of the base-case model allows additional westward sediment displacement. This extra displacement contributes, in turn, to the stress reduction present above the Sandia diapir in the base-case model (Figure 2.13b).

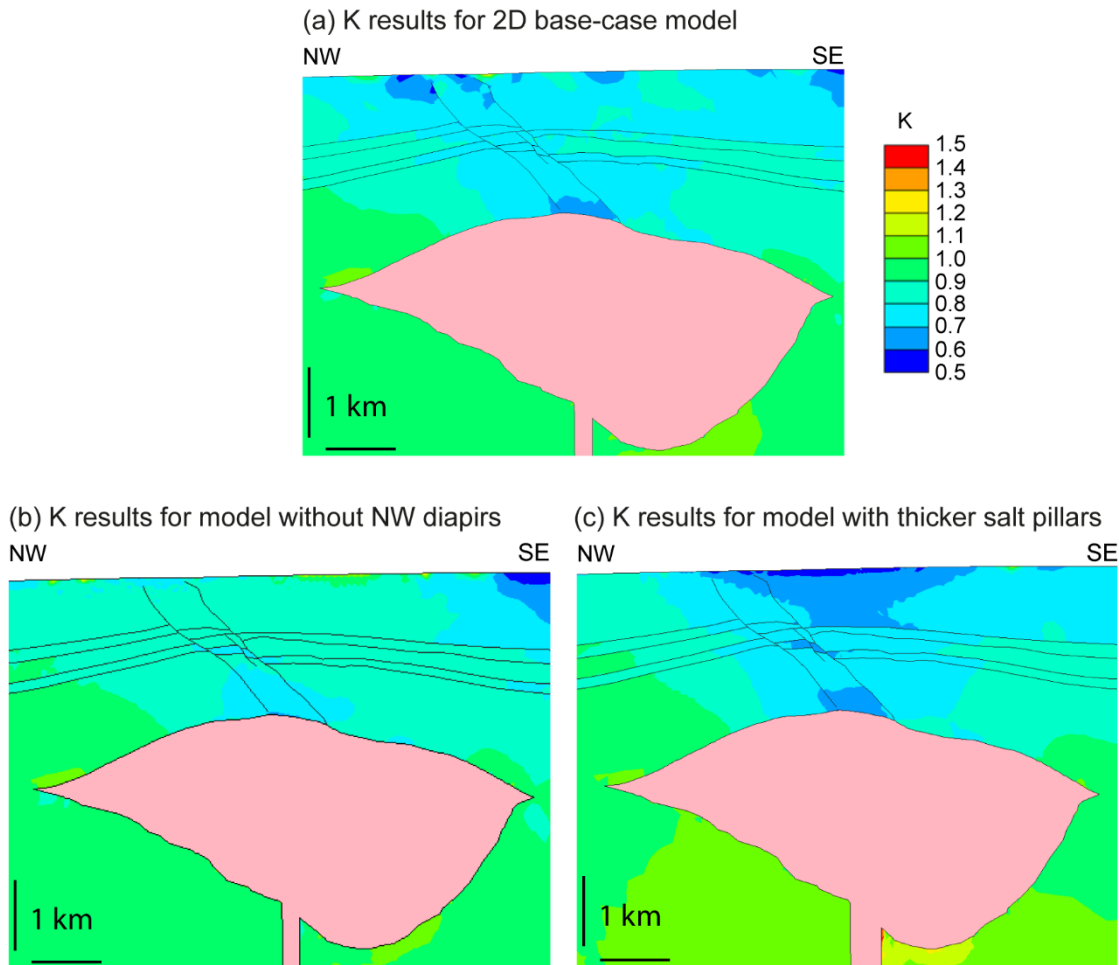


Figure 2.13: Stress ratio results above the Sandia diapir predicted by (a) the base-case model; (b) the model without the western diapirs; (c) the model with thicker salt columns.

Finally, we test the assumption of salt columns of 200 m width that connect all the salt diapirs to the salt source layer located at the base of the model. This parameter has an impact on the pressure connectivity between the source layer and the diapir bulbs. Setting the width of the salt columns to 200 m in the base case model (same size as the mesh elements in the 2D geomechanical model) ensures no pressure connectivity between the salt bodies. To test this parameter, we widen the salt columns to 400 m and observe the changes in the final model stress state (Figure 2.13c). The results from this change show a similar minimum stress ratio reduction than the base-case model (Figure 2.13a), with slightly broader contours both at the diapir crest and at the sea floor. Thus, the width of the diapir columns has a low influence over the stress results.

We summarize the results of the 2D sensitivity analyses in Figure 2.14 by showing the deviation of the principal stress values from the base-case model results due to each of the changes applied. The comparison of principal stresses is performed along a vertical section located at the crest of the Sandia diapir (same as Figure 2.11, inset). This location is chosen because it has the highest stress changes present in the base-case model. The greater the deviation due to a particular model change, the greater impact this model assumption has

over the results. This comparison clearly shows that changes in the elastic properties of the shale sediments have the least impact over the principal stress results. The changes in elastic modulus result in less than 1% difference, whereas the Poisson's Ratio changes do not alter the base-case stress results. The influence of the viscous salt lithology and the presence of other diapirs in the model result in the highest stress changes, 9% and more than 7% respectively. It is important to note that these changes mainly influence the minimum principal stress, which is sub-horizontal. Other changes like the sea floor geometry or the width of the salt feeders also have a noticeable influence on the stress results, affecting both principal stresses by 2 to 4%.

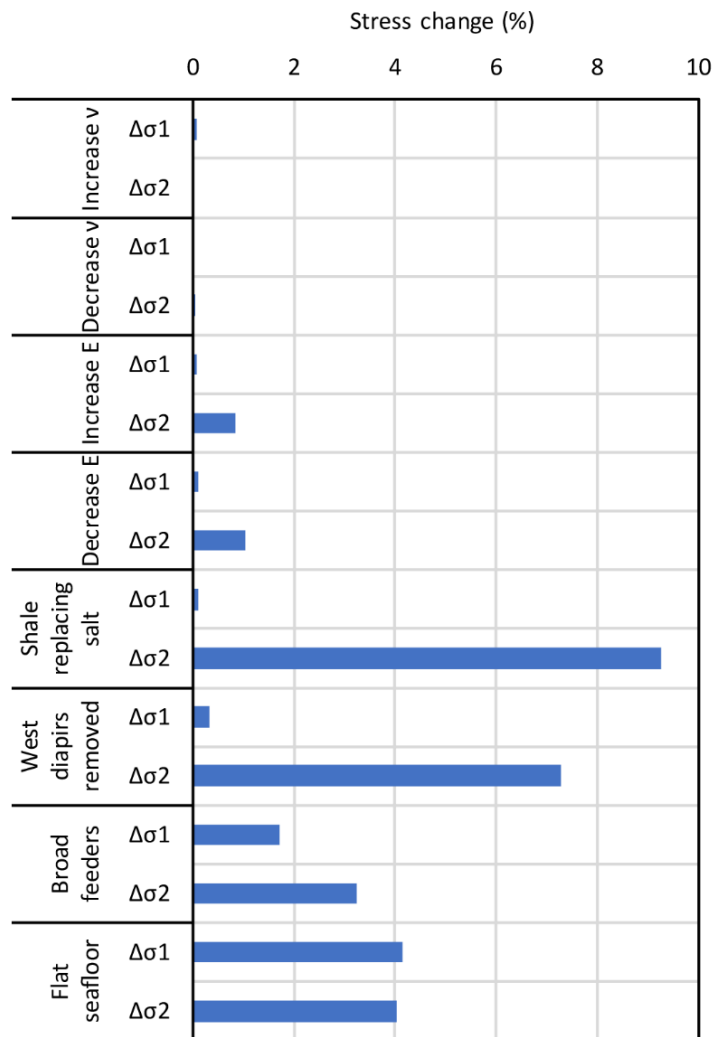


Figure 2.14: Change in principal stress values between 2D sensitivity analyses and base-case model results. Salt rheology and additional salt diapirs yield the greatest stress changes. Variation of elastic parameters does not noticeably affect the stress results.

2.4 2D evolutionary geomechanical model

The static geomechanical approach can be a convenient tool to model basin geometries at present day, usually obtained from seismic or field data. These models can provide a first-order approximation of the stresses, strains and pressures around existing structures. Despite that, the static approach lacks input from past geological processes during the evolution of the basins. In this section, we present a geomechanical study from the Tarfaya basin using an evolutionary approach that overcomes the limitations of the static approach. Here, the Sandia diapir geometry is not predefined as a model input, but results from the simulation of deposition, salt flow and shortening. That allows us to explore the different geological processes taking place during the basin formation that contributed to the present-day configuration of the basin.

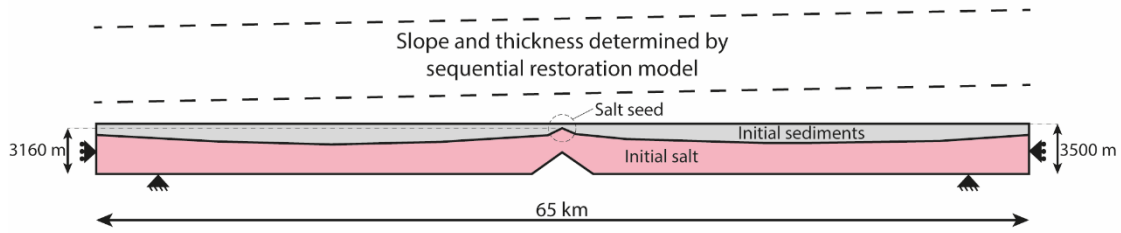
2.4.1 Model setup

We build a 2D plane strain geomechanical evolutionary model (called the base-case model, BC) using the software Elfen (Rockfield 2017). This model is based on a quasi-static, finite-element formulation accompanied by an automated adaptive-remeshing technique (Peric & Crook 2004). The remeshing is activated when the model reaches a threshold plastic strain of 0.7, generating an increase of smaller elements inside the remeshed region. The domain is discretized with a mesh composed by unstructured rectangular elements of 200 m in size and a minimum of 80 m when re-meshed. In addition, the model incorporates a geometric pinching technique that allows the removal of thin layers that would otherwise cause too much element distortion and may lead to numerical instabilities. The model is drained, meaning that the pressures are hydrostatic and no excess pore pressures are generated during the simulation. We assume a fully submerged basin, therefore, the stresses obtained from the model are expressed as effective stresses.

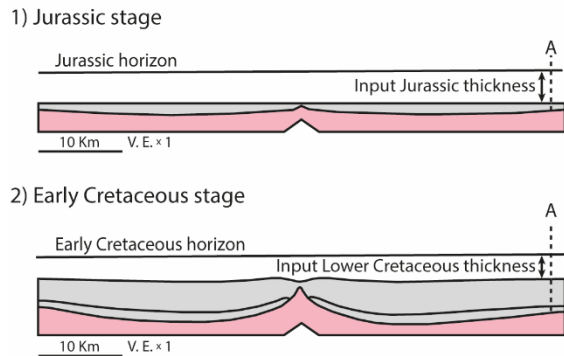
The initial geometry for the BC model is composed by a salt layer 2 km thick covered by a thinner shale layer averaging 1.1 km thickness on top (Figure 2.15a). The salt layer has an initial salt dent at the center of the salt top surface (salt seed) and slight sags at both sides of it to facilitate the initialization of the salt diapir. The shale layer on top of the salt has the role of preserving the initial geometry of the salt layer by preventing any lateral salt flow towards the lateral minibasins at the beginning of the analysis. We apply the boundary conditions at both sides of the model domain by restricting the horizontal displacements. We also restrict displacements in the horizontal and vertical direction at the base of the model. The upper part of the model is free to move in any direction, representing the sea floor during the basin history.

We define the sedimentary layers to be deposited on top of the salt by using both a burial history curve (Figure 2.16) and the paleo-bathymetries provided by the sequential kinematic restoration model of the basin (Figure 1.3).

a) Model set-up



b) Deposition mechanism



c) Shortening curves applied

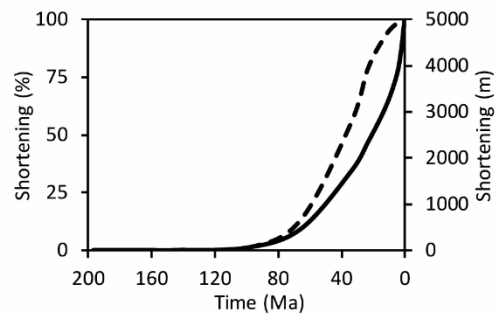
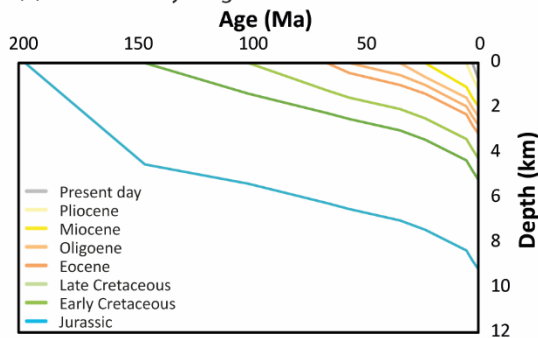


Figure 2.15: (a) Initial geometry for the salt (pink) and shale (gray) layers in the geomechanical evolutionary Elfen model (BC model), along with basic model dimensions and boundary conditions. (b) Definition of deposition horizons: at the beginning of each stage, the upcoming layer thickness is obtained from burial history curve (Figure 2.16a) and applied at the right side of the model (location A), starting at the current top surface. For example, for the Jurassic modelling stage, the deposited-layer thickness is 4500 m (blue line, Figure 2.16a) defines the elevation of the Jurassic deposition horizon at the right end of the evolutionary model (A). The Jurassic bathymetric slope obtained from the kinematic restoration (Figure 1.3; Table 2.7) is then used to define the Jurassic horizon across the model. Sediment compaction and salt mobilization modify the geometry of the sea floor, which becomes the baseline for the next deposition stage (b2) (c) Shortening application curves for the base-case model (solid line) and a variant model (sigmoid dashed line).

(a) Burial history diagram at location Y



(b) Burial history diagram at location Z

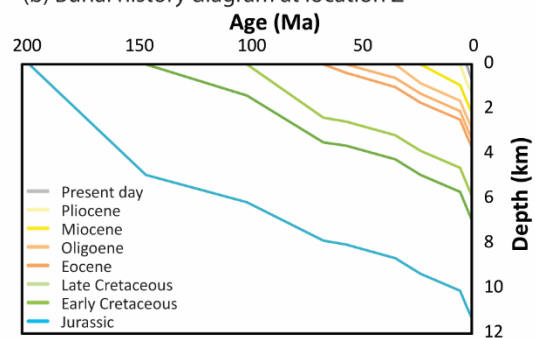


Figure 2.16: Burial history curves resulting from thickness extractions in the sequential kinematic restoration model of the Tarfaya basin section (Figure 1.3). (a) Burial history curve at location Y (SE of Sandia diapir, Figure 1.3). (b) Burial history curve at location Z (NW of Western diapir, Figure 1.3).

To obtain the burial history for the simulation of the Sandia diapir (Figure 2.16a), we extract the thickness of sedimentary layers from the kinematic restoration model along a vertical profile 10 km east of the diapir (location Y; Figure 1.3). We perform this extraction for each of the geologic intervals shown in the kinematic restoration model. The results from this extraction are shown in Figure 2.16. It is worth noting that the shallowest layer at each geologic interval in the kinematic restoration model is already de-compacted and, hence, its thickness is used in the BC evolutionary model with no further adjustment. Then, for each modelled geologic interval, the deposited-layer thickness provided by the burial history curve (Figure 2.16a) is added into the geomechanical evolutionary model on top of the current sea floor. This defines the elevation of the upcoming deposition horizon (Figure 2.15b). This calculation is applied at the right end of the evolutionary model, 30 km from the initial salt seed to ensure far-field conditions (arrow in location A, Figure 2.15b). We extend the deposition horizon across the evolutionary geomechanical model using the average bathymetric slope extracted from the kinematic restoration model at each geologic interval (Figure 1.3). Then, the model fills the space between the current sea floor and the upcoming horizon by adding sediments to simulate the deposition of a new layer (Figure 2.15b).

The movement of the salt in this evolutionary model is not prescribed. The differential loading generated by the weight of the deposited materials causes the salt to deform and flow, loading the newly deposited sediments. This, together with sediment compaction, modifies the topography of the sea floor in the model, which becomes the new baseline for the next deposition stage (Figure 2.15b). This means that the elevation of each deposition horizon depends on both the burial history and the preceding model evolution.

Table 2.7: Thickness and sea floor angles from sequential kinematic restoration model at the end of each geologic time interval.

Name	Duration (M. yr.)	Total thickness at end of stage (m)	Sea floor angle at end of stage (°)
Jurassic	52	4500	0.43
Lower Cretaceous	45	1270	0.32
Upper Cretaceous	34	1230	0.22
Paleocene/Eocene	32	1000	0.32
Oligocene	11	615	0.21
Miocene	17.1	1080	0.42
Pliocene	2.8	620	0.38
Present day	2.5	700	0.53

The BC evolutionary model also accounts for the tectonic shortening between Upper Cretaceous (100 Ma) and the present day, representing the Atlas inversion and the uplift of Africa at that time. We apply this shortening by deforming the geometry of the model base from its original length of 65 km to a final length of 60 km. The shortening deformation rate

increases gradually over the first 50 Myr to ensure numerical stability and follows an exponential curve thereafter (solid black line, Figure 2.15c). All the geometric features of the model base scale proportionally.

The BC evolutionary model is composed by two different lithologies: salt and shale. The salt is modelled using the same Munson-Dawson formulation (Munson & Dawson 1979) as the static models (see sections 2.2.1 and 2.3.1), with some variations on the input parameters to reduce the salt viscosity and to facilitate the first salt displacements (Table 2.8). The initial salt stress state is uniform ($K_0 = 1$). The model assumes a homogeneous and isotropic salt material, not accounting for inner layering and anisotropies.

The sediment behaviour is represented by an elastoplastic material using the SR3 constitutive model (Crook *et al.* 2006). The rheologic parameters of this model are listed in Table 2.9 and shown in Figure 2.17. This model is based on the critical state theory, following a single-surface, rate-independent, non-associated formulation. A key feature of the critical state model is the incorporation of both mean and differential stress to compaction. In other words, porosity evolves during the simulation because of deposition, salt loading, and tectonic shortening. Subsequently, density also changes as a function of porosity.

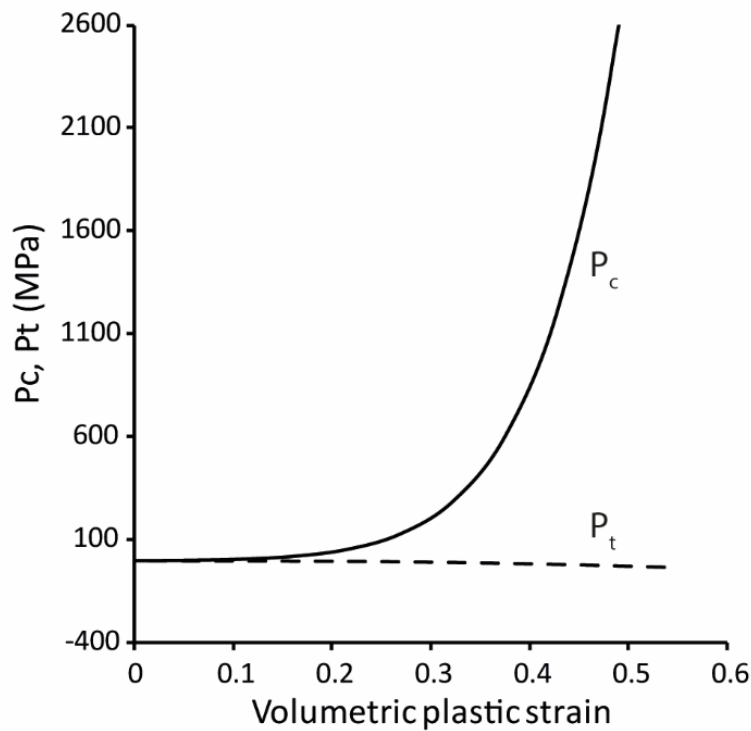
Finally, we introduce a constant temperature gradient in this model of 3.1°C per 100 m, following some examples present in the literature about this particular location (e.g., Rimi 2001; Zarhloule *et al.* 2010). The starting temperature at a sea floor temperature is 4°C.

Table 2.8: Material properties for salt (Munson 1997; Fredrich *et al.* 2007a)

Parameter	Units	Value	Parameter	Units	Value
E	Mpa	10000	N₂		5
v		0.35	Q₂	cal/mol	10000
ρ	Kg/m ³	2100	R	cal/°K/mol	1.987
A₁	1/myr	1.89E+39	T₀	°K	10
N₁		5.5	T_{const}	°K	273
Q₁	cal/mol	25000	G₀	MPa	12400
A₂	1/myr	2.17E+29	dG/dT	MPa/°K	10

Table 2.9: Material properties for sediments (Nygard et al. 2006; Rockfield 2017)

Parameter	Units	Value	Parameter	Units	Value
E	Mpa	40	Ψ	$^{\circ}$	51
ν		0.25	β_0		0.6
ρ_{water}	Kg/m ³	1000	β_1	1/Mpa	0.725
ρ_{grain}	Kg/m ⁴	2700	α		0.25
κ		0.01	N		1.3
$p_{t,0}$	MPa	0.085	n_0		0.38
$p_{c,0}$	MPa	-1	Hardening properties		Figure 2.17
β	$^{\circ}$	60			

**Figure 2.17:** Hardening parameters for SR3 material model used for the sediments (Rockfield 2017).

2.4.2 Model results

The aggrading sediments in the BC model and their unequal thickness impose a differential load on the salt layer. The resulting shear (differential) stress drives the viscous salt flow from the salt source layer towards the diapir. The average salt differential stress in the model ranges between 0.05 and 1 MPa and is comparable with values from published studies (e.g., Schlöder & Urai 2007). Despite its low value, this shear stress is able to mobilize the salt, given the salt's average viscosity. The relatively low strain rates and low upper crustal temperatures used in this study yield an average salt viscosity between 10^{17} to 10^{19} Pa·s, consistent with

typical values reported for salt rocks (van Keken *et al.* 1993; Marketos *et al.* 2016; Hamilton-Wright *et al.* 2019; Rowan *et al.* 2019).

The deposition of the earliest Jurassic sediments results in a differential overburden load between the higher salt point (the salt seed defined initially, Figure 2.15a, Figure 2.18a) and the lower points on the salt surface (the sagged areas in the middle of the two lateral minibasins, Figure 2.15a, Figure 2.18a). This differential overburden triggers the salt flow towards the centre of the model. Further Jurassic deposition causes the salt diapir to widen and rise, reaching the surface at 145 Ma (Figure 2.18b). At this time, the upper half of the diapir is narrower than its lower half and the 6.5 Km thick pedestal (triangular-shaped base connecting the diapir with the salt source layer; Vendeville & Nilsen, 1993). The pedestal allows the salt to flow from the source layer into the diapir. After that time, the Early Cretaceous sediments begin to deposit and at 123 Ma (Early Cretaceous, Figure 2.18c), the diapir morphology changes: its upper part widens considerably relative to the end of Jurassic. The salt pedestal is still considerably wider than the diapir, containing a large salt volume; however, the source layer has thinned significantly.

At the end of Early Cretaceous (100 Ma, Figure 2.18d), the source layer welds along both sides of the diapir, completely isolating the pedestal and the diapir. Despite that, the salt already accumulated on the pedestal allows the diapir to continue growing and the salt to flow on the basin surface. This forms a salt sheet downslope and an overhang upslope (Figure 2.18d). The salt sheet emplaced downslope has a total breadth of approximately 8 Km and is about 2 Km thick.

The Upper Cretaceous deposition from 100 to 66 Ma completely buries the salt system (Figure 2.18e). However, the diapir keeps rising and thickening the salt sheet by depleting salt from the pedestals and thinning the diapir stem (the slender part of the diapir structure that connects the upper part with the pedestal, Jackson & Hudec, 2017). At this time, the regional shortening begins (solid black line, Figure 2.15c) and contributes by facilitating the flow of salt towards the upper parts of the diapir and by further narrowing the salt stem (Figure 2.18f). The shortening remains active until the end of the simulation (present day, 0 Ma, Figure 2.18g) and drives salt flow from the salt sheets towards the centre of the diapir. Thus, the diapir crest inflates despite the subsequent deposition of Paleocene to Quaternary layers. This process causes the bending of the Tertiary layers emplaced on top of the salt structure.

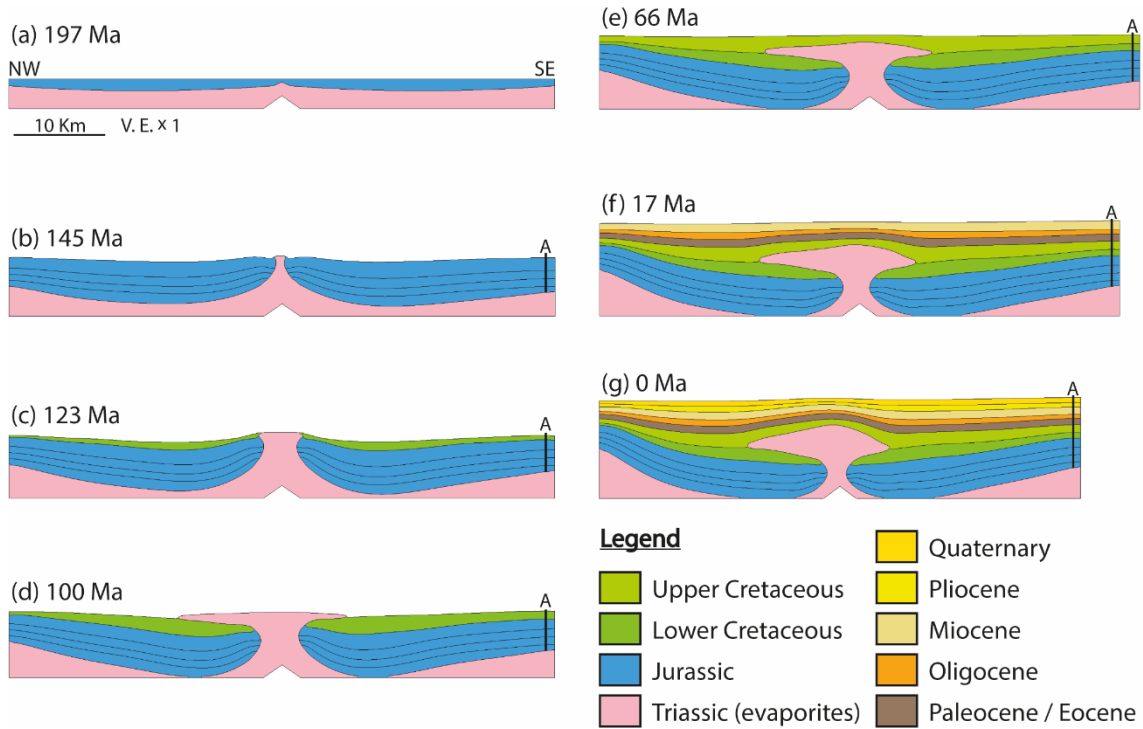


Figure 2.18: Evolution of the Sandia diapir predicted by the base-case geomechanical model. Profile A (vertical black line) indicates the location where the layer thicknesses from burial history diagram (Figure 2.16a) are applied. (a) Initial geometry representing the top Triassic evaporites (pink) and an initial thin layer of Jurassic sediments (blue); (b) End of Jurassic deposition (blue). The salt diapir reaches the sea floor; (c) Mid-stage of Lower Cretaceous sediment deposition (dark green). Salt is about to break out into a salt sheet and source layer has thinned; (d) End of Lower Cretaceous deposition (dark green) with salt sheet formed downslope and salt overhang upslope. The source layer is welded on both sides of diapir and connected to the upper part by a salt stem; (e) End of Upper Cretaceous deposition (light green). Diapir is buried. Regional shortening is activated during this stage; (f) Paleocene to Miocene deposition. Shortening continues. Salt volume in pedestal decreases and diapir stem thins, while the diapir bulges upwards, arching its roof sediments; (g) Present-day, following Pliocene and Quaternary deposition. Shortening continues. Salt volume in pedestal and in stem further decreases, as does the extent of the salt sheets. The diapir bulges upwards arching its roof sediments.

2.4.3 Sensitivity analysis results

The evolutionary geomechanical model for the Tarfaya basin depends on a number of parameters that control its progress, e.g., shortening rates, temperature gradient, sedimentation rate, etc. Some of these parameters also have a high level of uncertainty associated to them. This is the case, for example, for the presence of the basal structural high below the salt layer or the geometry of the shortening rate curves. We can reduce the uncertainties of the input parameters by analysing their influence over the final model results. For that, we built and ran further models using the same initial configuration as the base-case model (BC) presented in section 2.4.1 but changing one of the target parameters at a time to assess its influence. The model variants (Table 2.10) defined and run are:

- MV1: we use a shortening rate that increases, peaks and decreases progressively (dashed line, Figure 2.15c) instead of the BC exponential shortening rate (solid line, Figure 2.15c), maintaining the same shortening magnitude of 5 Km and its timing.
- MV2: we remove the basal triangular feature representing the rotated fault block interpreted below the diapirs (Figure 1.3. Also Figure 2.15a). Instead, the base of the salt in this model is totally flat.
- MV3: we increase the temperature gradient of the basin from 31°C/km (temperature used in the BC model) to 36°C/km.
- MV4: we extract the burial history and the initial salt thickness along a vertical location at the NW side of the basin (location Z, Figure 1.3), obtaining the curves from Figure 2.16b. The MV4 aims to reproduce the Western diapir and explore the effect of the deposition history on the evolution of a salt diapir.
- MV5: we reduce the sedimentation rates for Pliocene and Quaternary from 620 and 700 m/M.yr., respectively (BC model) to 61m/M.yr. The original values come from the extraction of the layer thicknesses from the kinematic restoration model (pale yellow and grey lines, Figure 2.16a). However, they are interpreted to be unrealistically high and the new value of 61m/M.yr. adopted here is more in line with the sedimentation rates during the previous Oligocene and Miocene stages.

Table 2.10: Summary of the sensitivity analysis run for the 2D evolutionary model.

Variable changed	Model Name	Original value	Changed value
Shortening ratio	MV1	Exponential (Figure 2.15c)	Sigmoidal (Figure 2.15c)
Salt base geometry	MV2	Basal triangular shape	Flat base
Temperature gradient	MV3	31°C/km	36°C/km
Thickness extraction at location (Figure 1.3)	MV4	location Y	location Z
Plio-Quaternary rates	MV5	620 to 700 m/M.yr.	60 m/M.yr.

2.4.3.1 MV1 results (variation of shortening rates)

Many salt basins around the world show evidence that salt flow can be driven by tectonic shortening (Vendeville & Nilsen 1993; Nilsen *et al.* 1996; Koyi 1998; Brun & Fort 2004; Dooley *et al.* 2009). The Tarfaya basin has suffered shortening during its history (Michard *et al.* 2008; Wenke *et al.* 2011; Tari & Jabour 2013) but the timing and the rate of deformation of the shortening is not confidently known. The model MV1 uses a sigmoidal shortening curve (dashed line, Figure 2.15c) instead of the exponential shortening curve used in the BC model (solid line, Figure 2.15c). The timing of the shortening application and the total magnitude of 5 Km are not changed with respect to the BC model. The diapir geometry obtained from the MV1 model shows little differences when compared to the BC model (Figure 2.19b vs Figure 2.19a). From that we infer the shortening rate changes applied to this particular case do not greatly alter the kinematics of the salt diapir.

We do find, however, that the final stress state between the models changes significantly when the shortening rates are varied (Figure 2.19c & d; Figure 2.20). We use the horizontal-to-vertical effective stress ratio K (colour contours, Figure 2.19c & d) to illustrate how stresses change compared to the uniaxial state ($K_0=0.8$). Effective stress-ratio values lower than 0.8 (darker blue contours, Figure 2.19c & d) indicate a decrease in horizontal effective stress (σ'_h) relative to the vertical effective stress (σ'_v). $K=1$ (green contours, Figure 2.19c & d) indicates a uniform stress state ($\sigma'_h = \sigma'_v$). K higher than 1 (warm contours, Figure 2.19c & d) indicates that σ'_h is higher than σ'_v . The final stress state in the BC model shows values around 1.2 on the sediments located at the flanks and higher than 1.3 near the diapir crest (Figure 2.19c). The shallowest sediments of the diapir roof, however, are affected by a decrease of the stress ratio, result from the bending of the layers. By contrast, the stress state from the MV1 model presents a general decrease of the stress ratio for the sediments located above the salt structure, reaching values of K around 0.6 (below uniaxial, Figure 2.19d). In this same model, the sediments located near the salt flanks of the salt diapir have values of K around uniaxial (0.8) for the sediments.

We can also compare the results from both the BC and the MV1 models by looking at the stress profiles along a vertical location crossing the sedimentary roof above the salt crest. This stress extraction is made at the end of the simulation. Both the BC and MV1 vertical effective stresses (solid blue lines, Figure 2.20) are very similar to the uniaxial vertical effective stress (dashed blue lines, Figure 2.20), with a slight increase at the bottom of the profile, near the salt. On the other hand, the horizontal effective stresses for the BC model (solid green line, Figure 2.20a) decrease below uniaxial values (dashed green line, Figure 2.20a) for the shallow section and increase more than 20 MPa above uniaxial values in the deepest section. However, the MV1 horizontal effective stresses (solid green line, Figure 2.20b) are below uniaxial conditions (dashed green line, Figure 2.20b) across the whole sedimentary roof. The

maximum horizontal effective stress decrease with respect uniaxial conditions in the MV1 model reaches 4 MPa, 750 m from the crest of the salt structure.

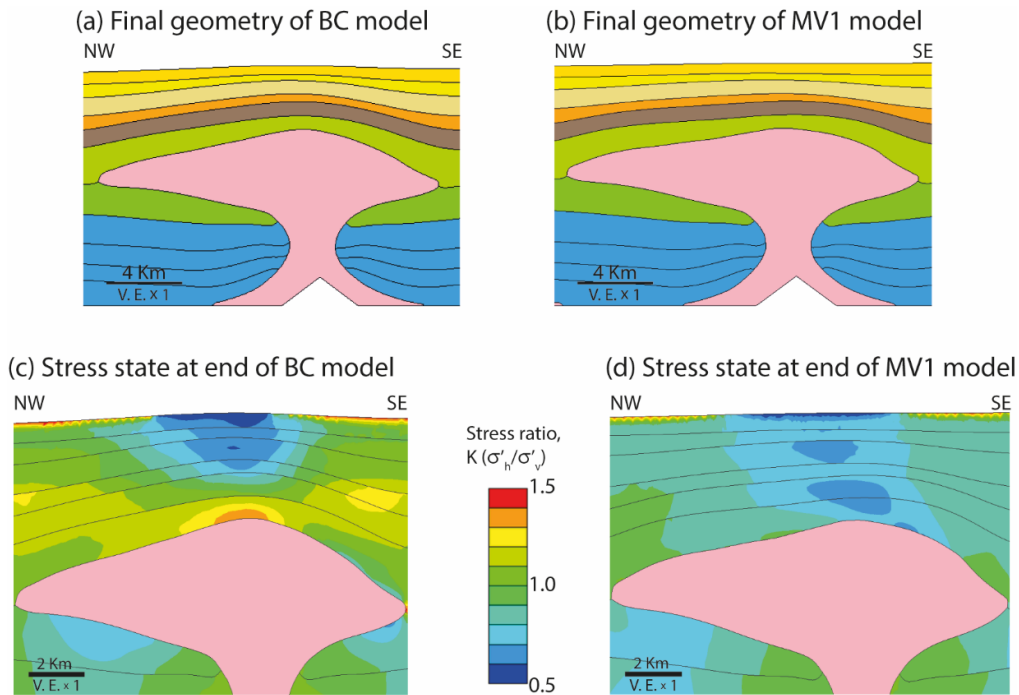


Figure 2.19: (a) Final geometry of the Sandia diapir as predicted by the BC model; (b) final geometry of the Sandia diapir as predicted by the MV1 model, using the sigmoidal shortening rates (dashed line Figure 2.15c); (c) present-day geometry and contours of the horizontal-to-vertical effective stress ratio K for BC model; (d) present-day geometry and contours of the horizontal-to-vertical effective stress ratio K for MV1 model. The uniaxial K_0 value is 0.8 (light blue contour colours). K higher than 1 (warm contour colours) represent σ'_h higher than σ'_v . K below 0.8 (darker blue contour colours) represent decreased σ'_h and lateral extension.

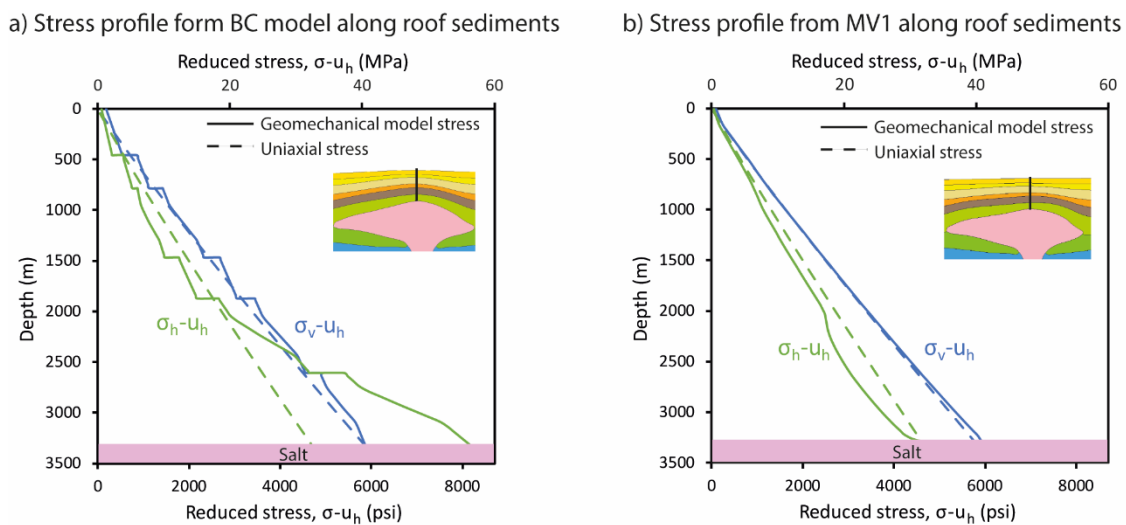


Figure 2.20: Stress profiles at vertical section along the sedimentary roof at present-day (inset) for (a) BC model and (b) model MV1. Depth zero indicates sea floor.

2.4.3.2 MV2 results (basal triangular feature)

Both the Sandia and the Western diapirs were initially assumed to develop on top of the highest points of the rotated fault blocks that form the basin basement (Figure 1.3). Other regional seismic interpretation and regional constraints from the bibliography seems to support this hypothesis (Le Roy & Piqué 2001; Tari & Jabour 2013). Nevertheless, these basal features below the diapirs cannot be established unambiguously with the available data because the seismic quality below the salt is poor.

The BC model assumes the Sandia diapir develops above one of these triangular basal features formed by the highest points of the basement. The model MV2 built here tests whether these salt-base highs have a notable effect on the evolution of the diapir by replacing the basal indentation present in the BC model (Figure 2.15a) with a flat salt base. The general characteristics of the resulting diapir in MV2 (Figure 2.21b) are similar to the BC one (Figure 2.21a): the diapir rises early during the deposition of Jurassic sediments, a salt sheet develops downslope during the Early Cretaceous and the source layer welds at both sides of the diapir pedestal at the same interval. However, the diapir at MV2 reaches the surface earlier than the BC diapir and has a thicker upper part at the end of Jurassic. This fact prevents the diapir to grow higher as happens in the BC model. At Early Cretaceous time, the diapir expands and forms shorter salt sheets at both sides. The burial of the structure happens shortly after that time, contrary to the BC model, where the salt is completely buried at 101 Ma (beginning of Late Cretaceous). The final diapir geometry in MV2 is 400 m shorter and with a salt stem twice as thick compared to the BC diapir (Figure 2.21).

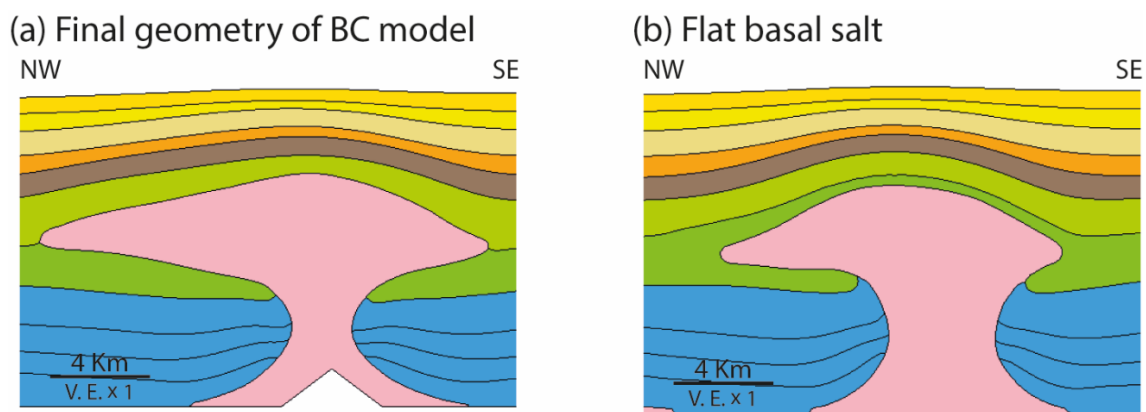


Figure 2.21: Final geometry of the Sandia diapir as predicted by (a) the BC model and (b) the MV2 model, with a flat salt base. The lack of the basal triangular feature below the diapir generates a shorter and thicker final salt geometry.

2.4.3.3 MV3 results (variation of temperature gradient)

The temperature gradient used in the BC model is not precisely known at the study location and may influence the salt viscosity and flow behaviour. The base-case model uses a temperature gradient of 31°C/km, considered a lower bound for the study area (Rimi 2001; Zarhloule *et al.* 2010). This value is based on an integrated 2D and 3D petroleum system model for thermal maturity evaluation that Repsol built internally prior to the drilling of the Sandia-1 exploratory well.

We investigate the effect of increasing the temperature gradient to 36°C/km on the evolution of the salt diapir and its final geometry (model MV3; Figure 2.22b). The resulting diapir rises during the Jurassic and generates a salt sheet during Early Cretaceous times, similar to the BC model. The source layer also welds during Early Cretaceous. The main effect of the higher temperature gradient in model MV3 is that the diapir upbuilds to the surface before the end of Jurassic, faster than the BC diapir and has a wider upper half. This small increase in salt-flow velocity results from the fact that the salt viscosity is at most an order of magnitude lower in the MV3 compared to the BC model (10^{17} and 10^{18} Pa·s), because of the higher temperature. The lateral expansion of the upper half part of the diapir starts at 131 Ma (Early Cretaceous) and generates a shorter salt sheet at the NW side and a shorter overhang at the SE at 122 Ma (Early Cretaceous). The structure is buried by ongoing sedimentation just after the formation of the salt sheet and overhang. The final diapir geometry in model MV3 (Figure 2.22b) is 600 m shorter and with a salt stem twice as thick compared to the BC diapir (Figure 2.22a).

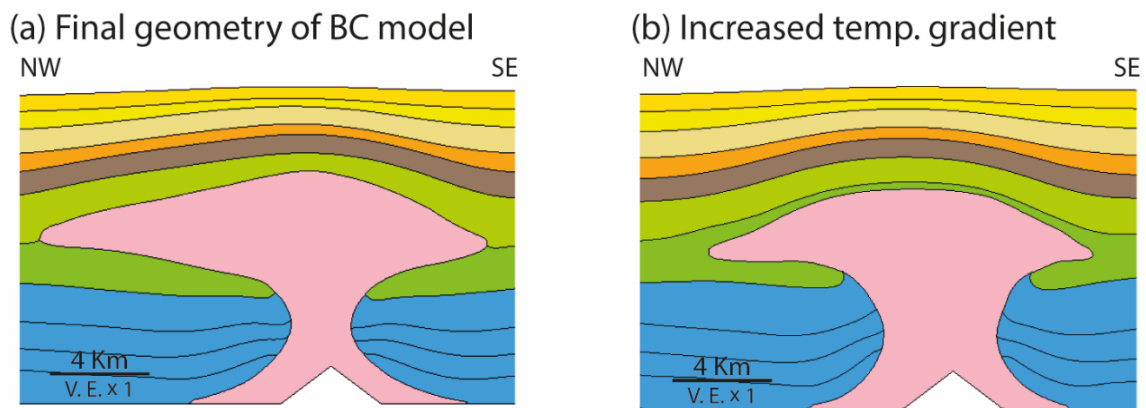


Figure 2.22: Final geometry of the Sandia diapir as predicted by (a) the BC model, using a temperature gradient of 31°C/km and (b) the MV3 model, using a temperature gradient of 36 °C/km. The higher temperature gradient used in MV4 generates a final diapir geometry that is shorter and thicker compared to the BC geometry.

2.4.3.4 MV4 results (variation of burial history)

The burial history curves extracted from the kinematic restoration model (Figure 2.16) show that Jurassic and Cretaceous periods have higher sedimentation rates at location Z (basinward part of the studied cross section, NW from the Western diapir, Figure 1.3), relative to location Y (location used to build BC model, SE from the Sandia diapir, Figure 1.3). These higher sedimentation rates imply a larger accommodation space for the sediments, hence larger volume of salt withdrawal at the basinward end of the basin.

We build the evolutionary model MV4 using the burial history (Figure 2.16b) obtained along location Z in the kinematic restoration model (Figure 1.3), combined with a thicker initial salt layer (Figure 2.23a). The main target is to explore whether model MV4 leads to a geometry somewhat similar to the Western diapir.

Similar to model BC, the deposition of the first Jurassic sediments in model MV4 results in a differential overburden stress between the salt seed and the topographic lows on the salt top surface. That allows the initiation of salt flow towards the centre of the model (Figure 2.23a & b). The subsequent deposition of Jurassic layers drives the salt from the source layer into the diapir. The fast deposition at this stage allows the diapir to upbuild to the surface at 158 Ma, before the end of Jurassic (Figure 2.23b). At this time, the upper diapir half is narrower than its lower half and pedestal. At 135 Ma (Early Cretaceous, Figure 2.23c) the salt source layer is significantly thinned at both sides of the diapir. The upper half of the salt structure remains at the surface and has grown wider and developed overhangs at both sides. The sedimentation of Early Cretaceous partially buries these overhangs, limiting their lateral extension. By 100 Ma (Figure 2.23d), Lower Cretaceous sediments have buried the diapir. However, a significant volume of salt remains in the pedestals, and continues to drive salt flow to the upper parts of the diapir. As a result, the diapir crest inflates and the overhangs continue to grow. The onset of the Atlas inversion and shortening during Late Cretaceous (66 Ma, Figure 2.23e) both narrows the diapir stem and drives salt from the overhangs toward the upper diapir. This inward and upward salt-flow volume is sufficient to sustain a gradual rise of the diapir through the sedimentary roof. Eventually, the salt is able to pierce the roof and upbuild to the present-day surface at 5 Ma (Figure 2.23g).

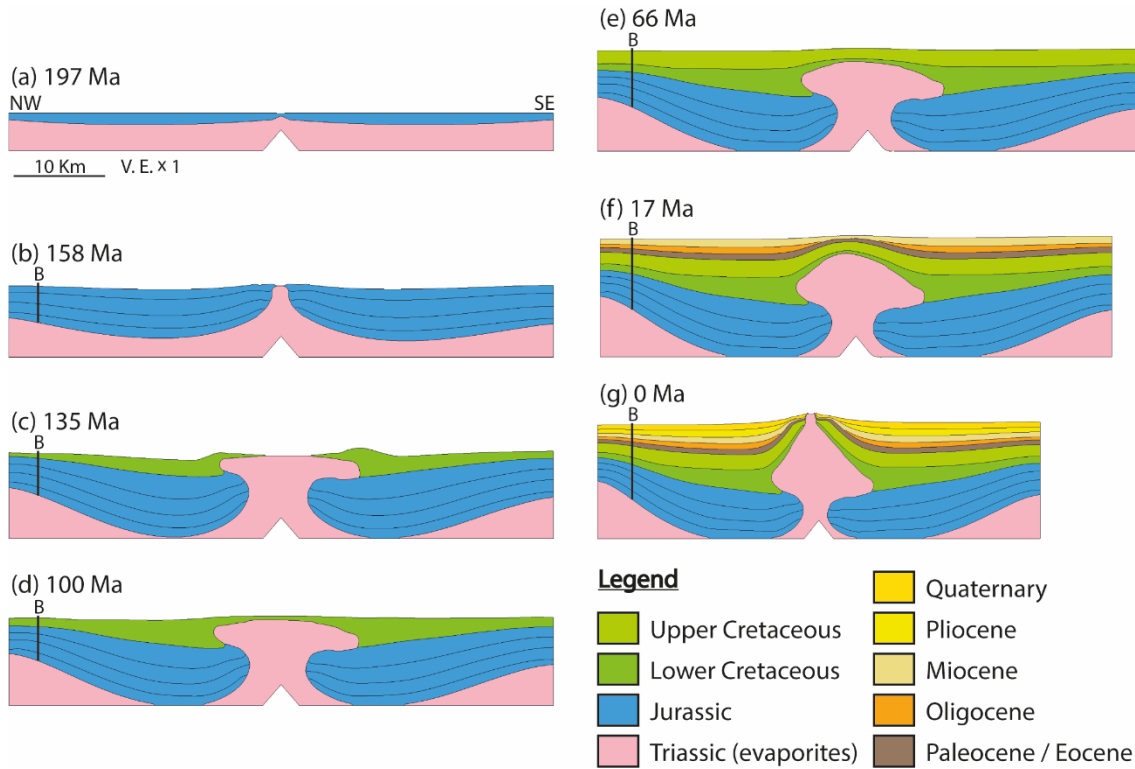


Figure 2.23: Stages of evolutionary model using the burial history curve from the NW end of the basin (Figure 2.16b) and applied at location B, together with a thicker initial salt source layer compared to the BC model. (a) Initial geometry representing the top Triassic, with salt layer (pink) and initial thin layer of Jurassic sediments (blue); (b) Salt diapir reaches the sea floor at the end of Jurassic; (c) Salt forms overhangs at both sides, buried by Early-Cretaceous sediments (dark green). Source layer welds. (d) Further Early-Cretaceous sedimentation buries the diapir. Salt from pedestals increases overhang thickness; (e) Late-Cretaceous sedimentation (light green) drive bulging of diapir crest. Shortening begins; (f) Shortening narrows the diapir stem and drives salt from overhangs toward the diapir centre. Salt bulges upward; (g) Salt pierces the roof and upbuilds to the surface at present day.

2.4.3.5 MV5 results (variation Plio-Quaternary sedimentation rates)

The sedimentation rates extracted from the kinematic restoration model and used in the BC model are significantly higher for the Plio-Quaternary interval (light yellow and gray blocks, Figure 2.24) when compared to the rest of the Tertiary rates of deposition, being 620 m/Myr and 700 m/Myr for the Pliocene and Quaternary, respectively.

Model MV5 tests the significance of this assumption by reducing the Plio-Quaternary rates to values similar to The Miocene rate (60 m/Myr, yellow block, Figure 2.24). The resulting present-day geometry of the basin in the model MV5 is not notably different from the BC model. This is because the duration of the Plio-Quaternary interval is short (5.3 Myr) and occurs also at the end of the simulation, once the salt structure is already formed. Despite the high sedimentation rates, the sediment layer thicknesses are small, and the additional overburden load applied by these layers does not produce any notable effect on the kinematics of the system.

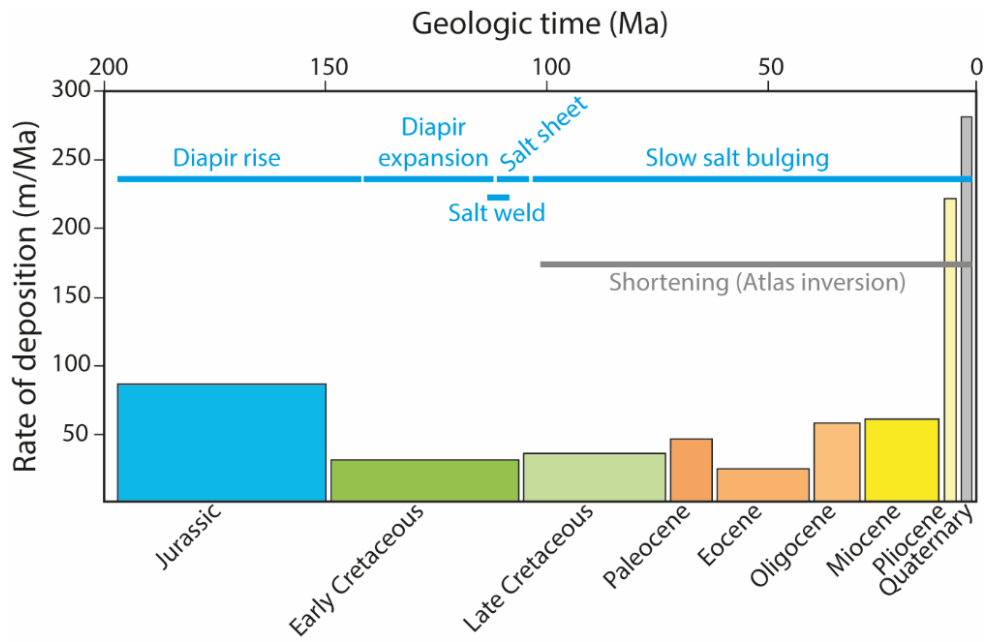


Figure 2.24: Rate of deposition for different geologic intervals from Jurassic until present day. Each interval is represented by a coloured block, the width of which is proportional to the duration of the geologic interval. The application of the tectonic shortening in the model is represented by the grey horizontal bar. The different diapiir evolution phases are shown by the blue horizontal bars.

CHAPTER 3. SUMMARY OF DISCUSSIONS

3.1 Introduction

This chapter aims to interpret the results obtained from the different modelling techniques used in this thesis and presented in CHAPTER 2. In particular, this chapter uses the results from the base-case model and the sensitivity analyses performed to understand the behaviour of each model approach discussed. For the case of the static approach, this discussion chapter also deals with the comparison between 3D and 2D modelling, discerning if the simpler 2D static approach can still represent the behaviour correctly represented by the 3D model. Finally, the sensitivity analyses for both the static and the evolutionary approaches also allows to identify which input parameters dominate the model results. This creates a series of guidelines for the static and evolutionary model definition of similar salt basins, indicating which parameters are paramount for the correct model design.

The discussion chapter is organized in two different sections: the first section focuses on the interpretation of the static modelling approach, summarizing the discussion given in the publications:

- Hooghvorst et al, 2019: Insights from sensitivity analysis of geomechanical modelling of a salt structure offshore west Africa
- Hooghvorst et al, 2020: Comparison of stresses in 3D v. 2D geomechanical modelling of salt structures in the Tarfaya Basin, West African coast

The second section summarizes the discussion of the evolutionary modelling approach that appear in the publication:

- Hooghvorst, et al, 2021: Geologically constrained evolutionary geomechanical modelling of diapir and basin evolution: A case study from the Tarfaya basin, West African Coast. Basin Research

3.2 Static modelling

3.2.1 Stress reduction mechanism

The results of both the 3D and 2D static models presented in the previous chapter show a horizontal stress reduction for the sediments located above the crest of the Sandia diapir (Figure 2.2b and Figure 2.8). Both static models also predict the same displacement pattern for the sediments above Sandia, where the SE region (hanging wall side of the fault) has a downward displacement and the NW region (footwall side of the fault) has a westward displacement (Figure 2.5a & c and Figure 2.9). The sediments located on top of the diapir crest are placed in the middle of these two differential displacements, hence they experience an extensional horizontal strain, identified in the 2D model by Figure 2.10 (red contours at the crest of the Sandia diapir). This horizontal extension is the cause of the stress reduction predicted by both the 3D (blue contours, Figure 2.2b) and the 2D (blue contours, Figure 2.8) static models above the Sandia diapir. Furthermore, it has been observed during the drilling operations of the Sandia-1 exploratory well (black circle; Figure 1.1).

The stress reduction and lateral strains predicted above the Sandia diapir are in agreement with the results from other geomechanical models using both idealized geometries (Luo *et al.* 2012; Nikolinakou *et al.* 2012) and actual salt geometries (Barnichon *et al.* 1999; Segura *et al.* 2016). In addition, other authors report the presence of normal faults in sediments above salt structures that are an indication of extensional regimes in these areas (Davis *et al.* 2000; Dusseault *et al.* 2004). In particular, Dusseault *et al.* (2004) report an area of exceptionally low values of minimum horizontal stress in an anticline structure located above a Gulf of Guinea salt dome.

The sensitivity analyses performed in the static models have been crucial for better understanding the cause for the stress reduction above Sandia. In particular, when we replace the salt lithology in the 2D static model with a shale material, we observe no stress reduction above Sandia (Figure 2.11). This result shows that the difference in rock properties between the salt and the sediments encasing the salt diapir is one of the main drivers of the stress reduction detected in the base-case models. In other words, the viscous rheology of the salt and its resulting relaxation causes the stress perturbation above the diapir.

Other sensitivity analyses have shown that the sea floor geometry also affects the sediment displacements above Sandia. The 2D static model predicts no differential displacements above the salt diapir when the sea floor is changed from the original 1° towards the west to horizontal (Figure 2.12). In addition, the stress reduction above Sandia is slightly reduced when the sea floor is changed to a flat surface. All this demonstrates the sea floor geometry also drives part of the reduction of stresses above the salt.

Other changes involving the variation of the number of diapirs modelled or the width of the diapir feeders further supports our conclusion that the contrast in properties between the

salt and the shale lithologies is the major factor causing the stress reduction above salt observed in the base-case static models.

3.2.2 Static model comparison

Part of the scope of this static modelling study includes the comparison between the 3D and the 2D approach. This comparison aims to identify the differences in prediction and investigate whether 2D modelling can still represent the stresses and strains in the salt basin adequately, despite its simplifications.

We have found that both the 3D and 2D models predict a reduction of stress ratios above the Sandia salt diapir. The area of this stress ratio reduction is broader and extends shallower in the 2D model (Figure 3.1b) when compared to the 3D model (Figure 3.1a). Only at the salt crest do both modelling approaches predict the same value, being 0.6 (compared to the initial value of 0.8).

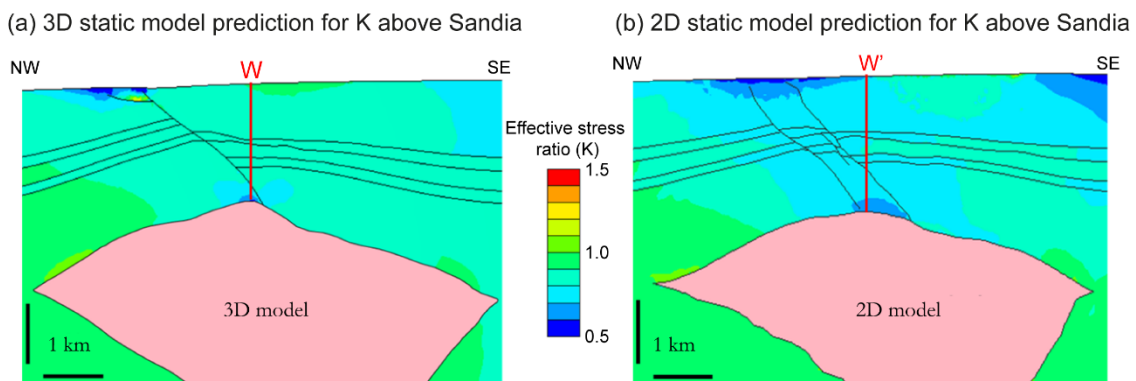


Figure 3.1: Horizontal to vertical effective stress ratio predicted for sediments above the Sandia diapir for (a) the 3D static model and (b) the 2D static model. Both models present a reduction of stress ratio of about 0.6 at the crest of the structure, compared with the initial 0.8. However, the reduction in the 2D model affects a broader area above the diapir. Vertical profiles W and W' are used to quantitatively compare the stress change between the 3D and 2D model (Figure 3.2).

When looking at the predicted displacement directions, both model approaches are consistent for the sediments above Sandia (Figure 2.5 and Figure 2.9). In both cases, the footwall has greater westward displacements than the hanging wall. At the same time, the hanging wall has greater downward displacement than the footwall. Even though these differential displacements are qualitatively similar in both approaches, the 2D model consistently predicts higher magnitudes of displacement than the 3D model. That is because there are no out-of-plane displacements in the 2D model, and, therefore, the salt deforms only on the modelled plane. On the other hand, the 3D model allows displacements along the three dimensions, and, hence, less displacement is needed to achieve the same level of relaxation.

We can further compare the stress results between both approaches by plotting the horizontal stress change (eq. 8) against the depth normalized by the depth of the salt crest, H .

$$\Delta\sigma'_h = \sigma'_{h,uniaxial} - \sigma'_{h,model} \quad (9)$$

This comparison is done along a vertical profile W for the 3D model and W' for the 2D model (red vertical profiles, Figure 3.1), located at the crest of the Sandia diapir. The values of horizontal stress change show the stress reduction above the diapir (Figure 3.2). Both models predict a similar reduction of 4.5 MPa for the sediments located at the crest of the salt structure (i.e., at a normalized depth H of 1). However, the 2D model (green line, Figure 3.2) predicts higher horizontal stress reduction along the vertical profile, reaching a maximum difference that approaches 1.5 MPa at 80% of the crest depth (i.e., at a normalized depth H of 0.8). The 3D model (red line, Figure 3.2) shows a horizontal stress change that becomes zero at half of the crest depth. At the same depth, the 2D horizontal stress reduction is still 0.7 MPa. In the 2D model, the salt influence extends two thirds of the vertical profile, reaching up to 30% of the crest depth. In other words, the stress reduction caused by the 2D diapir reaches shallower sediments on top of the salt structure when compared to the 3D diapir. In the 3D model, sediments located at depths shallower than $H = 0.5$ (shallower half of the sedimentary roof) are not affected by the diapir.

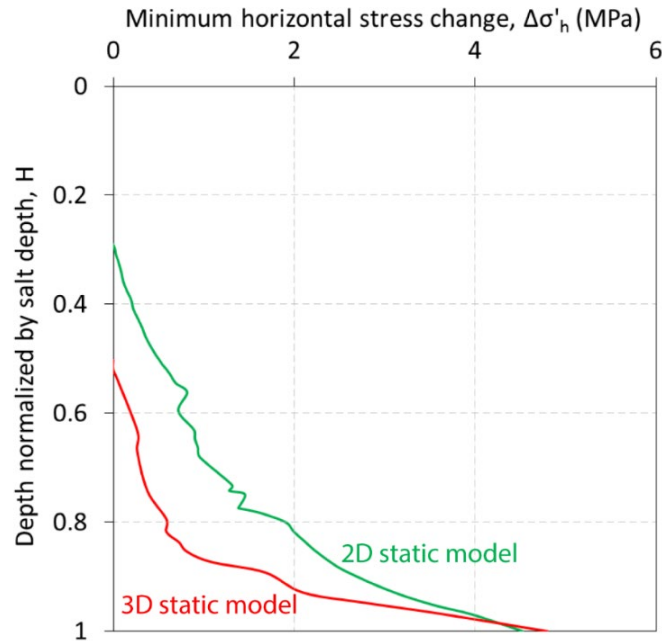


Figure 3.2: Horizontal stress change with depth normalized by salt depth for 3D static (red line) and 2D static (green line) models along vertical locations W and W' (Figure 3.1) above the salt body, respectively. The stress perturbation due to salt attenuates faster with distance from the salt body in the 3D model compared to the 2D case. Normalized depth of zero represents the sea floor and 1 represents the diapir crest.

We use the elastic theory to explain why the 2D model predicts broader areas of decreased horizontal stress, higher reduction of horizontal stress and higher sediment displacements above the Sandia diapir when compared to the 3D model. In particular, we use the elastic solutions for the stress distribution resulting from a load applied on a semi-infinite, elastic, isotropic and homogeneous medium (Boussinesq 1885). Different load configurations applied on the medium will generate different distributions of vertical stress in depth. Here, we compare the distributions of vertical stress caused by the application of a strip load (infinite out-of-plane length) with that of a circular load (Figure 3.3). Both loads have the same magnitude q and width B (the width of the strip load is equal to the diameter of the circular load). In this example, the strip load represents a 2D plane-strain solution, whereas the circular load represents a 3D axisymmetric solution.

The elastic solutions show that the vertical stress perturbation caused by the application of the strip load (equivalent to our plane-strain model) is broader than the application of the circular load (equivalent to our 3D model). The circular load generates a more localized stress perturbation that dissipates faster with distance. For example, if we consider a value of $B = 1$ m and an applied stress $q = 1$ MPa/m, then at a distance of 6 m from the load application surface, the vertical stress is 0.1 MPa for the case of the strip load (red dot, Figure 3.3) but only 0.015 MPa for the case of the circular load (blue dot, Figure 3.3).

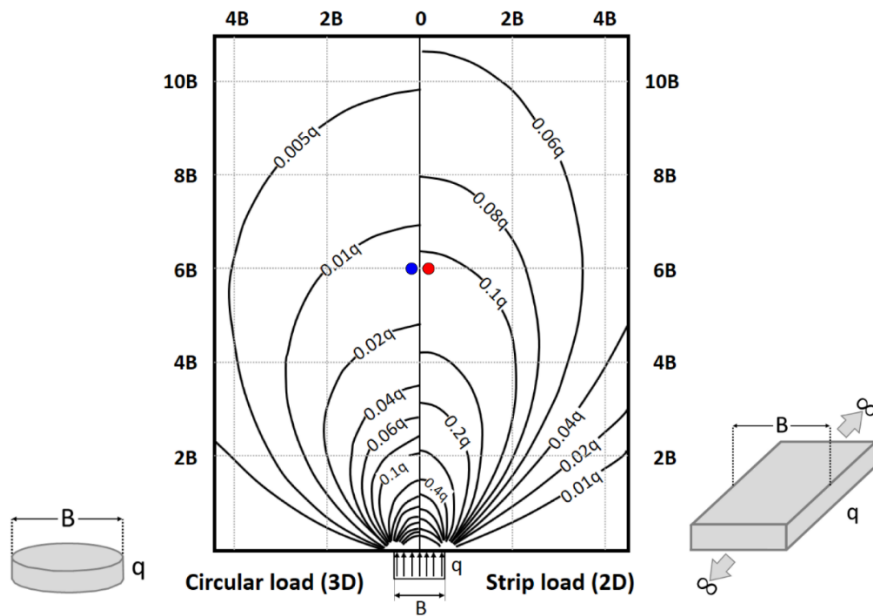


Figure 3.3: Illustration of the solution for the vertical stress distribution in an elastic, semi-infinite medium caused by the application of a 2D load (represented as a strip load) and a 3D load (represented as a circular load) using the solution from Boussinesq (1885). There is no gravity load. Blue and red dots correspond to the values of vertical stress at 6 m from the load for the 3D and 2D case, respectively, where $B = 1$ m and $q = 1$ MPa/m. The load in this figure is applied from below to represent the influence of the salt diapir on its sedimentary roof. Modified from US Army Corps of Engineers (1990).

This elastic theory analogy can be extended to our geomechanical models. In our case, the loading is applied by the salt diapir in the form of an imposed strain. Hence, for a simplified application, we consider the width of the salt crest to be the loading area (equivalent to the load B, Figure 3.3). The 2D model is analogous to the strip load case in Figure 3.3, because it is plane-strain, which corresponds to an infinitely long salt wall. The 3D model can be compared to the circular load from Figure 3.3. Based on Boussinesq's elastic theory, the 3D salt load should result in a smaller region of stress changes, closer to the crest (i.e., location of load application). Indeed, this is consistent with our geomechanical results seen in Figure 3.1.

3.2.3 Input uncertainty

The sensitivity analysis study allows us to quantitatively compare the influence of the different model assumptions. In particular, the 2D sensitivity analysis results show how the stress prediction from the base-case model changes when changing both elastic parameters and geometric and framework assumptions (Table 2.6). The comparison of these different stress results (Figure 2.14) allows us to rank the assumptions tested from higher to lower impact:

1. The presence of salt lithology (9%);
2. The presence of other salt diapirs in the 2D section (7%);
3. Sea floor slope which imposes a differential load across the width of the model (4%);
4. The connection between the diapirs and the autochthonous salt source layer (3%).
5. Elastic properties of the sediments (below 1%)

This ranking shows which assumptions should be more carefully determined when designing a similar geomechanical model. For example, according to the above list, the geometry and presence / absence of salt diapirs should be given a greater weight than the elastic properties of the sediments encasing the salt structures. The same is true between the sea-floor slope and the sediment elastic parameters.

The salt geometries and the sea-floor slope assumptions have not been tested in 3D due to the complexity of the process and by time restrictions. Nevertheless, the consistency on the stress and displacement results and the similar small sensitivity response of the elastic assumptions suggest that the same conclusions can be extended to the 3D approach.

3.2.4 Limitations and future research recommendations

The study of the Tarfaya basin using 3D and 2D static models has shown a series of limitations which are listed here and can serve as guidelines for future improvement of the present work:

- The static models built and discussed in this study are drained, meaning that we do not simulate the fluid flow inside the basin and we ignore pore-pressure generation.

The impermeable nature of the salt lithology can contribute to the pore pressure by blocking possible drainage paths inside the sediments and generating overpressures. Another mechanism for the salt to generate overpressures is by flowing and loading the surrounding sediments. Hence, coupling fluid flow with salt deformation in the static models would provide a more complete stress, strain and pore pressure prediction of the Tarfaya system.

- The sediments used for both the 3D and 2D static models behave as poroelastic materials. One of the results of the sensitivity analysis has been the low impact of the elastic properties of the sediments over the model results. Hence, future models using the same poroelastic rheology can benefit by adopting simpler elastic models other than the one adopted in this study (eq. 10). Nevertheless, the introduction of more sophisticated models for the sediments like elastoplastic models and the introduction of frictional strength will result in more realistic displacements of sediments and salt. These rheologic models can also help detect regions where the material is close to failure.
- The faults modelled assume one set of frictional properties that do not change during the sensitivity analysis. Studying the sensitivity of the frictional parameters would help better understand the interrelation between salt deformation and stress reduction.
- Similar to the previous point, the sensitivity analysis could have been expanded to include changes in temperature gradient in the 3D and 2D static models. Nevertheless, it is worth noting that variations in temperature in the static models would mainly affect the viscosity of the salt lithology and, hence, the time needed for the static model to converge to a solution. Temperature effects become more important in evolutionary models of salt systems.
- All the models used in this study are performed using the Finite Element Method (FEM) as implemented in the software Elfen (by Rockfield Ltd.). This particular approach was the natural option to continue the work Repsol began by building the 3D model of the study area, which was started with the same tool. In addition, the selection of FEM-based models and, in particular, the software Elfen, is supported by the validation given by other researchers from the field in recent years (Segura *et al.* 2016; Heidari *et al.* 2018b; Nikolinakou *et al.* 2018a; Thigpen *et al.* 2019). This ensured our work remains relevant for future years. Despite all that, we acknowledge that our work can be performed using different software, or altogether different numerical methods such as Discrete Element Methods (DEM). The selection of other methods may entail different assumptions of input requirements and may yield different results compared to our cases. The testing of all these other options was not one of the goals of the present research but may be the natural next step to our research, as an interesting line for a future investigation.

- Finally, the understanding of salt systems like the Tarfaya basin can greatly benefit from the introduction of evolutionary geomechanical modelling. This approach, contrary to the static one, can help study the complete stress and strain history through time. With evolutionary modelling, the initial assumption of a stress distribution introduced in the static approach is not needed. In addition, evolutionary modelling provides a complete evolution of the salt structures and how this evolution affect the basin stresses. We address this line of improvement in the 2D evolutionary geomechanical modelling of the Tarfaya basin in the present thesis.

3.3 Evolutionary modelling

3.3.1 Influence of sedimentation rates on diapir evolution

The base-case evolutionary model results together with the sensitivity analyses has shown that the sedimentation rates of the Tarfaya basin are a key driver for the system evolution. In particular, we show that the variation of rates of deposition with time (Figure 2.24) influences the development of the Sandia diapir (BC model, Figure 2.18). The rapid sedimentation at the beginning of the simulation (Jurassic) mobilizes the salt from the source layer towards the central part of the basin, initializing the rise of the diapir and allowing it to reach the surface at the end of Jurassic.

We quantify the effect of sedimentation on salt flow by plotting the salt horizontal pressure gradient (Figure 3.4). This gradient can be calculated by subtracting the sediment overburden load on salt away from the diapir from the salt pressure inside the diapir at the same depth (Figure 3.4-inset). The higher the salt horizontal pressure gradient, the more salt volume is driven toward the diapir and the faster the diapir growth is. The salt gradient for the Sandia diapir in the BC model (blue line, Figure 3.4) increases rapidly during the Jurassic, illustrating the acceleration of salt flow towards the diapir. As a result, by the end of the Jurassic interval (at 145 Ma), the diapir has upbuilt to the sea floor and a significant volume of salt has accumulated in the salt pedestals (Figure 2.18b). This creates a readily available salt stock near the diapir that contributes to its continuing development during Cretaceous times, despite the decrease in sedimentation rates (87 m/Myr during Jurassic, blue block in Figure 2.24 vs. 30 m/Myr during Cretaceous, dark and light green blocks in Figure 2.24). As a result, the diapir remains at the sea floor (Figure 2.18c), gradually widens during Early Cretaceous, and eventually breaks into a salt sheet at the end of this interval (Figure 2.18d). The salt at the pedestals sustains the diapir growth even though the source layer thins and welds at the end of Early Cretaceous. Eventually, the depletion of the pedestal salt volume combined with the continuous Late Cretaceous sedimentation buries the salt structure.

The evolution of model MV4 (Figure 2.23) further illustrates the importance of the sedimentation rates in the diapir evolution. In this model, the higher sedimentation rates during the Jurassic result in a higher horizontal pressure gradient in the salt source layer (green vs. blue line, Figure 3.4). This promotes a faster salt flow compared to the BC model, and a greater amount of salt pumped into the MV4 diapir, despite the fact that the source layer in MV4 welds much earlier than the one in the BC model. As a result, salt in MV4 not only accumulates in the pedestals and upbuilds to the sea floor, but also forms diapir overhangs (Figure 2.23d). The faster sedimentation during Early Cretaceous on the MV4 compared to the BC model prevents the formation of a long salt sheet at this stage, resulting instead in shorter and thicker overhangs. This geometry allows additional salt volume to be stored readily available to flow in response to the later-applied shortening. As a result, the system is able to sustain a second phase of diapir rise to the present-day sea floor. Contrary

to MV4 diapir, the BC diapir gets buried during Cretaceous times (Figure 2.18e) because a sufficient salt volume could not be mobilized.

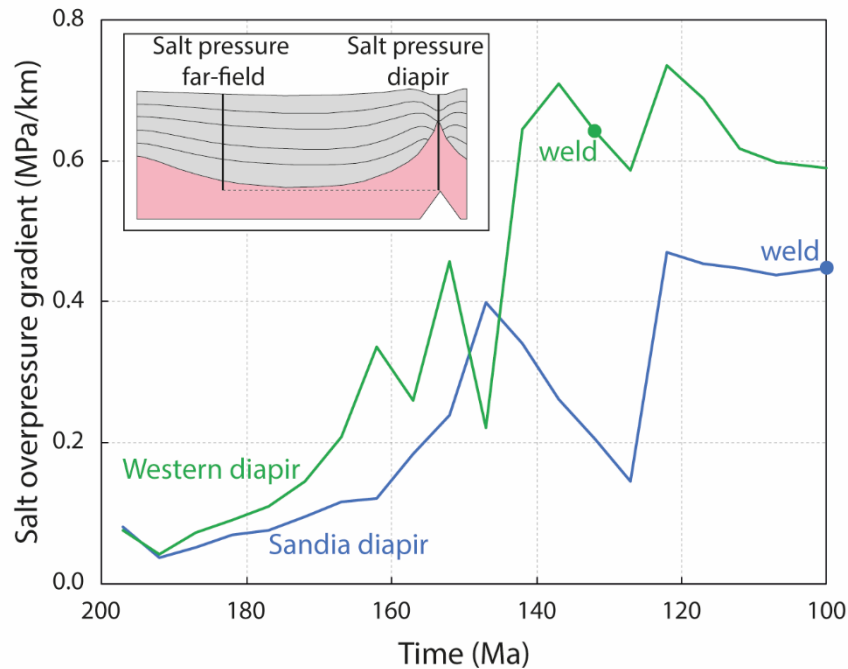


Figure 3.4: Comparison of horizontal salt pressure gradient between BC model (blue line) and MV4 model (green line). We define horizontal salt pressure gradient as the difference between the sediment overburden load on salt away from the diapir and the salt pressure inside the diapir at the same depth (inset). The higher sedimentation rates in model MV4 generate a consistently higher horizontal salt pressure gradient with time. The point in each line represents the time when the source layer welds.

3.3.2 Influence of shortening rates on stress distribution

The evolutionary geomechanical models provide the stress distribution around the salt structures resulting from the system evolution. This allows us to study the influence of shortening rates on the present-day stress state near the Sandia diapir (Figure 2.19).

The sensitivity analysis results obtained by building the MV1 model show that the rate of shortening (exponential or sigmoidal curve, Figure 2.15c) does not seem to greatly affect the diapir kinematics (Figure 2.19a vs. Figure 2.19b). This is because the formation of the Sandia diapir develops and matures between Jurassic and Late Cretaceous, under stable tectonic conditions. The onset of shortening begins just after this interval, when the diapir has already reached the surface and the salt sheet and overhangs are emplaced and buried under sediments. In other words, the shortening does not interfere with the main period of diapir rise and development. In addition, the rates applied are mostly the same except for the final parts of the model: in the exponential curve, the shortening accelerates at the end of the simulation, whereas in the sigmoidal curve, the shortening decreases and deactivates just before the end of the simulation. All these explain the lack of influence of the shortening on the final diapir geometry.

Nevertheless, the sensitivity analysis changing the shortening curves detected changes on the final stress state distribution around the salt. The exponential shortening curve (solid black line, Figure 2.15c) applied in the BC model (Figure 2.19a) results in an active regional compressive load at present day, which pressurizes the diapir salt. Because of the overburden thickness, the crest cannot expand, and instead loads the sediments around it. As a result, the stress ratio increases to values near 1 at the salt flanks (green/yellow contour colours, Figure 2.19a), and to $K=1.4$ around the crest (orange contour colours, Figure 2.19a), illustrating increase in horizontal stress compared to its uniaxial value ($K_0 = 0.8$).

In contrast, the sigmoidal shortening curve (increases progressively, peaks and decreases progressively, dashed black line, Figure 2.15c) applied in model MV1 (Figure 2.19b) results in decreasing shortening rates toward the end of the simulation and termination of shortening 2 Myr before present day. The lack of tectonic load causes the diapir to deform downward and outward to achieve a uniform stress state. This behaviour is equivalent to the one seen in our static model approaches built in this study for the same salt diapir. Consequently, the stress ratio at the crest decreases to values of K near 0.65, indicating a decrease in horizontal stress (Figure 2.19b). The 3D and 2D static models also show a decrease in horizontal stress at the crest of the structure caused by the same salt relaxation phenomenon (Figure 2.2b & Figure 2.8, respectively). In addition, this reduction was also detected during the drilling of the Sandia-1 exploratory well (Figure 1.5, also Annex 4: Sandia-1 well log data and CBIL data), indicating that the shortening rates following a sigmoidal curve are more appropriate to represent the tectonic history of the Tarfaya basin.

3.3.3 Layer thicknesses comparison between kinematic restoration and evolutionary geomechanical models

One of the advantages of the evolutionary geomechanical models built in the present study is that not only do they incorporate the geological inputs coming from the kinematic restoration model, but also incorporate the strength and deformation characteristics of sediments in the study of a salt-basin evolution. We can compare the layer thicknesses from the BC evolutionary geomechanical model against the kinematic restoration model to demonstrate this contribution. In particular, we compare both models at: (a) location close to the diapir, near the tip of the source-layer weld (locations X and C, Figure 1.3 & Figure 2.18, respectively); (b) location far from the diapir, above a salt high, where the salt source layer is not depleted (locations Y and A, same as the location used to constrain the evolutionary model, Figure 1.3 & Figure 2.18, respectively). Whereas both approaches predict the same thicknesses away from the diapir (solid shapes in Figure 3.5 fall on the 1:1 line), the geomechanical model predicts 20% thicker layers closer to the diapir (empty shapes in Figure 3.5 fall around the 1:1.2 line).

We perform this comparison for the Jurassic, Cretaceous and Oligocene sediments (colours blue, green and orange in Figure 3.5, respectively) and for the time intervals of Late

Cretaceous, Oligocene and present day (triangle, circle and square shapes in Figure 3.5, respectively). Consider, for example, the Jurassic sediments (blue shapes). Near the salt structure (empty shapes), at the end of Late Cretaceous (empty blue triangle, Figure 3.5), the restoration model provides a thickness of 4300 m, whereas the evolutionary model predicts 5000 m.

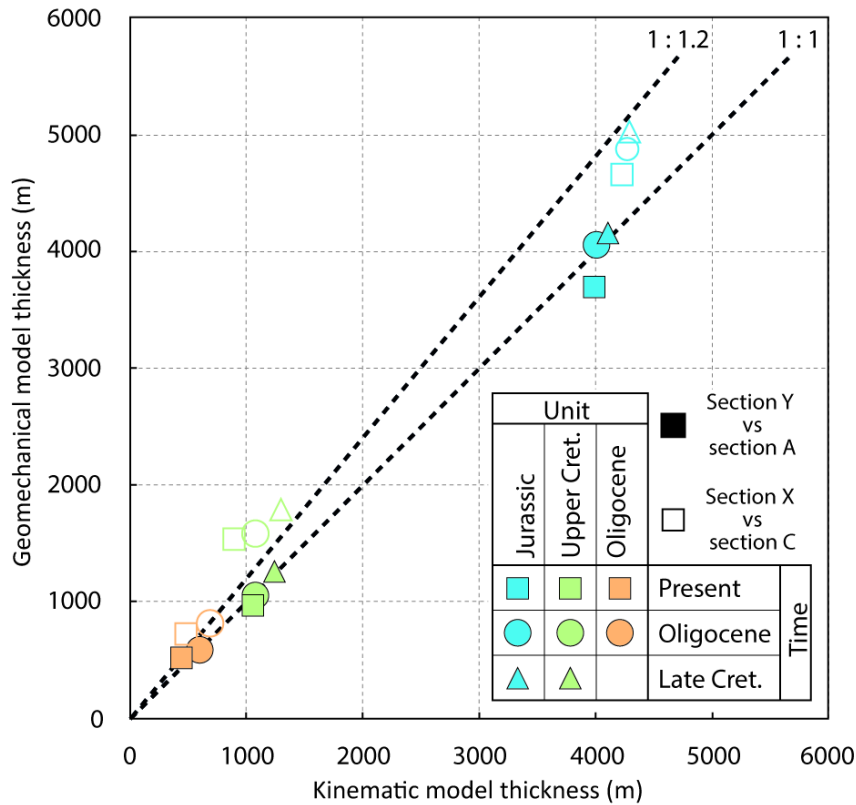


Figure 3.5: Comparison of layer thickness predicted by the kinematic restoration model (Figure 1.3) and the BC evolutionary geomechanical model (Figure 2.18) at 2 locations: (a) far from the diapir above a salt high (Y vs. A in Figure 1.3 & Figure 2.18; solid shapes); and (b) near the diapir, above a salt weld (X vs. C in Figure 1.3 & Figure 2.18; empty shapes). Layers considered: Jurassic, Upper Cretaceous and Oligocene units (blue, green and orange colours, respectively). Comparison times: Late Cretaceous, Oligocene and present day (triangular, circle and square shapes, respectively). Points on the 1:1 dashed line indicate agreement between the two models. Points closer to the 1:1.2 dashed line indicate that the evolutionary geomechanical model predicts more compaction.

In addition, the geomechanical model predicts a notably higher compaction of the Jurassic layer between Late Cretaceous and present day near the diapir (empty blue square, Figure 3.5): the final evolutionary model thickness is 4600 m (8% compaction), compared to 4200 m (2.3% compaction) in the restoration model. This can be explained by the presence of the salt weld below Jurassic. Particularly, the source-layer weld generates higher mean stresses near the tip and a zone of higher shear stress that radiates upwards from the weld (Heidari et al. 2016). The geomechanical model captures this contribution of mean and shear stress to compaction, because it simulates sediments as porous elasto-plastic material. The

additional sediment compaction cannot be accounted for in the restoration model and causes an increase in the deposition space in the evolutionary geomechanical model, allowing more material to be deposited on top of Jurassic. This, in turn, results in the thickness increase observed in the geomechanical model near the diapir (empty shapes in Figure 3.5) compared to the kinematic restoration model.

Overall, the insights obtained from the comparison between the evolutionary geomechanical and the kinematic restoration models highlight the importance of modelling the viscous salt flow and its response to sediment loading during the diapir and basin evolution.

3.3.4 Parameters with minor influence on the Tarfaya basin evolution

The sensitivity analyses have also shown that some of the changes applied do not seem to have a great influence on the overall model results. These changes are the shortening rates when looking only at the salt kinematics, the shape of the base of the salt and the temperature gradient of the basin.

We already discussed the influence of the shortening rates applied with regard to the diapir kinematics and its final geometry (3.3.2 Influence of shortening rates on stress distribution). It is important to know that, despite the little effect on the final diapir morphology, the shortening rate variation greatly changes the final stress distribution of the sediments around the diapir.

The presence or absence of the salt-base high does not greatly impact the evolution or final geometry of the diapir (MV2 model, Figure 2.21). The diapir geometry is similar to the BC geometry, with, the creation of a weld and the salt-sheet and overhang during Cretaceous and the buried structure under Tertiary sediments at the end of the simulation. However, there are some changes occurring on the timing of the different stages of diapir growth that generate some minor differences when compared to the BC model. Firstly, salt flows more easily into the MV2 diapir in the absence of a rotated fault block feature at the salt base (Figure 2.21b), causing the diapir to reach the surface slightly earlier than the BC diapir. This translates to an earlier maturation of the MV2 diapir. Secondly, the salt source layer welds at an earlier time (nearly 20 Myr earlier than BC model), preventing the diapir to rise further. This causes the generation of a shorter, wider final structure. In contrast, the presence of a salt-base high (BC model, Figure 2.21a) delays the diapir rise. It should be noted that a salt-base high may play a key role in focusing salt flow into a structure, whereas in both models the diapir location is predefined with a seed in the initial geometry (Figure 2.15a).

The increase in temperature gradient in the salt does not greatly change the overall evolution or the final diapir geometry either (MV3 model, Figure 2.22). The temperature increase causes the salt viscosity to decrease, which facilitates salt flow into the diapir during the Jurassic. This causes a net result similar to the previous case discussed (MV2 model, with a flat salt base) where the MV3 diapir evolves faster, reaching the surface and welding the salt

source layer at earlier times compared to the BC model. The resulting salt structure matures earlier, being buried by sediments during the Early Cretaceous, compared to the BC diapir that is buried during the Late Cretaceous. The final MV3 diapir geometry (Figure 2.22b) is shorter and wider compared to the BC structure (Figure 2.22a).

3.3.5 Limitations and future research recommendations

The study of the Tarfaya basin using a 2D evolutionary model has shown a series of limitations that are listed here. Future work could focus on overcoming some of these limitations.

- The present 2D evolutionary models simplify the Atlas inversion and shortening into a continuous event that extends from Late Cretaceous until present day. However, the Atlas shortening most probably happened in distinct pulses (Fraissinet *et al.* 1988; Görler *et al.* 1988; El Harfi *et al.* 1996; Frizon de Lamotte *et al.* 2000). Considering these shortening pulses may greatly affect the development of the salt diapirs, especially the Western diapir that continues to rise during the Tertiary until it reaches the sea floor.
- The simulations present in this study are 2-dimensional plane-strain models, not accounting for any out-of-plane salt flow. As a result, they require wider source layers for the interpreted salt thickness to overcome the lack of the out-of-plane component. Hence, they overestimate the lateral extent of source-layer withdrawal during diapir evolution and rise. 3D evolutionary models would better represent the Tarfaya salt basin, overcoming these limitations. Despite that, the difficulty to constrain these models and their computational power requirements may be a limitation of using 3D evolutionary models.
- The sediments used in the 2D evolutionary models use a poro-elastoplastic description, which is a significant improvement compared to the 2D and 3D static models built at the beginning of this study. Nevertheless, the material description can be further improved by calibrating the models for the specific study area. In addition, the constitutive formulation does not account for strain softening of faulting. As a result, differential stresses may be unrealistically high in locations where faults would otherwise form.
- Similar to the 3D and 2D static models, the 2D evolutionary models built are drained and do not model the generation of overpressures. Coupling fluid flow to salt flow and deposition would generate overpressures that can prevent compaction and reduce the accommodation space for each deposition stage (Swarbrick *et al.* 2002; Nikolinakou *et al.* 2018a; Heidari *et al.* 2019). In addition, overpressures would decrease the strength of the sediments by keeping the effective stress low, hence playing a key role in the kinematics of salt flow (Nikolinakou *et al.* 2018a).

- The sediment geology has been simplified to a single lithology. Data from wells drilled on the continental shelf of the area indicate the presence of carbonates in the Jurassic sediments. This study did not account for those lithologies because it is not clear whether such layers exist in the basinward location of the study area. The influence of such lithologies over the diapir evolution can be assessed by including them in a sensitivity analysis.

CHAPTER 4. CONCLUSIONS

4.1 Introduction

This chapter comprises the concluding points of the present study and aims to answer the initial goals listed at the beginning of the thesis. These conclusions are organized in two main parts based on the modelling approach.

Therefore, the first part lists the results obtained by the exhaustive study and comparison of the 3D and the 2D static geomechanical modelling approaches. We summarize the main points influencing our static models, inferring that this approach can be applied to study complex structural settings, even in the exploration stages, with limited data.

The second part focuses on the conclusions we obtained by adding the evolutionary approach to our study, listing the factors influencing the evolution of the Tarfaya basin. In addition, we point out that evolutionary modelling, despite being more challenging than its static counterpart, can be applied in basin studies with some basic geologic constraints to help its definition, yielding reasonable and useful results.

4.2 Static geomechanical modelling conclusions

The interpretation of the 3D static model results has shown a significant decrease in the horizontal stress for the sediments located near the crest of the Sandia salt diapir. The model also predicts a rotation of the horizontal principal stresses affecting the area. These results are consistent with the data coming from the Sandia-1 exploratory well, showing a region of decreased horizontal stress for the sediments on top of the salt diapir. In addition, the 3D geomechanical model also included higher horizontal east-west displacements at the foot-wall of the major fault above the Sandia diapir and the higher vertical displacements at its hanging wall.

The sensitivity analysis testing the elastic parameters on the 3D static geomechanical model has shown the negligible impact of these parameters on the final results. This is an interesting result, especially when these models are built in stages where the data from the sediments present in the basin is scarce and there are no samples available to constrain the rheology of those sediments.

The lack of the required computational power to run a large variety of these complex 3D models made impossible to further test other input parameters (such as the presence or absence of the salt pillars below the diapirs, the change of the sea floor slope, the presence or absence of salt, etc). Here is where the study of the same static models in a 2D framework becomes interesting, since they have offered a more simplified way to further study the same structures, allowing a deeper level of insight on the mechanisms generating the stress decrease seen both in the well data from Sandia-1 and in the 3D static model.

The 2D static geomechanical model results have shown a horizontal stress reduction near the Sandia diapir similar to the 3D static model results. This decrease reaches absolute values

around 4.5 MPa for both the 3D and the 2D versions. Nevertheless, further comparison between the 3D and 2D static model results indicated that the 2D version overestimates both the changes in stress and the displacements for the shallower sediments above the salt structure. In particular, the stress perturbation for the suprasalt sediments yielded by the 2D model comprised a broader area and affected sediments lying 20% shallower than the 3D prediction. The sediments located at the shallower half above the crest of the salt diapir in the 3D model did not experience any stress perturbation, whereas in the 2D model there was still 0.7 MPa of stress reduction (16%) induced by the salt at the sediments halfway the diapir depth. These differences between 3D and 2D static models are due to the fact that the plain-strain 2D model miscalculates the stress changes caused by a 3D loading. Despite these differences, the 2D static model has proved to be a useful tool to approximate and explore the more complete 3D model, since both approaches yield similar stress and strain distributions above the Sandia diapir.

The cheaper computational power requirements and less time consuming 2D static model has allowed for a more complete sensitivity analysis compared to the 3D version. Similarly, to the 3D study, the variation of the elastic parameters for the sediments has led to minimal changes on the model results, confirming the conclusions from the 3D sensitivity analysis.

More importantly, the sensitivity analysis study highlighted the difference in rock rheology between the salt and the encasing sediments as one of the main drivers of the stress changes. In particular, we showed that the ability of the salt to flow and relax in this model induces a series of differential displacements for the sediments located above the diapir: the sediments at the east side of the diapir roof move downwards, whereas the sediments at the west side of the diapir roof move westwards. The sediments comprised in the middle of these two regions of different displacements (the sediments located just on top of the diapir crest) experiment extensional horizontal strains, causing the stress reduction seen in the Sandia-1 data and in the 3D and 2D models. When the salt lithology in the 2D model was replaced by shale (hence, it does not flow as the salt does), the stress reduction disappeared. Thus, the salt rheology seems to be the main driver for the stress perturbations above the diapir and, as such, attention should be given to the correct definition of the geometries of the salt bodies.

As a second order sensitivity analysis result, the sea floor geometry also drives part of the reduction of stresses above the salt. A 2D without any sea floor slope led to slightly reduced stress perturbations compared to the original 2D model.

To summarize, the static geomechanical modelling study performed during this research has shown that the two essential points that have an important influence in our models are:

- 1) Large rheological contrasts between modelled materials, such as sediment and salt.
- 2) The geometry of these contrasting units.

That means we can apply static geomechanical studies as shown in this research for any basin for which we can construct models based on reflection seismic information, even when rheological characterization is not precise. Indeed, if large rheological contrasts actually exist, they should be detected on seismic as strong reflections caused by contrasts in impedance (which depends on rheology). As for the geometry of these contrasts (in other words, the geometry of salt structures for the case of this particular study), we can also derive them from seismic. However, additional effort may be required in structurally complex settings, requiring not only 2D but also 3D seismic acquisition. But even in such cases, carefully built 2D static models can be a sufficiently good approximation for these 3D complex settings, as we showed by the comparison of our 3D and 2D static geomechanical comparison. These 2D models, if representative, are much more flexible than a cumbersome 3D model of the whole area: despite the simplifications required to build them, they are a cheaper option compared to 3D models and provide a fast way to apply sensitivity analyses to test any uncertainties in the input parameters.

All this shows us that static geomechanical modelling can be used to understand complex settings, even in exploration stages where the uncertainties are high and sediment rheology data is not available. This study concluded that, even simple 2D static models, with their respective sensitivity analyses, can add value to the prognosis and help reduce uncertainties.

4.3 Evolutionary geomechanical modelling conclusions

The evolutionary 2D modelling provides a step forward compared to the previous static models built during this study, since it allowed to explore the formation and evolution of the Tarfaya basin, both under a kinematically and geomechanically point of view.

The 2D evolutionary geomechanical model used geological inputs of sea floor slope evolution and sedimentation rates from a kinematic restoration model. The Sandia diapir kinematics and evolution through time obtained from this model were similar to the one provided by the input restoration model:

- The Sandia diapir began its formation during Jurassic, where the diapirism was triggered by high sedimentation rates.
- At the end of Jurassic, the Sandia diapir reaches the sea floor and begins to spread laterally, forming a salt sheet downslope and an overhang upslope. This formation is possible thanks to the stock of salt accumulated at the pedestals during Jurassic and by the lower sedimentation rates of Early Cretaceous.
- At the end of Early Cretaceous the diapir stops spreading and welds its source layer. The sediments bury the salt structure under a thin roof.
- The Atlas shortening reactivates the diapirism during the beginning of Late Cretaceous. The salt from the sheet and overhang of the diapir flow towards the

centre and starts to bulge the crest of the structure, arching the sedimentary roof on top.

- The diapir at present day shows a geometry similar to the seismic data available, with a diapir welded at its base, buried by Tertiary sediments, with a salt sheet formed downslope and an overhang formed upslope.

The sensitivity analysis performed for the 2D evolutionary geomechanical model has identified the changes in the sedimentation rate during the basin formation to be the main driver of the halokinetic evolution. In particular, when the sedimentation rates are increased to represent deeper locations of the basin, the resulting diapir is able (in combination with a thicker initial salt source layer) to reach the sea floor at the end of the simulation thanks to the secondary growth during the Atlas shortening. This result is consistent with the Western diapir evolution from the seismic section, located in the deeper parts of the Tarfaya basin, to the west of the Sandia diapir.

We have also shown that the variation of shortening-rate histories on the evolutionary models had a low effect on the halokinetics in this particular basin because the diapirs mainly develop between Jurassic and Late Cretaceous, before the onset of shortening. However, the changes in shortening rates significantly affected the present-day stress state above the Sandia diapir. When a progressively increase and then decrease of the shortening history was applied, the sediments on top of Sandia showed a horizontal stress reduction compatible with both the 3D and 2D static models and with the drilling data coming from the Sandia-1 exploratory well.

Finally, other sensitivity analyses concluded that changes in the diapir base geometry and the temperature gradient generated shorter and wider diapirs but had a low impact on the salt structure evolution.

In conclusion, we have demonstrated that it is possible to take a step further from the static approach and model the evolution of a complex salt basin like Tarfaya. The incorporation of geological data (rates of deposition, sea floor geometry, shortening rates, etc) leads to more realistic evolutionary geomechanical models that helps us understand the present-day geometries of geologic structures and help illuminate the key drivers of their structural evolution. In turn, geomechanical models incorporate the mechanical interaction between salt and sediments and can provide valuable information on the evolution of stress, porosity and potentially pore pressure with time, ultimately providing a more complete picture of the basin history.

REFERENCES

- A**dachi, J., Nagy, Z.R., Sayers, C.M., Smith, M. & Becker, D.F. 2012. Drilling Adjacent to Salt Bodies: Definition of Mud Weight Window and Pore Pressure Using Numerical Models and Fast Well Planning Tool. *SPE Annual Technical Conference and Exhibition*, 1–11, <https://doi.org/10.2118/159739-MS>.
- Albertz, M. & Beaumont, C. 2010. An investigation of salt tectonic structural styles in the Scotian Basin, offshore Atlantic Canada: 2. Comparison of observations with geometrically complex numerical models. *Tectonics*, **29**, n/a-n/a, <https://doi.org/10.1029/2009TC002540>.
- Allen, J. & Beaumont, C. 2012. Impact of inconsistent density scaling on physical analogue models of continental margin scale salt tectonics. *Journal of Geophysical Research*, **117**, 1–22, <https://doi.org/https://doi.org/10.1029/2012JB009227>.
- Althaus, V.E. 1977. A new model for fracture gradient. *Journal of Canadian Petroleum Technology*, **16**, 89–108.
- B**arnichon, J.D., Havenith, H., Hoffer, B., Charlier, R., Jongmans, D. & Duchesne, J.C. 1999. The deformation of the Egersund-Ogna anorthosite massif, south Norway: Finite-element modelling of diapirism. *Tectonophysics*, **303**, 109–130, [https://doi.org/10.1016/S0040-1951\(98\)00247-9](https://doi.org/10.1016/S0040-1951(98)00247-9).
- Baumann, T.S., Kaus, B.J.P. & Eichheimer, P. 2017. 3D Numerical Modelling of Salt Tectonics. In: *79th EAGE Conference and Exhibition 2017*. 12–15., <https://doi.org/10.3997/2214-4609.201701173>.
- Beaumont, C., Muñoz, J.A., Hamilton, J. & Fullsack, P. 2000. Factors controlling the Alpine evolution of the central Pyrenees inferred from a comparison of observations and geodynamical models. *Journal of Geophysical Research: Solid Earth*, **105**, 8121–8145, <https://doi.org/10.1029/1999JB900390>.
- Beltrao, R.L.C., Sombra, C.L., Lage, A.C.V.M., Fagundes Netto, J.R. & Henriques, C.C.D. 2009. *Challenges and New Technologies for the Development of the Pre-Salt Cluster, Santos Basin, Brazil*. Houston, Texas, <https://doi.org/10.4043/19880-MS>.
- Ben-Awuah, J., Adda, G.W., Mijinyawa, A., Andriamihaja, S. & Siddiqui, N. 2013. 2D Basin modelling and petroleum system analysis of the triassic play in the hammerfest basin of the norwegian barents sea. *Research Journal of Applied Sciences, Engineering and Technology*, **6**, 3137–3150, <https://doi.org/10.19026/rjaset.6.3615>.
- Bolas, H.M.N., Hermanrud, C. & Teige, G.M.G. 2004. Origin of overpressures in shales: Constraints from basin modeling. *AAPG Bulletin*, **88**, 193–211, <https://doi.org/10.1306/10060302042>.
- Boussinesq, M.J. 1885. *Applications Des Potentiels à l'étude de l'équilibre et Du Mouvement Des Solides Élastiques*. Lille, Imprimerie L. Danel.
- Bradley, W.B. 1978. Bore hole failure near salt domes. *Society of Petroleum Engineers of AIME*.
- Brun, J.-P. & Fort, X. 2004. Compressional salt tectonics (Angolan margin). *Tectonophysics*, **382**, 129–150, <https://doi.org/10.1016/j.tecto.2003.11.014>.

- C**arracedo, J.C. & Perez-Torrado, F.J. 2013. *Teide Volcano*. Carracedo, J. C. & Troll, V. R. (eds). Berlin, Heidelberg, Springer Berlin Heidelberg, Active Volcanoes of the World, <https://doi.org/10.1007/978-3-642-25893-0>.
- Corti, G. & Dooley, T.P. 2015. Lithospheric-scale centrifuge models of pull-apart basins. *Tectonophysics*, **664**, 154–163, <https://doi.org/10.1016/j.tecto.2015.09.004>.
- Crook, A.J.L., Willson, S.M., Yu, J.G. & Owen, D.R.J. 2006. Predictive modelling of structure evolution in sandbox experiments. **28**, 729–744, <https://doi.org/10.1016/j.jsg.2006.02.002>.
- Crook, A.J.L., Obradors-Prats, J., Somer, D., Peric, D., Lovely, P. & Kaciewicz, M. 2018. Towards an integrated restoration/forward geomechanical modelling workflow for basin evolution prediction. *Oil & Gas Sciences and Technology – Revue d'IFP Energies nouvelles*, **73**, 19, <https://doi.org/10.2516/ogst/2018018>.
- D**avis, T., Warner, M., Elders, C. & Davison, I. 2000. *Tertiary Faulting Patterns and Growth History of Central Graben Salt Diapirs*.
- Dietl, C. & Koyi, H. 2011. Sheets within diapirs - Results of a centrifuge experiment. *Journal of Structural Geology*, **33**, 32–37, <https://doi.org/10.1016/j.jsg.2010.10.010>.
- Dooley, T.P. & Hudec, M.R. 2017. The effects of base-salt relief on salt flow and suprasalt deformation patterns - Part 2: Application to the eastern Gulf of Mexico. *Interpretation*, **5**, SD25–SD38, <https://doi.org/10.1190/INT-2016-0088.1>.
- Dooley, T.P. & Schreurs, G. 2012. Analogue modelling of intraplate strike-slip tectonics: A review and new experimental results. *Tectonophysics*, **574–575**, 1–71, <https://doi.org/10.1016/j.tecto.2012.05.030>.
- Dooley, T.P., Jackson, M.P.A. & Hudec, M.R. 2009. Inflation and deflation of deeply buried salt stocks during lateral shortening. *Journal of Structural Geology*, **31**, 582–600, <https://doi.org/10.1016/j.jsg.2009.03.013>.
- Dooley, T.P., Jackson, M.P.A. & Hudec, M.R. 2015. Breakout of squeezed stocks: Dispersal of roof fragments, source of extrusive salt and interaction with regional thrust faults. *Basin Research*, **27**, 3–25, <https://doi.org/10.1111/bre.12056>.
- Dooley, T.P., Hudec, M.R., Carruthers, D., Jackson, M.P.A. & Luo, G. 2017. The effects of base-salt relief on salt flow and suprasalt deformation patterns - Part 1: Flow across simple steps in the base of salt. *Interpretation*, **5**, SD1–SD23, <https://doi.org/10.1190/INT-2016-0087.1>.
- Duffy, O.B., Dooley, T.P., Fernandez, N., Jackson, C.A.L. & Peel, F.J. 2019. Obstructed minibasins on a salt - detached slope: An example from above the Sigsbee canopy, northern Gulf of Mexico. *Basin Research*, 1–20, <https://doi.org/https://doi.org/10.1111/bre.12380>.

- Durand-Riard, P., Shaw, J.H., Plesch, A. & Lufadeju, G. 2013. Enabling 3D geomechanical restoration of strike- and oblique-slip faults using geological constraints, with applications to the deep-water Niger Delta. *Journal of Structural Geology*, **48**, 33–44, <https://doi.org/10.1016/j.jsg.2012.12.009>.
- Dusseault, M.B., Maury, V. & Sanfilippo, F. 2004. Drilling Around Salt: Stresses, Risks, Uncertainties. *American Rock Mechanics Association. Paper 04-647*.
- E**l Harfi, A., Lang, J. & Salomon, J. 1996. Cenozoic continental infilling of the Ouarzazate foreland basin. Implications for the structural evolution of the Central High Atlas Mountains (Morocco). *Comptes Rendus de l'Academie de Sciences - Serie IIa: Sciences de la Terre et des Planetes*, **323**, 623–630.
- F**arzipour-Saein, A. & Koyi, H. 2014. Effect of lateral thickness variation of an intermediate decollement on the propagation of deformation front in the Lurestan and Izeh zones of the Zagros fold-thrust belt, insights from analogue modeling. *Journal of Structural Geology*, **65**, 17–32, <https://doi.org/10.1016/j.jsg.2014.03.004>.
- Fernandez, N. & Kaus, B.J.P. 2014. Tectonophysics Fold interaction and wavelength selection in 3D models of multilayer detachment folding. *Tectonophysics*, **632**, 199–217, <https://doi.org/10.1016/j.tecto.2014.06.013>.
- Fernandez, N. & Kaus, B.J.P. 2015. Pattern formation in 3-D numerical models of down-built diapirs initiated by a Rayleigh–Taylor instability. *Geophysical Journal International*, **202**, 1253–1270, <https://doi.org/10.1093/gji/ggv219>.
- Fernandez, O., Harrold, T., Ferguson, W., Gonzalez, H. & Bere, A. 2015. Three-dimensional Prediction of Stress Distribution Above a Salt Diapir - Application to a Deepwater Hydrocarbon Exploration Well. In: *77th EAGE Conference and Exhibition 2015: Earth Science for Energy and Environment*. 965–969., <https://doi.org/10.3997/2214-4609.201412715>.
- Fraissinet, C., El Zouine, M., Morel, J., Poisson, A., Andrieux, J. & Faure-Muret, A. 1988. Structural evolution of the southern and northern Central High Atlas in paleogene and Mio-Pliocene times. In: Jacobshagen, V. H. (ed.) *The Atlas System of Morocco: Studies on Its Geodynamic Evolution*. Berlin, Heidelberg, Springer Berlin Heidelberg, 273–291., <https://doi.org/10.1007/BFb0011597>.
- Fredrich, J.T., Coblenz, D., Fossum, A.F. & Thorne, B.J. 2003. Stress Perturbations Adjacent to Salt Bodies in the Deepwater Gulf of Mexico. *SPE Annual Technical Conference and Exhibition*, <https://doi.org/10.2118/84554-MS>.
- Fredrich, J.T., Fossum, A.F. & Hickman, R.J. 2007a. Mineralogy of deepwater Gulf of Mexico salt formations and implications for constitutive behavior. *Journal of Petroleum Science and Engineering*, **57**, 354–374, <https://doi.org/10.1016/j.petrol.2006.11.006>.
- Fredrich, J.T., Engler, B.P., Smith, J.A., Onyia, E.C. & Tolman, D.N. 2007b. Pre-drill Estimation of Subsalt Fracture Gradient: Analysis of the Spa Prospect to Validate Nonlinear Finite Element Stress Analyses. *SPE/IADC Drilling Conference*, **8**, <https://doi.org/10.2118/105763-MS>.

- Frizon de Lamotte, D., Saint Bezar, B., Bracène, R. & Mercier, E. 2000. The two main steps of the Atlas building and geodynamics of the western Mediterranean. *Tectonics*, **19**, 740–761, <https://doi.org/10.1029/2000TC90003>.
- Frizon de Lamotte, D., Zizi, M., et al. 2008. The Atlas System. In: Otto, J.-C. & Dikau, R. (eds) *Continental Evolution: The Geology of Morocco*. Berlin, Heidelberg, Springer Berlin Heidelberg, 133–202., https://doi.org/10.1007/978-3-540-77076-3_4.
- G**örler, K., Helmdach, F.-F., et al. 1988. The uplift of the central High Atlas as deduced from neogene continental sediments of the Ouarzazate province, Morocco BT - The Atlas System of Morocco: Studies on its Geodynamic Evolution. In: Jacobshagen, V. H. (ed.). Berlin, Heidelberg, Springer Berlin Heidelberg, 359–404., <https://doi.org/10.1007/BFb0011601>.
- Goteti, R., Ings, S.J. & Beaumont, C. 2012. Development of salt minibasins initiated by sedimentary topographic relief. *Earth and Planetary Science Letters*, **339–340**, 103–116, <https://doi.org/10.1016/j.epsl.2012.04.045>.
- Gouiza, M. 2011. *Mesozoic Source-to-Sink Systems in NW Africa: Geology of Vertical Movements during the Birth and Growth of the Moroccan Rifted Margin: Ph.D Thesis*. VU University Amsterdam.
- Gradmann, S. & Beaumont, C. 2012. Coupled fluid flow and sediment deformation in margin-scale salt-tectonic systems: 2. Layered sediment models and application to the northwestern Gulf of Mexico. *Tectonics*, **31**, 1–22, <https://doi.org/10.1029/2011TC003035>.
- Gradmann, S., Beaumont, C. & Ings, S.J. 2012. Coupled fluid flow and sediment deformation in margin-scale salt-tectonic systems: 1. Development and application of simple, single-lithology models. *Tectonics*, **31**, 1–17, <https://doi.org/10.1029/2011TC003033>.
- Gutierrez, M. & Wangen, M. 2005. Modeling of compaction and overpressuring in sedimentary basins. *Marine and Petroleum Geology*, **22**, 351–363, <https://doi.org/10.1016/j.marpetgeo.2005.01.003>.
- H**amilton-Wright, J., Dee, S., Von Nicolai, C. & Johnson, H. 2019. Investigating controls on salt movement in extensional settings using finite-element modelling. *Petroleum Geoscience*, **25**, 258–271, <https://doi.org/10.1144/petgeo2018-119>.
- Hantschel, T. & Kauerauf, A. 2009. *Fundamentals of Basin and Petroleum Systems Modeling*. Berlin, Heidelberg, Springer Berlin Heidelberg, <https://doi.org/10.1007/978-3-540-72318-9>.
- Heidari, M., Nikolinakou, M.A., Hudec, M.R. & Flemings, P.B. 2016. Tectonophysics Geomechanical analysis of a welding salt layer and its effects on adjacent sediments. *Tectonophysics*, **683**, 172–181, <https://doi.org/10.1016/j.tecto.2016.06.027>.
- Heidari, M., Nikolinakou, M.A. & Flemings, P.B. 2018a. Coupling geomechanical modeling with seismic pressure prediction. *Geophysics*, **83**, B253–B267, <https://doi.org/10.1190/geo2017-0359.1>.

- Heidari, M., Nikolinakou, M.A. & Flemings, P.B. 2018b. Coupling geomechanical modeling with seismic pressure prediction. *Geophysics*, **83**, B253–B267, <https://doi.org/10.1190/geo2017-0359.1>.
- Heidari, M., Nikolinakou, M.A., Hudec, M.R. & Flemings, P.B. 2019. Influence of a reservoir bed on diapirism and drilling hazards near a salt diapir: A geomechanical approach. *Petroleum Geoscience*, **25**, 282–297, <https://doi.org/10.1144/petgeo2018-113>.
- Hoogvorst, J.J., Harrold, T.W.D., Nikolinakou, M.A., Fernandez, O. & Marcuello, A. 2020. Comparison of stresses in 3D v. 2D geomechanical modelling of salt structures in the Tarfaya Basin, West African coast. *Petroleum Geoscience*, **26**, 36–49, <https://doi.org/10.1144/petgeo2018-095>.
- Hubbert, M.K. 1937. Theory of scale models as applied to the study of geologic structures. *Geological Society of America Bulletin*, **48**, 1459–1520, <https://doi.org/10.1130/GSAB-48-1459>.
- Hubbert, M.K. 1951. Mechanical basis for certain familiar geologic structures. *Bulletin of the Geological Society of America*, **62**, 355–372, [https://doi.org/10.1130/0016-7606\(1951\)62\[355:MBFCFG\]2.0.CO;2](https://doi.org/10.1130/0016-7606(1951)62[355:MBFCFG]2.0.CO;2).
- Hudec, M.R. & Jackson, M.P.A. 2004. Regional restoration across the Kwanza Basin, Angola: Salt tectonics triggered by repeated uplift of a metastable passive margin. *AAPG Bulletin*, **88**, 971–990, <https://doi.org/10.1306/02050403061>.
- Ismail-Zadeh, A., Tsepelev, I., Talbot, C. & Korotkii, A. 2004. Three-dimensional forward and backward modelling of diapirism: Numerical approach and its applicability to the evolution of salt structures in the Pricaspian basin. *Tectonophysics*, **387**, 81–103, <https://doi.org/10.1016/j.tecto.2004.06.006>.
- Ismail-Zadeh, A.T., Talbot, C.J. & Volozh, Y.A. 2001. Dynamic restoration of profiles across diapiric salt structures: Numerical approach and its applications. *Tectonophysics*, **337**, 23–38, [https://doi.org/10.1016/S0040-1951\(01\)00111-1](https://doi.org/10.1016/S0040-1951(01)00111-1).
- Jackson, M.P.A. & Hudec, M.R. 2017. *Salt Tectonics. Principles and Practice*. Cambridge University Press.
- Kaus, B.J.P., Steedman, C. & Becker, T.W. 2008. From passive continental margin to mountain belt: Insights from analytical and numerical models and application to Taiwan. *Physics of the Earth and Planetary Interiors*, **171**, 235–251, <https://doi.org/10.1016/j.pepi.2008.06.015>.
- Koyi, H. 1998. The shaping of salt diapirs. *Journal of Structural Geology*, **20**, 321–338, [https://doi.org/10.1016/S0191-8141\(97\)00092-8](https://doi.org/10.1016/S0191-8141(97)00092-8).
- Le Roy, P. & Piqué, A. 2001. Triassic-Liassic western Moroccan synrift basins in relation to the Central Atlantic opening. *Marine Geology*, **172**, 359–381, [https://doi.org/10.1016/S0025-3227\(00\)00130-4](https://doi.org/10.1016/S0025-3227(00)00130-4).

- Luo, G., Nikolinakou, M.A., Flemings, P.B. & Hudec, M.R. 2012. Geomechanical modeling of stresses adjacent to salt bodies: Part 1 - Uncoupled models. *AAPG Bulletin*, **96**, 43–64, <https://doi.org/10.130e/041111.10144>.
- Luo, G., Hudec, M.R., Flemings, P.B. & Nikolinakou, M.A. 2017. Deformation, stress, and pore pressure in an evolving suprasalt basin. *Journal of Geophysical Research: Solid Earth*, **122**, 5663–5690, <https://doi.org/10.1002/2016JB013779>.
- M**ackay, F., Inoue, N., Fontoura, S.A.B. & Botelho, F. 2008. Geomechanical effects of a 3D vertical salt well drilling by FEA. *42nd U.S. Rock Mechanics - 2nd U.S.-Canada Rock Mechanics Symposium*.
- Maerten, L. & Maerten, F. 2006. Chronologic modeling of faulted and fractured reservoirs using geomechanically based restoration□: Technique and industry applications. *AAPG Bulletin*, **90**, 1201–1226, <https://doi.org/10.1306/02240605116>.
- Marketos, G., Spiers, C.J. & Govers, R. 2016. Impact of rock salt creep law choice on subsidence calculations for hydrocarbon reservoirs overlain by evaporite caprocks. *Journal of Geophysical Research: Solid Earth*, **121**, 4249–4267, <https://doi.org/10.1002/2016JB012892>.
- Massoli, D., Koyi, H.A. & Barchi, M.R. 2006. Structural evolution of a fold and thrust belt generated by multiple décollements: analogue models and natural examples from the Northern Apennines (Italy). *Journal of Structural Geology*, **28**, 185–199, <https://doi.org/10.1016/j.jsg.2005.11.002>.
- McGuinness, D.B. & Hossack, J.R. 1993. The Development of Allochthonous Salt Sheets as Controlled by the Rates of Extension, Sedimentation, and Salt Supply. *Rates of Geologic Processes, Tectonics, Sedimentation, Eustasy and Climate - Implications for Hydrocarbon Exploration: 14th Annual*, 127–139, <https://doi.org/10.5724/gcs.93.14.0127>.
- McKenzie, D. 1978. Some remarks on the development of sedimentary basins. *Earth and Planetary Science Letters*, **40**, 25–32, [https://doi.org/10.1016/0012-821X\(78\)90071-7](https://doi.org/10.1016/0012-821X(78)90071-7).
- Meyer, D., Zarra, L., Rains, D., Meltz, B. & Hall, T. 2005. Emergence of the Lower Tertiary Wilcox trend in the deepwater Gulf of Mexico. *World Oil*, **226**, 72–77.
- Michard, A., Saddiqi, O., Chalouan, A. & Frizon de Lamotte, D. 2008. *Continental Evolution: The Geology of Morocco*. Otto, J.-C. & Dikau, R. (eds). Berlin, Heidelberg, Springer Berlin Heidelberg, Lecture Notes in Earth Sciences, <https://doi.org/10.1007/978-3-540-77076-3>.
- Moretti, I. & Guiton, M.L.E. 2006. KINE3D□: a New 3D Restoration Method Based on a Mixed Approach Linking Geometry and Geomechanics. *Oil & Gas Sciences and Technology – Revue d'IFP Energies nouvelles*, **61**, 277–289, <https://doi.org/10.2516/ogst:2006021>.
- Munson, D.E. 1997. Constitutive model of creep in rock salt applied to underground room closure. *International journal of rock mechanics and mining sciences & geomechanics abstracts*, **34**, 233–247, [https://doi.org/10.1016/S0148-9062\(96\)00047-2](https://doi.org/10.1016/S0148-9062(96)00047-2).
- Munson, D.E. & Dawson, P.R. 1979. Constitutive model for the low temperature creep of salt (with application to WIPP). SAND79-1853. Sandia National Laboratories, Albuquerque, NM. 31.

- N**ikolinakou, M.A., Luo, G., Hudec, M.R. & Flemings, P.B. 2012. Geomechanical modeling of stresses adjacent to salt bodies: Part 2 - Poroelastoplasticity and coupled overpressures. *AAPG Bulletin*, **96**, 65–85, <https://doi.org/10.130e/041111.10144>.
- Nikolinakou, M.A., Hudec, M.R. & Flemings, P.B. 2014. Comparison of evolutionary and static modeling of stresses around a salt diapir. *Marine and Petroleum Geology*, **57**, 537–545, <https://doi.org/10.1016/j.marpetgeo.2014.07.002>.
- Nikolinakou, M.A., Heidari, M., Flemings, P.B. & Hudec, M.R. 2018a. Geomechanical modeling of pore pressure in evolving salt systems. *Marine and Petroleum Geology*, **93**, 272–286, <https://doi.org/10.1016/j.marpetgeo.2018.03.013>.
- Nikolinakou, M.A., Flemings, P.B., Heidari, M. & Hudec, M.R. 2018b. Stress and Pore Pressure in Mudrocks Bounding Salt Systems. *Rock Mechanics and Rock Engineering*, **51**, 3883–3894, <https://doi.org/10.1007/s00603-018-1540-z>.
- Nilforoushan, F. & Koyi, H.A. 2007. Displacement fields and finite strains in a sandbox model simulating a fold-thrust-belt. *Geophysical Journal International*, **169**, 1341–1355, <https://doi.org/10.1111/j.1365-246X.2007.03341.x>.
- Nilsen, K.T., Johansen, J.-T. & Vendeville, B.C. 1996. Influence of Regional Tectonics on Halokinesis in the Nordkapp Basin, Barents Sea. In: Jackson, M. P. A., Roberts, D. G. & Snelson, S. (eds) *Salt Tectonics: A Global Perspective*. AAPG Memoir 65, 413–436.
- Nygaard, R., Gutierrez, M., Bratli, R.K. & Hoeg, K. 2006. Brittle-ductile transition, shear failure and leakage in shales and mudrocks. *Marine and Petroleum Geology*, **23**, 201–212.
- O**rlic, B. & Wassing, B.B.T. 2013. A Study of Stress Change and Fault Slip in Producing Gas Reservoirs Overlain by Elastic and Viscoelastic Caprocks. *Rock Mechanics and Rock Engineering*, **46**, 421–435, <https://doi.org/10.1007/s00603-012-0347-6>.
- P**eric, D. & Crook, A.J.L. 2004. Computational strategies for predictive geology with reference to salt tectonics. **193**, 5195–5222, <https://doi.org/10.1016/j.cma.2004.01.037>.
- Pichel, L.M., Finch, E., Huuse, M. & Redfern, J. 2017. The influence of shortening and sedimentation on rejuvenation of salt diapirs: A new Discrete-Element Modelling approach. *Journal of Structural Geology*, **104**, 61–79, <https://doi.org/10.1016/j.jsg.2017.09.016>.
- Piqué, A., Le Roy, P. & Amrhar, M. 1998. Transtensive synsedimentary tectonics associated with ocean opening: The Essaouira-Agadir segment of the Moroccan Atlantic margin. *Journal of the Geological Society*, **155**, 913–928, <https://doi.org/10.1144/gsjgs.155.6.0913>.
- R**amberg, H. 1981. The role of gravity in orogenic belts. *Geological Society Special Publication*, **9**, 125–140, <https://doi.org/10.1144/GSL.SP.1981.009.01.11>.

- Reber, J.E., Cooke, M.L. & Dooley, T.P. 2020. What model material to use? A Review on rock analogs for structural geology and tectonics. *Earth-Science Reviews*, **202**, 103107, <https://doi.org/10.1016/j.earscirev.2020.103107>.
- Rimi, A. 2001. Carte du gradient géothermique au Maroc. *Bulletin de l'institut scientifique, Rabat*, **23**, 1–6.
- Rockfield. 2017. *Elfen Explicit Manual (Version 4.10)*. Software, R. (ed.). Swansea, UK.
- Rowan, M.G. 1993. A systematic technique for the sequential restoration of salt structures. *Tectonophysics*, **228**, 331–348.
- Rowan, M.G. & Kligfield, R. 1989. Cross section restoration and balancing as aid to seismic interpretation in extensional terranes. *American Association of Petroleum Geologists Bulletin*, **73**, 955–966, <https://doi.org/10.1306/44b4a2bc-170a-11d7-8645000102c1865d>.
- Rowan, M.G. & Ratliff, R.A. 2012. Cross-section restoration of salt-related deformation: Best practices and potential pitfalls. *Journal of Structural Geology*, **41**, 24–37, <https://doi.org/10.1016/j.jsg.2011.12.012>.
- Rowan, M.G., Giles, K.A., Hearon, T.E. & Fiduk, J.C. 2016. Megaflaps adjacent to salt diapirs. *AAPG Bulletin*, **100**, 1723–1747, <https://doi.org/10.1306/05241616009>.
- Rowan, M.G., Urai, J.L., Fiduk, J.C. & Kukla, P.A. 2019. Deformation of intrasalt competent layers in different modes of salt tectonics. *Solid Earth*, **10**, 987–1013, <https://doi.org/10.5194/se-10-987-2019>.
- Schellart, W.P. & Strak, V. 2016. A review of analogue modelling of geodynamic processes: Approaches, scaling, materials and quantification, with an application to subduction experiments. *Journal of Geodynamics*, **100**, 7–32, <https://doi.org/10.1016/j.jog.2016.03.009>.
- Schléder, Z. & Urai, J.L. 2007. Deformation and recrystallization mechanisms in mylonitic shear zones in naturally deformed extrusive Eocene-Oligocene rocksalt from Eyvanekey plateau and Garmsar hills (central Iran). *Journal of Structural Geology*, **29**, 241–255, <https://doi.org/10.1016/j.jsg.2006.08.014>.
- Schreurs, G., Buitter, S.J.H., et al. 2016. Benchmarking analogue models of brittle thrust wedges. *Journal of Structural Geology*, **92**, 116–139, <https://doi.org/10.1016/j.jsg.2016.03.005>.
- Schultz-Ela, D.D. 1992. Restoration of cross-sections to constrain deformation processes of extensional terranes. *Marine and Petroleum Geology*, **9**, 372–388, [https://doi.org/10.1016/0264-8172\(92\)90049-K](https://doi.org/10.1016/0264-8172(92)90049-K).
- Sclater, J.G. & Christie, P.A.F. 1980. Continental stretching: An explanation of the Post-Mid-Cretaceous subsidence of the central North Sea Basin. *Journal of Geophysical Research: Solid Earth*, **85**, 3711–3739, <https://doi.org/10.1029/JB085iB07p03711>.
- Segura, J.M., Matos da Cruz, A., Stachlewski, G., Alvarellos, J., Vargas, P.E. & Lakshmikantha, M.R. 2016. Fault stability assessment for well planning: a case study related to salt structures. *American Rock Mechanics Association. Paper 16-518*.

- Seymour, K.P., Rae, G., Peden, J.M. & Ormston, K. 1993. Drilling close to salt diapirs in the North Sea. *Offshore Europe*, 193–204, <https://doi.org/10.2118/26693-MS>.
- Stigall, J. & Dugan, B. 2010. Overpressure and earthquake initiated slope failure in the Ursa region, northern Gulf of Mexico. *Journal of Geophysical Research*, **115**, B04101, <https://doi.org/10.1029/2009JB006848>.
- Swarbrick, R.E., Osborne, M.J. & Yardley, G.S. 2002. Comparison of Overpressure Magnitude Resulting from the Main Generating Mechanisms Generating Mechanisms. *AAPG Memoir*, **76**, 1–12.
- Sweatman, R., Faul, R. & Ballew, C. 1999. New Solutions for Subsalt-Well Lost Circulation and Optimized Primary Cementing. *SPE Annual Technical Conference and Exhibition*.
- T**ari, G. & Jabour, H. 2013. Salt tectonics along the Atlantic margin of Morocco. *Geological Society, London, Special Publications*, **369**, 337–353, <https://doi.org/10.1144/SP369.23>.
- Thibaut, M., Jardin, A., Faille, I., Willien, F. & Guichet, X. 2014. Advanced Workflows for Fluid Transfer in Faulted Basins. *Oil & Gas Science and Technology – Revue d'IFP Energies nouvelles*, **69**, 573–584, <https://doi.org/10.2516/ogst/2014016>.
- Thigpen, J.R., Roberts, D., Snow, J.K., Walker, C.D. & Bere, A. 2019. Integrating kinematic restoration and forward finite element simulations to constrain the evolution of salt diapirism and overburden deformation in evaporite basins. *Journal of Structural Geology*, **118**, 68–86, <https://doi.org/10.1016/j.jsg.2018.10.003>.
- Trudgill, B.D. & Rowan, M.G. 2004. Integrating 3D Seismic Data with Structural Restorations to Elucidate the Evolution of a Stepped Counter-Regional Salt System, Eastern Louisiana Shelf, Northern Gulf of Mexico. *Geological Society, London, Memoirs*, **29**, 165–176, <https://doi.org/10.1144/GSL.MEM.2004.029.01.16>.
- U**S Army Corps of Engineers. 1990. *Engineering and Design: Settlement Analysis*. Engineering Manual 1110-1-1904, CECW-EG Date 30 September 1990.
- V**an der Zee, W., Ozan, C., Brudy, M. & Holland, M. 2011. 3D geomechanical modeling of complex salt structures. *SIMULLA Customer Conference*, 1–16.
- van Keken, P.E., Spiers, C.J., van den Berg, A.P. & Muyzert, E.J. 1993. The effective viscosity of rocksalt: implementation of steady-state creep laws in numerical models of salt diapirism. *Tectonophysics*, **225**, 457–476, [https://doi.org/10.1016/0040-1951\(93\)90310-g](https://doi.org/10.1016/0040-1951(93)90310-g).
- Vendeville, B.C. & Nilsen, K. 1993. Episodic growth of salt diapirs driven by horizontal shortening. *In: Salt, Sediment and Hydrocarbons*. Society of Economic Paleontologists and Mineralogists Gulf Coast Section, 285–295., <https://doi.org/10.5724/gcs.95.16.0285>.
- W**arren, J.K. 2006. *Evaporites: Sediments, Resources and Hydrocarbons*. Netherlands, Springer, <https://doi.org/10.1007/3-540-32344-9>.

Wenke, A., Zühlke, R., Jabour, H. & Kluth, O. 2011. High-resolution sequence stratigraphy in basin reconnaissance: Example from the Tafaya Basin, Morocco. *First Break*, **29**, 85–96.

Willson, S.M., Fossum, A.F. & Fredrich, J.T. 2002. Assessment of Salt Loading on Well Casings. *Proceedings of the Drilling Conference*, 711–720, <https://doi.org/10.2523/74562-ms>.

Yu, Y., Tang, L., Yang, W., Huang, T., Qiu, N. & Li, W. 2014. Salt structures and hydrocarbon accumulations in the Tarim Basin, northwest China. *AAPG Bulletin*, **98**, 135–159, <https://doi.org/10.1306/05301311156>.

Zarhloule, Y., Rimi, A., Boughriba, M., Barkaoui, A.E. & Lahrach, A. 2010. The Geothermal Research in Morocco: History of 40 Years. *In: World Geothermal Congress*.

Zoback, M.D. 2007. *Reservoir Geomechanics*, 1st editio. Cambridge University Press (ed.). New York.

ANNEXES

**Annex 1: Comparison of stresses in 3D vs. 2D
geomechanical modelling of salt structures in the Tarfaya
Basin, West African coast**

Comparison of stresses in 3D v. 2D geomechanical modelling of salt structures in the Tarfaya Basin, West African coast



Jean Joseph Hoogvorst^{1*}, Toby W. D. Harrold², Maria A. Nikolinakou³, Oscar Fernandez⁴ & Alejandro Marcuello⁵

¹ Facultat de Ciències de la Terra, Universitat de Barcelona, Martí I Franqués, s/n, 08028 Barcelona, Spain

² Geohazards Team, Repsol Exploración S.A., Méndez Álvaro 44, 28043 Madrid, Spain

³ Bureau of Economic Geology, Jackson School of Geosciences, The University of Texas at Austin, 10100 Burnet Road, Building PRC-130, Austin, TX 78758, USA

⁴ Department Geodynamics and Sedimentology, University of Vienna, Althanstrasse 14, 1090 Vienna, Austria

⁵ Facultat de Ciències de la Terra, Universitat de Barcelona, Martí I Franqués, s/n, 08028 Barcelona, Spain

ORCID iD: MAN, 0000-0003-3194-3477; OF, 0000-0003-1584-2684; AM, 0000-0002-6216-4436

* Correspondence: jeanjo_90@hotmail.com

Abstract: We predict stresses and strains in the Tarfaya salt basin on the West African coast using a 3D static geomechanical model and compare the results against a simplified 2D plane-strain model. Both models are based on present-day basin geometries, are drained, and use a poroelastic description for the sediments and visco-plastic description for salt. We focus on a salt diapir, where an exploratory well has been drilled crossing a major fault. The 3D model shows a significant horizontal stress reduction in sediments at the top of the diapir, validated with measured data later obtained from the well. The 2D model predicts comparable stress reduction in sediments at the crest of the diapir. However, it shows a broader area affected by the stress reduction, overestimating its magnitude by as much as 1.5 MPa. Both models predict a similar pattern of differential displacement in sediments along both sides of the major fault, above the diapir. These displacements are the main cause of horizontal stress reduction detected at the crest of the diapir. Sensitivity analysis in both models shows that the elastic parameters of the sediments have a minimal effect on the stress–strain behaviour. In addition, the 2D sensitivity analysis concludes that the main factors controlling stress and strain changes are the geometry of the salt and the difference in rock properties between encasing sediments and salt. Overall, our study demonstrates that carefully built 2D models at the exploration stage can provide stress information and useful insights comparable to those from more complex 3D geometries.

Received 31 July 2018; revised 8 July 2019; accepted 16 July 2019

A great number of hydrocarbon reservoirs in basins around the world are located near or below salt structures (Meyer *et al.* 2005; Warren 2006; Beltrao *et al.* 2009; Yu *et al.* 2014). This fact has led to a large number of drilling operations close to salt diapirs. The viscous rheology of the salt makes it unable to sustain deviatoric stresses, therefore salt flows and changes its shape until it reaches an isostatic (uniform) stress state. As a result, sediments encasing salt structures may experience deformation and changes in their stress state and pore-pressure distribution (Orlic & Wassing 2013; Luo *et al.* 2017; Nikolinakou *et al.* 2018). This uncertainty in stress and pressure state has led to major problems during drilling operations in salt-related basins, including hazardous conditions and additional expense. For example, Bradley (1978) discussed borehole collapse incidents next to a salt structure in the Gulf of Mexico, Eugene Island. Seymour *et al.* (1993) reported 26.3% of non-productive drilling time for wells close to salt diapirs in the North Sea. Narrow drilling windows near salt formations in the Gulf of Mexico, leading to severe lost circulation, hole instabilities and high-pressure kicks, are also reported by Sweatman *et al.* (1999). Finally, Dusseault *et al.* (2004) exemplified the case of a well above a Gulf of Guinea salt dome, where lower than expected minimum horizontal stresses resulted in 92 lost drilling days.

In the last 20 years, geomechanical modelling has been established as a tool to reduce uncertainty in complex prospects with salt-related structures. Geomechanical models employ poro-mechanical constitutive formulations to predict stress, strain and pore pressure of sediments in basins. Geomechanical models can be

static (e.g. Segura *et al.* 2016; Heidari *et al.* 2018) or evolutionary (e.g. Goteti *et al.* 2012; Nikolinakou *et al.* 2018; Thigpen *et al.* 2019). Static models are built based on present-day geometry, while evolutionary models simulate the evolution of the salt system (Nikolinakou *et al.* 2014). Therefore, static models are most often used to study specific prospects. Most published static studies employ 2D geomechanical models. Early examples use idealized salt geometries (e.g. Fredrich *et al.* 2003), which provide insights into salt–sediment interaction but do not describe real field cases. Several 2D studies of actual salt geometries – derived from seismic surveys – have also been documented (Fredrich *et al.* 2007a; Segura *et al.* 2016; Heidari *et al.* 2018). Such 2D models allow preliminary results to be obtained faster than a complete 3D model. However, 2D models can only represent complex 3D salt structures with a plane-strain or axisymmetrical geometry; hence, they cannot incorporate stress changes and deformation associated with the three-dimensional nature of the salt system. There are a few studies that perform a full 3D geomechanical model of actual salt geometries (van der Zee *et al.* 2011; Adachi *et al.* 2012; Segura *et al.* 2016) overcoming the limitations of the 2D models. These models, however, have the downside of being computationally expensive and labour-intensive.

At an early exploration stage, the selection of a 3D v. 2D geomechanical model becomes important. The final choice can be influenced by time and budget constraints or the required accuracy of the results. Geometrical variability, complex fault networks, changes in lithologies or salt–sediment interaction can be factors that tip the balance from one approach to another.

This work presents a case study for the Tarfaya salt basin on the NW African coast (Fig. 1). A rank wildcat exploration well was drilled above a salt-cored anticline. A 3D elastic static geomechanical model was developed before the drilling of the exploration well to obtain a stress–strain understanding of the area, as well as to assess the stability of the complex 3D pattern of faults above the diapir. This 3D model concludes that a significant horizontal stress reduction is present in the sediments above the salt structure. Results of the 3D analysis were later validated with data from drilling of the exploration well. Sensitivity analysis on input material properties has also been performed because of the lack of data for a precise material description. This analysis shows almost no effect on the results.

A 2D model has been built from a representative transect of the full 3D geometry that includes the exploration well. The results from this simpler model are consistent with the horizontal stress reduction above the salt structure seen in the 3D model. The sensitivity analysis also shows a low influence of the sediment elastic properties. In addition, it allows us to identify the high contrast between salt–sediment properties and the seafloor geometry as the main causes of stress and strain changes in the poroelastic model.

We compare the results between the 3D and 2D models in order to explore whether the simplified 2D case can lead to similar results to the 3D case. The comparison shows a similar reduction in magnitude of horizontal stresses in sediments located near the salt crest. However, the 2D model predicts a more extensive area of stress and strain perturbations above salt. The displacements of the roof sediments in both models have similar patterns but the 2D model yields higher magnitudes. These results allow us to consider the 2D simplification as a realistic first-order simulation of the basin, in agreement with available data and results from the more complex 3D model.

Prospect geological system

The study zone is located in the Tarfaya Basin, between the Moroccan shore and the island of Lanzarote from the Canary archipelago (Fig. 1). It extends approximately 3250 km² and comprises numerous salt bodies that are part of the structures identified along the NW African margin (Tari & Jabour 2013).

The Tarfaya Basin is characterized as a passive margin formed during the Late Triassic–Early Jurassic rifting and opening of the Central Atlantic and the separation of the NW African margin from the North American margin. The rifting caused stretching of the basement, forming fault-controlled graben that were filled by siliciclastic and evaporitic sediments. These evaporites were the source layer for the present-day salt structures. The uneven distribution of salt along these graben is the principal cause for the distribution of individual salt structures at the present day (Tari & Jabour 2013).

Post-rift differential thermal subsidence and submersion of the basin towards the west favoured the formation of a carbonate shelf and triggered the salt tectonics (Tari & Jabour 2013). During the Late Jurassic–Early Cretaceous, a relative sea-level fall caused a subaerial exposure and karstification of the carbonate platform (Wenke *et al.* 2011). A very significant sedimentary influx from the continental margin also takes place during the Early Cretaceous, depositing thick sand layers forming the Tan-Tan deltaic formation (Gouiza 2011).

During the Late Cretaceous, the initial compression of the Atlas began, causing a moderate sediment input (Wenke *et al.* 2011) and reactivating pre-existing salt structures until the Miocene. This period of time is considered by Tari & Jabour (2013) to be the main period for the formation of salt sheets and canopies seen north of the Tarfaya Basin, and also coincides with the volcanic emplacement of the Canary archipelago (Carracedo & Perez-Torrado 2013). Most of

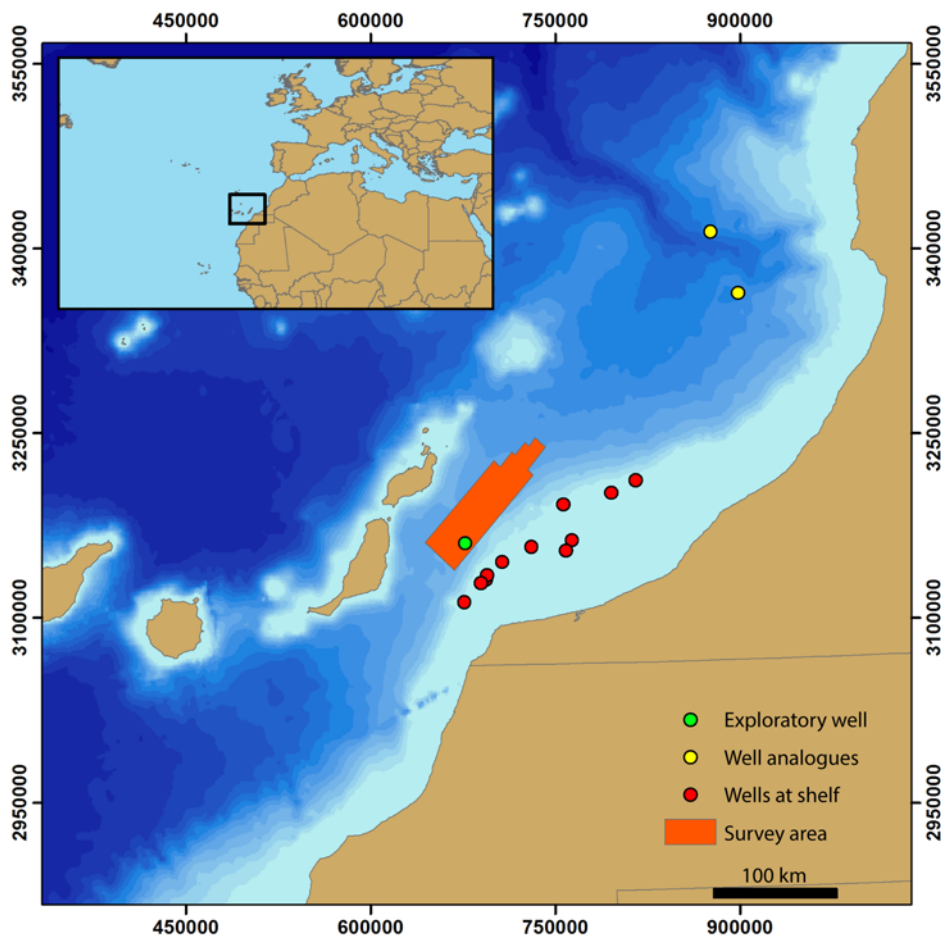


Fig. 1. Location map of the survey area (red polygon) situated between the Canary archipelago and the southern Moroccan shore. The green dot indicates the location of the exploratory well.

3D/2D geomechanical modelling comparison: Tarfaya

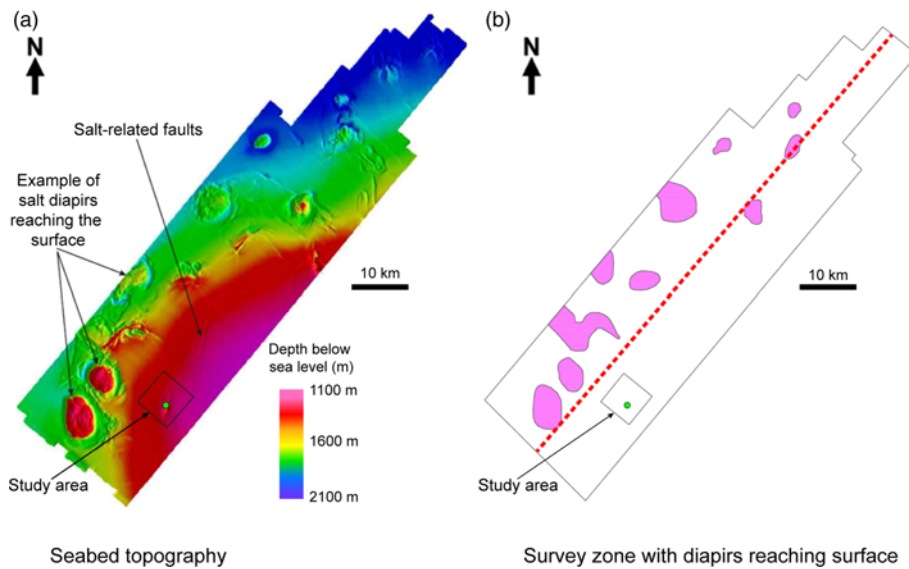


Fig. 2. (a) Survey area seafloor topography. The general NW downwards slope is perturbed by salt-related morphologies: domes with moats caused by the salt reaching the surface and seafloor troughs related to buried salt-induced faults. The rectangle indicates the study area and the green dot represents the exploration well. (b) The location of major diapirs with seabed expression (pink polygons). The red dashed line separates two different salt regions: the NW side has a thicker salt source layer, which allows diapirs to reach the seafloor, whereas the SE side has a thinner salt source layer and buried diapirs.

the salt structures present in the study area are still active at the present day, affecting in some cases the seafloor bathymetry (Fig. 2). The same figure shows other diapirs not reaching the seafloor, due to their early welded stem, forming pinched diapirs within the basin. An exploratory well path was proposed above one of these buried salt structures and through the overlying network of faults (Fig. 3). The crest of this Triassic salt diapir is at 3000 m bsl (below sea level). The salt bulb at the top of the diapir has been interpreted on seismic to be disconnected from its autochthonous source layer due to welding of its stem. The folded geometry of the overlying Tertiary sediments indicates that salt in the bulb has risen after its original emplacement. The main objective of the exploratory well was to test the presence of hydrocarbons at four different sand-rich turbiditic deposits in the supra-salt Tertiary sediment package. A fault network located above the salt diapir cross-cuts the reservoir intervals.

Model set-up

We built a 3D geomechanical model using Elfen (Rockfield 2017). The model is based on a quasistatic, drained, finite-element formulation. It uses an unstructured finite-element mesh containing 3.97 million linear tetrahedral elements, with a mesh size of 400 m. A refined mesh region (4000×4000 m) centred in the well location

is used with an element size of 50 m. The boundary conditions applied restrict horizontal displacements at the four lateral sides of the model and restrict vertical displacements at the base. The predefined faults are modelled using double-sided discrete contact that allows sliding to occur along the faults, as well as a stress redistribution around them. The faults use a Coulomb friction law using a cohesion of 0 MPa and a coefficient of friction of 0.3.

The input parameters of the model include the initial pore-pressure profile, initial stress ratios (the ratio between the vertical and horizontal effective stresses considering uniaxial conditions) and material properties for each horizon. We calibrated these inputs using offset well and seismic velocity analyses. The offset wells used (yellow dots in Fig. 1) are the closest deep-water analogues to the studied location. Closer wells (red dots in Fig. 1) are discarded for being located on the continental shelf, a too dissimilar environment when compared with the studied zone.

Geometry

The domain included in the 3D model covers a subset of about 570 km² of the total area of the survey shown in Figure 2 and comprises the location of the well trajectory. The geometries for the different horizons modelled are extracted from the interpretation of the seismic survey. The base of the model is at a depth approximately

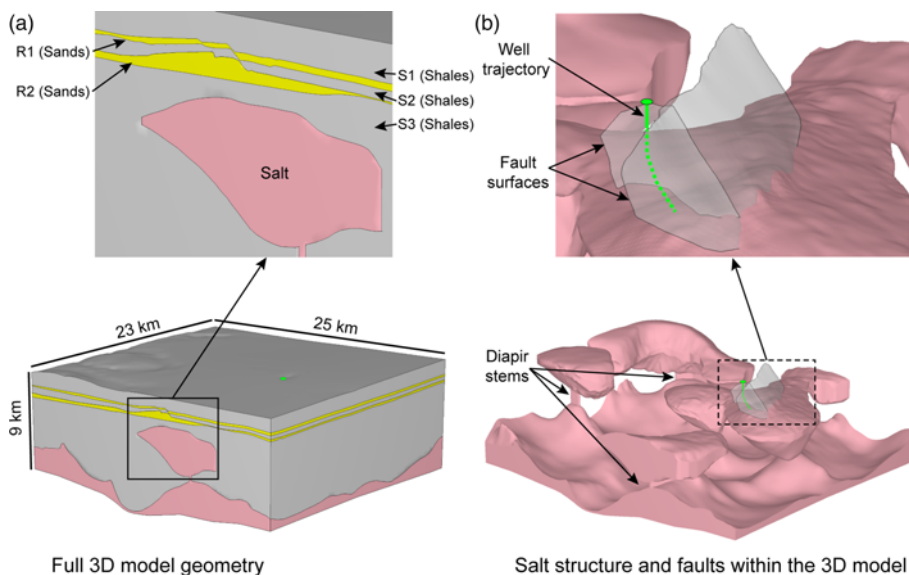


Fig. 3. Static 3D geomechanical model. (a) Model geometry representing the stratigraphic distribution of sand, shale and salt horizons. The green dot indicates the position of the well. (b) 3D salt structure, major faults and the well trajectory (green line).

9 km below the seafloor, along the interpreted base of the autochthonous salt layer. Two sand layers represent the system of reservoirs above the salt (Fig. 3a). The autochthonous and allochthonous salt structures are connected by 200 m-wide salt columns. This is contrary to the seismic interpretation which shows independent bodies, but is necessary because of the software's initialization procedures. To ensure there is no salt flow from the source layer, the width of the salt columns is sufficiently narrow (Fig. 3b).

The complex fault network above the salt diapir is simplified and represented by only two faults: a north–south-trending fault, which is the only one to have a maximum throw in excess of 400 m, and a secondary fault that intersects the trajectory of the exploratory well (Fig. 3b).

Initial stress state

In sediments, stress calculations are uncoupled from porous fluid flow (drained analysis). The initial pore-pressure profile for each horizon is obtained from a pre-drill offset well analysis, using wells in equivalent depths from the sea surface (yellow dots in Fig. 1). The pore-pressure profile for the shallowest and intermediate shale layers (S1 and S2; Table 1) is hydrostatic, whereas a constant overpressure is present in the sand layers and the deepest shale layer (R1, R2 and S3 layers; Table 1). There is zero pore pressure in salt.

Input stress ratios (K_H and K_h , see Appendix A for the nomenclature) are used in the model initialization to obtain the initial horizontal effective stresses (σ'_H , σ'_h) as a fraction of the initial vertical effective stress, σ'_v :

$$\sigma'_v = \sigma_v - u \quad (1)$$

$$K_H = \frac{1}{2}(1 + K_h) \quad (2)$$

$$K_h = \frac{\sigma'_h}{\sigma'_v} \quad K_H = \frac{\sigma'_H}{\sigma'_v} \quad (3)$$

where σ_v is the overburden, u is the pore pressure, σ_H is the maximum horizontal stress and σ_h is the minimum horizontal stress.

It is assumed that the maximum horizontal stress, σ_H , in the studied area acts in the east–west direction due to basinwards gliding of sediments on the basal salt layer. Consequently, the minimum horizontal stress, σ_h , is orientated in the north–south direction. K_h and K_H (equation 2) are used to obtain the initial σ'_h and σ'_H , respectively (equation 3). The initial stress ratio values can be found in Table 1 and have been obtained using the offset well data from the well analogues (Fig. 1). The salt structures have an assigned initial stress ratio value of 1 because salt is assumed to have a uniform stress state.

Material properties

Porosity–depth profiles for each horizon material are calibrated at the well location based on log data. An estimate for the bulk density, ρ_b , of sediments is obtained from the measured interval velocity at

the well location. The porosity is then calculated assuming values of grain and fluid densities (Table 1):

$$n = \frac{\rho_b - \rho_s}{\rho_w - \rho_s} \quad (4)$$

where ρ_w and ρ_s are the water and grain densities, respectively. Because horizons have different thicknesses across the field than at the well location, porosity–depth profiles for each horizon are extrapolated for the maximum depth of the given horizon.

The shales and sands are modelled as poroelastic materials. Because of very limited experimental or field data, the input elastic parameters are calibrated based on observations from regional wells (Table 1). The poroelastic behaviour is defined using an empirical expression to incorporate porosity changes (Rockfield 2017):

$$E = E_{\text{ref}} \left[\frac{\sigma' + A}{B} \right]^r n^c \quad (5)$$

where E is the elastic modulus, E_{ref} is a reference elastic modulus, n the porosity, and A , B , r and c are material constants used to define the shape of the elastic modulus profile. Input values can be found in Table B1 of Appendix B.

Note that the two reservoirs (R1 and R2; Fig. 3a) and the shale layer between them have a constant elastic modulus, E , that is equal to E_{ref} . The shallowest and deepest shale horizons have an elastic modulus that varies with depth. This allows us to account for depth variations of material properties within these thicker horizons. The range of values of the elastic modulus, E , for each horizon is shown in Table 1.

The salt bodies are modelled using a steady-state creep model. This is a reduced form of the Munson–Dawson formulation (the two steady-state terms are included and the transient term is omitted, considered negligible over geological timescales) (Munson & Dawson 1979). This constitutive model considers the salt viscosity as a function of both effective stress and temperature. In the absence of field-specific data, input parameters for the salt (Appendix B, Table B2) are calibrated based on Avery Island salt (Munson 1997; Fredrich *et al.* 2007b), considered to represent average salt behaviour.

A temperature gradient of 3.61°C per 100 m is used in the model, based on an integrated 2D and 3D petroleum system model for thermal maturity evaluation. The model was calibrated to the offset wells, taking into consideration the variation in sedimentation, salt presence and crustal structure. The gradient value used is in line with published results from the area (Rimi 2001; Zarhoulou *et al.* 2010).

2D model set-up

The 2D model is plane strain. The geometry is defined by taking a cross-section through the 3D model orientated SE–NW that passes through the exploratory well (Fig. 4). This section is not orientated parallel to the maximum horizontal stress in the 3D model. The orientation of the section was chosen to capture several key elements of the 3D model, such as the faults crossing the well trajectory, the diapir located below the well and the anticline in the sediments

Table 1. Summary of input properties for the different horizon layers defined in the 3D model

Stratigraphy	Description	Depth at well location (m)	ρ_s (kg m ⁻³)	ρ_f (kg m ⁻³)	Overpressure (MPa)	ν	Range of E (MPa)	K_h	K_H
S1	Shales and siltstones	885–1600	2650	1025	–	0.3	290–2250	0.73	0.87
R1	Sand	1600–1746	2650	1025	0.9	0.3	2500	0.77	0.89
S2	Shales with silt in upper region	1746–1950	2650	1025	–	0.3	2800	0.80	0.90
R2	Sand	1950–2075	2650	1025	2.7	0.3	3100	0.75	0.88
S3	Shales and siltstones	2075–3100	2600	1300	1.3	0.3	3650–50 000	0.80	0.90

Grain and fluid densities for the first four layers are 2650 and 1025 kg m⁻³, respectively, and are 2600 and 1300 kg m⁻³, respectively, for the deepest shale layer (S3).

3D/2D geomechanical modelling comparison: Tarfaya

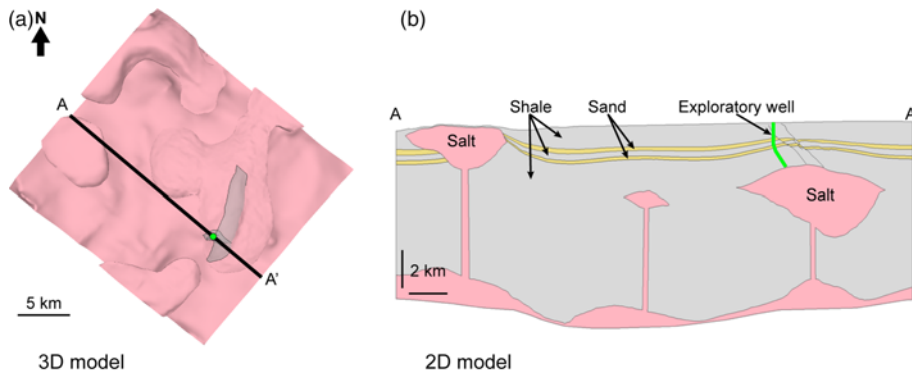


Fig. 4. (a) Location of cross-section A–A' used for the 2D model geometry. The green dot indicates the position of the exploratory well. (b) Geometry of cross-section A–A' used to build the 2D model.

overlying the salt body. In addition, other diapirs present in the 3D model are included to incorporate possible interactions between the different salt bodies. The difference between values of K_H and K_h shown in Table 1 are small, averaging 0.11. Hence, choosing an orientation of 2D section that is not parallel to the original K_H direction in the 3D model has a low impact on the stress results. The boundary conditions applied restrict horizontal displacements at both sides of the model, and restrict both horizontal and vertical displacements at the base.

The initial pore-pressure profiles, stress ratio and material properties for each layer used in the 2D model are the same as in the 3D model to allow a more consistent comparison between the model results.

3D modelling

Model results

The viscous rheology of the salt makes it unable to sustain deviatoric stresses; therefore salt flows and changes its shape until it reaches an isostatic (uniform) stress state. In the 3D model, salt stresses relax within 50 kyr. This salt movement loads the encasing sediments and changes their stress state. Hence, the stresses and strains at the end of the simulation represent the current-day geomechanical conditions for the studied area before any drilling activity or hydrocarbon extraction.

Stresses

The minimum stress ratio (Fig. 5) is obtained from the calculated values of horizontal and vertical effective stress (equation 3). This ratio illustrates locations in the salt system where the stresses have changed with respect to the initial stress state. Because the analysis is static (no deposition) and drained, the overburden profile and the pore pressure do not change during the simulation. As a result, the vertical effective stress (equation 1) does not change either. Hence, a minimum stress ratio higher than its initial value implies an increase in σ'_h . On the other hand, a minimum stress ratio lower than its initial value reflects a decrease in σ'_h .

We identify notable stress changes in areas located near the salt structures and around the faults. Along the section A–A' and near the well location (Fig. 5b) we observe an increase in K_{min} near the salt source layer and a decrease above the salt diapir, both at seafloor (around the shallowest part of the fault) and near the crest of the salt body. Stress reduction above the salt is greater on the footwall side of the fault, where the well is located, reaching values below 0.55.

We find that the maximum principal stress remains vertical and the minimum principal stress horizontal with the exception of a few small areas near salt, where the maximum stress rotation (on a vertical plane) is less than 10° . In contrast, we find a notable rotation of principal stresses on the horizontal plane (Fig. 6), especially near salt diapirs (blue and red colour contours in Fig. 6). This rotation of

horizontal principal stresses from their initial orientation (east–west for the maximum principal stress; azimuth 90° : Fig. 6) indicates loading from salt. For example, the sediments between the two diapirs located at the NW model edge experience compression from both diapirs, rotating the azimuth of the maximum horizontal stress counterclockwise from 90° to less than 60° . The horizontal principal stresses also rotate around the major fault.

Displacements

We focus on the direction of predicted displacements, because the assumption of elastic behaviour for the sediments underestimates their magnitude. Displacement direction can provide insights into possible patterns of salt relaxation, and the interaction between diapirs and their neighbouring sediments.

The horizontal east–west displacements mainly develop towards the west throughout the model domain (blue contours in Fig. 7a and b), and are greater for the sediments located above the eastern diapir and around the major fault. Displacements are greater in the footwall of the fault, compared to the hanging wall (darker blue contours at the footwall side in Fig. 7b). This difference in displacement magnitudes causes extension in the sediments above the diapir that explains the predicted reduction of stresses (Fig. 5b). Horizontal displacements are negligible along a north–south section through the well.

Vertical displacements are localized around the major fault above the eastern diapir, indicating a downwards movement of the hanging wall (blue contours in Fig. 7c and d).

Sensitivity analysis

All input conditions may affect the final static solution. The input with the highest uncertainty in the 3D geomechanical model is the elastic properties for the sediments, due to the lack of field data. In order to understand the influence of the elastic constants on the geomechanical results, we perform a sensitivity analysis (Table 2) focusing on the elastic modulus and Poisson's ratio of the shale formations (non-reservoir sediments). Variation of the elastic properties of the sand layers in the model was omitted. Sand layers represent a very small fraction of the sediment column and have little or no influence on the basin stress field.

Comparison across the model volume using model subtraction

We illustrate the effect of parameter variation in sensitivity analyses by subtracting a given result of a sensitivity analysis from the base-case model:

$$\text{comparison ratio } (S) = \frac{\text{base-case model} - \text{sensitivity model}}{\text{base-case model}} \quad (6)$$

This is possible because the numerical mesh is the same in all models, allowing node by node comparison. Values of S close to 0 imply a small change in the results caused by changing the studied

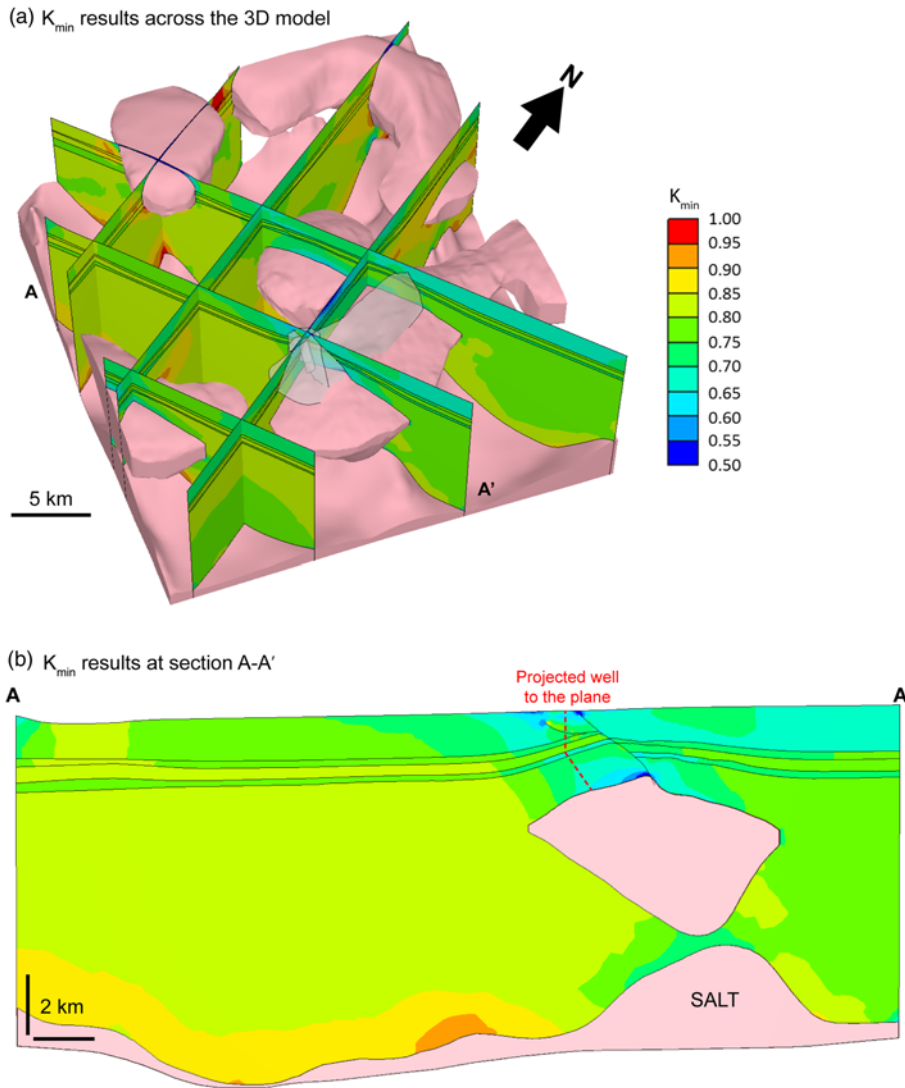


Fig. 5. (a) Minimum stress ratio (K_{min}) for different vertical sections across the model. The stress ratio is higher than its corresponding initial value for sediments below the salt or near deeper salt structures. In contrast, the stress ratio is lower than its initial value at shallow depths above the salt, around the faults and near the crest of the eastern salt body. (b) Minimum stress ratio (K_{min}) for section A–A' near the well location. The stress ratio is notably reduced at the bottom part of the well above the salt. The initial minimum stress ratio is 0.8 (light green contour colour) for intermediate and deepest shales, and 0.75 (dark green contour colours) for the shallowest shales and two reservoirs.

elastic parameter. In contrast, larger values of S indicate that the difference between the compared models is greater and, thus, the impact of the studied elastic parameter is more significant.

A statistical summary of the sensitivity analysis comparison results is shown in Table 3. In addition to the values of average, median and standard deviation, the percentage of omitted nodes for the analysis is also presented for each variable studied. These have locally spurious values that would skew the comparison between models if they were included. They constitute a very small fraction of the nodes in the model (0–2%: Table 3).

The median values for the principal stresses are very close to 0 in each of the comparison cases with small standard deviations, meaning that the changes imposed on the elastic parameters had little impact on the base-case results.

The median and standard deviation values for the displacement results are greater than the ones for the principal stresses. However, they still represent a small change in the base-case results. It should

be noted that because of the elastic assumption for sediment behaviour, displacements in all these models are very low, less than 2 m in any of the three principal directions (Fig. 7).

Comparison of sensitivity results along the well trajectory

We also compare results of the sensitivity analysis (Table 2) along the well trajectory (Fig. 8) for the first 1000 m below seafloor. We find that variations in either the elastic modulus or Poisson's ratio have little impact on the horizontal stress, with the greatest difference being lower than an equivalent mud weight of 0.15 ppg (pounds per gallon).

2D modelling

Modelling results

Similar to the 3D case, the 2D geomechanical results represent the current-day stress and strain conditions.

Displacements calculated with the 2D model illustrate how the salt flows, and how this affects the sediment strain and stress state. In particular, the eastern diapir exhibits a downwards flux at its eastern side and a westwards movement at its western part, causing the diapir to collapse and spread laterally (red arrows in Fig. 9). The same differential movement is also seen in the sediments encasing the diapir (green arrows in Fig. 9). As a result, the footwall of the fault undergoes a greater westwards displacement than the hanging

Table 2. Summary of sensitivity analysis for the 3D static model

Variable changed	Original value	Modified value
Poisson's ratio	0.3	0.25 0.4
Elastic modulus	Horizon- and depth-dependent (Table 1)	Increased 20% Decreased 20%

3D/2D geomechanical modelling comparison: Tarfaya

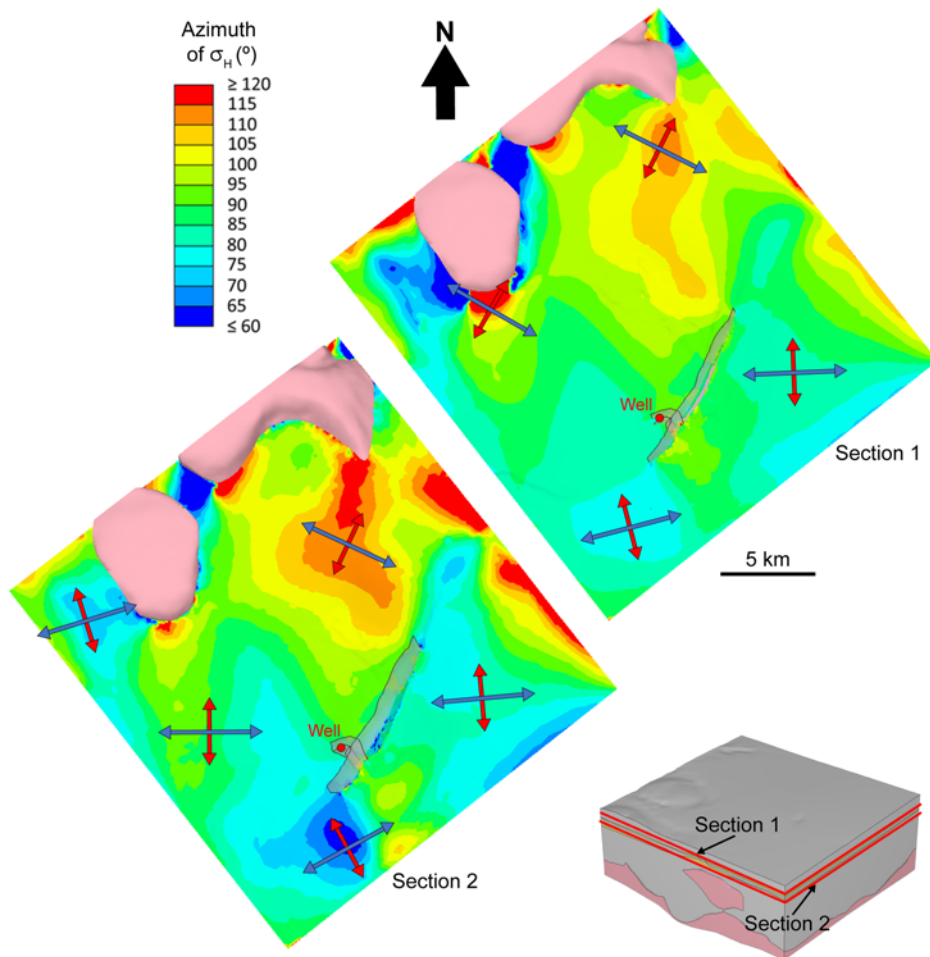


Fig. 6. Orientation of the maximum and minimum horizontal stresses, σ_H and σ_h , for two horizontal sections of the 3D model. Contours represent the azimuth of σ_H . The blue and red arrows illustrate the directions of σ_H and σ_h , respectively. The original east–west direction of σ_H changes in locations near the salt structures and around the major fault.

wall, which moves mainly downwards. In other words, the pattern of salt relaxation can explain the differential displacements above salt observed both in 2D (Fig. 9) and 3D (Fig. 7b) models, and is interpreted to be responsible for the decrease in horizontal stress above the diapir's crest.

The horizontal strain profile confirms the extensional zone located above the eastern diapir due to the differential sediment displacements (red contours in Fig. 10). The maximum extension occurs immediately above the crest of the salt structure. Localized shortening horizontal strains develop near the flanks of the western diapir (blue contours in Fig. 10), resulting from the lateral expansion of the salt diapir in the shallow section.

Extensional strains (Fig. 10) correspond to a horizontal-to-vertical effective stress ratio lower than its initial value of 0.8 (blue contours in Fig. 11a). In contrast, shortening strains (Fig. 10) correspond to a stress ratio higher than its initial value (red contours in Fig. 11a). The stress ratio reduction in the sediments above the eastern diapir is maximum immediately above the crest of the salt structure and where the faults reach the seafloor.

A stress profile has been extracted along the crest of the salt structure (W profile in Fig. 11a) in order to compare geomechanical stress results with uniaxial stresses along a sediment column having the same burial depth (Fig. 11b). The uniaxial vertical effective stress (dashed lines in Fig. 11b) is calculated from the overburden weight of sediments and assigned pore pressure (equation 1). Then, the horizontal effective stress is calculated using the initial stress ratio (equation 3). We find that the geomechanical horizontal stress (solid green line in Fig. 11b) is consistently lower than its uniaxial value and decreases notably within 1 km from the crest of the salt structure, with a maximum difference of around 4.5 MPa at the salt–sediment interface. This reduction is consistent with the stress ratio reduction

near the crest of the eastern diapir (Fig. 11a) and illustrates the effect of the extensional strains on sediment stress. The vertical stress predicted by the geomechanical model (solid blue line in Fig. 11b) remains close to the uniaxial value, with a slight increase just above the salt.

Sensitivity analysis

Similar to the 3D model, a 2D model sensitivity analysis has been performed to assess the influence of the different model assumptions over the final results. In addition to changes in elastic parameters, other structural framework changes have been tested using 2D models (Table 4) that were too complex to test in 3D, due to limitations of computational power and time availability. Performing these additional changes and studying their impact on the final results provides insights into the main mechanisms that change stress and strain in the salt basin.

Changes in the shale elastic parameters resulted in less than 0.01% variation in the magnitude of stress relative to the base-case 2D model. The magnitude of stress changes is 10 times greater than that seen in the 3D sensitivity analysis models; however, both changes are insignificant. Hence, changing the elastic parameters within reasonable values does not affect the overall results.

Substitution of salt with shale in all three diapirs allows us to explicitly see the contribution of salt creep in the stress and strain changes across the model. Stresses along vertical profile W (Fig. 11a) remain uniaxial when the salt volumes are assigned the shale rheology (Fig. 11b). This confirms that the decrease in horizontal stress (solid green line in Fig. 11b) and stress ratio (blue contours above eastern diapir in Fig. 11a) result from the deformation of the salt (red arrows in Fig. 9).

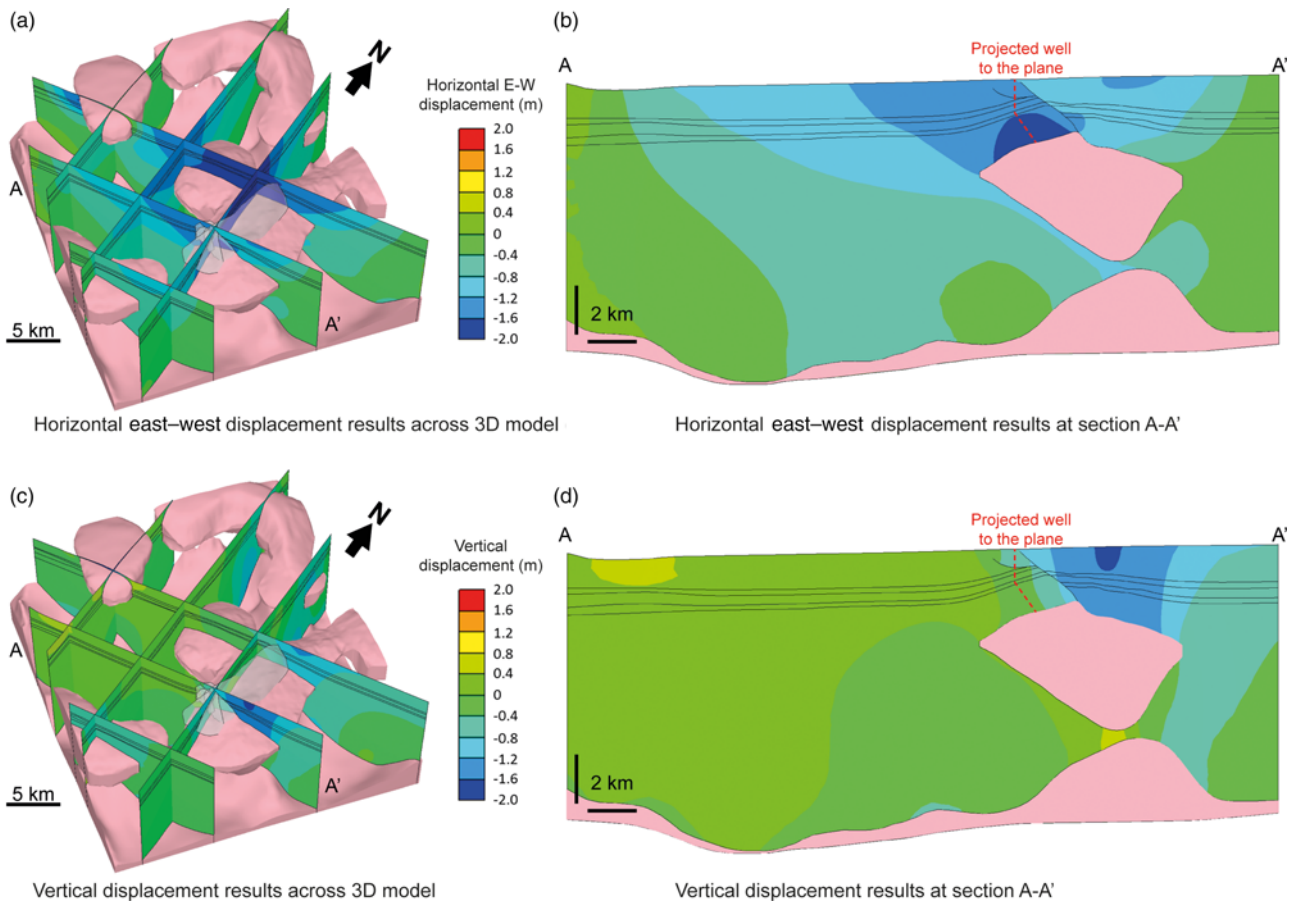


Fig. 7. (a) Horizontal east–west displacements across the model, showing mostly westwards displacements (blue contours) concentrated above the eastern diapir and around the major fault. (b) Horizontal east–west displacements for section A–A' (shown in a) passing near the well location, displaying greater westward displacements for the sediments in the footwall compared to the hanging wall. (c) Vertical displacements across the model, showing downwards movement (blue contours) in the hanging wall of the major fault. (d) Vertical displacements for section A–A' (shown in c) passing near the well location.

Defining a flat seafloor mainly changes the pattern of sediment displacements across the model. Sediment displacements are primarily westwards in the base-case model but they become vertical when the seafloor slope is removed.

A model without the central and western diapirs shows less horizontal stress reduction above the eastern diapir when compared to the base-case model. The displacements above the eastern diapir have the same distribution as the base case (Fig. 9) but with a lower magnitude on its western side. In other words, the presence of the other diapirs translates to higher westwards displacements across the model.

Finally, increasing the width of the salt columns that connect the salt source layer with the diapirs has a low influence in the final stress field.

Discussion

Stress reduction mechanism

The stress results from both the 3D and 2D models show a horizontal stress reduction located at the crest of the eastern diapir. In addition, both models agree on the two different displacement patterns seen above the eastern diapir (Figs 7 and 9):

- A significant downwards component of displacement in the hanging wall (eastern side of the main fault) caused by the salt withdrawal below.
- A westwards displacement in both the salt and the footwall sediments of the main fault.

This differential movement causes extensional horizontal strain above the diapir (Fig. 10). This extension is directly linked to the

horizontal stress reduction and, hence, the stress ratio reduction seen both in the 3D model and the 2D model (Figs 5 and 11). Furthermore, it is manifested by the faults located above the diapir.

When the salt lithology in the 2D model is replaced by shale, the lateral strain and the stress reduction are not present (Fig. 11b). From this we conclude that the difference in rock properties between the salt and the encasing sediments is one of the main drivers of the reduction in horizontal stress above the salt body.

In addition, the two different displacement patterns above the eastern diapir causing the extension of the sediments at the crest are not present when the seafloor is horizontal. This demonstrates that the seafloor geometry also drives the stress reduction above salt.

During the drilling operations of the exploratory well, the stress reduction was validated with data from formation integrity test (FIT) and leak-off test (LOT) measurements (Fig. 12). Detection of drilling-induced tensile fractures (DITF) at a depth of 2600 m allowed an additional estimation of the minimum horizontal stress (green dots in Fig. 12), which agrees with the LOT data and confirms the stress reduction.

Horizontal stress reduction and lateral extensional strains in sediments above diapirs has been observed in geomechanical models using both idealized geometries (Luo *et al.* 2012; Nikolinaou *et al.* 2012) and actual salt geometries (Barnichon *et al.* 1999; Segura *et al.* 2016). Other authors reported the presence of normal faults in the sediments above salt structures (Davis *et al.* 2000; Dusseault *et al.* 2004), indicating extensional regimes in these areas. Dusseault *et al.* (2004) also reported an area of exceptionally low values of minimum horizontal stress in an anticlinal structure above a Gulf of Guinea salt dome.

3D/2D geomechanical modelling comparison: Tarfaya

Table 3. Statistical summary of sensitivity analysis results, reporting comparison ratio S (equation 6)

		σ_1	σ_2	σ_3	East-west displacement	North-south displacement	Vertical displacement
Increase ν	Average	-4.45×10^{-5}	7.34×10^{-5}	-1.70×10^{-5}	1.02×10^{-3}	7.06×10^{-4}	-3.87×10^{-3}
	Median	-2.40×10^{-5}	-2.70×10^{-5}	-2.00×10^{-6}	2.08×10^{-3}	4.18×10^{-4}	8.60×10^{-5}
	SD	5.07×10^{-3}	3.02×10^{-3}	1.86×10^{-3}	0.02	0.04	0.06
	Points omitted (%)	1.80×10^{-3}	2.28×10^{-4}	0	0.04	0.13	0.47
Decrease ν	Average	3.02×10^{-5}	-5.09×10^{-5}	-9.71×10^{-7}	-2.75×10^{-4}	-1.97×10^{-3}	3.42×10^{-3}
	Median	6.00×10^{-6}	4.00×10^{-6}	-1.00×10^{-6}	-9.10×10^{-4}	-1.10×10^{-5}	-1.07×10^{-4}
	SD	2.43×10^{-3}	1.26×10^{-3}	6.44×10^{-4}	0.01	0.03	0.04
	Points omitted (%)	4.06×10^{-4}	5.07×10^{-5}	0	0.02	0.08	0.20
Increase E	Average	-3.62×10^{-5}	-3.34×10^{-4}	-7.21×10^{-5}	0.15	0.12	0.18
	Median	9.10×10^{-5}	-3.71×10^{-4}	3.90×10^{-5}	0.16	0.16	0.15
	SD	0.02	6.84×10^{-3}	3.14×10^{-3}	0.04	0.09	0.11
	Points omitted (%)	0.02	2.46×10^{-3}	0	0.15	0.83	1.31
Decrease E	Average	-4.19×10^{-5}	4.02×10^{-4}	6.03×10^{-5}	-0.21	-0.15	-0.30
	Median	-2.24×10^{-4}	5.37×10^{-4}	-4.70×10^{-5}	-0.22	-0.22	-0.21
	SD	0.02	7.90×10^{-3}	3.87×10^{-3}	0.06	0.12	0.14
	Points omitted (%)	0.03	3.35×10^{-3}	0	0.25	1.43	2.42

2D v. 3D modelling comparison

Comparison of results from the 3D and the 2D models allow us to identify differences in prediction and to investigate whether 2D modelling – despite its simplifications – can still represent stresses in the salt basin adequately.

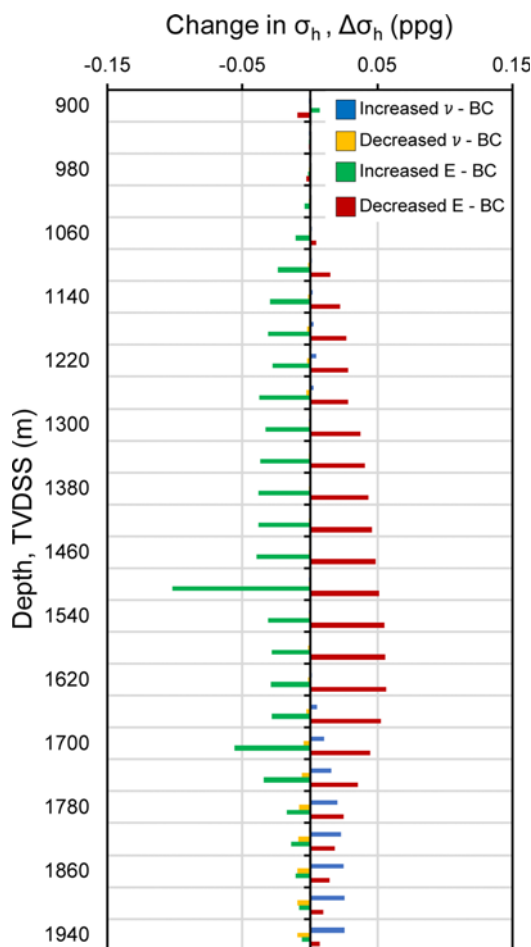


Fig. 8. The difference in the prediction of horizontal stress, σ_h , between sensitivity analysis and base-case models along the first 1000 m of the exploration well. The major difference is obtained when varying the elastic modulus, but it does not exceed 0.15 ppg. This indicates little effect of the elastic parameter variation on horizontal stress. TVDSS, true vertical depth subsea.

We have found that both 3D and 2D models predict a reduction in the stress ratio above the salt crest. However, the area of low stress ratio is broader and extends shallower in the 2D model (Fig. 11) than in the 3D model (Fig. 5). Only at the salt crest do both modelling approaches predict the same value (stress ratio of 0.6, reduced from the initial value of 0.8). We also found that the direction of displacements in the sediments above the salt structure is consistent between the 3D and 2D models (Figs 7 and 9). In both cases, the footwall has greater westward displacements than the hanging wall. At the same time, the hanging wall has a greater downwards displacement than the footwall. Although displacements are qualitatively similar, the 2D model consistently predicts higher magnitudes than the 3D model.

Elastic theory can explain why the 2D model predicts broader areas of decreased horizontal stress and higher magnitudes of sediment displacement above salt than the 3D model. We use elastic solutions for stress distribution resulting from a load applied on a semi-infinite, elastic, isotropic and homogeneous medium (Boussinesq 1885). Specifically, we compare the vertical stress distribution with depth caused by the application of a strip load (infinite out-of-plane length) with that of a circular load (Fig. 13). Both loads result in the same

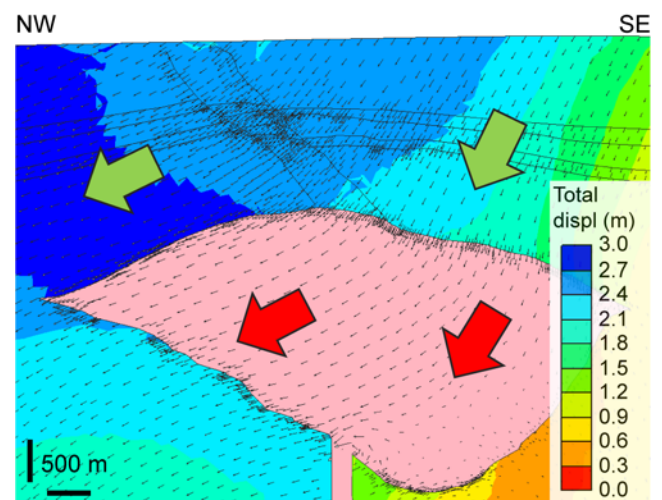


Fig. 9. Displacements of salt at the eastern diapir and the sediments encasing it. Salt displacements (red arrows) show a downwards movement for the eastern side of the diapir and a westwards movement for its western side. Sediment displacements above the diapir (green arrows) follow a pattern similar to the salt displacements. Colour contours indicate magnitudes of displacements for the sediments.

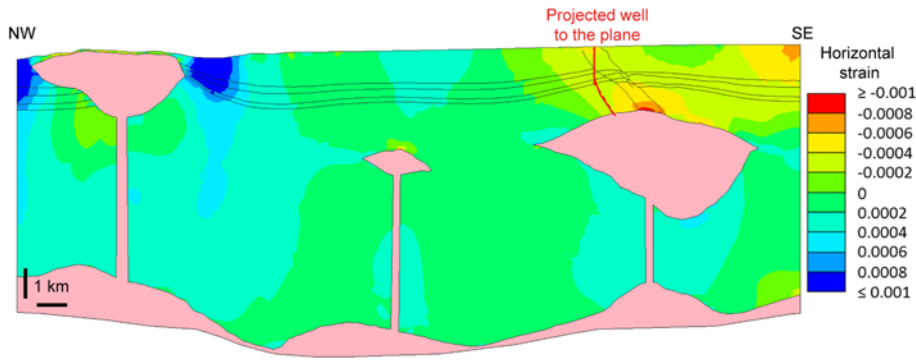


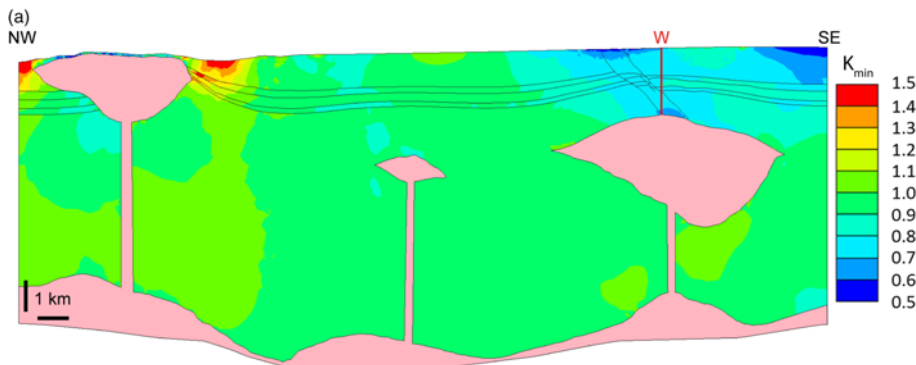
Fig. 10. Horizontal strain across the 2D model. Red contours represent extensional strains and blue contours represent shortening strains. A region of extensional horizontal strain develops at the crest of the eastern diapir, between the two faults. Shortening horizontal strains develop at both sides of the western diapir.

applied stress q . The width of the strip load, B , is equal to the diameter of the circular load (Fig. 13). The strip and circular case represent a 2D plane strain and a 3D axisymmetrical load, respectively. Elastic theory shows that the vertical stress perturbation caused by the application of the strip load (equivalent to the plane-strain model) is broader than the application of circular load (equivalent to the axisymmetrical model); the circular load generates a stress perturbation that is more localized and dissipates faster with distance. For example, if we consider a value of $B = 1$ m and an applied stress $q = 1$ MPa m⁻¹, then at a distance of 6 m from the load application surface the vertical stress is 0.1 MPa for the strip-load case (red dot in Fig. 13) but only 0.015 MPa for the circular-load case (blue dot in Fig. 13).

In our geomechanical models, loading is applied by the salt (in the form of imposed strain). Hence, for a simplified application,

we consider the width of the salt crest to be the loading area (equivalent to B in Fig. 13). The 2D model is analogous to the strip-load case in Figure 13 because it is plane strain, which corresponds to an infinitely long salt wall. Similarly, the 3D model can be compared to the circular load from Figure 13 because the salt geometry in 3D is relatively circular (Fig. 3). Based on Boussinesq's elastic theory, the 3D salt load should result in a smaller region of stress changes, closer to the crest (i.e. the location of load application). Indeed, this is consistent with our geomechanical results (Fig. 14).

The difference between the 2D and 3D models is further illustrated by plotting the horizontal stress change (equation 7), against the depth normalized by the depth of the salt crest, H (Fig. 15) for both models along vertical profile W for the 2D model



K_{min} results for the 2D model

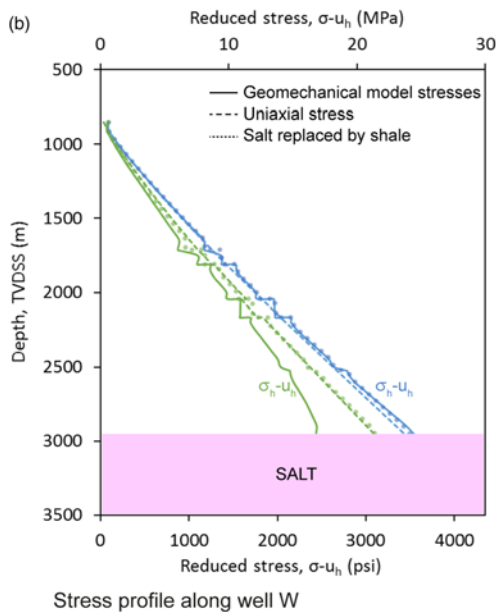


Fig. 11. (a) Horizontal to vertical stress ratio predicted by the 2D model. The ratio changes near the salt structures compared to its initial value of 0.8 (green contours). Specifically, it decreases above the eastern diapir, reaching values of around 0.6. (b) Geomechanical prediction (solid lines) for horizontal (green) and vertical (blue) stress along a vertical profile W compared with uniaxial stresses (dashed lines) and a model where salt is replaced by shale (dotted lines). Geomechanical horizontal stress is lower than uniaxial, reaching a maximum difference of 4.5 MPa at the salt-sediment interface. When salt is replaced by shale, there is no stress reduction and stresses are close to uniaxial conditions. TVDSS, true vertical depth subsea.

3D/2D geomechanical modelling comparison: Tarfaya

Table 4. Summary of the sensitivity analysis run for the 2D static model

Variable changed	Original value	Modified value
Poisson's ratio	0.3	0.25 0.4
Young modulus	Horizon- and depth-dependent (Table 1)	Increased 20% Decreased 20%
Salt replaced by shale	Salt	Shale
Flattened seafloor	1° seafloor slope	Horizontal seafloor
Number of diapirs	3	1 (eastern diapir)
Width of salt columns (m)	200	400

and W' for the 3D model (Fig. 14):

$$\Delta\sigma'_h = \sigma'_{h, \text{initial}} - \sigma'_{h, \text{model}} \quad (7)$$

Both models predict a horizontal stress reduction of around 4.5 MPa at the crest of the salt structure. However, the 2D model predicts a higher horizontal stress reduction along the vertical profile, reaching a maximum difference of 1.5 MPa from the 3D model at 80% of the crest depth. In the 3D model, the horizontal stress change becomes 0 at half the crest depth. At the same depth, the 2D horizontal stress reduction is 0.7 MPa. In fact, the salt influence in the 2D model extends along two-thirds of the vertical profile, up to 30% of the crest depth. Note that this difference between the 2D and 3D geomechanical results would be less if the simulated structure resembled more closely a salt wall.

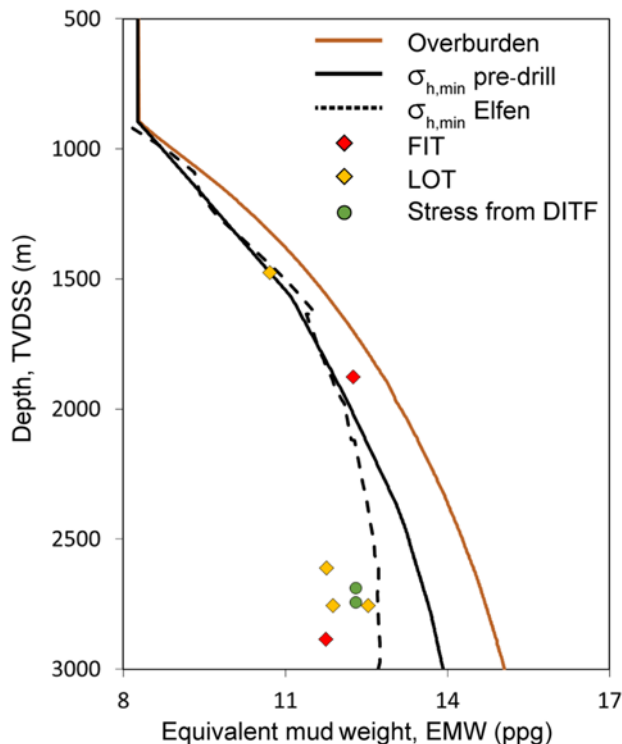


Fig. 12. Profile along the exploration well (Fig. 3) comparing minimum horizontal stress, σ_h , from the pre-drill study (solid black line) with σ_h predicted by the 3D model (dashed black line). The decrease in σ_h near the salt interface (at 3000 m) predicted by the 3D model was validated by data obtained during the drilling operations, including leak-off test (LOT) measurements, formation integrity test (FIT) measurements and the drilling-induced tensile fractures (DITF) observed (yellow, red and green dots, respectively). Overburden stress, σ_v , is shown with a solid orange line. TVDSS, true vertical depth subsea.

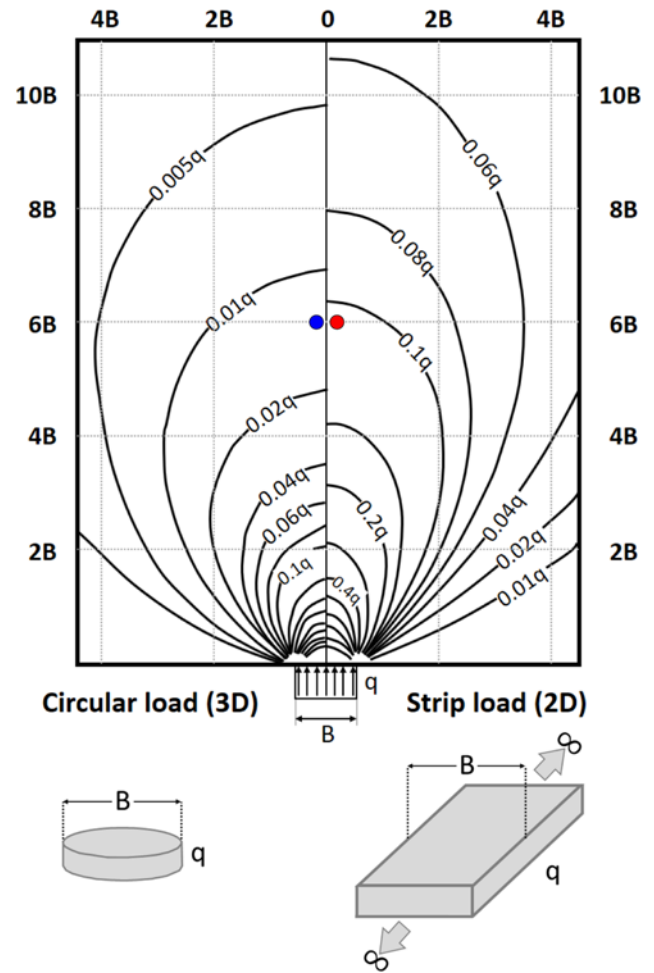


Fig. 13. Illustration of the solution for the vertical stress distribution in an elastic, semi-infinite medium caused by the application of a 2D load (represented as a strip load) and a 3D load (represented as a circular load) using the solution from Boussinesq (1885). There is no gravity load. Blue and red dots correspond to the values of vertical stress at 6 m from the load for the 3D and 2D cases, respectively, where $B = 1$ m and $q = 1$ MPa m^{-1} . Modified from US Army Corps of Engineers (1990).

Input uncertainty and limitations

Sensitivity analysis allowed us to quantitatively compare the effect of different model assumptions. We found that a change in the elastic parameters had no significant effect in both the 2D and 3D models. Parameters that have a larger impact on the stress distribution in this study are:

- the presence of salt lithology (9%);
- the presence of other salt diapirs in the 2D section (7%);
- the seafloor slope which imposes a differential load across the width of the model (4%);
- the connection between the diapirs and the autochthonous salt source layer (3%).

The percentage indicated for each scenario represents the change in stress relative to the base case.

These are interesting fundamental observations that should be considered when designing a geomechanical model and given greater weight than the elastic properties of the sediments.

In this study, we focus on the understanding and comparison of 3D and 2D geomechanical static model approaches. This study can be improved in various ways:

- We assume these models are drained; hence, the effect of salt movement on pore-pressure generation is not considered.

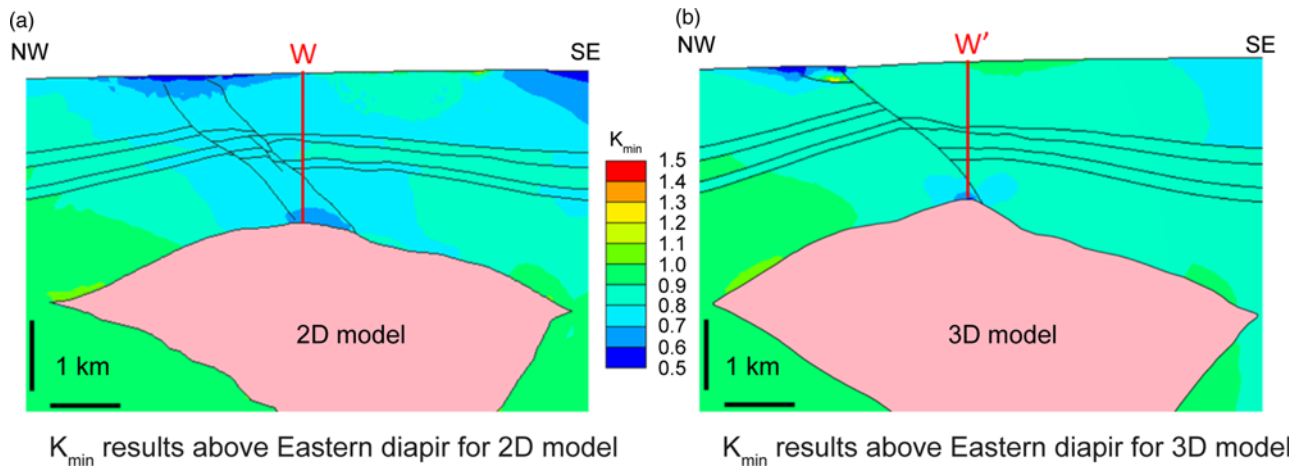


Fig. 14. Horizontal to vertical stress ratio predicted for sediments above the eastern diapir for (a) the 2D model and (b) the 3D model. Both models present a reduction in the stress ratio of about 0.6 at the crest of the structure compared with the initial 0.8. However, the reduction in the 2D model affects a broader area above the diapir. Vertical profiles W and W' are used to quantitatively compare the stress change between the 2D and 3D models (Fig. 15).

Coupling porous fluid flow with salt deformation in our models would provide a more complete prediction of stress, strain and pore pressure.

- Sediments are modelled to behave as poroelastic materials. One of the conclusions of the sensitivity analysis is the low impact of elastic properties over the results. Hence, a simpler elastic model other than equation (5) could be used.
- Introducing plasticity and frictional strength in the sediment description will result in more realistic displacements and can help to detect regions where the material is close to failure.
- One set of frictional properties were assumed for the faults. A sensitivity analysis of these frictional parameters would help to better understand the interrelation between salt deformation and sediment stress reduction.

- The temperature gradient used in the 3D and 2D models has not been varied during the sensitivity analysis. This is because a variation in temperature would mainly affect the viscosity of the salt lithology and, hence, the time needed for the static model to converge to a solution. Temperature effects become more important in evolutionary models of salt systems.

In fact, the introduction of evolutionary geomechanical modelling can help in studying the complete stress–strain history through time. Our models are static and assume an initial stress distribution that changes when the salt moves. An evolutionary approach would forego this initial assumption, and would provide a complete evolution of the salt structures and how this evolution affects the basin stresses. Nonetheless, our study presents an explanation for the stress and strain changes due to the presence of salt in the Tarfaya Basin and provides considerations for deciding between a 2D and a 3D approach.

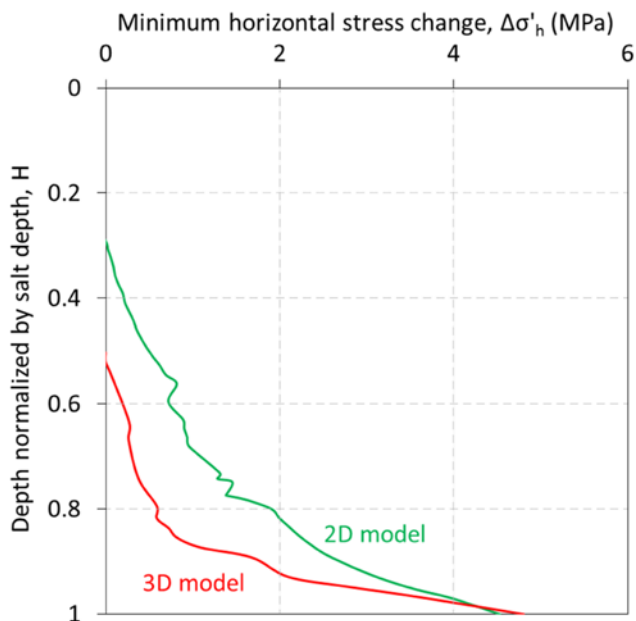


Fig. 15. Horizontal stress change with depth normalized by salt depth for both 2D (green line) and 3D (red line) models along vertical profiles W and W' (Fig. 14) above the salt body. The stress perturbation due to salt attenuates faster with distance from the salt body in the 3D model compared to the 2D case.

Summary

We developed a 3D model of the Tarfaya salt basin, on the West African coast. We focused on a salt structure where an exploratory well was later drilled. We found a decrease in horizontal stress near the crest of the salt and rotation of the horizontal principal stresses. Sensitivity analysis performed on the elastic parameters for the different shale horizons showed a negligible impact on the final results. In addition, we detected higher horizontal east–west displacements at the footwall of the major fault above the salt structure and higher vertical displacements at its hanging wall.

A 2D section was built from the 3D geometry to intersect the salt and exploration well. The stress results from the 2D model show a similar horizontal stress reduction. The 2D model, however, predicts a broader area of stress perturbation above the salt. Overall comparison between the 3D and 2D models show that the 2D model overestimates both stress changes and displacements in areas above the salt. A quantitative comparison between the models along a vertical well passing through the salt crest shows that the extent of salt influence on suprasalt sediments is 20% shallower in the 2D model: sediments located at the shallower half of the vertical profile in the 3D model do not experience any stress change, whereas in the 2D model there is still 0.7 MPa of stress reduction (16%) in the middle of the vertical profile. This is due to the fact that a plane-strain 2D model misrepresents the stress changes caused by a 3D loading.

3D/2D geomechanical modelling comparison: Tarfaya

The 2D model allows for a more exhaustive sensitivity analysis thanks to the considerably reduced number of elements present and the computational power required. We found that the difference in rock rheology between the salt and the encasing sediments is one of the main drivers of stress changes. As such, attention should be given to the definition of the salt geometry.

In conclusion, we found that a 2D model of the prospect is a valid alternative to the more complex and time-consuming 3D modelling. The insights provided by the 2D model can be used to obtain stress and strain information in an early exploration stage despite the overestimation in their magnitude and extent. A 2D approach would be more accurate for a prospect with salt walls or elongated diapirs. On the other hand, 2D models would overestimate stress and strain in prospects with more circular salt bodies. In such cases, a 3D model may be considered as a better approach.

Acknowledgements We are grateful to Repsol for granting access to the data for this study. We would also like to thank Rockfield for their support in the modelling using ELFEN licences and their cluster for the 3D sensitivity analysis. We thank Dr Kevin J. Smart, Dr Christopher Beaumont, as well as the co-editor, Dr Rajesh Goteti, for their thoughtful corrections.

Funding This work is funded by Repsol Exploración S.A.

Author contributions JJH: Writing – Original Draft (Lead), Writing – Review & Editing (Equal); TWDH: Supervision (Lead), Validation (Lead), Writing – Review & Editing (Equal); MAN: Supervision (Lead), Validation (Lead), Writing – Review & Editing (Equal); OF: Writing – Review & Editing (Equal); AM: Writing – Review & Editing (Equal).

Appendix A. Nomenclature

Table A1. Nomenclature

Symbol	Name	Dimensions
E	Elastic (Young's) modulus	$L^{-1}M^1T^{-2}$
K_H	Maximum initial stress ratio	$L^0M^0T^0$
K_h	Minimum initial stress ratio	$L^0M^0T^0$
n	Porosity	$L^0M^0T^0$
p'	Mean effective stress	$L^{-1}M^1T^{-2}$
S	Comparison ratio (equation 6)	$L^0M^0T^0$
λ	Normalized horizontal stress change ratio	$L^0M^0T^0$
ν	Poisson's ratio	$L^0M^0T^0$
ρ_b	Bulk density	$L^{-3}M^1T^0$
ρ_s	Density of sediments	$L^{-3}M^1T^0$
ρ_w	Density of fluid	$L^{-3}M^1T^0$
σ	Effective stress	$L^{-1}M^1T^{-2}$
σ_v	Vertical stress	$L^{-1}M^1T^{-2}$
σ_H	Maximum horizontal stress	$L^{-1}M^1T^{-2}$
σ_h	Minimum horizontal stress	$L^{-1}M^1T^{-2}$
σ_1	Maximum principal stress	$L^{-1}M^1T^{-2}$
σ_2	Intermediate principal stress	$L^{-1}M^1T^{-2}$
σ_3	Minimum principal stress	$L^{-1}M^1T^{-2}$

Appendix B. Material input

Table B1. Input material parameter values for poroelastic sediments (sands and shales)

	E_{ref} (MPa)	A (MPa)	B (MPa)	r	c
Shallow shales (S1)	100	-1	-1	0.4	-2.1
Sands (R1)	2500	-1	-1	0	0
Intermediate shales (S2)	2800	-1	-1	0	0
Sands (R2)	3100	-1	-1	0	0
Deep shales (S3)	150	-1	-1	0.55	-1.4

Table B2. Input material parameter values for the viscoplastic Munson–Dawson model (Munson 1997; Fredrich et al. 2007a)

Parameter	Units	Value
E	MPa	31 000
ν		0.25
ρ	$kg\ m^{-3}$	2100
A_1	1/s	5.95×10^{22}
N_1		5.5
Q_1	cal/mol	25 000
A_2	1/s	$6.87E \times 10^{12}$
N_2		5
Q_2	cal/mol	10 000
R	cal/°K/mol	1.987
T_0	°K	0
T_{const}	°K	273
G_0	MPa	12 400
dG/dT	MPa/°K	10

References

- Adachi, J., Nagy, Z.R., Sayers, C.M., Smith, M. & Becker, D.F. 2012. Drilling adjacent to salt bodies: Definition of mud weight window and pore pressure using numerical models and fast well planning tool. Paper SPE-159739 presented at the SPE Annual Technical Conference and Exhibition, 8–10 October 2012, San Antonio, Texas, USA, <https://doi.org/10.2118/159739-MS>
- Barnichon, J.D., Havenith, H., Hoffer, B., Charlier, R., Jongmans, D. & Duchesne, J.C. 1999. The deformation of the Egersund-Ogna anorthosite massif, south Norway: Finite-element modelling of diapirism. *Tectonophysics*, **303**, 109–130, [https://doi.org/10.1016/S0040-1951\(98\)00247-9](https://doi.org/10.1016/S0040-1951(98)00247-9)
- Beltrao, R.L.C., Sombra, C.L., Lage, A.C.V.M., Fagundes Netto, J.R. & Henriques, C.C.D. 2009. Challenges and new technologies for the development of the pre-salt cluster, Santos Basin, Brazil. Paper presented at the Offshore Technology Conference, 4–7 May 2009, Houston, Texas, USA, <https://doi.org/10.4043/19880-MS>
- Boussinesq, M.J. 1885. *Applications Des Potentiels à l'étude de l'équilibre et Du Mouvement Des Solides Élastiques*. L. Danel, Lille, France.
- Bradley, W.B. 1978. Bore hole failure near salt domes. Paper SPE-7503 presented at the SPE Annual Fall Technical Conference and Exhibition, 1–3 October 1978, Houston, Texas, USA.
- Carracedo, J.C. & Perez-Torrado, F.J. 2013. Geological and geodynamic context of the Teide Volcanic Complex. In: Carracedo, J.C. & Troll, V.R. (eds) *Teide Volcano. Geology and Eruptions of a Highly Differentiated Oceanic Stratovolcano*. Active Volcanoes of the World. Springer, Berlin, https://doi.org/10.1007/978-3-642-25893-0_2
- Davis, T., Warner, M., Elders, C. & Davison, I. 2000. Tertiary faulting patterns and growth history of Central Graben salt diapirs. Paper presented at the Canadian Society of Exploration Geophysicists Annual Meeting.
- Dusseault, M.B., Maury, V. & Sanfilippo, F. 2004. Drilling around salt: Stresses, risks, uncertainties. Paper 04-647 presented at Gulf Rocks 2004, the 6th North America Rock Mechanics Symposium (NARMS), 5–9 June 2004, Houston, Texas, USA.
- Fredrich, J.T., Coblenz, D., Fossum, A.F. & Thorne, B.J. 2003. Stress perturbations adjacent to salt bodies in the deepwater Gulf of Mexico. Paper SPE-84554 presented at the SPE Annual Technical Conference and Exhibition, 5–8 October 2003, Denver, Colorado, USA, <https://doi.org/10.2118/84554-MS>
- Fredrich, J.T., Engler, B.P., Smith, J.A., Onyia, E.C. & Tolman, D.N. 2007a. Predrill estimation of subsalt fracture gradient: Analysis of the spa prospect to validate nonlinear finite element stress analyses. Paper SPE-105763 presented at the SPE/IADC Drilling Conference, 20–22 February 2007, Amsterdam, The Netherlands, <https://doi.org/10.2118/105763-MS>
- Fredrich, J.T., Fossum, A.F. & Hickman, R.J. 2007b. Mineralogy of deepwater Gulf of Mexico salt formations and implications for constitutive behavior. *Journal of Petroleum Science and Engineering*, **57**, 354–374, <https://doi.org/10.1016/j.petrol.2006.11.006>
- Goteti, R., Ings, S.J. & Beaumont, C. 2012. Development of salt minibasins initiated by sedimentary topographic relief. *Earth and Planetary Science Letters*, **339–340**, 103–116, <https://doi.org/10.1016/j.epsl.2012.04.045>
- Gouiza, M. 2011. *Mesozoic source-to-sink systems in NW Africa: Geology of vertical movements during the birth and growth of the Moroccan rifted margin*. PhD thesis, VU University Amsterdam, Amsterdam, The Netherlands.
- Heidari, M., Nikolinkou, M.A. & Flemings, P.B. 2018. Coupling geomechanical modeling with seismic pressure prediction. *Geophysics*, **83**, 1–54, <https://doi.org/10.1190/geo2017-0359.1>
- Luo, G., Nikolinkou, M.A., Flemings, P.B. & Hudec, M.R. 2012. Geomechanical modeling of stresses adjacent to salt bodies: Part 1 – Uncoupled models. *AAPG Bulletin*, **96**, 43–64, <https://doi.org/10.1306/041111010144>
- Luo, G., Hudec, M.R., Flemings, P.B. & Nikolinkou, M.A. 2017. Deformation, stress, and pore pressure in an evolving suprasalt basin. *Journal of Geophysical Research: Solid Earth*, **122**, 5663–5690, <https://doi.org/10.1002/2016JB013779>

- Meyer, D., Zarra, L., Rains, D., Meltz, B. & Hall, T. 2005. Emergence of the Lower Tertiary Wilcox trend in the deepwater Gulf of Mexico. *World Oil*, **226**, 72–77.
- Munson, D.E. 1997. Constitutive model of creep in rock salt applied to underground room closure. *International Journal of Rock Mechanics and Mining Sciences & Geomechanics Abstracts*, **34**, 233–247, [https://doi.org/10.1016/S0148-9062\(96\)00047-2](https://doi.org/10.1016/S0148-9062(96)00047-2)
- Munson, D.E. & Dawson, P.R. 1979. *Constitutive Model for the Low Temperature Creep of Salt (with Application to WIPP)*. SAND79-1853. Sandia National Laboratories, Albuquerque, NM, USA.
- Nikolinakou, M.A., Luo, G., Hudec, M.R. & Flemings, P.B. 2012. Geomechanical modeling of stresses adjacent to salt bodies: Part 2 – Poroelastoplasticity and coupled overpressures. *AAPG Bulletin*, **96**, 65–85, <https://doi.org/10.1306/04111110143>
- Nikolinakou, M.A., Hudec, M.R. & Flemings, P.B. 2014. Comparison of evolutionary and static modeling of stresses around a salt diapir. *Marine and Petroleum Geology*, **57**, 537–545, <https://doi.org/10.1016/j.marpetgeo.2014.07.002>
- Nikolinakou, M.A., Heidari, M., Flemings, P.B. & Hudec, M.R. 2018. Geomechanical modeling of pore pressure in evolving salt systems. *Marine and Petroleum Geology*, **93**, 272–286, <https://doi.org/10.1016/j.marpetgeo.2018.03.013>
- Orlic, B. & Wassing, B.B.T. 2013. A study of stress change and fault slip in producing gas reservoirs overlain by elastic and viscoelastic caprocks. *Rock Mechanics and Rock Engineering*, **46**, 421–435, <https://doi.org/10.1007/s00603-012-0347-6>
- Rimi, A. 2001. Carte du gradient géothermique au Maroc. *Bulletin de l'Institut Scientifique, Rabat*, **23**, 1–6.
- Rockfield. 2017. *Elfen Explicit Manual (Version 4.10)*. Software. Rockfield, Swansea, UK.
- Segura, J.M., Matos da Cruz, A., Stachlewski, G., Alvarelos, J., Vargas, P.E. & Lakshmikantha, M.R. 2016. Fault stability assessment for well planning: a case study related to salt structures. Paper 16-518 presented at the 50th US Rock Mechanics/Geomechanics Symposium, 26–29 June 2016, Houston, Texas, USA.
- Seymour, K.P., Rae, G., Peden, J.M. & Ormston, K. 1993. Drilling close to salt diapirs in the North Sea. *Offshore Europe*, 193–204, <https://doi.org/10.2118/26693-MS>
- Sweatman, R., Faul, R. & Ballew, C. 1999. New solutions for subsalt-well lost circulation and optimized primary cementing. Paper SPE-26693 presented at SPE Offshore Europe, 7–10 September 1999, Aberdeen, UK.
- Tari, G. & Jabour, H. 2013. Salt tectonics along the Atlantic margin of Morocco. In: Mohriak, W.U., Danforth, A., Post, P.J., Brown, D.E., Tari, G.C., Nemčok, M. & Sinha, S.T. (eds) *Conjugate Divergent Margins*. Geological Society, London, Special Publications, **369**, 337–353, <https://doi.org/10.1144/SP369.23>
- Thigpen, J.R., Roberts, D., Snow, J.K., Walker, C.D. & Bere, A. 2019. Integrating kinematic restoration and forward finite element simulations to constrain the evolution of salt diapirism and overburden deformation in evaporite basins. *Journal of Structural Geology*, **118**, 68–86, <https://doi.org/10.1016/j.jsg.2018.10.003>
- US Army Corps of Engineers. 1990. *Engineering and Design: Settlement Analysis*. Engineering Manual 1110-1-1904, CECW-EG. US Army Corps of Engineers, Department of the Army, Washington, DC, USA.
- van der Zee, W., Ozan, C., Brudy, M. & Holland, M. 2011. 3D geomechanical modeling of complex salt structures. Paper presented at the 2011 SIMULIA Customer Conference, 2011SCC, 17–19 May 2011, Barcelona, Spain.
- Warren, J.K. 2006. *Evaporites: Sediments, Resources and Hydrocarbons*. Springer, Dordrecht, The Netherlands, <https://doi.org/10.1007/3-540-32344-9>
- Wenke, A., Zühlke, R., Jabour, H. & Kluth, O. 2011. High-resolution sequence stratigraphy in basin reconnaissance: Example from the Tarfaya Basin, Morocco. *First Break*, **29**, 85–96.
- Yu, Y., Tang, L., Yang, W., Huang, T., Qiu, N. & Li, W. 2014. Salt structures and hydrocarbon accumulations in the Tarim Basin, northwest China. *AAPG Bulletin*, **98**, 135–159, <https://doi.org/10.1306/05301311156>
- Zarhloule, Y., Rimi, A., Boughriba, M., Barkaoui, A.E. & Lahrach, A. 2010. The geothermal research in Morocco: history of 40 years. In: *Proceedings of the World Geothermal Congress, 2010*. International Geothermal Association, Bonn, Germany, <http://www.geothermal-energy.org/pdf/IGAstandard/WGC/2010/0110.pdf>

Annex 2: Insights from sensitivity analysis of geomechanical modelling of a salt structure offshore west Africa

Insights from sensitivity analysis of geomechanical modelling of a salt structure offshore west Africa

Hooghvorst, J.J.

Facultat de ciències de la Terra, Universitat de Barcelona, Barcelona, Spain

Harrold, T.D.

Repsol Exploración S.A., Madrid, Spain

Nikolinakou, M.A.

The University of Texas at Austin, Austin, Texas, USA

Fernández, O.

University of Vienna, Vienna, Austria

Marcuello, A.

Facultat de ciències de la Terra, Universitat de Barcelona, Barcelona, Spain

Copyright 2019 ARMA, American Rock Mechanics Association

This paper was prepared for presentation at the 53rd US Rock Mechanics/Geomechanics Symposium held in New York, NY, USA, 23–26 June 2019. This paper was selected for presentation at the symposium by an ARMA Technical Program Committee based on a technical and critical review of the paper by a minimum of two technical reviewers. The material, as presented, does not necessarily reflect any position of ARMA, its officers, or members. Electronic reproduction, distribution, or storage of any part of this paper for commercial purposes without the written consent of ARMA is prohibited. Permission to reproduce in print is restricted to an abstract of not more than 200 words; illustrations may not be copied. The abstract must contain conspicuous acknowledgement of where and by whom the paper was presented.

ABSTRACT: We predict stresses in the Tarfaya salt basin on the West African Coast using a 3D static geomechanical model and compare the results against a 2D static plane-strain model built from a 3D transect. Both models are built using present-day geometries derived from a seismic survey. Models are drained and use poro-elastic material behavior for the sediments and viscoplastic behavior for the salt. We found that both models show a horizontal stress reduction above the salt diapir that was targeted by an exploratory well. These results were validated by the data coming from the posterior drilling of the well. The horizontal stress reduction predicted by both models reaches a magnitude of 4.5 MPa at the crest of the salt structure. However, the 2D model predicts a broader area of sediments affected by the stress reduction. Sensitivity analyses applied on the simpler, faster 2D model concludes that the elastic properties of the material modelled does not have a great impact on the final results. On the other hand, the presence of salt structures and the seafloor geometry are the key features that drive the stress changes in these models.

1. INTRODUCTION

A great number of hydrocarbon reservoirs in basins around the world are located near or below salt structures (Warren, 2006; Beltrao et al., 2009; Yu et al., 2014). This fact has led to a large number of drilling operations close to salt diapirs. The presence of salt structures may cause changes in the stress state and pore pressure distribution of the sediments encasing them (Luo et al., 2017; Nikolinakou et al., 2018). The resulting uncertainty of the stress and pressure state in this locations can cause difficulties during the drilling operations, leading to potential hazardous conditions and additional expenses (Sweatman et al., 1999; Dusseault et al., 2004).

In the last decade, geomechanical modelling has increasingly been used to reduce the uncertainty near salt. Several examples use 2D geomechanical models of actual salt geometries derived from seismic surveys (Fredrich et al., 2007b; Segura et al., 2016; Heidari et al., 2018). Other studies perform a full 3D geomechanical model of actual salt geometries (van der Zee et al., 2011; Adachi et al.,

2012; Segura et al., 2016). 2D models allow fast preliminary results but their plane-strain or axisymmetric simplification cannot represent the full three-dimensional stress changes caused by salt deformation. On the other hand, 3D models overcome the limitations of 2D cases at the expense of being computationally expensive and labor intensive.

We present a case study in the Tarfaya salt basin, located on the NW African coast, where a rank wildcat exploration well was planned to be drilled above a salt structure. A predrill 3D elastic static and drained geomechanical model was built using Elfen (Rockfield, 2017) to obtain a full stress and strain description around the salt structure. The model geometry was built using information from a seismic survey. Initial conditions (stress ratio, pore pressure, material properties) were defined using data from an offset well analysis. The 3D model results showed a significant horizontal stress reduction in the sediments above the salt structure, affecting the part of the well trajectory closest to salt. These results were later validated with data from the

drilling of the exploratory well. A 2D model was then build using a transect of the 3D geometry that included the exploration well. That allowed us to compare the results from both models and perform a more exhaustive sensitivity analysis of the input parameters. The 3D model sensitivity analysis only examined changes in the elastic properties of the shale materials present in the model. In contrast, the 2D sensitivity analysis included changes in diapir and seafloor geometry, presence or absence of salt and the same elastic properties changes performed in 3D.

Overall, we show a 3D vs 2D geomechanical comparison on an actual salt-related basin and perform sensitivity analysis for both models to identify the mechanism that drives the changes in stress and strain on this area.

2. MODEL DESCRIPTION

2.1. 3D model description

We use Elfen (Rockfield, 2017) to build a 3D geomechanical model based on a quasistatic, drained, finite-element formulation (Fig. 1a). It uses an unstructured finite element mesh containing 3.97 million linear tetrahedral elements, with a mesh size of 400 m. The boundary conditions applied restrict horizontal displacements at the four lateral sides of the model and restrict vertical displacements at its base. The pre-defined faults are modelled using double-sided discrete contact that allows sliding to occur along the faults as well as a stress redistribution. The faults use a Coulomb friction law.

The geometries for the salt and the sediment layers modelled are extracted from the interpretation of the seismic survey. The autochthonous and allochthonous salt structures are connected by 200 m wide salt columns that prevent any salt flow from the source layer (Fig. 1b).

The model is drained with an initial non-hydrostatic pore pressure profile. This profile assigns a constant overpressure for both sand reservoirs and for the deepest shales (Table 1). The initial stress state (Table 1) assumes that the maximum horizontal stress, σ_H , acts in the east-west direction due to basinward gliding of the sediments on the basal salt layer. Consequently, the minimum horizontal stress, σ_h , acts in the north-south direction. The initial minimum and maximum stress ratio, K_h and K_H , are defined as:

$$K_h = \frac{\sigma'_h}{\sigma'_v}, K_H = \frac{\sigma'_H}{\sigma'_v} \quad (1)$$

where σ'_v is the vertical effective stress, σ'_H is the maximum horizontal effective stress and σ'_h is the minimum horizontal effective stress. Values for K_h and K_H (Table 1) have been determined using offset well data. The salt structures have an initial stress ratio of one because they are assumed to have a uniform stress state.

Table 1: Summary of input properties for modelled horizons.

Horizons	ρ_s (Kg/m ³)	ρ_f (Kg/m ³)	Overpressure (MPa)	ν	Range of E (MPa)	K_h	K_H
1 st shale	2650	1025	-	0.3	290 - 2250	0.73	0.87
1 st sand	2650	1025	0.9	0.3	2500	0.77	0.89
2 nd shale	2650	1025	-	0.3	2800	0.80	0.90
2 nd sand	2650	1025	2.7	0.3	3100	0.75	0.88
3 rd shale	2600	1300	1.3	0.3	3650 - 50000	0.80	0.90

We model the shale and sand sediments with a poro-elastic constitutive model, calibrating the material parameters using offset well log data. The salt is modelled using a viscoplastic model that accounts for salt creep (Munson & Dawson, 1979). The material calibration is based on the Avery Island salt (Munson, 1997; Fredrich et al., 2007a), which – in the absence of field data – is considered to represent average salt behavior.

2.2. 2D model description

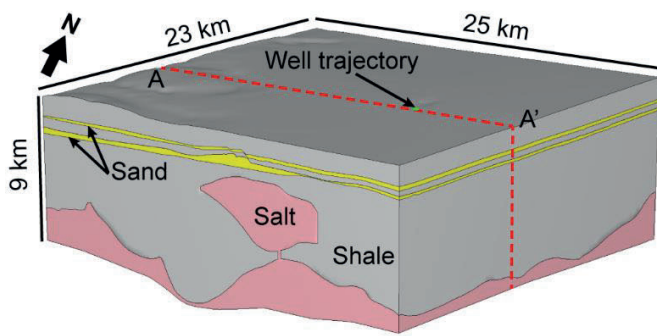
The geometry used to build the plane strain 2D model is extracted from a transect of the 3D geometry (Fig. 1a). This transect captures key elements from the 3D model such as the main diapir above the well, the well trajectory and faults crossing it, as well as two more diapirs located at the west (Fig. 1c).

The initial pore pressure profiles, initial stress ratios for each layer and the material properties used are the same in both 3D and 2D models, to allow a more consistent comparison of results. The boundary conditions applied restrict horizontal displacements at both sides of the model and both horizontal and vertical displacements at the base.

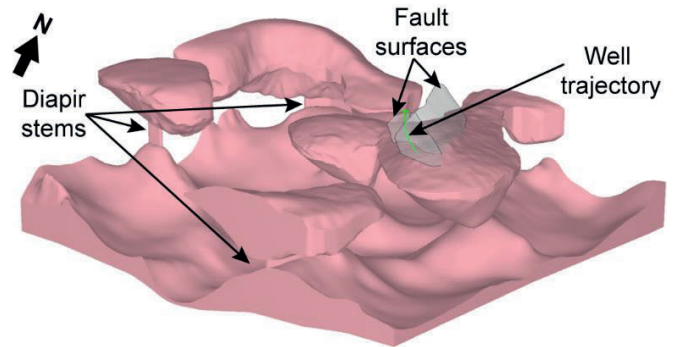
3. MODEL RESULTS

The results of stress and strain at the end of the simulation for both the 3D and 2D models represent the current day geomechanical conditions for the location modelled before the drilling of the well and the hydrocarbon extraction. Both models predict a decrease in the minimum stress ratio, K_{min} , (Fig. 2) for the sediments located above the eastern salt structure when compared with their initial values from Table 1. This decrease in the stress ratio is primarily caused by changes in the minimum horizontal stress.

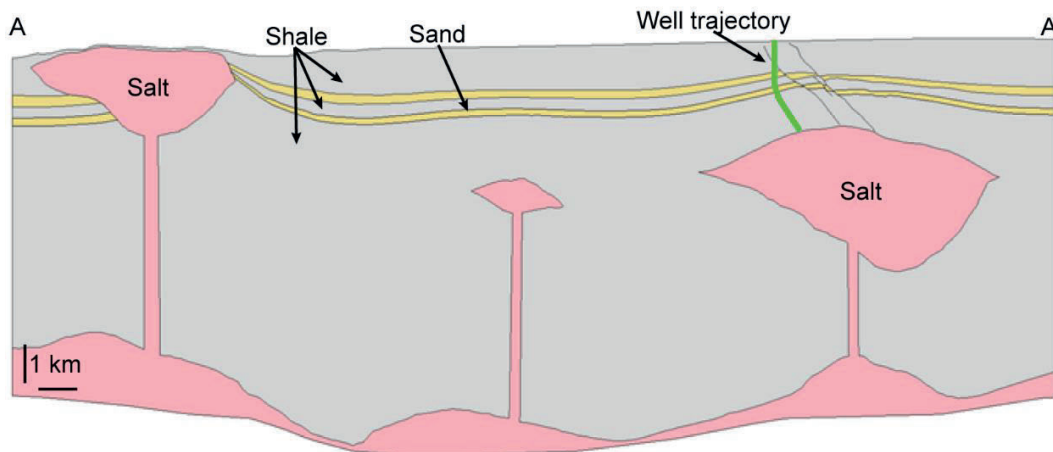
The 3D model shows a significant reduction of the minimum principal stress strongly localized both at the crest of the salt diapir and at the upper part of the faults, where these reach the seafloor (dark blue contours in Fig. 2a). According to Table 1, the value of initial K_h for the



(a) 3D model geometry

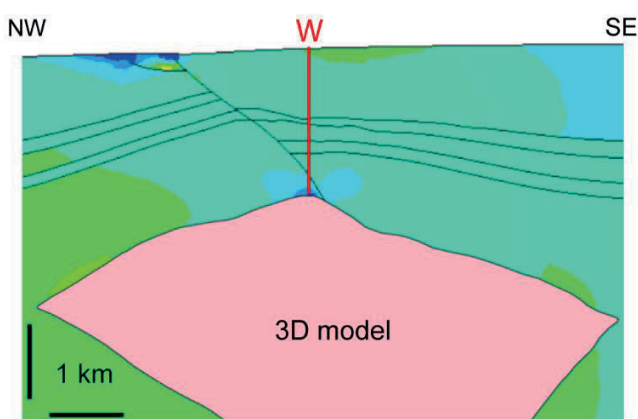


(b) Salt structure and faults within 3D model

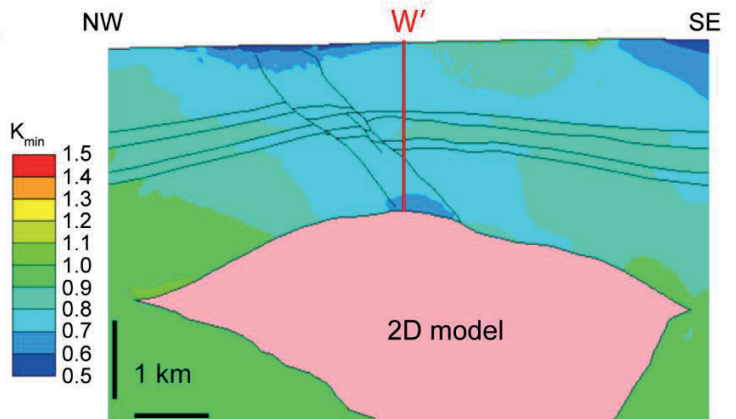


(c) 2D model geometry

Fig. 1: (a) Full 3D geomechanical model geometry, showing the salt (in pink), the sand reservoirs (in yellow), the shales (in gray) and the location of the exploratory well (green dot). The dashed red section labeled as A-A' shows the transect used to build the 2D model. (b) Geometry of the salt and the faults in the 3D model. (c) 2D model built from the geometry of the 3D A-A' transect.



(a) K_{min} results above Eastern diapir for 3D model



(b) K_{min} results above Eastern diapir for 2D model

Fig. 2: Minimum horizontal to vertical stress ratio predicted for the sediments above eastern diapir for (a) the 3D model and (b) the 2D model. Both models show a stress ratio reduction at the crest of the structure when compared with the initial value of 0.8. The reduction of the 2D model affects a broader area above the diapir. Vertical sections W and W' are used to quantitatively compare the stress changes between models in Fig. 3.

deepest shales is 0.8 and 0.73 for the shallowest shales. The stress ratio results imply a reduction of 0.2 at both locations, reaching values of 0.6 at the salt crest and 0.5 at the seafloor.

On the 2D model case, the reduction is maximum approximately at the same locations as the 3D case (dark blue contours in Fig. 2b). The magnitude of the maximum reduction is about the same as in the 3D model. However, the stress ratio decreases in a much larger area in the 2D model, compared to the 3D results.

A more explicit comparison between both cases is shown in Fig. 3, where the horizontal stress change, $\Delta\sigma'_h$ (eq. 2) along the vertical profiles W and W' (Fig. 2) is plotted against the depth from seafloor normalized by salt depth, H.

$$\Delta\sigma'_h = \sigma'_{h,initial} - \sigma'_{h,model} \quad (2)$$

The greatest $\Delta\sigma'_h$ occurs at the salt crest for both models ($H = 1$), reaching values of around 4.5 MPa. The 2D model predicts higher horizontal stress reduction along a greater part of the vertical profile, reaching a maximum difference of 1.5 MPa from the 3D model at 80% of the crest depth. The stress reduction in the 2D model extends along two thirds of the vertical profile, becoming zero at 30% of the crest depth. On the other hand, the horizontal stress change in the 3D model becomes zero at half the crest depth.

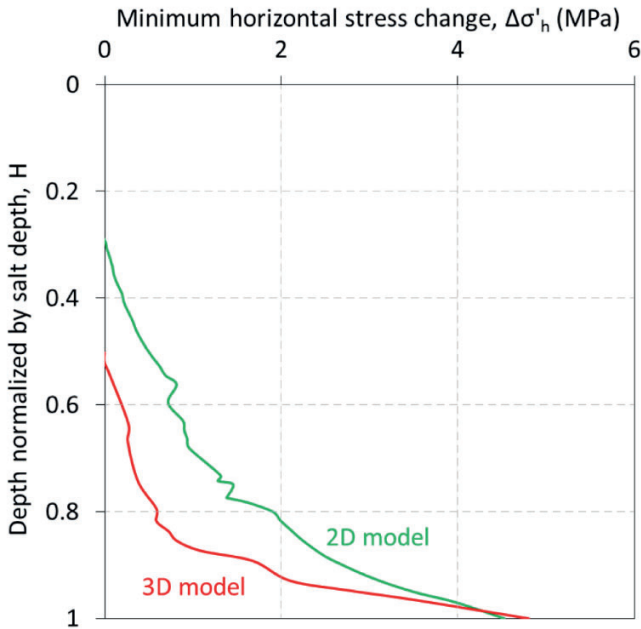


Fig. 3: Minimum horizontal stress change ($\Delta\sigma'_h$) with depth from seafloor normalized by salt depth (H), for both 2D (green line) and 3D (red line) models along vertical profiles W and W' (Fig. 2). The stress perturbation affects shallower sediments in the 2D model compared to the 3D case.

The decrease in horizontal stress above the eastern diapir is caused by the movement of the salt and resulting

sediment deformation (Fig. 4). The 2D model shows a downwards salt flux at the eastern side of the diapir and a mainly westwards salt flux at its western side, causing the diapir to collapse and extend laterally (red arrows Fig. 4). As a result, the footwall of the fault moves westwards, whereas the hanging wall moves mainly downward. (green arrows Fig. 4) This difference in displacements causes the sediments at the crest of the salt diapir to undergo horizontal extension, which reduces the in-plane horizontal stress.

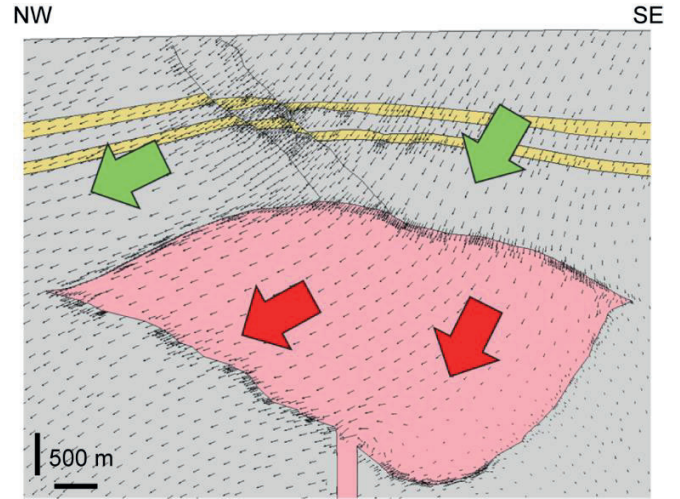


Fig. 4: Sediment (green arrows) and salt (red arrows) displacements around the eastern diapir in the 2D model. The difference in sediment displacement at each side of the faults causes the stress reduction predicted by the 2D and 3D models.

4. SENSITIVITY ANALYSIS RESULTS

We performed several sensitivity analyses in both 3D and 2D models, to assess the influence of our assumptions over the final results (Table 2).

Table 2: Summary of sensitivity analyses for 3D and 2D models.

Variable changed	Original value	Modification	3D	2D
Poisson's Ratio (ν)	0.3	0.25	✓	✓
		0.4	✓	✓
Elastic Modulus (E)	Horizon and depth dependent (Table 1)	Incr. 20%	✓	✓
		Decr. 20%	✓	✓
Salt by shale	Salt	Shale	✗	✓
Flat seafloor	1° slope	0° slope	✗	✓
Number of diapirs	3 diapirs	1 diapir	✗	✓
Salt columns width	200 m	400 m	✗	✓

4.1. Elastic parameters

To understand the influence of input elastic parameters, we varied the Poisson's ratio and elastic modulus in both 2D and 3D models. In both cases, the increase or decrease of the elastic parameters does not have substantial impact

on the stress results. The maximum difference from the basecase prediction was in the order of 0.1ppg.

4.2. Role of viscous salt movement

We replace the salt material with shale lithology in all the salt structures to illustrate the contribution of salt viscous movement over the stress changes across the model (2D model, Fig. 5).

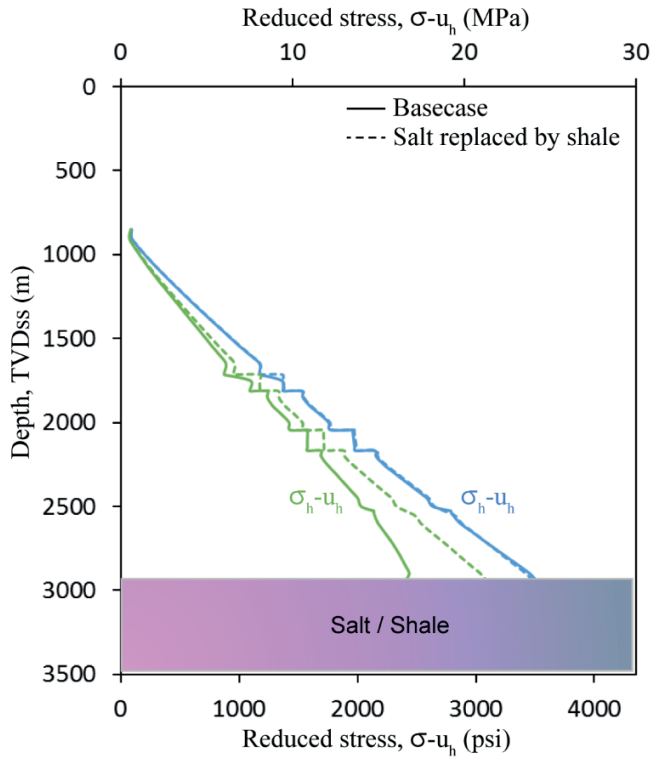


Fig. 5: Reduced stress profiles (stress σ minus hydrostatic u) along vertical section W' (Fig. 2b) for basecase model (solid green line) and shale lithology (dashed green line). The horizontal stress reduction near the salt structure is not present when the diapirs are substituted by shale lithology. Vertical stress is similar in both cases (blue line).

We compare the decrease in horizontal stress along the vertical well W' (Fig. 2b), for the base case (solid green line, Fig. 5) and shale-lithology (dashed green line, Fig. 5). The decrease in horizontal stress only occurs above salt, highlighting that stress changes are caused by the viscous salt deformation.

4.3. Seafloor geometry

The 2D basecase model has a seafloor slope of about 1° towards the NW. That seems to cause a general NW displacement of the modelled sediments (red arrows in Fig. 6a). When the seafloor is modified and set horizontal, displacement becomes mainly vertical (red arrows in Fig. 6b). The stress ratio decreases above the eastern diapir (Fig. 6b), however, the change is less pronounced than in the basecase. Hence, we find that displacements caused by the seafloor slope contribute to the stress reduction above the diapir.

4.4. Interaction between diapirs

We run a 2D model with only the eastern diapir present, in order to study the influence of the 2 western diapirs on the stress changes above the eastern diapir (Fig. 7). We find that stress changes are less pronounced compared with the basecase model. This indicates that the presence of deformable salt at the west end of the studied basin allows for additional westward sediment movement, which, in turn, contributes to the stress reduction above the eastern diapir.

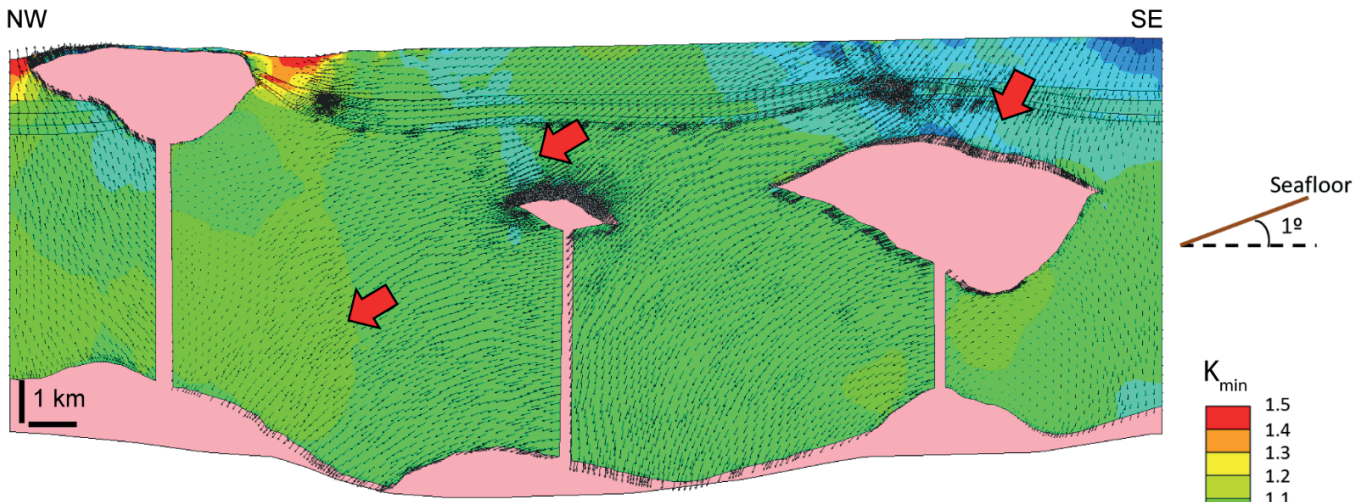
4.5. Salt column width

The salt columns in all 3 diapirs of the 2D basecase have been widened from 200 m to 400 m to test their contribution over the model results (Fig. 8). The results above the eastern diapir show a minimum stress ratio reduction similar to the basecase (Fig. 2b), with contours slightly broader at the crest and near the seafloor. Hence, the applied column-width change has a low influence over the stress results.

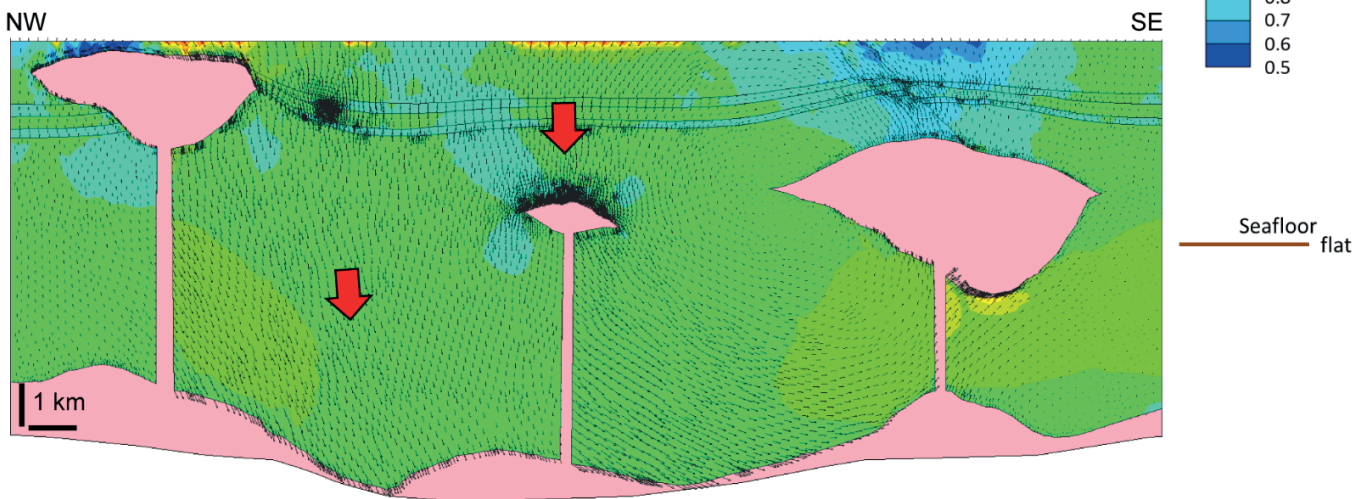
5. DISCUSSION

We show that both 3D and 2D static geomechanical models predict extension above the eastern diapir and, as a result, decrease in horizontal stress. The magnitude of the reduction is around 4.5 MPa in both 2D and 3D immediately above the crest. However, the area of sediments affected by the stress reduction is broader in the 2D model, reaching sediments at shallower depths. This difference can be explained by the plane-strain simplification in the 2D model. In the 3D case, the salt flow can be distributed in all three directions, whereas in the 2D case, the salt flow is constrained on the modeled plane, resulting in greater deformations of the salt and higher stress changes for the sediments encasing it.

We apply a series of changes in the 3D and 2D models to discern what are the principal model inputs that most affect the final stress and strain results. The influence of these changes over the principal stresses is summarized in Fig. 9. This figure shows the deviation of the principal stress results from the basecase model due to the changes introduced in each of the sensitivity analyses. These deviations are taken along a vertical section located at the crest of the eastern salt diapir (vertical section W' in Fig. 2b). The higher the deviation due to a particular model change, the higher impact this model assumption has over the results. The changes in the elastic properties of the sediments have the least effect over the principal stress results. In particular, changes in Poisson's ratio are negligible, whereas changes in the Elastic modulus of the sediments result in less than 1% of stress change for the minimum principal stress. Other aspects such as the salt lithology or the presence of other diapirs in the model have the highest influence over the stress changes, resulting in nearly 9% and 7% difference compared with



(a) Sediment displacements (arrows) and K_{min} (contours) for 2D basecase model



(b) Sediment displacements (arrows) and K_{min} (contours) for 2D model with flat seafloor

Fig. 6: Results of minimum stress ratio (contours) and sediment displacements (arrows) for (a) 2D basecase model and (b) 2D model with flat seafloor. The leftwards displacement trend in (a) disappears when the seafloor is flat. The stress ratio reduction above the eastern diapir in the basecase is slightly reduced when the seafloor is flattened.

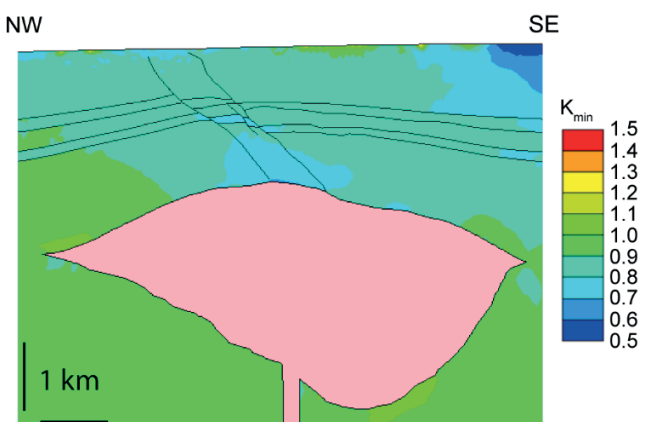


Fig. 7: Minimum stress ratio results predicted by 2D model around eastern diapir for a model with no other diapirs present.

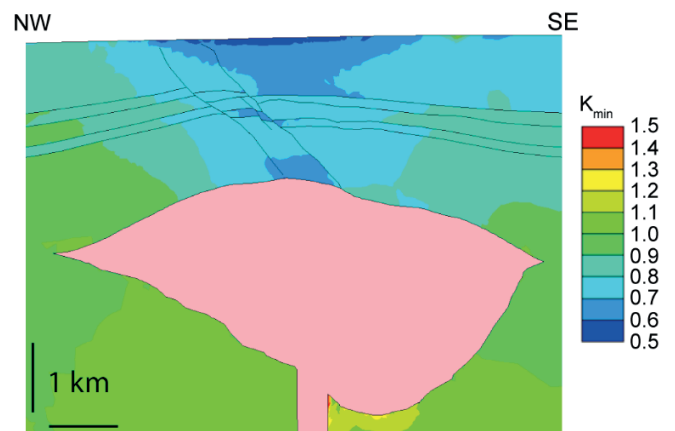


Fig. 8: Minimum stress ratio results predicted by 2D model around eastern diapir for a model with widened salt columns.

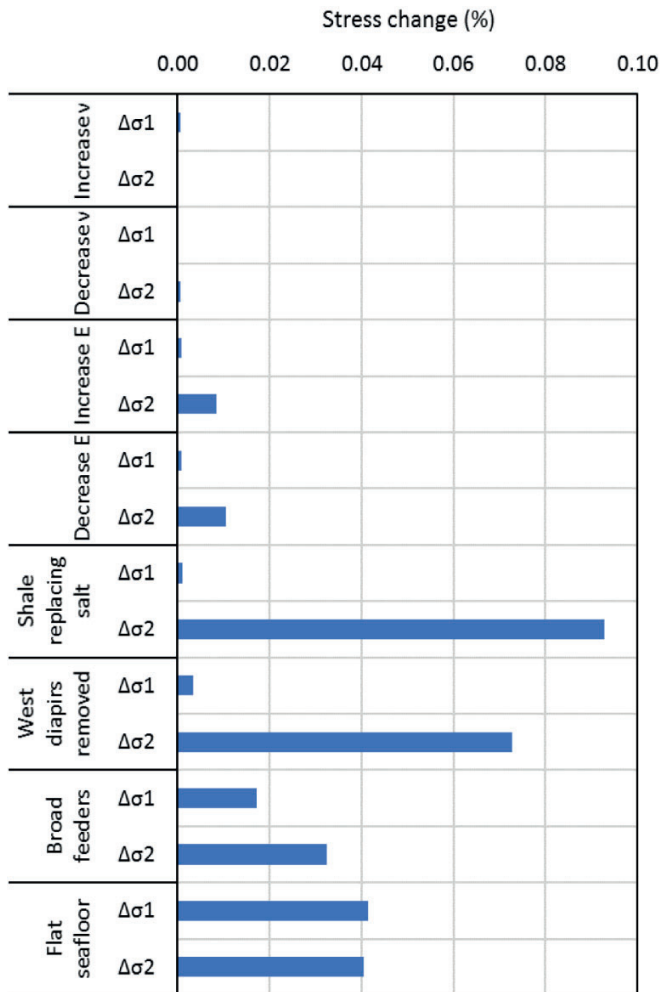


Fig. 9: Change in principal stresses between 2D sensitivity cases against basecase model. Cases involving changes in salt presence and its geometry show the greater stress changes. The variation of elastic properties of the materials does not affect the stress results.

the basecase model, respectively. These changes affect mainly the minimum principal stress. The seafloor geometry also has a noticeable influence, affecting both principal stresses by 4%.

The 2D sensitivity analyses help us identify the main mechanisms that cause stress reduction above the eastern diapir. We find two different displacement patterns above the eastern diapir:

- A significant downwards component of displacement in the hanging wall (eastern side of the main fault) caused by the salt withdrawal below (salt presence and its viscous rheology being the primary mechanism; Fig. 9).
- A westwards displacement in both the salt and the footwall sediments of the main fault due to the seafloor slope (seafloor geometry being the secondary mechanism; Fig. 9).

This differential movement above the diapir (Fig. 4) causes extensional horizontal strains that lead to a decrease in horizontal stress and, hence, minimum stress ratio reduction at the salt crest (Fig. 2). Salt movement is the primary mechanism that causes the stress changes above salt. This highlights the importance of properly defining salt geometry in geomechanical models.

6. SUMMARY

We develop a 3D geomechanical model of the Tarfaya salt basin, located on the West African Coast. The model predicts a decrease in horizontal stress near the crest of the salt structure targeted by an exploratory well. This result was later validated once the well was drilled.

We also build a 2D model using the geometry from a 3D transect and the same model inputs as the 3D geomechanical model. The 2D model predicts similar horizontal stress reduction at the crest of the salt structure. However, the area of sediments above the salt affected by the stress reduction is broader in the 2D model, indicating that 2D models may overestimate stress changes in some locations.

The 2D model allows for a more complete sensitivity analysis because it requires less computational power and has significantly less number of elements when compared with the 3D version. We identify that the viscous salt movement and the regional slope of the seafloor are the main mechanisms that drive stress changes above the eastern diapir.

ACKNOWLEDGEMENTS

This work is funded by Repsol Exploración S. A. We are grateful to Repsol for granting access to the data for this study. We would also like to thank Rockfield for their support in the modelling using ELFEN licenses and their cluster for the 3D sensitivity analysis.

REFERENCES

1. Adachi, J., Nagy, Z.R., Sayers, C.M., Smith, M. & Becker, D.F. 2012. Drilling Adjacent to Salt Bodies: Definition of Mud Weight Window and Pore Pressure Using Numerical Models and Fast Well Planning Tool. *SPE Annual Technical Conference and Exhibition*, 1–11.
2. Beltrao, R.L.C., Sombra, C.L., Lage, A.C.V.M., Fagundes Netto, J.R. & Henriques, C.C.D. 2009. *Challenges and New Technologies for the Development of the Pre-Salt Cluster, Santos Basin, Brazil*. Houston, Texas.
3. Dusseault, M.B., Maury, V. & Sanfilippo, F. 2004. Drilling Around Salt: Stresses, Risks,

- Uncertainties. *American Rock Mechanics Association. Paper 04-647*.
4. Fredrich, J.T., Fossum, A.F. & Hickman, R.J. 2007a. Mineralogy of deepwater Gulf of Mexico salt formations and implications for constitutive behavior. *Journal of Petroleum Science and Engineering*, 57, 354–374.
 5. Fredrich, J.T., Engler, B.P., Smith, J.A., Onyia, E.C. & Tolman, D.N. 2007b. Predrill Estimation of Subsalt Fracture Gradient: Analysis of the Spa Prospect to Validate Nonlinear Finite Element Stress Analyses. *SPE/IADC Drilling Conference*, 8.
 6. Heidari, M., Nikolinakou, M.A. & Flemings, P.B. 2018. Coupling geomechanical modeling with seismic pressure prediction. *Geophysics*, 83, 1–54.
 7. Luo, G., Hudec, M.R., Flemings, P.B. & Nikolinakou, M.A. 2017. Deformation, stress, and pore pressure in an evolving suprasalt basin. *Journal of Geophysical Research: Solid Earth*, 122, 5663–5690.
 8. Munson, D.E. 1997. Constitutive model of creep in rock salt applied to underground room closure. *International journal of rock mechanics and mining sciences & geomechanics abstracts*, 34, 233–247.
 9. Munson, D.E. & Dawson, P.R. 1979. Constitutive model for the low temperature creep of salt (with application to WIPP). SAND79-1853. Sandia National Laboratories, Albuquerque, NM. 31.
 10. Nikolinakou, M.A., Heidari, M., Flemings, P.B. & Hudec, M.R. 2018. Geomechanical modeling of pore pressure in evolving salt systems. *Marine and Petroleum Geology*, 93.
 11. Rockfield. 2017. *Elfen Explicit Manual (Version 4.10)*. Software, R. (ed.). Swansea, UK.
 12. Segura, J.M., Matos da Cruz, A., Stachlewski, G., Alvarellos, J., Vargas, P.E. & Lakshmikantha, M.R. 2016. Fault stability assessment for well planning: a case study related to salt structures. *American Rock Mechanics Association. Paper 16-518*.
 13. Sweatman, R., Faul, R. & Ballew, C. 1999. New Solutions for Subsalt-Well Lost Circulation and Optimized Primary Cementing. *SPE Annual Technical Conference and Exhibition*.
 14. van der Zee, W., Ozan, C., Brudy, M. & Holland, M. 2011. 3D geomechanical modeling of complex salt structures. *SIMULIA Customer Conference*, 1–16.
 15. Warren, J.K. 2006. *Evaporites: Sediments, Resources and Hydrocarbons*. Netherlands, Springer.
 16. Yu, Y., Tang, L., Yang, W., Huang, T., Qiu, N. & Li, W. 2014. Salt structures and hydrocarbon accumulations in the Tarim Basin, northwest China. *AAPG Bulletin*, 98, 135–159.

**Annex 3: Geologically constrained evolutionary
geomechanical modelling of diapir and basin evolution: A
case study from the Tarfaya basin, West African coast**

Geologically constrained evolutionary geomechanical modelling of diapir and basin evolution: A case study from the Tarfaya basin, West African coast

Jean Joseph Hooghvorst¹  | Maria A. Nikolinakou²  | Toby W. D. Harrold³ | Oscar Fernandez⁴  | Peter B. Flemings⁵  | Alejandro Marcuello⁶ 

¹Department Dinàmica de la Terra i de l'Oceà, Universitat de Barcelona, Barcelona, Spain

²Bureau of Economic Geology, Jackson School of Geosciences, The University of Texas at Austin, Austin, TX, USA

³P-TEN Geomechanics Services S, L, Alcobendas, Spain

⁴Department Geology, University of Vienna, Vienna, Austria

⁵Department of Geological Sciences and Institute for Geophysics, Jackson School of Geosciences, The University of Texas at Austin, Austin, TX, USA

⁶Inst. Geomodells, Department Dinàmica de la Terra i de l'Oceà, Univeristat de Barcelona, Barcelona, Spain

Correspondence

Jean Joseph Hooghvorst, Department Dinàmica de la Terra i de l'Oceà, Facultat de Ciències de la Terra, Universitat de Barcelona, Martí I Franqués, s/n, 08028 Barcelona, Spain.
Email: jeanjo_90@hotmail.com

Funding information

Repsol

Abstract

We systematically incorporate burial history, sea floor geometry and tectonic loads from a sequential kinematic restoration model into a 2D evolutionary geomechanical model that simulates the formation of the Sandia salt diapir, Tarfaya basin, NW African Coast. We use a poro-elastoplastic description for the sediment behaviour and a viscoplastic description for the salt. Sedimentation is coupled with salt flow and regional shortening to determine the sediment porosity and strength and to capture the interaction between salt and sediments. We find that temporal and spatial variation in sedimentation rate is a key control on the kinematic evolution of the salt system. Incorporation of sedimentation rates from the kinematic restoration at a location east of Sandia leads to a final geomechanical model geometry very similar to that observed in seismic reflection data. We also find that changes in the variation of shortening rates can significantly affect the present-day stress state above salt. Overall, incorporating kinematic restoration data into evolutionary models provides insights into the key parameters that control the evolution of geologic systems. Furthermore, it enables more realistic evolutionary geomechanical models, which, in turn, provide insights into sediment stress and porosity.

KEYWORDS

burial history, evolutionary geomechanical model, kinematic restoration, salt tectonics, Sandia diapir, Tarfaya basin

Highlights

- High sedimentation rates during Jurassic is the key driver for the Sandia diapir evolution
- The Atlas shortening reactivates the Tarfaya diapirs during Late Cretaceous by mobilizing salt towards the crest
- Higher sedimentation rates at early stages of diapir formation affect whether the diapir will upbuild to the sea floor
- Different shortening rates have significant effect on the present-day stress state above Sandia

1 | INTRODUCTION

The study of the formation and evolution of sedimentary basins provides valuable information on the key geological processes that led to the present-day geometry and state of stress and pore pressure. Both inverse (kinematic restoration) and forward (physical, basin and geomechanical modelling) approaches have been developed to identify and study the fundamentals of these processes.

Kinematic restoration (Hudec & Jackson, 2004; McGuinness & Hossack, 1993; Rowan, 1993; Rowan et al. 2016; Trudgill & Rowan, 2004) is an inverse approach that starts with the present-day geometry of a basin and reconstructs past deformation states by taking into account the deposition of sediments and their compaction, eustasy, fault-controlled deformations, isostasy, thermal subsidence and salt movements (Rowan & Ratliff, 2012). However, this method does not simulate the evolution of stresses during the basin restoration. In addition, established kinematic restoration techniques of salt systems do not explicitly model salt flow. Recently, there have been efforts to combine kinematic restorations with finite-element modelling (Crook et al. 2018; Durand-Riard et al. 2013; Maerten & Maerten, 2006; Moretti & Guiton, 2006). These approaches simulate the stress–strain behaviour of sediments to better approximate the past deformation of the studied systems but do not include viscous laws for the salt flow.

Physical (analogue) modelling is a forward method that studies the evolution of geologic systems using rock analogues with predefined rheologies and boundary conditions within a laboratory set-up that deforms at smaller spatial and temporal scales (Reber et al. 2020; Schellart & Strak, 2016). The rules for model scaling were initially established by King Hubbert (Hubbert, 1937) using three aspects of similarity: geometric, kinematic and dynamic (Koyi, 1997). Physical models have been used to represent a wide variety of processes including strike-slip fault systems (Corti & Dooley, 2015; Dooley & Schreurs, 2012; Hubbert, 1951), fold and thrust belts (e.g. Farzipour-Saein & Koyi, 2014; Massoli et al. 2006; Nilforoushan & Koyi, 2007; Ramberg, 1981), plutonism (Dietl & Koyi, 2011) or salt-related deformation (e.g. Dooley et al. 2015, 2017; Dooley & Hudec, 2017; Koyi, 1998). The principal limitations of these models are associated with material and topography scaling, leading to uncertainty on the timing and duration of the geological processes, exaggerated topographies and no information on the internal stress state of the modelled systems and its evolution through time (Schellart & Strak, 2016). Furthermore, model reproducibility is highly related to human factors affecting the model set-up (Schreurs & Buiter, 2016). Despite these limitations, physical modelling is a particularly strong tool for investigating and visualizing geologic processes.

Basin modelling is another forward method that studies geological processes in sedimentary basins using geological, petrophysical, geophysical and geochemical data (Hantschel & Kauerauf, 2009). Basin modelling has been extensively used by the oil and gas industry to model petroleum systems. Simulated processes range from deposition and compaction, erosion, heat flow, phase dissolution, to hydrocarbon generation and its accumulation and migration (Ben-Awuah et al. 2013). Some basin models incorporate stress and/or pressure calculations. However, the method commonly assumes that the sediments deform uniaxially, hence it cannot capture stress, strain and pore pressure perturbations caused by complex deformation processes such as faulting or halokinesis (e.g. Bolas et al. 2004; Gutierrez & Wangen, 2005; Stigall & Dugan, 2010; Thibaut et al. 2014).

Recent advances in understanding the evolution of geological systems result from the incorporation of non-uniaxial deformation in basin models and the introduction of poromechanical numerical models (Albertz & Beaumont, 2010; Beaumont et al. 2000; Fernandez & Kaus, 2015; Kaus et al. 2008; Nikolinakou et al. 2018). Poromechanical (geomechanical) models, in particular, incorporate coupled porous fluid flow and the full stress tensor in modelling the compression behaviour and strength of sediments. Geomechanical models are now commonly used for the study of hydrocarbon prospects, especially in non-uniaxial frontier settings such as salt systems or compressional systems (e.g. Dusseault et al. 2004; Willson et al. 2002). Static geomechanical models are often built using the basin geometry at the present day (e.g. acquired from seismic data), and can provide a first-order estimate of stress and pressure around existing structures (e.g. Fredrich et al. 2007; Heidari et al., 2018; Hoogvorst et al. 2020; Segura et al. 2016). Stress calculation, however, lacks input from past geological processes during the evolution of the structures (Nikolinakou et al. 2014). Evolutionary geomechanical (forward) modelling can simulate time-dependent processes, such as deposition, tectonic loading, salt flow and porous fluid flow. Hence, it couples the deformation and strength of sediments with the development of geologic systems (Goteti et al. 2012; Gradmann & Beaumont, 2012; Gradmann et al. 2012; Hamilton-Wright et al. 2019; Nikolinakou et al. 2018; Thigpen et al. 2019). The principal limitation of the evolutionary models is the difficulty in producing the observed present-day geometry (Nikolinakou et al. 2014). To the best of our knowledge, very few studies have tried to incorporate the geologic history of a given basin into an evolutionary geomechanical model (e.g. Crook et al. 2018; Thigpen et al. 2019).

Our study is one of the first systematic approaches to incorporate burial history, sea floor geometry and tectonic loads from a sequential kinematic restoration into an evolutionary geomechanical model of a salt basin. In addition to using the kinematic restoration to constrain the geomechanical model,

we employ a poromechanical description of sediment behaviour to capture the interaction between salt movement, sediment deposition and deformation and to study parameters that drive the salt system evolution. We simulate the development of the Sandia diapir in the Tarfaya basin, West African Coast and compare our model predictions with the inferred kinematic evolution of the basin. We find that the depositional history, and especially the variation in early sedimentation rates, is the key parameter that drives the evolution of the Sandia diapir to its present-day geometry. We also illustrate the importance of tectonic shortening to diapirism and the present-day stress state. Overall, we show that careful representation of the depositional and tectonic history can enable more realistic evolutionary geomechanical models, with final model geometries that resemble the seismic interpretation of geologic structures.

2 | GEOLOGICAL CONTEXT

The Tarfaya basin is a passive continental margin basin located offshore SW Morocco (Gouiza, 2011) and bound by the Agadir and Essaouira basins to the north and by the Aaiun basin to the south (Figure 1). On the west, the basin ends against the eastern Canary Islands (Lanzarote and Fuerteventura islands) and the Conception Bank that separate it from the deep abyssal plain. To the east, the basin is bound on the onshore, from north to south, by the Atlas belt, the Anti-Atlas and their undeformed foreland. At present, a SW-NE trending, 2000 m deep bathymetric trough defines the most distal part of the basin at the edge of the continental shelf.

The Tarfaya basin formed during Late Triassic to Early Jurassic rifting and opening of the Central Atlantic and

the separation of the NW African margin from the North American margin. Rifting caused extension of the basement, forming fault-controlled half-grabens trending NNE-SSW to NE-SW (Le Roy & Piqué, 2001; Piqué et al. 1998), which were infilled by thick syn-rift sequences of continental siliciclastic red beds and evaporites of Triassic age. The Triassic evaporites are the source layer for the present-day salt-cored structures in this area (Tari & Jabour, 2013).

During the Jurassic, post-breakup thermal subsidence of the basin caused the western part to deepen. A carbonate platform formed along the eastern, shallower, continental margin. Initial development of salt structures began during the Jurassic and continued during Early Cretaceous, affecting the sea floor surface at these times (Michard et al. 2008). The location of individual salt structures was strongly controlled by the uneven distribution of Triassic salt thickness within the half-graben system (Tari & Jabour, 2013).

A relative sea-level fall during the Late Jurassic–Early Cretaceous (Berriasian to Valanginian) caused subaerial exposure and karstification of the carbonate platform. This was followed by sedimentation of alluvial siliciclastic materials forming the Tan Tan Delta complex (Michard et al. 2008; Wenke et al. 2011).

The Tarfaya basin was then compressed by inversion of the Atlas and uplift of northwestern Africa. This started during the Late Cretaceous (Coniacian) and lasted until the Quaternary with episodes of activity followed by quiescence (Frizon de Lamotte & Zizi, 2008). Atlasic uplift increased the sediment input (Wenke et al. 2011) and the compression reactivated pre-existing salt structures formed during the Jurassic and Early Cretaceous (Tari & Jabour, 2013). In addition, volcanic emplacement of the Canary Islands

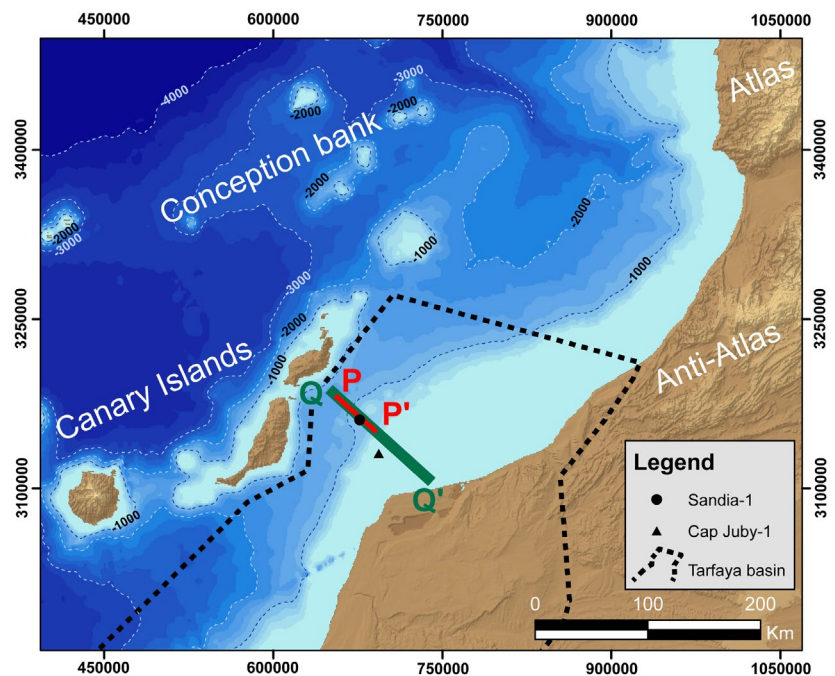


FIGURE 1 Location map for the Tarfaya basin and geological features. Seismic section (Figure 2) is indicated by the red line PP'. Restored section (Figure 3) is indicated by the green line QQ'. Sandia-1 (black circle) and Cap Juby-1 (black triangle) well-head locations are also shown. The Geographic Coordinate System used is ETRS 1989

archipelago occurred during the Cenozoic (Carracedo & Perez-Torrado, 2013).

3 | STRUCTURE AND EVOLUTION

The study area is located at the most distal part of the Tarfaya Basin (Figure 1) and centres around the Sandia and the Western diapirs (Figure 2). Seismic interpretation of proprietary 3D seismic migrated in time and depth was complemented with vintage 2D reflection multi-channel seismic profiles (acquired in 1983) migrated in time. Interpretation was constrained with data from two exploration wells. The Cap Juby-1 well (black triangle, Figure 1) was drilled by Mobil in 1983 and reached diapiric Triassic evaporites below Upper Jurassic carbonates. The Sandia-1 well (black circle, Figure 1) was drilled by Repsol in 2015 and reached Paleocene siliciclastics above the Sandia salt diapir (Figure 2).

The good quality of the seismic data in the shallowest 5 km together with the well data makes the interpretation of the Tertiary section straightforward (Figure 2). The interpretation of the deeper units is more ambiguous because of the different geologic history of the deeper water basin (in the NW) compared to the shallower platform area (in the SE), where the Cap Juby-1 control well is located. In the platform area, the Jurassic and Triassic units are found at shallower depths as a result of the Atlasic inversion that started in the Late Cretaceous. Seismic reflection data suggest that this Atlasic inversion resulted in significant erosional truncation of units and accounted for 500–1000 m of uplift of the shelf area. Because thicknesses of pre-inversion (Mesozoic) units in the platform area were used as guides for their interpretation in the deep-water sector (Figure 2), there is more uncertainty in the interpretation of deeper units.

The key regional-scale feature of the study area is a thick Tertiary basin (up to 4 km thick) in the deep-water domain (Figure 2). This Tertiary basin wedges towards the SE onto the continental shelf and overlies a regional erosional unconformity in the continental shelf and across the shelf break. Basinward, and barring areas deformed by diapirism, Tertiary units lie conformably over Cretaceous sediments.

Both Tertiary and Mesozoic (Jurassic and Cretaceous) sediments display thickness changes and deformation related to diapirism of the underlying Triassic evaporites. These evaporites cut through the overlying units in the form of diapirs at two locations on this cross section (Figure 2).

Published observations of half-graben geometries suggest that these salt diapirs may have nucleated above rotated basement fault-blocks along the Moroccan Atlantic margin (Le Roy & Piqué, 2001; Tari & Jabour, 2013). The basinward diapir (Western diapir) is active at the present day and deforms the seabed. The landward diapir (Sandia diapir), which was the target of the Sandia-1 exploratory well (black circle, Figure 1), ceased growth during the Tertiary. Both diapirs display geometries that are consistent with passive down-building development during the Mesozoic, and a phase of lateral expansion during the Cretaceous. Folding of Paleogene strata above the diapirs indicates that they were reactivated by shortening during the Tertiary. Shortening caused further growth of the Western diapir and extrusion onto the seabed. However, in the case of the Sandia diapir, shortening only caused folding of the overburden and lateral flow of salt towards the centre of the salt structure.

The geomechanical model we present is based on a sequential kinematic restoration of the regional cross section to Triassic times, during the deposition of the evaporites (Figure 3). This restoration accounted for decompaction of sediments by assuming average shale or sandy shale lithology and compaction curves of Sclater and Christie (1980). Despite the presence of carbonates in the Jurassic section of the shallow-water domain, the restoration assumed sandy shale materials for the entire Jurassic. This is the expected lithology in the deeper part of the basin, which is the objective of the geomechanical modelling. The restoration also considered local isostasy and corrected for the effect of thermal subsidence by applying the curves of McKenzie (1978) (the beta factor was estimated from the expected crustal thickness based on the interpreted top of the basement and assuming an isostatically equilibrated crust). It accounted for the effects of salt diapirism following the approach of Rowan and Ratliff (2012). Finally, the sequential restoration accounted for the Atlasic shortening of 5 km based on the unfolded

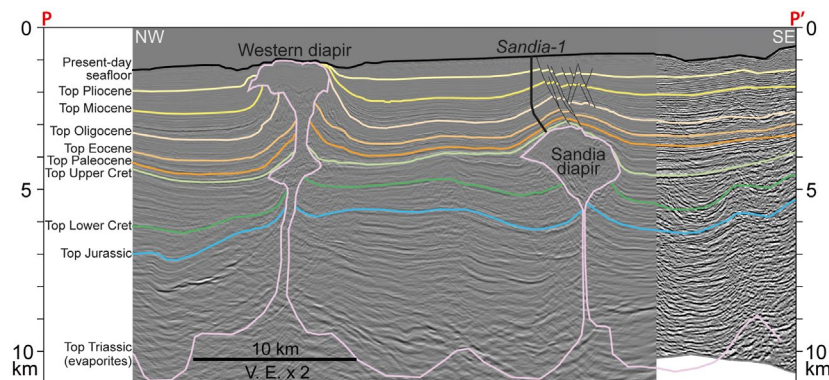


FIGURE 2 Seismic interpretation across a transect in the deep part of Tarfaya basin (red line PP', Figure 1). This section combines 3D seismic (NW side) with vintage 2D reflection multi-channel (SE side). Location of the seismic line is also highlighted with the red rectangle on the present-day section in Figure 3

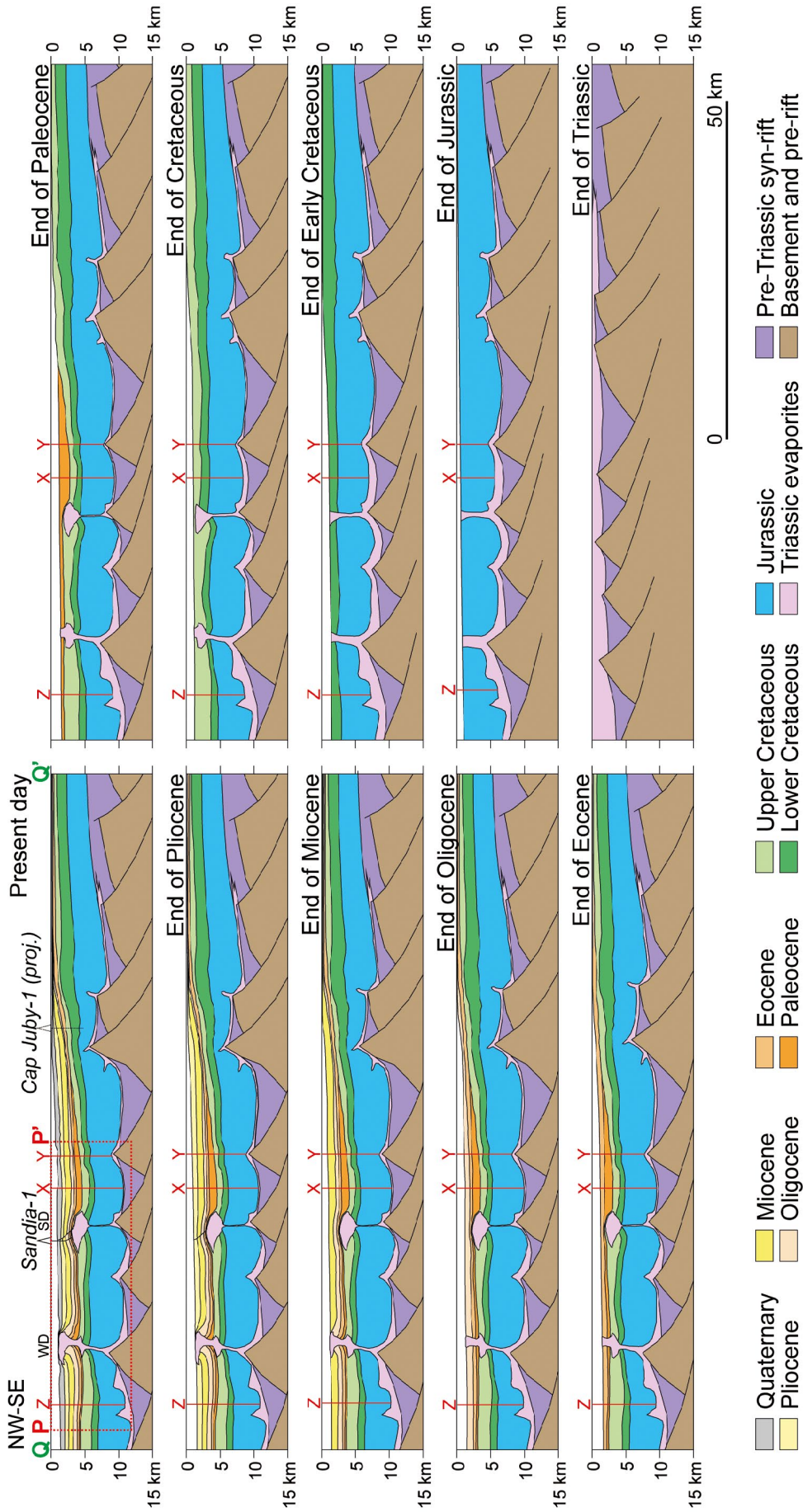


FIGURE 3 Sequential kinematic restoration of a section across the Tarfaya basin (green line QQ', Figure 1) from Triassic to present day. Locations X, Y and Z in red are used for thickness extraction and burial history reconstruction (Figure 5 and Figure 12). Location of Sandia-1 exploratory well and projection of Cap Juby-1 well are shown on the present-day panel. Dashed red box indicates location of seismic section in Figure 2. WD: Western diapir; SD: Sandia diapir. A seismic section near the Cap Juby has been published in Davison (2005)

Name	Variable changed	Original value	Changed value
Base-case			
BC	–	–	–
Sensitivity analysis			
MV1	Shortening rate	Exponential (Figure 4c)	Sigmoidal (Figure 4c)
MV2	Basal geometry	With triangular shape	No triangular shape
MV3	Temperature gradient	31°C/km	36°C/km
MV4	Burial history	Figure 5a	Figure 5b
MV5	Plio-Quaternary sed. rates	620 and 700 m/Myr	61 m/Myr

TABLE 1 Summary of evolutionary models

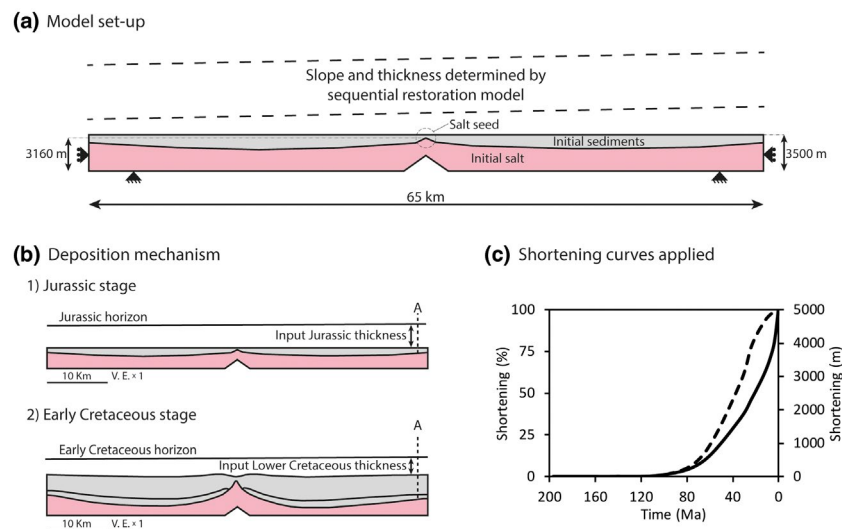


FIGURE 4 (a) Initial geometry for the salt (pink) and shale (gray) layers in the evolutionary geomechanical Elfen model, along with model dimensions and boundary conditions. The seed and sag of the salt surface geometry are introduced to numerically facilitate initiation of diapir. Dashed lines represent layers that will be deposited on top of the model (b) Definition of deposition horizons: at the beginning of each stage, the upcoming layer thickness is obtained from burial history curve (Figure 5a) and applied at the right side of the model (location A), starting at the current top surface. For example, for the Jurassic modelling stage, the deposited-layer thickness is 4500 m (blue line in Figure 5a) and defines the elevation of the Jurassic deposition horizon at the right end of the evolutionary model (A). The Jurassic bathymetric slope obtained from the kinematic restoration (Figure 3, Table 2) is then used to define the Jurassic horizon across the model. Sediment compaction and salt mobilization modify the geometry of the sea floor, which becomes the baseline for the next deposition stage (b2) (c) Shortening application curves for the BC and MV2 to MV5 models (solid line) and for the MV1 model (sigmoid dashed line)

length of the Cretaceous–Paleocene horizon, considered to be pre-Atlantic.

4 | EVOLUTIONARY MODEL DEFINITION

We built a series of 2D plane strain evolutionary geomechanical models using the finite element program Elfen (Rockfield, 2017). A base-case model (BC, Table 1) is used as reference model for comparison in a series of sensitivity analyses. A number of model variants (MV, Table 1) explore the influence of selected input parameters. Each variant modifies one parameter compared to the BC model (Table 1).

4.1 | Base-case model

The base-case (BC) model has an initial geometry that includes a 2-km thick salt layer and a shale layer averaging 1.1 km thickness on top (Figure 4). The role of the shale layer is to preserve the initial geometry of the salt top surface by preventing the salt from moving laterally towards the minibasins during the model (gravity) initialization step. We introduce an initial seed (in the form of a small salt dent circled in Figure 4a) at the centre of the salt top surface and a slight sag of the salt surface at both sides of the seed to facilitate the initiation of the salt diapir. Displacements are constrained in both the horizontal and vertical directions at the base of the model and only in the horizontal direction at the sides of the model.

We use both a burial history curve (Figure 5a) and the paleobathymetries provided by the sequential kinematic restoration model (Figure 3) as boundary conditions for the evolutionary model (Figure 4b). To obtain the burial history for the simulation of the Sandia diapir (Figure 5a), we extract the thickness of sedimentary layers from the kinematic restoration model along a vertical location 10 km east of the diapir (location Y; Figure 3), at the end of each geologic interval

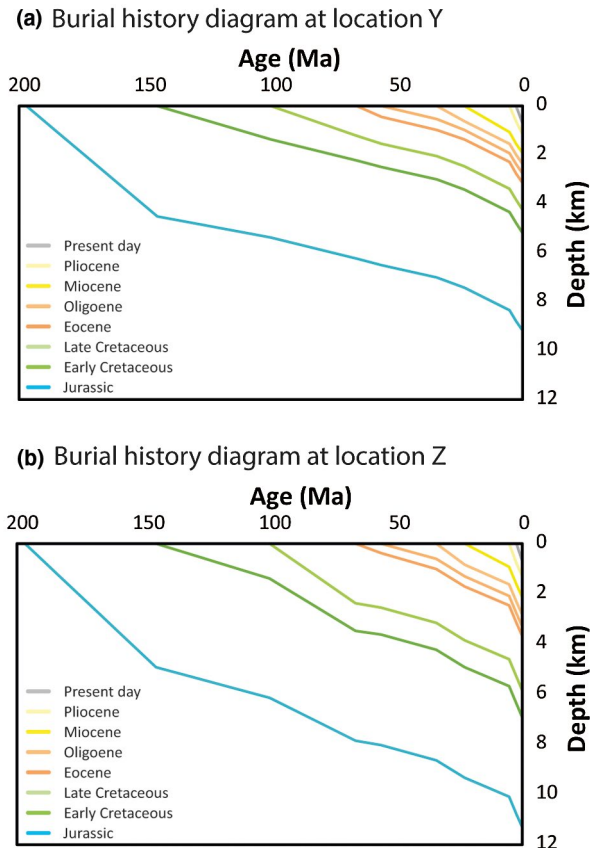


FIGURE 5 Burial history curves resulting from thickness extractions in the sequential kinematic restoration model of the Tarfaya basin section (Figure 3). (a) Burial history curve at location Y (SE of Sandia diapir, Figure 3) used in all but the MV4 models. (b) Burial history curve at location Z (NW of Western diapir, Figure 3) used in MV4

TABLE 2 Thickness and sea floor angles from sequential kinematic restoration model at the end of each geologic time interval

Name	Duration (Myr)	Total thickness at end of stage (m)	Sea floor angle at end of stage (°)
Jurassic	52	4500	0.43
Lower cretaceous	45	1270	0.32
Upper cretaceous	34	1230	0.22
Paleocene/eocene	32	1000	0.32
Oligocene	11	615	0.21
Miocene	17.1	1080	0.42
Pliocene	2.8	620	0.38
Present day	2.5	700	0.53

(Table 2). The shallowest layer at each geologic interval in the restoration model is de-compacted and, hence, its thickness is used in the evolutionary model with no further adjustment: for each modelled geologic interval, the deposited layer thickness provided by the burial history curve (Figure 5a) is added to the current sea floor in the evolutionary model to define the elevation of the upcoming deposition horizon (Figure 4b). This calculation is applied at the right end of the evolutionary model, 30 km from the Sandia diapir, to ensure far-field conditions (arrow in location A, Figure 4b). We extend the deposition horizon across the model using an average bathymetric slope (Table 2), which we determine from the kinematic restoration by measuring the average sea floor slope angle at each geologic interval. We then simulate deposition in the evolutionary model by filling the space between the current sea floor and the upcoming horizon (Figure 4b).

The movement of the salt in this evolutionary model is not prescribed. The differential loading imposed by the weight of the deposited material causes the salt to deform and flow. This, together with sediment compaction, modifies the topography of the sea floor in the model. Because the seafloor geometry at the end of a given deposition step becomes the baseline for the next deposition stage, the upper surface of each deposition horizon depends on both the burial history and the preceding model evolution (e.g. Early Cretaceous stage, Figure 4b).

We simulate the tectonic shortening between Upper Cretaceous (100 Ma) and the present day by imposing shortening on the model that deforms it from its original length of 65 km to a final length of 60 km. The shortening deformation rate increases gradually over the first 50 Myr to ensure numerical stability and follows an exponential curve thereafter (solid curve, Figure 4c).

The salt is modelled using the Munson–Dawson formulation (Appendix A; Munson & Dawson, 1979). The Munson–Dawson model has been extensively used to simulate the viscous flow of salt in deep-water salt basins such as Gulf of Mexico, West African coast or offshore Brazil (Fredrich et al. 2003; Hooghorst et al. 2020; Marketos et al. 2016; Segura et al. 2016; Thigpen et al. 2019). The salt viscosity

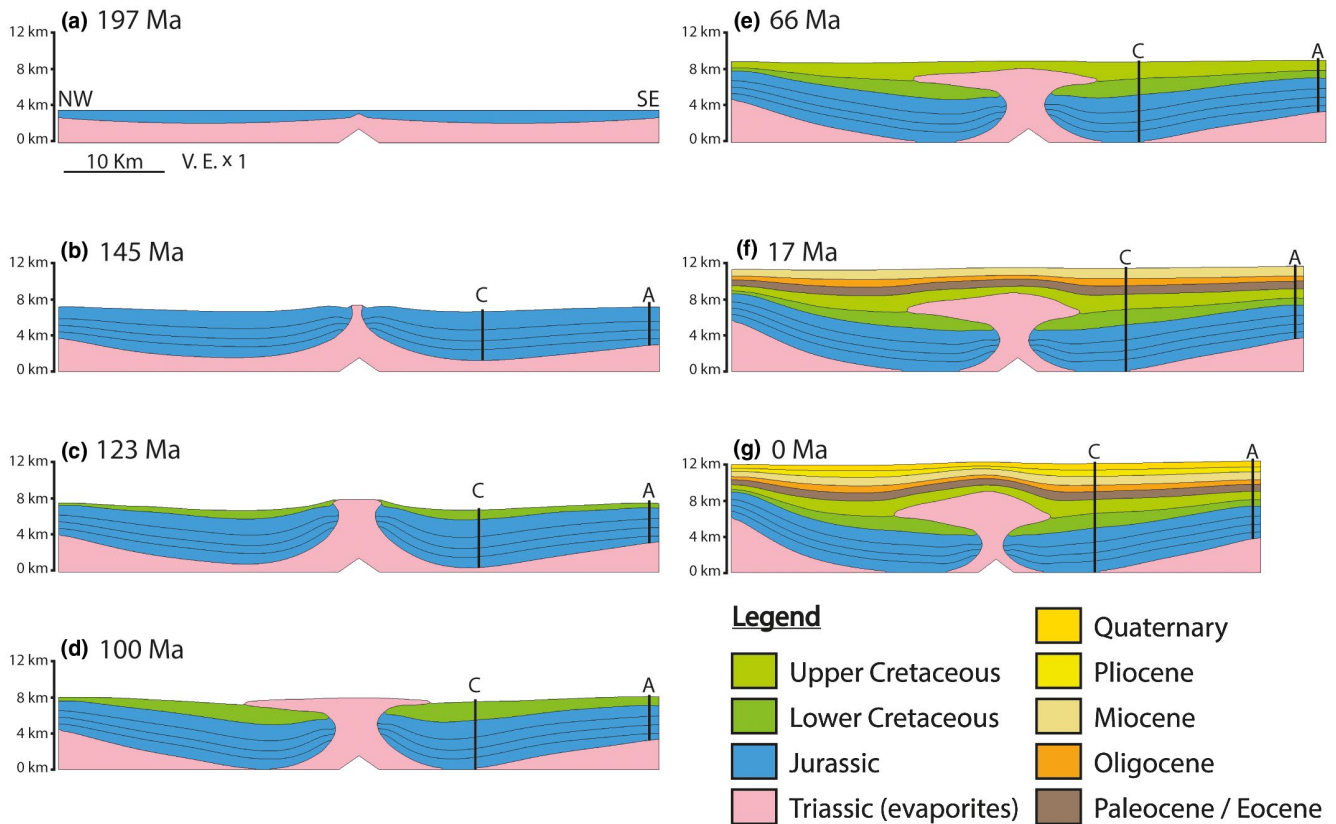


FIGURE 6 Evolution of the Sandia diapir predicted by the BC model. Location A (vertical black lines) indicates the location where the layer thicknesses from the burial history (Figure 5a) are applied. Locations A and C are used to compare the BC model thicknesses with the kinematic restoration model (Figure 12). (a) Initial geometry representing the top Triassic evaporites (pink) and an initial thin layer of Jurassic sediments (blue); (b) End of Jurassic deposition (blue). The salt diapir reaches the sea floor; (c) Mid-stage of Lower Cretaceous sediment deposition (dark green). Salt is about to break out into a salt sheet and source layer has thinned; (d) End of Lower Cretaceous deposition (dark green) with salt sheet formed downslope and salt overhang upslope. The source layer is welded on both sides of diapir and connected to the upper part by a salt stem; (e) End of Upper Cretaceous deposition (light green): diapir is buried. Regional shortening is activated during this stage; (f) Paleocene to Miocene deposition. Shortening continues. Salt volume in pedestal decreases and diapir stem thins, while the diapir bulges upwards arching the roof sediments; (g) Present-day, following Pliocene and Quaternary deposition. Shortening continues. Salt volume in pedestal and in stem further decreases, as does the extent of the salt sheets. The diapir bulges upwards arching the roof sediments. [Corrections updated on 25 July 2021, after initial online publication: Figure 6 caption has been corrected in this version.]

depends on both differential stress and temperature. Because of the absence of field data, input parameters for the salt (Table A1) are calibrated based on Avery Island salt (Fredrich et al. 2007; Munson, 1997), which is considered to represent average behaviour for Gulf of Mexico salt. The initial salt stress state is uniform ($K_0 = 1$, see Appendix B for nomenclature), but differential stresses develop later in the model because of sediment loading. In addition, we assume the salt to be a homogeneous and isotropic material and we do not account for inner layering and anisotropies. A temperature gradient of 3.1°C per 100 m is used (e.g. Rimi, 2001; Zarhloule et al., 2010), starting with a sea floor temperature of 4°C . This gradient is based on an integrated 2D and 3D petroleum system model for thermal maturity evaluation.

The sediment is modelled as a porous elastoplastic material using the SR3 constitutive model (Crook et al. 2006, see Appendix A). This model is based on the critical state theory, following a single-surface, rate-independent, non-associated

formulation. Density also changes as a function of porosity (Figure A2). A key feature of the critical state model is the incorporation of both mean and differential stress to compaction. In other words, porosity evolves during the simulation because of deposition, salt loading and tectonic shortening. Because at shallow depths, the horizontal stress in a salt column is higher than the uniaxial horizontal stress of sediments at the same depth (Heidari et al. 2017), a salt diapir loads sediments laterally. A key difference from commonly used basin models is that salt deforms the wall rocks and physically widens, when sediments deform plastically. In this case, sediment layer line lengths are not being preserved, the salt diapir can upbuild through the roof and/or flow laterally within sediments and the shape of the salt structure may not be dictated by the relative magnitudes of sedimentation and salt-rise rates (Nikolinakou et al. 2017).

The evolutionary Elfen model is based on a quasi-static, finite-element formulation accompanied by an automated

FIGURE 7 Final geometry of Sandia diapir as predicted by: (a) BC model; (b) MV1 model with sigmoidal shortening rates (dashed line, Figure 4c); (c) MV2 model with no basal fault; and (d) MV3 model with temperature gradient increased to 36°C/km. [Corrections updated on 25 July 2021, after initial online publication: Figure 7 caption has been corrected in this version.]

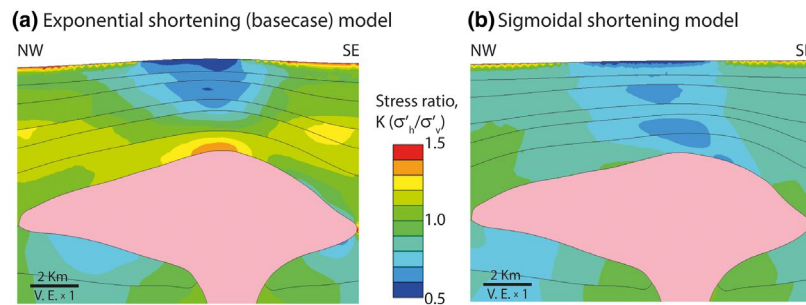
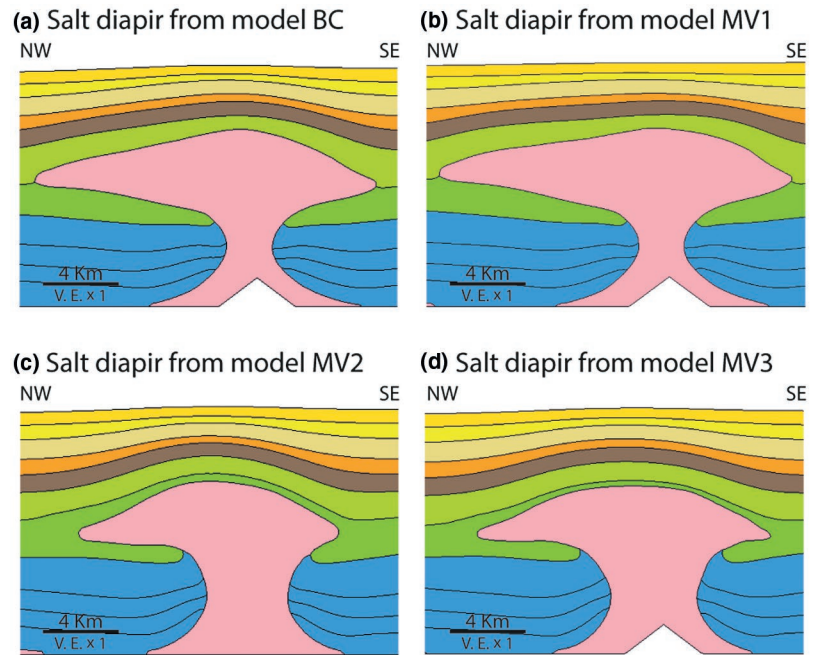


FIGURE 8 Present-day geometry and contours of the horizontal-to-vertical effective stress ratio K for (a) base-case evolutionary model using an exponential shortening curve (solid line, Figure 4c); and (b) evolutionary model using a sigmoidal shortening curve (dashed line, Figure 4c). The uniaxial K_0 value is 0.8 (light blue contour colours). K higher than 1 (warm contour colours) represent s'_h higher than s'_v . K below 0.8 (darker blue contour colours) represent decreased s'_h and lateral extension. See Appendix C for vertical stress profiles above these diapirs and Appendix B for figure nomenclature. [Corrections updated on 25 July 2021, after initial online publication: Figure 8 caption has been corrected in this version.]

adaptive-remeshing technique (Peric & Crook, 2004) that activates when the model reaches a threshold plastic strain of 0.7. When activated, the remeshing technique locally generates an increase of smaller elements. The model is drained (i.e. pore pressures are hydrostatic) and we assume a fully submerged basin; therefore, the stresses obtained from the model are effective stresses. The mesh is composed of unstructured rectangular elements with an initial size of 200 m and a minimum size of 80 m when re-meshed. In addition, geometric pinching allows the removal of very thin layers that would otherwise cause element distortion and numerical instabilities.

4.2 | Model variants

A number of parameters control the basin and diapir evolution (e.g. shortening rates, temperature gradient, sedimentation

rate, etc.). Some of these parameters, like the presence of a basal structural high or the very high sedimentation rates for the Pliocene and Quaternary intervals, also have a high level of uncertainty. We built and ran further models using the same initial configuration as the BC model but changing one of these parameters at a time to assess its influence. The model variants are:

- MV1: we use a sigmoidal shortening rate (dashed line, Figure 4c) instead of the BC exponential shortening rate (solid line, Figure 4c), maintaining the same shortening magnitude of 5 Km and its timing.
- MV2: we remove the basal triangular feature representing the rotated fault block interpreted below the diapirs (Figure 3).
- MV3: we increase the temperature gradient of the basin from 31°C/km to 36°C/km.
- MV4: we extract the burial history and the initial salt thickness along a vertical location at the NW side of the

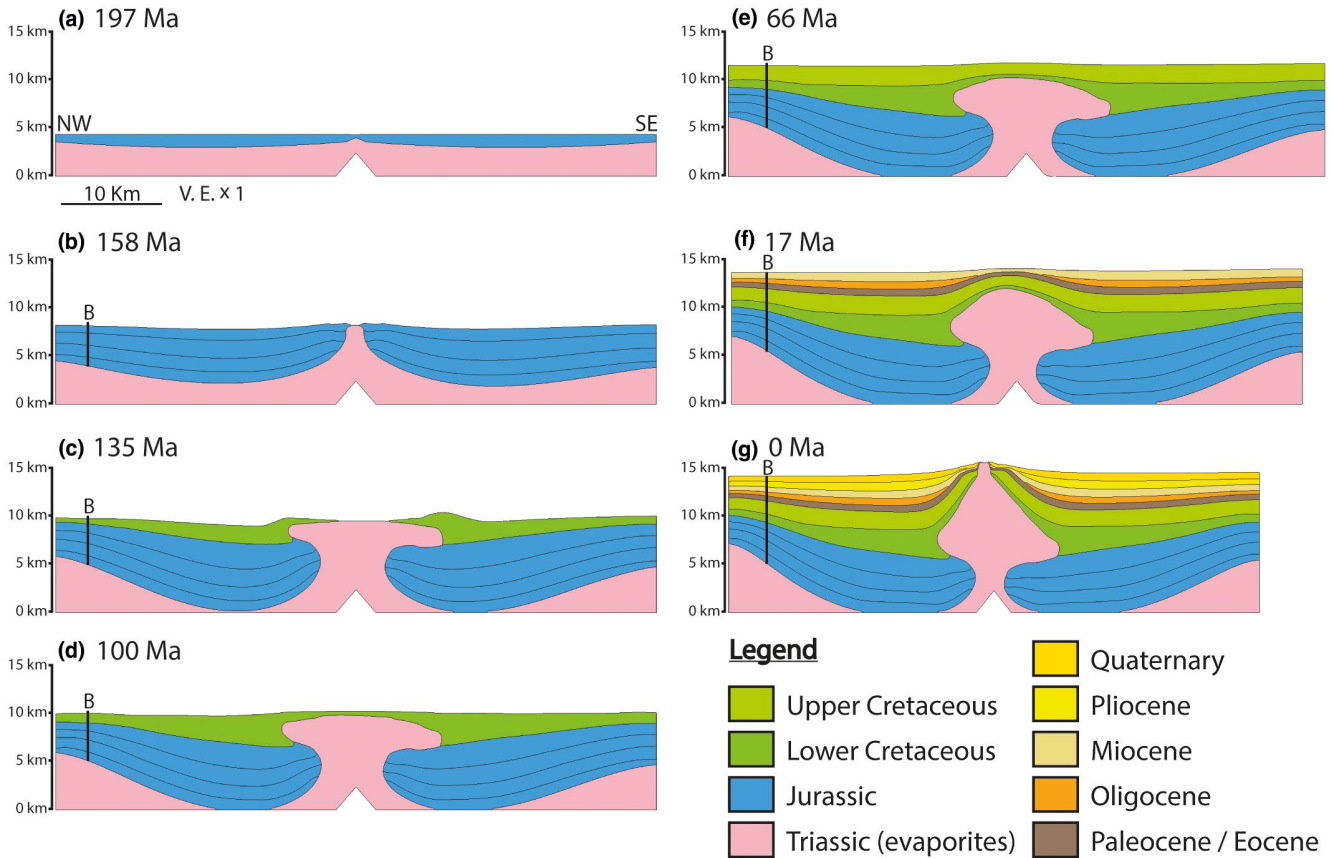


FIGURE 9 Stages of MV4 model where we use the burial history curve from the NW end of the basin (Figure 5b) applied at location B, together with a thicker initial salt source layer compared to the BC model (Figure 4a). (a) Initial geometry representing the top Triassic, with salt layer (pink) and initial thin layer of Jurassic sediments (blue); (b) Salt diapir reaches the sea floor at the end of Jurassic; (c) Salt forms overhangs at both sides, buried by Early-Cretaceous sediments (dark green). Source layer welds. (d) Further Early-Cretaceous sedimentation buries the diapir. Salt from pedestals increases overhang thickness; (e) Late-Cretaceous sedimentation (light green) drive bulging of diapir crest. Shortening begins; (f) Shortening narrows the diapir stem and drives salt from overhangs toward the diapir centre. Salt bulges upward; (g) Salt pierces the roof and upbuilds to the surface at present day. [Corrections updated on 25 July 2021, after initial online publication: Figure 9 caption has been corrected in this version.]

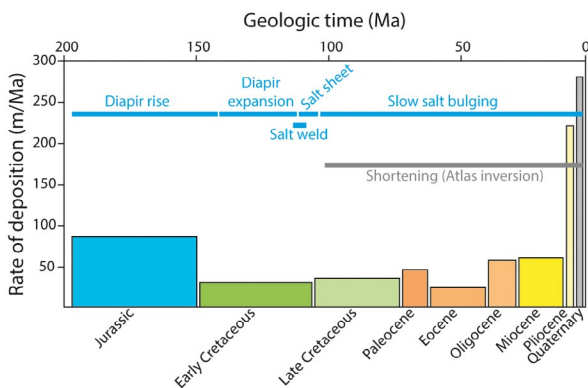


FIGURE 10 Rate of deposition for different geologic intervals from Jurassic until present day. Each interval is represented by a coloured block, the width of which is proportional to the duration of the geologic interval. The application of the tectonic shortening in the model is represented by the grey horizontal bar. The different diapir evolution phases are shown by the blue horizontal bars. [Corrections updated on 25 July 2021, after initial online publication: Figure 10 caption has been corrected in this version.]

basin (location Z; Figure 3). This model aims to reproduce the Western diapir and explore the effect of deposition history on the evolution of a salt diapir.

- MV5: we reduce the sedimentation rates for Pliocene and Quaternary from 620 and 700 m/Myr, respectively, to 61 m/Myr. The original values come from the extraction of the layer thicknesses from the kinematic restoration model. However, they are interpreted to be unrealistic. The new values for this model are more in line to the sedimentation rates for Oligocene and Miocene.

5 | EVOLUTIONARY MODEL RESULTS

The prograding sediment wedge imposes a differential load on the salt layer. The resulting shear (differential) stress drives viscous salt flow. The average salt differential stress in the model varies between 0.05 and 1 MPa and is comparable

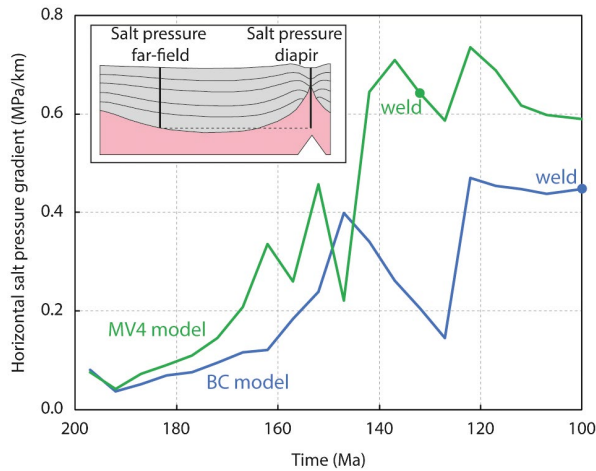


FIGURE 11 Comparison of horizontal salt pressure gradient between BC model (blue line) and MV4 model (green line). We define horizontal salt pressure gradient as the difference between the sediment overburden load on salt away from the diapir and the salt pressure inside the diapir at the same depth (inset). The higher sedimentation rates in model MV4 generate a consistently higher horizontal salt pressure gradient with time. The point in each line represents the time when the source layer welds. [Corrections updated on 25 July 2021, after initial online publication: Figure 11 caption has been corrected in this version.]

with published values (e.g. Schlöder & Urai, 2007). Despite its low value, this shear stress is able to mobilize the salt, given the salt's average viscosity. The relatively low strain rates and low upper crustal temperatures used in this study yield an average salt viscosity between 10^{17} and 10^{19} Pa·s, consistent with typical values reported for salt rocks (Hamilton-Wright et al., 2019; Marketos et al. 2016; Rowan et al. 2019; van Keken et al. 1993).

5.1 | Base-case model results

The deposition of the earliest Jurassic sediments results in a differential overburden load between the salt seed (initial salt dent; dashed circle in Figure 4a) and the topographic lows on the salt top surface, triggering the salt flow into a diapir (Figure 6a,b). Further Jurassic deposition drives salt from the source layer into the diapir, which widens and rises, reaching the surface at 145 Ma (Figure 6b). At this time, the upper half of the diapir is narrow compared to the lower half and the 6.5 km thick pedestal (triangular-shaped base connecting the diapir with the salt source layer; Vendeville & Nilsen, 1993). The thick pedestal allows salt to flow from the source layer into the diapir. At 123 Ma (Early Cretaceous, Figure 6c), the diapir morphology changes: the diapir remains at surface but the upper part has grown considerably wider relative to the previous time illustrated in Figure 6b. At 123 Ma (Figure 6c),

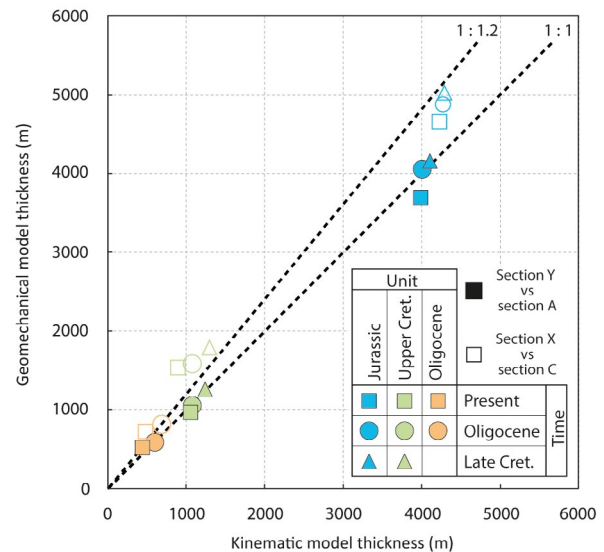


FIGURE 12 Comparison of layer thickness predicted by the kinematic restoration model (Figure 3) and the evolutionary geomechanical model (Figure 6) at 2 locations: (a) far from the diapir above a salt high (Y vs. A in Figure 3 & 6; solid shapes); and (b) near the diapir, above a salt weld (X vs. C in Figure 3 & 6; empty shapes). Layers considered: Jurassic, Upper Cretaceous and Oligocene units (blue, green and orange colours, respectively). Comparison times: Late Cretaceous, Oligocene and present day (triangular, circle and square shapes, respectively). Points on the 1:1 dashed line indicate agreement between the two models. Points closer to the 1:1.2 dashed line indicate that the evolutionary geomechanical model predicts more compression. [Corrections updated on 25 July 2021, after initial online publication: Figure 12 caption has been corrected in this version.]

the salt pedestal is still wider than the diapir; however, the source layer has thinned significantly.

At 100 Ma (end of Early Cretaceous, Figure 6d), the source layer welds along both sides of the diapir, leaving the pedestal completely isolated. However, a significant volume of salt exists in the pedestal, which allows for the diapir to continue growing and for salt to flow on the basin surface. This forms a salt sheet downslope (salt breadth several times greater than its thickness; Jackson & Hudec, 2017) and an overhang upslope (enlarged periphery of the diapir crest; Jackson & Hudec, 2017; Figure 6d). In our case, the salt sheet developed downslope has a total breadth of approximately 8 km and a thickness of 2 km. Deposition of the Upper Cretaceous (100–66 Ma; Figure 6e) buries the salt. However, the diapir keeps rising and thickening the salt sheet by depleting salt from the pedestals and thinning the diapir stem (slender part of the salt diapir connecting its upper part with the pedestal; Jackson & Hudec, 2017). Further salt flow is facilitated by the regional shortening, which is activated during the Late Cretaceous stage. This shortening, which remains active to the present day (Figure 6f,g), continues to narrow the diapir stem and to drive the salt upwards. In addition, it drives salt flow from the salt sheets towards

the centre of the diapir. As a result, the diapir crest bulges upwards, despite the subsequent deposition of Paleocene to Quaternary layers.

5.2 | MV1 results (Shortening rate)

There is evidence, in many salt basins, that salt flow can be driven by tectonic shortening (Brun & Fort, 2004; Dooley et al. 2009; Koyi, 1998; Nilsen et al., 1996; Vendeville & Nilsen, 1993). Shortening is documented for the Tarfaya basin (Michard et al. 2008; Tari & Jabour, 2013; Wenke et al. 2011), but the history and rate of deformation during shortening are not confidently known. In this model variant, we use a sigmoidal shortening curve (dashed line, Figure 4c) instead of the exponential shortening curve used in BC (solid line, Figure 4c) while maintaining the same timing and total magnitude of shortening (5 km). This sigmoidal shape does not greatly alter the kinematics of the salt diapir and its end geometry (Figure 7a,b), for the given shortening and deposition rates, and the timing of shortening application.

We do find, however, that the different shortening rates (Figure 4c) significantly impact the present-day stress state (Figure 8, also Figure C1, Appendix C). We use the horizontal-to-vertical effective stress ratio K (colour contours, Figure 8) to illustrate how stresses change compared to the uniaxial state ($K_0 = 0.8$, light blue colours, Figure 8). Effective stress ratio values lower than 0.8 (darker blue colours) indicate a decrease in horizontal effective stress (σ'_h) relative to the vertical effective stress (σ'_v). $K = 1$ (green colours, Figure 8) indicates a uniform stress state ($\sigma'_h = \sigma'_v$). K higher than 1 (warm colours, Figure 8) indicates that σ'_h is higher than σ'_v . In the BC model, the values of K are higher than 1.3 near the salt crest and around 1.2 at the salt flanks. Instead, in model VM1, the values of K near the salt crest are around 0.6 (below uniaxial), with uniaxial values at the salt flanks.

5.3 | MV2 results (Basal triangular feature)

Regional seismic interpretation and regional constraints (Le Roy & Piqué, 2001; Tari & Jabour, 2013) indicate that both the Sandia and the Western diapirs developed over the highest points of rotated fault blocks (Figure 3). However, seismic image quality below salt in this area is poor and the presence of this basal high cannot be confirmed. We investigate whether salt base highs have a notable effect on the evolution of the diapir by replacing the basal indentation present in the BC model (Figure 7a) with a flat salt base in MV2 model (Figure 7c). The general characteristics of the resulting diapir in MV2 are similar to the BC one: The diapir rises early during the deposition of Jurassic sediments, a salt

sheet develops downslope during the Early Cretaceous and the source layer welds at both sides of the diapir pedestal at the same interval. However, the diapir at MV2 reaches the surface earlier than the BC diapir and has a thicker upper part at the end of Jurassic. At Early Cretaceous time, the diapir expands and forms shorter salt sheets at both sides. The burial of the structure happens shortly after that time, contrary to the BC model, where the salt is completely buried at 101 Ma (beginning of Late Cretaceous). The final diapir geometry in MV2 is 400 m shorter and with a salt stem twice as thick compared to the BC diapir (Figure 7a,c).

5.4 | MV3 results (Temperature)

The temperature gradient present in the basin affects the viscosity of the salt. The 31°C/km gradient used in the BC model is a lower bound for the study area (Rimi, 2001; Zarhloule et al., 2010) based on an integrated 2D and 3D petroleum system model for thermal maturity evaluation. We investigate the effect of increasing the temperature gradient to 36°C/km on the evolution of the salt diapir and its final geometry (model MV3; Figure 7d). The resulting diapir rises during the Jurassic and generates a salt sheet during Early Cretaceous times, similar to the BC model. The source layer also welds during Early Cretaceous. The main effect of the higher temperature gradient in model MV3 is that the diapir upbuilds to the surface before the end of Jurassic, faster than the BC diapir (Figure 6b), and has a wider upper half. This small increase in salt flow velocity results from the fact that the salt viscosity is at most an order of magnitude lower in the MV3 compared to the BC model (10^{17} and 10^{18} Pa·s), because of the higher temperature. The lateral expansion of the upper half part of the diapir starts at 131 Ma (Early Cretaceous) and generates a shorter salt sheet at the NW side and a shorter overhang at the SE at 122 Ma (Early Cretaceous). The structure is buried by ongoing sedimentation just after the formation of the salt sheet and overhang. The final diapir geometry in model MV3 is 600 m shorter and with a salt stem twice as thick compared to the BC diapir (Figure 7a,d).

5.5 | MV4 results (Western diapir)

According to the kinematic restoration model, Jurassic and Cretaceous times have a higher sedimentation rate at location Z (basinward part of the studied cross section; Figure 3), relative to location Y. These higher sedimentation rates imply a larger accommodation space, hence larger volume of salt withdrawal at the basinward end of the basin. To explore this, we build the evolutionary model MV4 using the burial history (Figure 5b) along location Z in the kinematic restoration model (Figure 3) with a thicker initial salt layer (Figure 9a).

Similar to model BC, the deposition of the first Jurassic sediments in model MV4 results in a differential overburden stress between the salt seed and the topographic lows on the salt top surface, initiating salt flow towards the diapir (Figure 9a,b). The subsequent deposition of Jurassic layers drives the salt from the source layer into the diapir. The fast deposition (Figure 5b) allows the diapir to upbuild to the surface at 158 Ma, before the end of Jurassic (Figure 9b). At this time, the upper diapir half is narrower than its lower half and pedestal. At 135 Ma (Early Cretaceous, Figure 9c), the salt source layer is significantly thinned at both sides of the diapir. The upper half of the salt structure remains at the surface and has grown wider and developed overhangs at both sides. The sedimentation of Early Cretaceous partially buries these overhangs, limiting their lateral extension. By 100 Ma (Figure 9d), Lower Cretaceous sediments have buried the diapir. However, a significant volume of salt remains in the pedestals, and continues to drive salt flow to the upper parts of the diapir. As a result, the diapir crest inflates and the overhangs continue to grow. The onset of regional shortening (Figure 4c, solid curve) during Late Cretaceous (66 Ma; Figure 9e) both narrows the diapir stem and drives salt from the overhangs towards the upper diapir. This inward and upward salt flow volume is sufficient to sustain a gradual rise of the diapir through the sedimentary roof. Salt eventually upbuilds to the present-day surface at 5 Ma (Figure 9g).

5.6 | MV5 results (Plio-Quaternary sedimentation rates)

The sedimentation rates extracted from the kinematic restoration model at location Y (Figure 3) present very high values of 620 and 700 m/Myr for the time intervals of Pliocene and Quaternary respectively (light yellow and grey blocks, Figure 10). We use the model MV5 to reduce the Plio-Quaternary sedimentation rates to equal the value of the Miocene rate (61 m/Myr, yellow block, Figure 10). The resulting present-day geometry of the basin in the model MV5 is not notably different from the BC model. This is because the duration of the Plio-Quaternary interval is short (5.3 Myr). Despite the high sedimentation rates, the sediment layer thicknesses are small, and the additional overburden load does not produce any notable effect on the kinematics of the system.

6 | DISCUSSION

6.1 | The role of sedimentation rate on diapir evolution

Sedimentation rates of the Tarfaya basin are a key driver for the system evolution. The rapid sedimentation at the

beginning of the simulation (Jurassic) mobilizes the salt from the source layer towards the central part of the basin. We quantify the effect of sedimentation on salt flow by plotting the salt horizontal pressure gradient (Figure 11). We calculate this gradient by subtracting the sediment overburden load on salt away from the diapir from the salt pressure inside the diapir at the same depth (Figure 11-inset). The salt gradient increases rapidly during the Jurassic (blue line, Figure 11), illustrating the acceleration of salt flow towards the diapir. As a result, by the end of the Jurassic interval (at 145 Ma), the diapir has upbuilt to the sea floor and a significant volume of salt has accumulated in the salt pedestals (Figure 6b). Salt in this broad pedestal area further maintains the diapir rise during the Cretaceous interval, despite decrease in sedimentation rates (87 m/Myr during Jurassic, blue block in Figure 10 vs. 30 m/Myr during Cretaceous, dark and light green blocks in Figure 10).

The evolution of model MV4 (Figure 9) further illustrates the importance of the sedimentation rates in the diapir evolution. In this model, the higher sedimentation rates during Jurassic result in a higher horizontal pressure gradient in the salt source layer (green vs. blue line, Figure 11). This promotes a faster salt flow, and a greater amount of salt pumped into the MV4 diapir, despite the fact that the source layer in MV4 welds much earlier than the one in the BC model. As a result, salt in MV4 not only accumulates in the pedestals and upbuilds to the sea floor but also forms diapir overhangs (Figure 9d). This geometry allows additional salt volume to be stored in the diapir and be readily available to flow in response to the later applied shortening. As a result, the system is able to sustain a second phase of diapir rise to the present-day sea floor. Contrary to MV4 diapir, the BC diapir gets buried during Cretaceous times (Figure 6e) because a sufficient salt volume could not be mobilized.

6.2 | Comparison of layer thicknesses estimated by kinematic restoration and predicted by evolutionary geomechanical model

Kinematically constrained geomechanical models, such as that presented here, incorporate the strength and deformation characteristics of sediments in the study of a salt basin evolution. We demonstrate this contribution by comparing the layer thicknesses from the BC model against the kinematic restoration model at: (a) location close to the diapir, near the tip of the source layer weld (locations X and C, Figures 3 and 6 respectively); (b) location far from the diapir, above a salt high, where the salt source layer is not depleted (locations Y and A, same as the location used to constrain the evolutionary model; Figures 3 and 6 respectively). Whereas both approaches predict the same thicknesses away from the diapir (solid shapes in Figure 12 fall on the 1:1 line), the geomechanical model

predicts 20% thicker layers closer to the diapir (empty shapes in Figure 12 fall around the 1:1.2 line).

We perform this comparison for the Jurassic, Cretaceous and Oligocene sediments (colours blue, green and orange in Figure 12 respectively) and for the time intervals of Late Cretaceous, Oligocene and present day (triangle, circle and square shapes in Figure 12 respectively). Consider, for example, the Jurassic sediments (blue shapes). Near the salt structure (empty shapes), at the end of Late Cretaceous (empty blue triangle, Figure 12), the restoration model provides a thickness of 4,300 m, whereas the evolutionary model predicts 5,000 m. The same is true for the Upper Cretaceous and Oligocene sediments (empty green and orange markers, respectively, Figure 12). These differences are associated with the depletion of the salt source layer and the formation of a salt weld during Cretaceous and highlight the importance of modelling the viscous salt flow and its response to sediment loading.

In addition, the geomechanical model predicts a notably higher compaction of the Jurassic layer between Late Cretaceous and present day (empty blue square, Figure 12). The final evolutionary model thickness is 4,600 m (8% compaction), compared to 4,200 m (2.3% compaction) in the restoration model. The source layer weld generates higher mean stresses near the tip and a zone of higher shear stress that radiates upwards from the weld (Heidari et al. 2016). The geomechanical model captures this contribution of mean and shear stress to compression, because it simulates sediments as porous elasto-plastic material. This additional sediment compaction cannot be accounted for in the restoration model.

6.3 | Influence of shortening rates on stress distribution

The geomechanical model provides the stress distribution around the salt structures resulting from the system evolution. This allows us to study the influence of shortening rates on the present-day stress state near the Sandia diapir (Figure 8).

The exponential shortening curve (solid black line, Figure 4c) applied in the BC model (Figure 8a) results in an active regional compressive load at present day, which pressurizes the diapir salt. Because of the overburden thickness, the crest cannot expand, and instead loads the sediments around it. As a result, the stress ratio increases to values near 1 at the salt flanks (green/yellow contour colours, Figure 8a), and to $K = 1.4$ around the crest (orange contour colours, Figure 8a), illustrating increase in horizontal stress compared to its uniaxial value ($K_0 = 0.8$).

In contrast, the sigmoidal shortening curve (dashed black line, Figure 4c) applied in model MV1 (Figure 8b) results in decreasing shortening rates towards the end of the simulation and termination of shortening 2 Myr before present day. Because there is no active tectonic load, the diapir

deforms downward and outward to achieve a uniform stress state (Hooghorst et al. 2020). Consequently, the stress ratio at the crest decreases to values of K near 0.65, indicating decrease in horizontal stress (Figure 8b). Measurements in the Sandia-1 exploratory well (black circle, Figure 1) drilled in 2015 (Fernandez et al., 2015) show stress reduction above the Sandia diapir, indicating that a sigmoidal curve is more appropriate for this basin.

6.4 | Parameters with minor influence on the Tarfaya basin evolution

Despite the importance of shortening rates on the final stress state, they have minor effect on the final salt geometry (Figure 8 BC vs. MV1 models; solid vs. dashed line, Figure 4c). This is because shortening begins during the Late Cretaceous, whereas the salt system mainly develops between Jurassic and Late Cretaceous. The role of shortening is better highlighted in the Western diapir (MV4) model. In this case, because of the higher salt volume accumulated in the diapir, overhang and pedestal areas, the application of shortening is able to drive the salt to the present-day seafloor. The timing of shortening application, as well as the relative deposition and shortening rates affect the role of shortening in basin and diapir evolution.

The presence or absence of the salt base high does not greatly impact the evolution or final geometry of the diapir (BC model, Figure 7a vs. MV2 model, Figure 7c). However, salt flows easier into the MV2 diapir in the absence of a rotated fault block feature at the salt base (Figure 7c), causing an earlier maturation of the structure. In addition, the salt source layer welds at an earlier time (nearly 20 Myr earlier than BC model), preventing the diapir to rise further and generating a shorter, wider structure. In contrast, the presence of a salt base high (BC model, Figure 7a) delays the diapir rise. It should be noted that a salt base high may play a key role in focusing salt flow into a structure, whereas in both models, the diapir location is predefined with a seed in the initial geometry (Figure 4a).

Increase in temperature gradient in the salt does not greatly change the overall evolution or the final diapir geometry either (BC model, Figure 7a vs. MV3 model, Figure 7d). The temperature increase causes the salt viscosity to decrease, which facilitates salt flow into the diapir during Jurassic. This causes the diapir at MV3 to evolve faster, reaching the surface and welding the salt source layer at earlier times compared to the BC model. The resulting salt structure matures earlier, being buried by sediments during the Early Cretaceous, compared to the BC diapir that is buried during the Late Cretaceous. The final MV3 diapir geometry (Figure 7d) is shorter and wider compared to the BC structure (Figure 7a).

7 | MODELLING UNCERTAINTIES AND LIMITATIONS

The evolutionary models built in this study simplify the Atlas inversion and shortening into a continuous curve that extends from Late Cretaceous until the present day (Figure 4c). However, Atlasic shortening most probably happened in distinct pulses (El Harfi et al. 1996, 2001; Fraissinet et al. 1988; Frizon de Lamotte et al. 2000; Görler & Helmdach, 1988).

The simulations in this study are two-dimensional plane-strain models. They cannot account for any out-of-plane salt flow and require a wider source layer for the interpreted initial salt thickness. Hence, they overestimate the lateral extent of source layer withdrawal during the diapir rise. The models also simulate a salt wall, whereas Sandia diapir geometry is closer to a dome (Hooghorst et al. 2020). Evolutionary 3D models would represent more accurately the Tarfaya salt basin—but they are difficult to constrain and expensive to run.

Model input for the sediments has not been calibrated specifically for the study area, but it provides a good approximation of compressibility and strength for marine deposits (e.g. Heidari et al. 2019; Nikolinakou, Flemings, et al., 2018). The constitutive formulation does not account for strain softening of faulting. As a result, differential stresses may be unrealistically high in locations where faults would otherwise form.

Sediment geology has been simplified to a single shale lithology. Data from wells drilled on the continental shelf Cap Juby-1 well (black triangle, Figure 1) indicate the presence of carbonates between the Jurassic sediments; however, it is not clear whether such layers exist in the basinward location of the study area.

All models in this study are drained and do not model the generation of overpressures. Overpressures would prevent compression and reduce the accommodation space for each deposition stage (Heidari et al. 2019; Nikolinakou, Heidari, et al., 2018; Swarbrick et al. 2002). In addition, overpressures would decrease the strength of mudrocks by keeping the effective stress low, hence play a key role in the kinematics of the salt flow (Nikolinakou, Heidari, et al., 2018).

Despite these limitations, this study is one of the first efforts to incorporate the geologic constraints provided by a sequential kinematic restoration model into an evolutionary geomechanical model of a salt basin.

8 | CONCLUSIONS

We use burial history, sea floor geometry and tectonic loading extracted from a sequential kinematic restoration model to constrain a 2D geomechanical forward model and reproduce the evolution of the Sandia diapir (Tarfaya basin, NW African coast). The resulting final geometry of the geomechanical

model is comparable with the present-day interpretation of the Sandia diapir. We find that sedimentation rates are a key driver for the halokinetic evolution of the system: higher rates at the early stages of the salt diapir formation affect whether the diapir will get buried or upbuild to the sea floor, when the Atlas shortening is introduced later in the basin history. We also find that shortening rate histories significantly affect the present-day stress state above the Sandia diapir: a sigmoidal shortening curve leads to a decrease in horizontal stresses above the crest of the structure, which is in agreement with field observations from an exploratory well.

More broadly, we show that incorporation of burial and tectonic histories from a sequential kinematic restoration leads to more realistic evolutionary geomechanical models that predict interpreted present-day geometries of geologic structures and help illuminate the key drivers of their structural evolution. In turn, geomechanical models incorporate the mechanical interaction between salt and sediments and can provide valuable information on the evolution of stress, porosity and potentially pore pressure with time, ultimately providing a more complete picture of the basin history.

ACKNOWLEDGEMENTS

We are grateful to Repsol for granting access to the data of this study and for funding this work. We thank Pablo Hernandez for his contribution on building the sequential kinematic restoration model. We thank the UT GeoFluids consortium for their funding and continuous investment in this project. We sincerely thank Prof. Thigpen and Prof. Urai for their constructive criticism and review of the manuscript. We would also like to thank Rockfield for their support in the modelling using ELFEN licences and their help solving software-related doubts and numerical issues.

PEER REVIEW

The peer review history for this article is available at <https://publons.com/publon/10.1111/bre.12547>.

DATA AVAILABILITY STATEMENT

The data that support the findings of this study are available from the corresponding author upon reasonable request.

ORCID

Jean Joseph Hooghorst  <https://orcid.org/0000-0001-5975-6169>

Maria A. Nikolinakou  <https://orcid.org/0000-0003-3194-3477>

Oscar Fernandez  <https://orcid.org/0000-0003-1584-2684>

Peter B. Flemings  <https://orcid.org/0000-0002-5377-3694>

Alejandro Marcuello  <https://orcid.org/0000-0002-6216-4436>

REFERENCES

- Albertz, M., & Beaumont, C. (2010). An investigation of salt tectonic structural styles in the Scotian Basin, offshore Atlantic Canada: 2. Comparison of observations with geometrically complex numerical models. *Tectonics*, 29. <https://doi.org/10.1029/2009TC002540>
- Beaumont, C., Muñoz, J. A., Hamilton, J., & Fullsack, P. (2000). Factors controlling the Alpine evolution of the central Pyrenees inferred from a comparison of observations and geodynamical models. *Journal of Geophysical Research: Solid Earth*, 105, 8121–8145. <https://doi.org/10.1029/1999JB900390>
- Ben-Awuah, J., Adda, G. W., Mijinyawa, A., Andriamihaja, S., & Siddiqui, N. (2013). 2D Basin modelling and petroleum system analysis of the triassic play in the hammerfest basin of the norwegian barents sea. *Research Journal of Applied Sciences, Engineering and Technology*, 6, 3137–3150. <https://doi.org/10.19026/rjaset.6.3615>
- Bolas, H. M. N., Hermanrud, C., & Teige, G. M. G. (2004). Origin of overpressures in shales : Constraints from basin modeling. *AAPG Bulletin*, 88, 193–211. <https://doi.org/10.1306/10060302042>
- Brun, J.-P., & Fort, X. (2004). Compressional salt tectonics (Angolan margin). *Tectonophysics*, 382, 129–150. <https://doi.org/10.1016/j.tecto.2003.11.014>
- Carracedo, J. C., & Perez-Torrado, F. J. (2013). Teide Volcano. J. C. Carracedo, & V. R. Troll (Eds.), *Active volcanoes of the world*. .
- Corti, G., & Dooley, T. P. (2015). Lithospheric-scale centrifuge models of pull-apart basins. *Tectonophysics*, 664, 154–163. <https://doi.org/10.1016/j.tecto.2015.09.004>
- Crook, A. J. L., Obradors-Prats, J., Somer, D., Peric, D., Lovely, P., & Kacwicz, M. (2018). Towards an integrated restoration/forward geomechanical modelling workflow for basin evolution prediction. *Oil & Gas Sciences and Technology – Revue d'IFP Energies Nouvelles*, 73, 19. <https://doi.org/10.2516/ogst/2018018>
- Crook, A. J. L., Willson, S. M., Yu, J. G., & Owen, D. R. J. (2006). Predictive modelling of structure evolution in sandbox experiments. *Journal of Structural Geology*, 28(5), 729–744. <https://doi.org/10.1016/j.jsg.2006.02.002>
- Davison, I. (2005). Central Atlantic margin basins of North West Africa: Geology and hydrocarbon potential (Morocco to Guinea). *Journal of African Earth Sciences*, 43, 254–274. <https://doi.org/10.1016/j.jafrearsci.2005.07.018>
- Dietl, C., & Koyi, H. (2011). Sheets within diapirs - Results of a centrifuge experiment. *Journal of Structural Geology*, 33, 32–37. <https://doi.org/10.1016/j.jsg.2010.10.010>
- Dooley, T. P., & Hudec, M. R. (2017). The effects of base-salt relief on salt flow and suprasalt deformation patterns - Part 2: Application to the eastern Gulf of Mexico. *Interpretation*, 5, SD25–SD38. <https://doi.org/10.1190/INT-2016-0088.1>
- Dooley, T. P., Hudec, M. R., Carruthers, D., Jackson, M. P. A., & Luo, G. (2017). The effects of base-salt relief on salt flow and suprasalt deformation patterns - Part 1: Flow across simple steps in the base of salt. *Interpretation*, 5, SD1–SD23. <https://doi.org/10.1190/INT-2016-0087.1>
- Dooley, T. P., Jackson, M. P. A., & Hudec, M. R. (2009). Inflation and deflation of deeply buried salt stocks during lateral shortening. *Journal of Structural Geology*, 31, 582–600. <https://doi.org/10.1016/j.jsg.2009.03.013>
- Dooley, T. P., Jackson, M. P. A., & Hudec, M. R. (2015). Breakout of squeezed stocks: Dispersal of roof fragments, source of extrusive salt and interaction with regional thrust faults. *Basin Research*, 27, 3–25. <https://doi.org/10.1111/bre.12056>
- Dooley, T. P., & Schreurs, G. (2012). Analogue modelling of intraplate strike-slip tectonics: A review and new experimental results. *Tectonophysics*, 574–575, 1–71. <https://doi.org/10.1016/j.tecto.2012.05.030>
- Durand-Riard, P., Shaw, J. H., Plesch, A., & Lufadeju, G. (2013). Enabling 3D geomechanical restoration of strike- and oblique-slip faults using geological constraints, with applications to the deep-water Niger Delta. *Journal of Structural Geology*, 48, 33–44. <https://doi.org/10.1016/j.jsg.2012.12.009>
- Dusseault, M. B., Maury, V., Sanfilippo, F., & Santarelli, F. J. (2004, June). *Drilling Around Salt: Risks, Stresses, And Uncertainties*. Paper presented at the Gulf Rocks 2004, the 6th North America Rock Mechanics Symposium (NARMS), ARMA-04-647, Houston, Texas.
- El Harfi, A., Lang, J., & Salomon, J. (1996). Cenozoic continental infilling of the Ouarzazate foreland basin. Implications for the structural evolution of the Central High Atlas Mountains (Morocco). *Comptes Rendus De L'academie De Sciences - Serie Ila: Sciences De La Terre Et Des Planetes*, 323, 623–630.
- El Harfi, A., Lang, J., Salomon, J., & Chellai, E. H. (2001). Cenozoic sedimentary dynamics of the Ouarzazate foreland basin (Central High Atlas Mountains, Morocco). *International Journal of Earth Sciences*, 90, 393–411. <https://doi.org/10.1007/s005310000115>
- Farzipour-Saein, A., & Koyi, H. (2014). Effect of lateral thickness variation of an intermediate decollement on the propagation of deformation front in the Lurestan and Izeh zones of the Zagros fold-thrust belt, insights from analogue modeling. *Journal of Structural Geology*, 65, 17–32. <https://doi.org/10.1016/j.jsg.2014.03.004>
- Fernandez, N., & Kaus, B. J. P. (2015). Pattern formation in 3-D numerical models of down-built diapirs initiated by a Rayleigh-Taylor instability. *Geophysical Journal International*, 202, 1253–1270. <https://doi.org/10.1093/gji/ggv219>
- Fernandez, O., Harrold, T., Ferguson, W., Gonzalez, H., & Bere, A. (2015). Three-dimensional Prediction of Stress Distribution Above a Salt Diapir - Application to a Deepwater Hydrocarbon Exploration Well. In: 77th EAGE Conference and Exhibition 2015: Earth Science for Energy and Environment. 965–969. <https://doi.org/10.3997/2214-4609.201412715>
- Fraissinet, C., El Zouine, M., Morel, J., Poisson, A., Andrieux, J., & Faure-Muret, A. (1988). Structural evolution of the southern and northern Central High Atlas in paleogene and Mio-Pliocene times. In V. H. Jacobshagen (Ed.), *The atlas system of morocco: studies on its geodynamic evolution* (pp. 273–291). . <https://doi.org/10.1007/BFb0011597>
- Fredrich, J. T., Coblenz, D., Fossum, A. F., & Thorne, B. J. (2003). Stress perturbations adjacent to salt bodies in the deepwater Gulf of Mexico. Paper SPE-84554 presented at the SPE Annual Technical Conference and Exhibition, 5–8 October 2003, Denver, CO. <https://doi.org/10.2118/84554-MS>
- Fredrich, J. T., Engler, B. P., Smith, J. A., Onyia, E. C., & Tolman, D. N. (2007). Pre-drill estimation of subsalt fracture gradient: Analysis of the spa prospect to validate nonlinear finite element stress analyses. *Paper SPE-105763 presented at the SPE/IADC Drilling Conference, 20–22 February 2007, Amsterdam, The Netherlands*. <https://doi.org/10.2118/105763-MS>
- Fredrich, J. T., Fossum, A. F., & Hickman, R. J. (2007). Mineralogy of deepwater Gulf of Mexico salt formations and implications for constitutive behavior. *Journal of Petroleum Science and Engineering*, 57, 354–374. <https://doi.org/10.1016/j.petrol.2006.11.006>

- Frizon de Lamotte, D., Saint Bezar, B., Bracène, R., & Mercier, E. (2000). The two main steps of the Atlas building and geodynamics of the western Mediterranean. *Tectonics*, *19*, 740–761. <https://doi.org/10.1029/2000TC900003>
- Frizon de Lamotte, D., Zizi, M. et al (2008). The Atlas System. In J.-C. Otto, & R. Dikau (Eds.), *Continental evolution: The geology of morocco* (pp. 133–202). . https://doi.org/10.1007/978-3-540-77076-3_4
- Görlér, K., Helmdach, F.-F. et al (1988). The uplift of the central High Atlas as deduced from neogene continental sediments of the Ouarzazate province, Morocco BT - The Atlas System of Morocco: Studies on its Geodynamic Evolution. In: Jacobshagen, V. H. (Ed.). Berlin, Heidelberg, Springer Berlin Heidelberg, 359–404.
- Goteti, R., Ings, S. J., & Beaumont, C. (2012). Development of salt minibasins initiated by sedimentary topographic relief. *Earth and Planetary Science Letters*, *339–340*, 103–116. <https://doi.org/10.1016/j.epsl.2012.04.045>
- Gouiza, M. (2011). Mesozoic Source-to-Sink Systems in NW Africa: Geology of Vertical Movements during the Birth and Growth of the Moroccan Rifted Margin. Ph.D Thesis. VU University Amsterdam.
- Gradmann, S., & Beaumont, C. (2012). Coupled fluid flow and sediment deformation in margin-scale salt-tectonic systems: 2. Layered sediment models and application to the northwestern Gulf of Mexico. *Tectonics*, *31*, 1–22. <https://doi.org/10.1029/2011TC003035>
- Gradmann, S., Beaumont, C., & Ings, S. J. (2012). Coupled fluid flow and sediment deformation in margin-scale salt-tectonic systems: 1. Development and application of simple, single-lithology models. *Tectonics*, *31*, 1–17. <https://doi.org/10.1029/2011TC003033>
- Gutierrez, M., & Wangen, M. (2005). Modeling of compaction and overpressuring in sedimentary basins. *Marine and Petroleum Geology*, *22*, 351–363. <https://doi.org/10.1016/j.marpetgeo.2005.01.003>
- Hamilton-Wright, J., Dee, S., von Nicolai, C., & Johnson, H. (2019). Investigating controls on salt movement in extensional settings using finite element modelling. *Petroleum Geoscience*, *25*, 258–271. <https://doi.org/10.1144/petgeo2018-119>
- Hantschel, T., & Kauerauf, A. (2009). Fundamentals of Basin and Petroleum Systems Modeling. Berlin, Heidelberg, Springer Berlin Heidelberg. <https://doi.org/10.1007/978-3-540-72318-9>
- Heidari, M., Nikolinakou, M. A., & Flemings, P. B. (2018). Coupling geomechanical modeling with seismic pressure prediction. *Geophysics*, *83*, B253–B267. <https://doi.org/10.1190/geo2017-0359.1>
- Heidari, M., Nikolinakou, M. A., Flemings, P. B., & Hudec, M. R. (2017). A simplified stress analysis of rising salt domes. *Basin Research*, *29*, 363–376. <https://doi.org/10.1111/bre.12181>
- Heidari, M., Nikolinakou, M. A., Hudec, M. R., & Flemings, P. B. (2016). Tectonophysics Geomechanical analysis of a welding salt layer and its effects on adjacent sediments. *Tectonophysics*, *683*, 172–181. <https://doi.org/10.1016/j.tecto.2016.06.027>
- Heidari, M., Nikolinakou, M. A., Hudec, M. R., & Flemings, P. B. (2019). Influence of a reservoir bed on diapirism and drilling hazards near a salt diapir: A geomechanical approach. *Petroleum Geoscience*, *25*, 282–297. <https://doi.org/10.1144/petgeo2018-113>
- Hooghorst, J. J., Harrold, T. W. D., Nikolinakou, M. A., Fernandez, O., & Marcuello, A. (2020). Comparison of stresses in 3D v. 2D geomechanical modelling of salt structures in the Tarfaya Basin, West African Coast. *Petroleum Geoscience*, *26*, 36–49. <https://doi.org/10.1144/petgeo2018-095>
- Hubbert, M. K. (1937). Theory of scale models as applied to the study of geologic structures. *Geological Society of America Bulletin*, *48*, 1459–1520. <https://doi.org/10.1130/GSAB-48-1459>
- Hubbert, M. K. (1951). Mechanical basis for certain familiar geologic structures. *Bulletin of the Geological Society of America*, *62*, 355–372.
- Hudec, M. R., & Jackson, M. P. A. (2004). Regional restoration across the Kwanza Basin, Angola: Salt tectonics triggered by repeated uplift of a metastable passive margin. *AAPG Bulletin*, *88*, 971–990. <https://doi.org/10.1306/02050403061>
- Jackson, M. P. A., & Hudec, M. R. (2017). *Salt tectonics. Principles and practice*.
- Kaus, B. J. P., Steedman, C., & Becker, T. W. (2008). From passive continental margin to mountain belt: Insights from analytical and numerical models and application to Taiwan. *Physics of the Earth and Planetary Interiors*, *171*, 235–251. <https://doi.org/10.1016/j.pepi.2008.06.015>
- Koyi, H. (1997). Analogue modelling: From a qualitative to a quantitative technique - A historical outline. *Journal of Petroleum Geology*, *20*, 223–238. <https://doi.org/10.1111/j.1747-5457.1997.tb00774.x>
- Koyi, H. (1998). The shaping of salt diapirs. *Journal of Structural Geology*, *20*, 321–338. [https://doi.org/10.1016/S0191-8141\(97\)00092-8](https://doi.org/10.1016/S0191-8141(97)00092-8)
- Le Roy, P., & Piqué, A. (2001). Triassic-Liassic western Moroccan synrift basins in relation to the Central Atlantic opening. *Marine Geology*, *172*, 359–381. [https://doi.org/10.1016/S0025-3227\(00\)00130-4](https://doi.org/10.1016/S0025-3227(00)00130-4)
- Maerten, L., & Maerten, F. (2006). Chronologic modeling of faulted and fractured reservoirs using geomechanically based restoration: Technique and industry applications. *AAPG Bulletin*, *90*, 1201–1226. <https://doi.org/10.1306/02240605116>
- Marketos, G., Spiers, C. J., & Govers, R. (2016). Impact of rock salt creep law choice on subsidence calculations for hydrocarbon reservoirs overlain by evaporite caprocks. *Journal of Geophysical Research: Solid Earth*, *121*, 4249–4267. <https://doi.org/10.1002/2016JB012892>
- Massoli, D., Koyi, H. A., & Barchi, M. R. (2006). Structural evolution of a fold and thrust belt generated by multiple décollements: Analogue models and natural examples from the Northern Apennines (Italy). *Journal of Structural Geology*, *28*, 185–199. <https://doi.org/10.1016/j.jsg.2005.11.002>
- McGuinness, D. B., & Hossack, J. R. (1993). The Development of Allochthonous Salt Sheets as Controlled by the Rates of Extension, Sedimentation, and Salt Supply. Rates of Geologic Processes, Tectonics, Sedimentation, Eustasy and Climate - Implications for Hydrocarbon Exploration. 14th Annual, 127–139. <https://doi.org/10.5724/gcs.93.14.0127>
- McKenzie, D. (1978). Some remarks on the development of sedimentary basins. *Earth and Planetary Science Letters*, *40*, 25–32. [https://doi.org/10.1016/0012-821X\(78\)90071-7](https://doi.org/10.1016/0012-821X(78)90071-7)
- Michard, A., Saddiqi, O., Chalouan, A., & Frizon de Lamotte, D. (2008). Lecture Notes in Earth Sciences. In J.-C. Otto, & R. Dikau (Eds.), *Continental evolution: The geology of morocco*. . <https://doi.org/10.1007/978-3-540-77076-3>
- Moretti, I., & Guiton, M. L. E. (2006). KINE3D: A new 3D restoration method based on a mixed approach linking geometry and geomechanics. *Oil & Gas Sciences and Technology – Revue d'IFP Energies Nouvelles*, *61*, 277–289. <https://doi.org/10.2516/ogst:2006021>
- Munson, D. E. (1997). Constitutive model of creep in rock salt applied to underground room closure. *International Journal of Rock Mechanics and Mining Sciences & Geomechanics Abstracts*, *34*, 233–247. [https://doi.org/10.1016/S0148-9062\(96\)00047-2](https://doi.org/10.1016/S0148-9062(96)00047-2)

- Munson, D. E., & Dawson, P. R. (1979). Constitutive model for the low temperature creep of salt (with application to WIPP). SAND79-1853. Sandia National Laboratories, Albuquerque, NM. 31.
- Nikolinakou, M. A., Flemings, P. B., Heidari, M., & Hudec, M. R. (2018). Stress and Pore Pressure in Mudrocks Bounding Salt Systems. *Rock Mechanics and Rock Engineering*, *51*, 3883–3894. <https://doi.org/10.1007/s00603-018-1540-z>
- Nikolinakou, M. A., Heidari, M., Flemings, P. B., & Hudec, M. R. (2018). Geomechanical modeling of pore pressure in evolving salt systems. *Marine and Petroleum Geology*, *93*, 272–286. <https://doi.org/10.1016/j.marpetgeo.2018.03.013>
- Nikolinakou, M. A., Heidari, M., Hudec, M. R., & Flemings, P. B. (2017). Initiation and growth of salt diapirs in tectonically stable settings: Upbuilding and megafaults. *AAPG Bulletin*, *101*, 887–905. <https://doi.org/10.1306/09021615245>
- Nikolinakou, M. A., Hudec, M. R., & Flemings, P. B. (2014). Comparison of evolutionary and static modeling of stresses around a salt diapir. *Marine and Petroleum Geology*, *57*, 537–545. <https://doi.org/10.1016/j.marpetgeo.2014.07.002>
- Nilforoushan, F., & Koyi, H. A. (2007). Displacement fields and finite strains in a sandbox model simulating a fold-thrust-belt. *Geophysical Journal International*, *169*, 1341–1355. <https://doi.org/10.1111/j.1365-246X.2007.03341.x>
- Nilsen, K. T., Johansen, J.-T., & Vendeville, B. C. (1996). Influence of regional tectonics on Halokinesis in the Nordkapp Basin, Barents Sea. In: M. P. A. Jackson, D. G. Roberts, & S. Snelson (Eds.), *Salt Tectonics: A Global Perspective*. *AAPG Memoir*, *65*, 413–436.
- Nygaard, R., Gutierrez, M., Bratli, R. K., & Hoeg, K. (2006). Brittle-ductile transition, shear failure and leakage in shales and mudrocks. *Marine and Petroleum Geology*, *23*, 201–212.
- Peric, D., & Crook, A. J. L. (2004). Computational strategies for predictive geology with reference to salt tectonics. *Computer Methods in Applied Mechanics and Engineering*, *193*(48-51), 5195–5222. <https://doi.org/10.1016/j.cma.2004.01.037>
- Piqué, A., Le Roy, P., & Amrhay, M. (1998). Transpressive synsedimentary tectonics associated with ocean opening: The Essaouira-Agadir segment of the Moroccan Atlantic margin. *Journal of the Geological Society*, *155*, 913–928. <https://doi.org/10.1144/gsjgs.155.6.0913>
- Ramberg, H. (1981). The role of gravity in orogenic belts. *Geological Society Special Publication*, *9*, 125–140. <https://doi.org/10.1144/GSL.SP.1981.009.01.11>
- Reber, J. E., Cooke, M. L., & Dooley, T. P. (2020). What model material to use? A Review on rock analogs for structural geology and tectonics. *Earth-Science Reviews*, *202*, 103107. <https://doi.org/10.1016/j.earscirev.2020.103107>
- Rimi, A. (2001). Carte du gradient géothermique au Maroc. *Bulletin De L'institut Scientifique, Rabat*, *23*, 1–6.
- Rockfield (2017) Elfen Explicit Manual (Version 4.10). Software, R. (ed.). Swansea, UK.
- Rowan, M. G. (1993). A systematic technique for the sequential restoration of salt structures. *Tectonophysics*, *228*, 331–348.
- Rowan, M. G., Giles, K. A., Hearon, T. E., & Fiduk, J. C. (2016). Megafaults adjacent to salt diapirs. *AAPG Bulletin*, *100*, 1723–1747. <https://doi.org/10.1306/05241616009>
- Rowan, M. G., & Ratliff, R. A. (2012). Cross-section restoration of salt-related deformation : Best practices and potential pitfalls. *Journal of Structural Geology*, *41*, 24–37. <https://doi.org/10.1016/j.jsg.2011.12.012>
- Rowan, M. G., Urai, J. L., Fiduk, J. C., & Kukla, P. A. (2019). Deformation of intrasalt competent layers in different modes of salt tectonics. *Solid Earth*, *10*, 987–1013. <https://doi.org/10.5194/se-10-987-2019>
- Schellart, W. P., & Strak, V. (2016). A review of analogue modelling of geodynamic processes: Approaches, scaling, materials and quantification, with an application to subduction experiments. *Journal of Geodynamics*, *100*, 7–32. <https://doi.org/10.1016/j.jog.2016.03.009>
- Schléder, Z., & Urai, J. L. (2007). Deformation and recrystallization mechanisms in mylonitic shear zones in naturally deformed extrusive Eocene-Oligocene rocksalt from Eyvanekey plateau and Garmsar hills (central Iran). *Journal of Structural Geology*, *29*, 241–255. <https://doi.org/10.1016/j.jsg.2006.08.014>
- Schreurs, G., Buitter, S. J. H., Boutelier, J., Burberry, C., Callot, J.-P., Cavozi, C., Cerca, M., Chen, J.-H., Cristallini, E., Cruden, A. R., Cruz, L., Daniel, J.-M., Da Poian, G., Garcia, V. H., Gomes, C. J. S., Grall, C., Guillot, Y., Guzmán, C., Hidayah, T. N., ... Yamada, Y. (2016). Benchmarking analogue models of brittle thrust wedges. *Journal of Structural Geology*, *92*, 116–139. <https://doi.org/10.1016/j.jsg.2016.03.005>
- Sclater, J. G., & Christie, P. A. F. (1980). Continental stretching: An explanation of the Post-Mid-Cretaceous subsidence of the central North Sea Basin. *Journal of Geophysical Research: Solid Earth*, *85*, 3711–3739. <https://doi.org/10.1029/JB085iB07p03711>
- Segura, J. M., Matos da Cruz, A., Stachlewski, G., Alvarellós, J., Vargas, P. E., & Lakshminantha, M. R. (2016). Fault stability assessment for well planning : a case study related to salt structures. American Rock Mechanics Association. Paper 16-518.
- Stigall, J., & Dugan, B. (2010). Overpressure and earthquake initiated slope failure in the Ursa region, northern Gulf of Mexico. *Journal of Geophysical Research*, *115*, B04101. <https://doi.org/10.1029/2009J B006848>
- Swarbrick, R. E., Osborne, M. J., & Yardley, G. S. (2002). Comparison of overpressure magnitude resulting from the main generating mechanisms generating mechanisms. *AAPG Memoir*, *76*, 1–12.
- Tari, G., & Jabour, H. (2013). Salt tectonics along the Atlantic margin of Morocco. *Geological Society, London, Special Publications*, *369*, 337–353. <https://doi.org/10.1144/SP369.23>
- Thibaut, M., Jardin, A., Faille, I., Willien, F., & Guichet, X. (2014). Advanced Workflows for Fluid Transfer in Faulted Basins. *Oil & Gas Science and Technology – Revue d'IFP Energies Nouvelles*, *69*, 573–584. <https://doi.org/10.2516/ogst/2014016>
- Thigpen, J. R., Roberts, D., Snow, J. K., Walker, C. D., & Bere, A. (2019). Integrating kinematic restoration and forward finite element simulations to constrain the evolution of salt diapirism and overburden deformation in evaporite basins. *Journal of Structural Geology*, *118*, 68–86. <https://doi.org/10.1016/j.jsg.2018.10.003>
- Trudgill, B. D., & Rowan, M. G. (2004). Integrating 3D seismic data with structural restorations to elucidate the evolution of a stepped counter-regional salt system, Eastern Louisiana Shelf, Northern Gulf of Mexico. *Geological Society, London, Memoirs*, *29*, 165–176. <https://doi.org/10.1144/GSL.MEM.2004.029.01.16>
- van Keken, P. E., Spiers, C. J., van den Berg, A. P., & Muzert, E. J. (1993). The effective viscosity of rocksalt: Implementation of steady-state creep laws in numerical models of salt diapirism. *Tectonophysics*, *225*, 457–476. [https://doi.org/10.1016/0040-1951\(93\)90310-g](https://doi.org/10.1016/0040-1951(93)90310-g)
- Vendeville, B. C., & Nilsen, K. (1993). Episodic growth of salt diapirs driven by horizontal shortening. In: *Salt, Sediment and Hydrocarbons*. Society of Economic Paleontologists and Mineralogists Gulf Coast Section, 285–295. <https://doi.org/10.5724/gcs.95.16.0285>

- Wenke, A., Zühlke, R., Jabour, H., & Kluth, O. (2011). High-resolution sequence stratigraphy in basin reconnaissance: Example from the Tarfaya Basin, Morocco. *First Break*, 29, 85–96.
- Willson, S. M., Fossum, A. F., & Fredrich, J. T. (2002). Assessment of salt loading on well casings. *Proceedings of the Drilling Conference*, 711–720, doi: 10.2523/74562-ms.
- Zarhloule, Y., Rimi, A., Boughriba, M., Barkaoui, A. E., & Lahrach, A. (2010). The Geothermal Research in Morocco : History of 40 Years. World Geothermal Congress.

How to cite this article: Hooghvorst JJ, Nikolinakou MA, Harrold TWD, Fernandez O, Flemings PB, Marcuello A. Geologically constrained evolutionary geomechanical modelling of diapir and basin evolution: A case study from the Tarfaya basin, West African coast. *Basin Res.* 2021;33:2049–2068. <https://doi.org/10.1111/bre.12547>

APPENDIX A

Material laws and input properties

The salt creep behaviour is described by the following equations (Munson, 1997). The transient term of the formulation is omitted, considered negligible over geological timescales. The list of parameters used is listed in Table A1.

$$\dot{\epsilon}_c = A_1 \left[\frac{q}{\mu} \right]^{n_1} e^{-Q_1/RT} + A_2 \left[\frac{q}{\mu} \right]^{n_2} e^{-Q_2/RT} \quad (A1)$$

$$\mu = \mu_0 - \frac{d\mu}{dT} (T - T_0) \quad (A2)$$

where $\dot{\epsilon}_c$ is the salt viscosity, q is the shear stress, T is the temperature, R is the universal gas constant, μ is the shear modulus and A_1, A_2, n_1, n_2 are material constants.

The sediment behaviour is represented by the constitutive SR3 model (Crook et al. 2006) that assumes an homogeneous, isotropic and porous elastoplastic material. At a high level, at each mechanical calculation step, the overall strain increment:

$$\Delta \epsilon = \Delta \epsilon_e + \Delta \epsilon_p \quad (A3)$$

is coupled to the effective stress increment with the stiffness tensor D_T :

$$\Delta \sigma' = D_T \Delta \epsilon \quad (A4)$$

where σ' is the effective stress tensor, ϵ_e the elastic strain tensor and ϵ_p the plastic strain tensor.

TABLE A1 Material properties for salt (Fredrich, Fossum, et al., 2007; Munson, 1997)

Parameter	Units	Value
E	MPa	10,000
ν		0.35
ρ	kg/m ³	2,100
A_1	1/Myr	1.89E + 39
n_1		5.5
Q_1	cal/mol	25,000
A_2	1/Myr	2.17E + 29
n_2		5
Q_2	cal/mol	10,000
R	cal/°K/mol	1.987
T_0	°K	10
T_{const}	°K	273
μ_0	MPa	12,400
$d\mu/dT$	MPa/°K	10

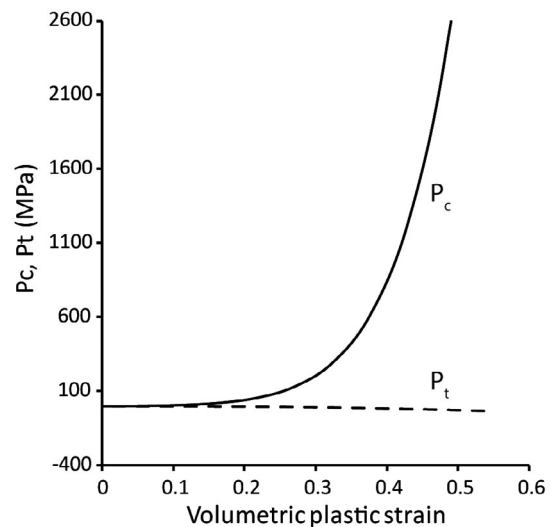


FIGURE A1 Hardening parameters for SR3 material model used for the sediments (Rockfield 2017). [Corrections updated on 25 July 2021, after initial online publication: Figure A1 and caption has been corrected in this version.]

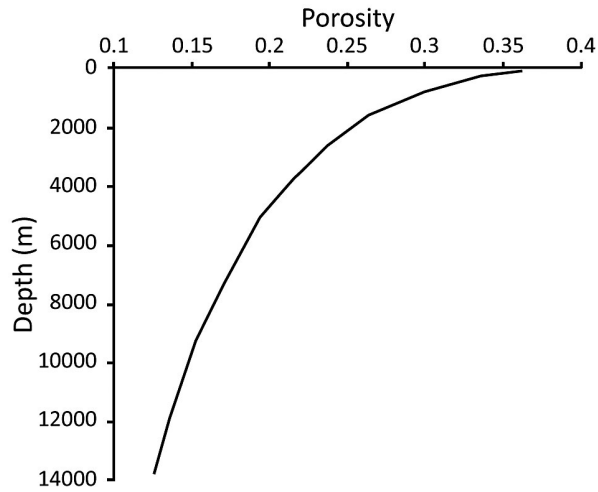


FIGURE A2 Compaction curve used for SR3 material model used for the sediments and assuming uniaxial conditions.[Corrections updated on 25 July 2021, after initial online publication: Figure A2 and caption has been corrected in this version.]

TABLE A2 Material properties for sediments (Nygard et al. 2006; Rockfield, 2017)

Parameter	Units	Value
E_{ref}	MPa	40
ν		0.25
r_w	kg/m ³	1,000
r_s	kg/m ³	2,700
k		0.01
$P_{t,0}$	MPa	0.085
$P_{c,0}$	MPa	-1
b	°	60
θ	°	51
b_0		0.6
b_1	1/MPa	0.725
a		0.25
N		1.3
n_0		0.38
Hardening properties		Figure A1

APPENDIX B

Nomenclature

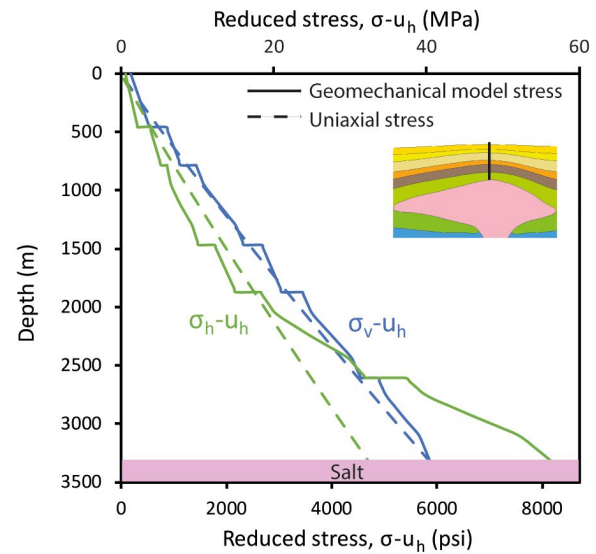
TABLE B1 Nomenclature

Symbol	Name	Dimensions
σ'_v	Vertical effective stress	L ⁻¹ M ¹ T ⁻²
σ'_h	Horizontal effective stress	L ⁻¹ M ¹ T ⁻²
u_h	Hydrostatic pore pressure	L ⁻¹ M ¹ T ⁻²
K	Horizontal-to-vertical effective stress ratio	L ⁰ M ⁰ T ⁻⁰

APPENDIX C

Stress profiles at diapir crest.

(a) Stress profile from exponential shortening (basecase) model



(b) Stress profile from sigmoidal shortening model

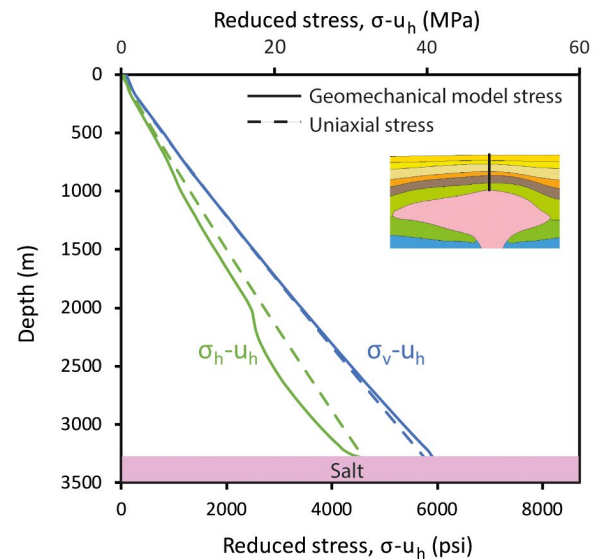
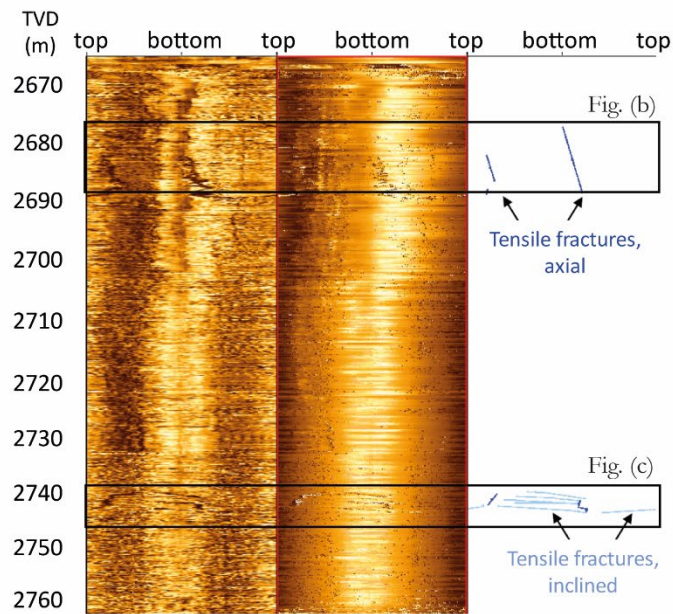


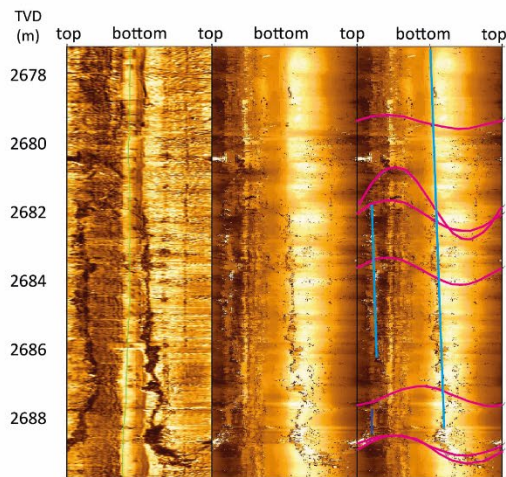
FIGURE C1 Stress profiles at vertical section along the sedimentary roof at present-day for a) BC model and b) model MV4. See Appendix B for figure nomenclature.[Corrections updated on 25 July 2021, after initial online publication: Figure C1 caption has been corrected in this version.]

Annex 4: Sandia-1 well log data and CBIL data

(a) Well section studied with CBIL (2670 to 2760 mTVD)



(b) CBIL for first fractured interval (2678 to 2690 mTVD)



(c) CBIL for second fractured interval (2740 to 2745 mTVD)

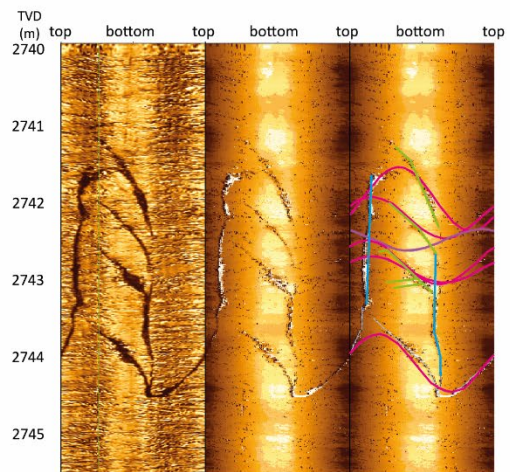


Figure A4.2: CBIL image logs acquired during the Sandia-1 well drilling between depths 2670 mTVD and 2760 mTVD (a) to establish the cause of mud losses. The zoom-in images in (b) and (c) show the pre-existing natural fractures in pink and drilling related tensile fractures in blue and green.